Three Dimensional Cell Reconstructions for Morphological Analysis and Modelling

Jonathan Albert Ratcliffe, BSc (Hons)

The University of
Nottingham

Thesis submitted to the University of Nottingham for the Degree of Doctor of Philosophy, September 2010

I would like to thank Prof. David Grant, Dr. Colin Scotchford and Dr. Jim Oliver for their unfaltering support and guidance throughout this project. I also appreciate having worked with Laura Gallimore, who is further developing the modelling aspect of this project, for being so enthusiastic and a pleasure to work with. Thanks also go to the technical staff whom have assisted my acquisition of data, particularly George Anderson and Julie Thronhill.

I am grateful to my friends, especially those who are also members of the Nottingham University Society of Change Ringers, for providing a distraction from work and for being supportive and understanding as my workload increased.

Finally, I would like to mention my parents, Albert and Julie Ratcliffe, to whom I am eternally grateful for all their love and support. I am especially thankful for all the many opportunities they have enabled me to experience through life, often at their own personal sacrifice, which have ultimately helped me to achieve this goal.

Abstract

It is highly desirable to devise a systematic approach to predict cell – material interactions, especially for novel biomaterial surfaces, and to further understanding in the complex area of attachment and spreading. The aim of this research was to produce a new method of studying morphology in real time, whereby data from live spreading cells can be collected for mathematical modelling. There is an abundance of models for sub-cellular elements, however, there are few calibrated models of whole cells; in particular, three-dimensional models predicting attachment, spreading and cell morphology have yet to be produced.

Live HOS cells were imaged using LavaCell membrane stain and CLSM every 5 min for a period of 75 min in this study, capturing sufficient detail to produce three dimensional representations of cells during initial attachment and spreading. In order for the contact line to be measured, the interface between the cell membrane and the substrate had to be imaged in sufficient resolution for accurate measurements of the angles to be made.

An image processing algorithm developed using Matlab was able to detect the edge of cells in the CLSM z-stack optical sections. These were then used to create contour plots onto which a surface representing the cell membrane could be added. These reconstructions of cells can be easily manipulated to enable the dynamic contact line of attaching cells to be measured for a model based on two-phase poroviscous flow equations. The three dimensional representations not only showed the changing morphology of spreading cells, but gave data on contact radius and area, contact angle and cell height.

The main modelling prediction is a near contact line law, which is given by;

$$\Theta^3 - \Phi^3 = \frac{3\mu(n)\ln(R/\lambda)}{\gamma}\left(3nV - J(V,n,...)\right)$$

where Θ is the dynamic contact angle (which remains to be determined by experimental means as the cell is spreading), Φ is the static contact angle, n the network density at the contact-line, J is the mass transfer rate from G- to F-actin at contact line and V equals the outward normal velocity of contact line.

Once the method had been developed for glass surfaces, the influence on attachment and spreading of various material substrate and protein conditioning layers was investigated. This was achieved by using transparent thin film coated surfaces of titanium nitride and titanium oxide and pre-coating glass with fibronectin and albumin respectively. Three dimensional representations showed the ability to reproduce the different cell response to each surface and gave comparable morphologies to cells fixed for SEM and immunocytochemical staining.

Table of Contents

List of Abbreviations

BSA	Bovine serum albumin
CLSM	Confocal laser scanning microscopy
DiI	1,1'-Dioctadecyl- 3,3,3',3'-tetramethylindocarbocyanine iodide
DMEM	Dulbecco's modified eagles media
ECM	Extracellular matrix
FA	Focal adhesion
FBS	Foetal bovine serum
FITC	Fluorescein isothiocyanate
Fn	Fibronectin
FPE	Fluoresceinphosphosphatidylethanolamine
GAXRD	Glancing (or grazing) angle x-ray diffraction
HBSS	Hank's balanced salt solution
HEPES	4-(2-hydroxyethyl)-1-piperazineethanesulfonic acid
HOB	Human Osteoblast
HOS	Human Osteosarcoma
HSA	Human serum albumin
IP	Image processing
PBS	Phosphate buffered saline solution
PVD	Physical vapour deposition
SEM	Scanning electron microscopy
SBF	Simulated Body Fluid
TiN	Titanium Nitride
TiO	Titanium Oxide
TRITC	Tetramethylrhodamine-5(and 6)-isothiocyanate
XPS	X-ray photoelectron spectroscopy
XRD	X-ray diffraction

1. Introduction

Understanding the fundamental processes of cell attachment and spreading is imperative in the biomaterials field. From the initial interactions of a cell with a surface, it is possible to make limited predictions on how that material will perform *in vivo*. The model will give an insight into the important cell-material interactions which govern whether a biomaterial elicits an appropriate host response by looking at the different morphologies adopted on different substrates. The shape that a cell adopts on a surface has been shown to have direct ramifications on the behaviour of the cell, such as affecting DNA synthesis, cytoskeletal organisation and phenotype expression [1, 2, 3, 4, 5]. Modelling how cells attach and spread may lead to increased understanding and the ability to predict how cells will react to a surface. This has implications from the conception of novel coatings with specific surface chemistries on the femoral component of a hip prosthesis, to the design of scaffolds used in tissue engineering applications to assist colonisation. Ratner *et al.* [6] draw attention to the usefulness of modelling with respect to biomaterials, describing cell-scale models as 'powerful hypotheses generators' and the need for a more quantitative understanding of the biological, chemical and physical mechanisms involved in cell adhesion and spreading.

Mathematical biology is a rapidly expanding area. Frequently, modelling is offering insights into mechanisms and interactions that are not yet fully understood. This may direct experimental approaches to test theories put forward, or explain processes that cannot yet be determined by experimental means. There have been significant recent advances on the molecular basis of cell movement, but these have highlighted that the complexity of the processes and interactions involved cannot be fully

understood by reductive experiments alone. This has led to a rapidly growing field where a number of models have been produced which attempt to account for cell spreading. However, most of these theoretical models only examine individual components; the actin network and cytoplasm, the 'free' plasma membrane, adhesion of the cell to a substrate and the underlying molecular biology that controls and coordinates these, rather than the cell as a whole [7].

This study is part of the work to develop a model of a whole cell as it undergoes attaching and spreading on a substrate. The model intends to describe cell polarization, with symmetry breaking behaviour, built upon the work described and referenced by Oliver *et al.*, King *et al.* and Herant *et al.* [7, 8, 9] rather than the one- and two-dimensional travelling wave configurations, applicable only to keratocytes or fibroblasts [10], that other models have concentrated on. For this, gaining accurate data on the contact line between the cell membrane and the substrate as the cell begins to spread and polarise will, theoretically, allow the development of a model to make predications on lamellipodial protrusion and retraction.

Once this fundamental data can be recorded, it is hoped that the model will be further developed to describe cell crawling. This is also of high relevance to the biomaterials field as cells must crawl and migrate to colonise a scaffold in tissue engineering or the surface of orthopaedic implants and fixation devices after surgery [11] and cell migration is essential to many biological phenomena, from morphogenesis in embryonic development to wound healing, the immune response, biofilm encrustation and metastasis [12].

The study aims to develop a means of measuring the dynamic contact line, where the dorsal and ventral plasma membrane intersect on the substrate, the contact

radius, and height of HOS cells as they attach and spread on a substrate. This is to aid the development and testing of a three dimensional model which intends to describe cell spreading, polarisation and resultant morphology and cell crawling.

To meet the main aim of providing contact line data, specific objectives must be met. A protocol must be developed whereby images of live cells can be gained using CLSM for extended periods during attachment without affecting the cell's behaviour, yet capturing enough detail for image processing.

The images gained by CLSM then must be processed in such a way to produce three dimensional representations of the cell's morphology, which also give quantitative data on the cell, such as contact radius, cell height and contact angle.

In order to provide data for the advancement of a mathematical model, measurements of the dynamic contact line of spreading cells must be gained to enable predictions on attachment and spreading on surfaces with different chemistries.

The trial of different stains and steps taken to optimise the CLSM image acquisition will be discussed along with the findings from the different techniques employed to characterise the substrates used.

The results of the cell spreading experiments and subsequent development of the model will then be discussed in context with other experimental data and modelling approaches presented in the current literature.

1.2. Historical Background

1.2.1. Cells

Robert Hooke is attributed with discovering cells while looking at cork through his microscope in 1665. He applied the word 'cell', from the Latin 'cellula' meaning small room, as they reminded him of the rooms monks lived in.

> *'. . . I could exceedingly plainly perceive it to be all perforated and porous, much like a Honey-comb, but that the pores of it were not regular. . . . these pores, or cells, . . . were indeed the first microscopical pores I ever saw, and perhaps, that were ever seen, for I had not met with any Writer or Person, that had made any mention of them before this. . .'*

Robert Hooke - Observation XVIII, Micrographia, or some Physiological Descriptions of Minute Bodies made by Magnifying Glasses with Observations and Inquiries thereupon (MDCLXV), 112-6.

Cell motility has intrigued scientists almost from this date when, a decade later, van Leeuwenhoek described 'pleasing and nimble' motions of tiny creatures in rainwater that put out 'horns' that extended and retracted, a significant discovery constituting the main steps of cell crawling [13]. Despite these early observations, it was not until 1839 when Schleiden and Schwann proposed the cell as the basic building block of all life.

1.2.2. Biomaterials

The terms biomaterial and biocompatibility will occur frequently throughout this thesis. Definitions of these terms were proposed by Williams in 1987 [14] and endorsed by a consensus of experts in the field.

1. A **biomaterial** is a nonviable material used in a medical device, intended to interact with biological systems.

2. **Biocompatibility** is the ability of a material to perform with an appropriate host response in a specific application.

It is inconceivable for us to imagine modern life without biomaterials; such is their prevalence and significance in medicine, dentistry and biotechnology. Yet a little more than 50 years ago, there was no understanding of biocompatibility, no medical device manufacturers (excluding external prostheses) and no usage of the word 'biomaterial' [6]. This is not to say that there was no utilisation of what we would call biomaterials today, in fact, they can be traced back through many thousands of years of human history.

Perhaps the earliest evidence of the employment of biomaterials dates back 32,000 years with linen sutures used to close large wounds [178]. Teeth are examples of early implants, with a skull of a Gallo-Roman found with a wrought iron upper premolar in a French necropolis dating from 200 A.D. and the Maya using sea shells around 600 A.D. Interestingly, both of these materials achieved osseointegration, seamless integration into the bone, despite the lack of biological understanding or knowledge of materials science [6].

The concept of biocompatibility, linking factors such as chemistry of the implant, mechanics, design, leachables and shape, wasn't properly understood until the 1950s. However, the effect of different materials in the body started to be studied properly in the 19th Century. Levert in 1829 [6] assessed the *in vivo* bioreactivity of platinum, gold, silver and lead by implanting them into dogs; reporting that platinum performed particularly well. A study in 1886 looked at bone fixation plates of nickel plated sheet steel with nickel plated screws.

During World War II, Sir Harold Ridley found that poly(methyl methacrylate) shrapnel from the cockpits of Spitfires and Hurricanes which became unintentionally implanted in the eyes of aircrew did not provoke an immune response, leading to him designing the first intraocular lens. Although attempts at hip prosthesis had been made as early as 1891 by German surgeon, Theodore Gluck, it was another British surgeon, Sir John Charnley, that developed the first successful total hip joint prosthesis in 1961, using a stainless steel 316L stem along with a high molecular weight polyethylene acetabular cup. It was during this period that the field of biomaterials was laying down its foundation principles and ideas. At this time, concepts of cell-surface receptors, cell attachment proteins, gene delivery, nuclear control of protein expression and phenotype were either little understood or undiscovered, so pioneers in the field could not have designed materials with these in mind. Ratner [6] highlights the speed at which pioneers working in the field adopted and embraced new ideas from Biology and so lists important ideas for what he believes shapes Biomaterials Science today:

- Protein adsorption
- Biospecific biomaterials
- Nonfouling materials

- Healing and the foreign-body reaction
- Controlled release
- Tissue engineering
- Regenerative medicine

Even despite significant recent advances, the complexity of the interactions involved in the above cannot be fully understood by reductive experimental approaches alone [15]. For Biologists, this has led to interest in mathematical models growing rapidly in recent years. However, they are still relatively underused in the field of Biomaterials, despite Ratner calling them 'powerful hypothesis generators'.

1.2.2.1. Biomaterials today

The biomaterials field is a rapidly expanding, multi-billion pound industry. In 2000, the lives of over 20 million patients were sustained, supported or improved by biomaterials and it is estimated that this figure increases year on year at 10 per cent. The field represents 7-8 per cent of global health care spending, exceeding $300 billion US dollars per annum. During 2008, in the UK alone, 151,746 hip and knee replacement procedures were performed [16]. Of these, 9.7 per cent of hip and 5.6 per cent of knee procedures were revisions. Although only one area of biomaterials, this not only highlights the scale of usage, but also, even after many years of development and recent scientific advances, the high revision rate is indicative of the fact that there is still much room for improvement across all areas of the field. Understanding the fundamental principles governing cell interactions with materials, for which modelling is an important tool, will lead to the next generation of implants.

Biomaterials is an interdisciplinary science and the figures above indicate the importance of its continued development. It draws upon a multiplicity of areas such as materials science, medicine, genetics, molecular and cellular biology, biomechanics, chemistry, engineering, manufacturing, mathematics and computer modelling.

Selecting and designing materials for the body is a complex procedure. One of the two main issues to consider is the host response to the insertion of the implanted material. This can be classified as [17]:

- Structural; the reaction to the mechanical properties of the material.
- Physiological; the reaction to the material itself
- Bacteriological; the invasion of microorganisms
- Immunological; the activation of complement - proteases that cleave specific proteins to release cytokines and initiate the amplification of the immune response.
- Carcinogenic; neoplasms can arise in response to chronic inflammation or chemical reaction.

Secondly, the material can also be classified as either bioinert, which causes no additional reaction above that of the foreign body response, or bioactive where the material is designed to elicit a specific response. However, in the majority of applications, it is no longer deemed sufficient for a biomaterial to merely be bioinert.

2. Literature Review

Introduction

This chapter covers the current literature available on cell attachment, spreading, morphology and mathematical modelling relating to them and the underlying sub-cellular elements that drive these processes.

In order to model cell morphology and events such as attachment and spreading on a substrate, it is necessary to understand the underlying biological processes which drive these events. The chapter begins by looking at the early attachment and spreading behaviour of cells in section 2.1 and the role of structures such as the cytoskeleton and focal adhesions in spreading dynamics and changes in morphology.

In section 2.2, cell morphology is studied in relation to the cell's underlying machinery with examples of where models have helped provide theories on processes which are not able to be resolved by experimental means alone.

The chapter then looks at the experimental methods required to validate the model. Section 2.3. looks at confocal microscopy and cell staining as a method of visualising living cells so that they can be studied as they adhere to a surface. Section 2.4. notes the effect of surface chemistry on adhering cells and details physical vapour deposition as a method of altering surface chemistries that conform to the underlying substrate. This enables chemical changes to be investigated without the influence of changes in topography.

2.1. Early Attachment and Spreading Behaviour

Many mammalian cells are spherical whilst in suspension in media. On attachment to a surface, the cell starts to change morphology, flatten and spread. The degree to which the cell spreads and the resultant morphology are good indicators as to whether the surface is suited to its intended role and its biocompatibility.

The processes of cellular adhesion can be separated into four distinct steps: protein adsorption, cell–substratum contact, cell–substratum attachment, and cell adhesion/spreading, for which there are no set time periods as they can vary greatly between surfaces and cell types [18], shown schematically in figure 2.1.

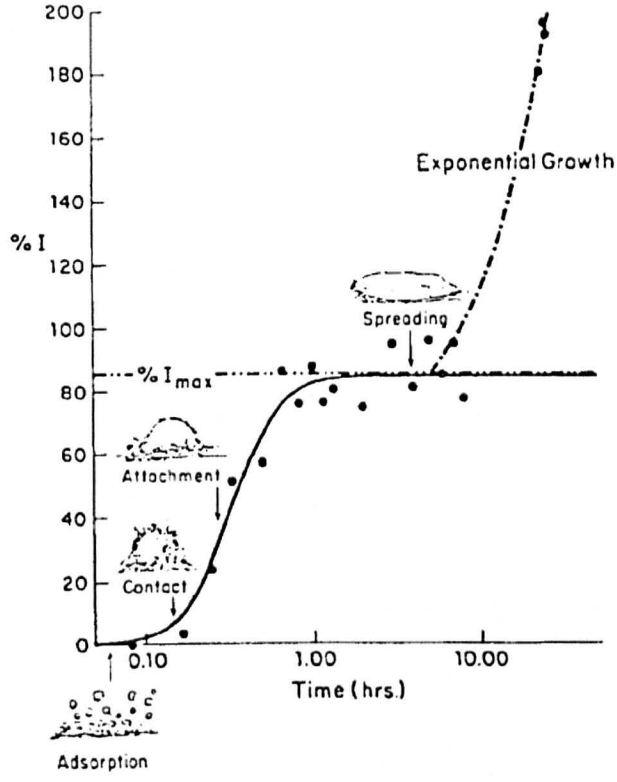

Figure 2.1. Representative curve for attaching cells. Percent of inoculum attached, % I, as a function of time, t, in hours (logarithmic). (From: [19]).

2.1.1. Protein Adsorption

Protein adsorption onto a surface to form a conditioning layer is a complex process, involving molecular- scale interactions with a surface that occur instantaneously comparative to the overall time required for cell adhesion [20, 21]. This protein layer will vary from surface to surface, as their individual properties will be conducive for binding of some proteins and not others and also influence the conformation that the bound proteins adopt, making some more conducive to cell binding and others not.

Protein adsorption from plasma *in vivo* and serum *in vitro* occurs rapidly on a material surface. It has been reported that for cells that secrete and assemble an extracellular matrix, surface properties such as chemical composition, wettability and topography may affect the ability of the cell to deposit its ECM by stabilising the protein deposits or by affecting the orientation of cell-binding domains in the deposits [22, 23].

2.1.2. Sedimentation

Cell contact and attachment involve the sedimentation of the cell to approximately 50 nm of a surface, at which point physical and biochemical forces begin to close the gap between the cell and surface. Cells arriving at a surface experience both repulsive and attractive forces. Repulsive forces arise due to the distribution of electrostatic charges on cell and substrate surfaces. Attraction is due to electromotive forces between cell and the substrate. The total potential between a cell and substrate at a given separation can be calculated from these giving a potential energy function that has two attractive potential wells separated by a repulsive barrier. For physiological saline, it has been calculated that the first

encountered well exists between 5-8 nm from the substrate. Gravitational sedimentation of cells to the first potential well is very rapid. A stochastic process similar to Brownian motion causes cells to cross the electrostatic barrier, leading initially to an exponential decay in the number of depositing cells at the first well.

As a significant fraction of cells become adherent to the substrate the surface potentials change. These changes lead to a coverage-dependent attachment rate. Rates of attachment can reach saturation. Both the initial rate of percentage cells attaching and plateau value are, therefore, dependent on the starting cell number [19].

Initial cell contact with the substratum occurs by spreading as a viscous droplet, which is independent of the surface or cell type [24]. The spreading stage can be separated into two parts, passive and active spreading [24]. Initially spreading is likened to the manner in which a liquid adheres to a surface [25] and expends no metabolic energy. Once in the active stage, the cell employs such methods as actin polymerisation and myosin II contraction to determine its own morphology.

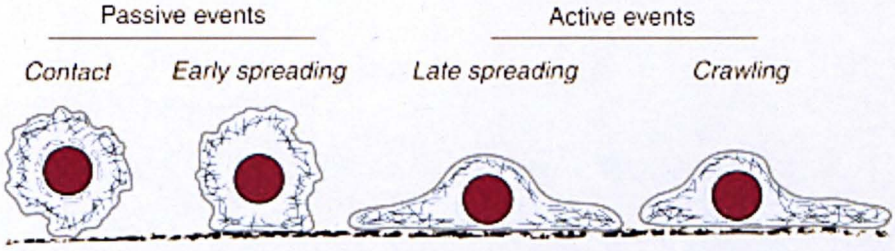

Figure 2.2. The stages of cell spreading. (From: [24]).

2.1.3. Early stage spreading

Cuvellier [26] showed that early stage spreading was isotropic when measuring contact area as a function of time for different cell types and different adhesive coatings on glass cover slips. He also found that the spreading curves all had the same slope, when plotted on a log log axis.

2.1.4. Active Spreading and Pseudopodia

The exact mechanism of the active stage of cell spreading is still not fully understood. It is widely accepted that the main mechanical components responsible for locomotion of an animal cell are similar across species [12]. During the active stage, the cell starts to lose its spherical morphology and projections, lamellipodia and filopodia, may be extended out from the cell body. The subsequent movement of the cell body can then be credited to traction forces between the advancing part of the cell and its rear [27]. Lamellipodia play an important role in adhesion as well as, when they form ruffles, the processes of macropinocytosis and phagocytosis [28]. Lamellipodia can be subdivided into different domains shown schematically in figure 2.3.

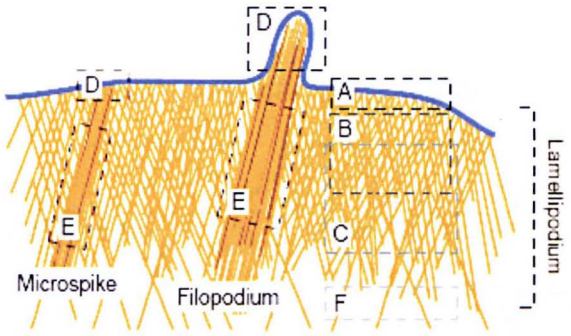

Figure 2.3. Schematic representation of subdomains in lamellipodia and filopodia: (A) tip of lamellipodium; (B) actin meshwork; (C) region of major disassembly; (D) tip of filopodium; (E) bundle; (F) undegraded filament that contributes to the cytoplasmic network. (From: [28]).

2.1.4.1 Signalling during Active spreading

The signalling molecules found at the tip of lamellipodia and filopodia are Rho GTPases. Research in the 1980s led Ridley *et al.* [29] to microinject RhoA into mouse 3T3 fibroblasts whilst screening growth factors for their effects on the actin cytoskeleton. She found that RhoA/B/C were required for serum-induced stress fibre formation and thus showed that Rho had a regulatory effect on the actin cytoskeleton.

Nobes and Hall [30] showed that it was Rac1 and Cdc42 that were responsible for the formation of lamellipodia and filopodia respectively. They also found that there was a degree of cross-talk as Ras can activate Rac and Cdc42 can activate Rac so they concluded that filopodia are intimately associated with lamellipodia and outlined the signal pathway in figure 2.4.

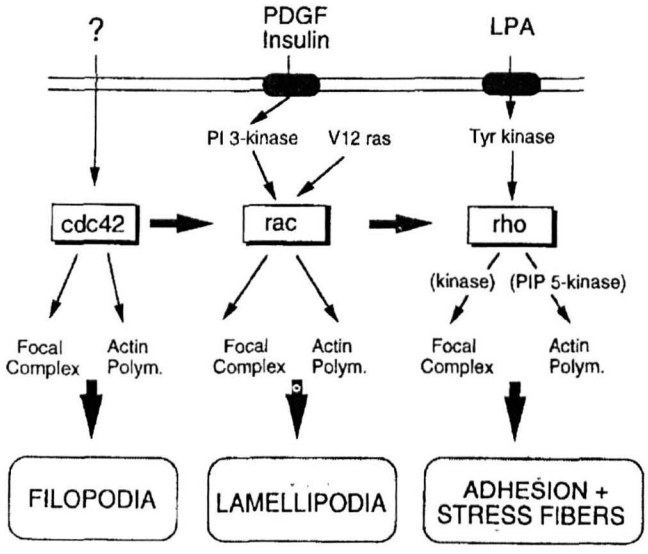

Figure 2.4. Rho, Rac, and Cdc42 Signal Transduction Pathways in Swiss 3T3 Fibroblasts which lead to the formation of lamellipodia. (From: [30]).

GDP-GTP exchange factors (GEFs), such as Vav and Sos, are required as mediators for the activation of Rho GTPases by growth factor and integrin receptors [28]. It is unknown whether GEFs are located at the sites of actin assembly or if Rho GTPases are recruited to these sites after being activated elsewhere in the cell by GEFs. However, Kranewitter *et al.* [31] showed by live video fluorescence and immunoelectron microscopy that GFP-tagged Vav-1 was concentrated at the tip of filopodia, suggesting that GEFs are located at the sites of actin assembly. The importance of actin polymerisation is outlined in the following section.

2.1.4.2. Actin Polymerisation

Actin polymerisation is the main driving force behind cell movement during spreading [15, 26, 28, 32]. It has been shown that gel osmotic pressure or hydrostatic pressure cannot account for lamellipodia extension as the length of the lamellipodia

do not extend at the same rate for cells in the early stage of spreading, as these two models would suggest [33]. Actin can be divided into two domains, which themselves can be subdivided into a further two subdomains [34]. An ATP or ADP molecule is located in the crevice between the domains and a calcium ion binds to the β- and/or β- and γ-phosphates. The two domains are composed of a five-standard β sheet which consists of a β meander and a right handed βαβ unit [34] which can be seen schematically in figure (4). Actin subunits (G-actin) are polymerised to form helical actin filaments (F-actin) that push against the leading edge of the cell [35]. The filaments are subsequently disassembled and recycled at the front, known as actin turnover. X-ray fibre diffraction patterns and electron microscopy have been used to establish the structure of F-actin. It forms a helical filament with 13 actin molecules per turns repeated at approximately 360Å [35]. The filaments have a barbed end, where subunits attach rapidly, and a pointed end, where the dynamics are slower.

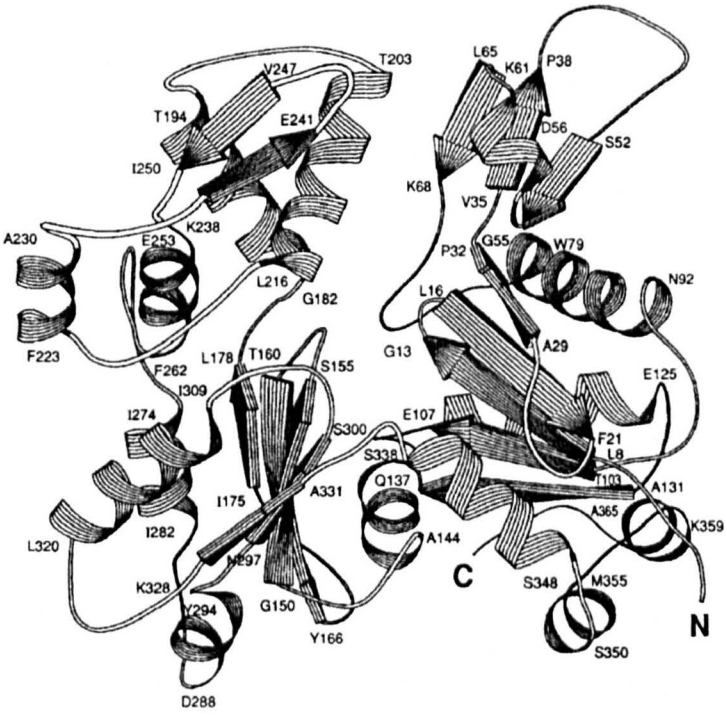

Figure 2.5. Schematic diagram of actin, showing the two domains. (From: [34]).

Carlier and Pantaloni [36] showed that as ATP hydrolysis is involved with actin polymerisation, G-actin binds one molecule of ATP which is hydrolysed to ADP on polymerisation. The critical concentration at ATP-G-actin is maintained by monomer-polymer exchange reactions, under steady-state conditions. The steady state concentration (Css) when both ends of the F-actin are free in solution can be written as [37]:

$$Css = \frac{k_+^B C_C^B + k_+^P C_C^P}{k_+^B + k_+^P}$$

where k_+^B and k_+^P are the association rate constants of ATP-G-actin to the barbed and pointed ends, respectively and C_C^B and C_C^P are the critical concentrations of the barbed and pointed ends.

2.1.4.3 The Dendritic Structure of F-actin

Arp2/3 complex is vital in causing actin to nucleate and organise the filaments in a dendritic orientation [32]. It was one of the first molecules associated with actin polymerisation to be identified using *in vitro* techniques [28]. Electron microscopy (EM), using critical-point drying was employed by Svitkina and Borisy [38] showing the dendritic nature of actin in lamellipodia *in vivo* using keratocytes and fibroblasts. Using immunofluorescence and immuno-EM, they concluded that Arp2/3 complex is responsible for incorporating actin filaments and protecting the ends from depolymerisation as well as promoting branching at an angle of 70°. They also showed that actin depolymerising factor (ADF) / cofilin promotes depolymerisation at the rear after dissociation of the Arp2/3 complex. They found that their results

supported the dendritic nucleation model whereby the Arp2/3 complex initiates a new filament as a branch on the side of an existing filament [39] and suggested that a branched actin array is recycled from the rear to the leading edge of the actin structure, rather than individual filaments.

2.1.4.4. Other Molecules involved in Actin Polymerisation

The use of Green Fluorescent Protein (GFP) and live-cell microscopy has enabled many of the other components involved in polymerisation and disassembly to be identified. Frischknecht and Way [40] used pathogens to show that the tips of lamellipodia and filopodia serve the function of directing actin polymerization. They showed that GFP labeled vasodilator-stimulated phosphoprotein (VASP) accumulates at the tip of lamellipodia and filopodia and corresponded to where the fast growing end of the actin meets the cell membrane. Rottner [41] was able to prove that the amount of VASP recruited to the lamellipodium tip increased with protrusion rate.
Other proteins that play a part in stabilising the actin network include cortactin, which Kaksonen [42] *et al.* found to be co-localised with Arp3. By using GFP-actin and cortactin-RFP and then phalloidin in fixed cells, they found that F-actin bundles that remained stable for periods of around four minutes were not stained for cortactin-RFP and showed that it was only associated with a dynamic sub-set of F-actin. It was also shown that cortactin-RFP and GFP-Arp3 co-localise in the lamellipodia and movement of both stopped when actin polymerisation was inhibited by cytochalasin D. They suggest that cortactin may act as a linker between the branched actin and transmembrane receptors via PDZ-proteins, as it can bind to these with its SH3 domain.

Actin crosslinking proteins such as filamin, α-actinin and coronin also work to stabilise the network [28]. Filamin may also act as a transmembrane linker as it can bind membrane proteins with its C-terminal region whilst bound to actin [43]. Small *et al.* [28], also suggest that it could be a docking site for Rho GEF proteins and small GTPases, although say that the significance is unclear. Rivero *et al.* [44] found that motility was unaffected by generating Dictyostelium double mutants lacking α-actinin, but was stopped when filamin was also removed, showing a degree of complementation between the two. The rate of polymerisation is kept in check by capping proteins, such as CapZ, which attach to the fast growing barbed ends and control filament growth by stopping further polymerisation [45].

2.1.4.5. Filopodia

Filopodia are finger-like projections that protrude from the lamellipodia, as can be seen in figure 2. They are formed by the bundling of fascin, f-actin and fimbrin (plastin) which are found as filaments in the lamellipodia [28]. These bundles are assumed to be extensions of pre-existing filaments in the lamellipodia, as antibody staining has shown that there is an absence of Arp2/3 within the filopodia [38]. Filopodia often experience rapid lateral movement which is attributed to the geometry and flow of filaments in the lamellipodium [46]. Filopodia also differ from lamellipodia in that they have a different complement of proteins at their tip. They have an unknown, heavily phosphorylated protein, are able to recruit Vav and do not have Scar/WAVE-1 [28].

2.1.4.6. Actin Depolymerisation.

Theriot and Mitchison [47] showed that in goldfish keratocytes, depolymerisation occurs uniformly throughout the meshwork. Depolymerisation only occurs at the free pointed ends and not at the barbed ends concentrated at the leading edge [38]. The ADF/cofilin protein family is responsible for actin depolymerisation [28]. ADF/cofilin binds the ADP-bound forms of G and F actin and under physiological conditions, Carlier *et al.* [48] found that ADF1 binds ADP-G-actin with 100 fold higher affinity than ATP-G-actin. ADF/cofilin also increases the rate constant for actin dissociation at the pointed ends. The actin filament is held together by weak diagonal bonds and strong longitudinal bonds between the carboxyl termini of actin molecules [47]. As Brownian motion causes the filament to bend, the longitudinal bonds break and reform. ADF/Cofilin can bind to subdomain 1 and 2 of the actin monomer where the bond breaks occur. This prevents the bond reforming and causes a rotation at this point, straining surrounding bonds and increasing the likelihood that they will break, thus severing the filament. It is also suggested that cofilin may bind at the pointed end, changing the conformation of actin and weakening the longitudinal bond leading to its release [49].

2.1.5. Cell Locomotion

Abercrombie [50] summarised cell crawling as a five step cycle:

1. Protrusion of a lamellipodia over the surface;
2. Adhesion of the lamellipodia via focal adhesions;
3. Translocation of the cell body towards the leading edge;
4. Detachment of the cell's rear edge
5. Retraction of the cell's rear edge.

This is shown schematically in figure 2.6.

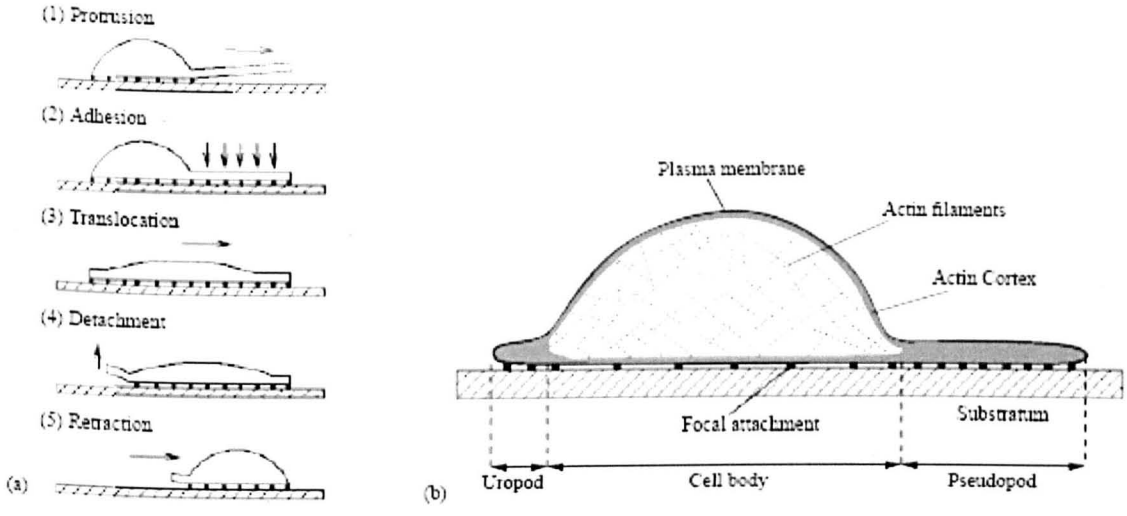

Figure 2.6. A. The 5 stage crawling cycle outlined by Abercrombie and B. The main components of animal cell crawling. (From: [7]).

These stages are more perceptible in slow moving cell types such as osteoblasts and fibroblasts. Cells which migrate rapidly, such as leukocytes and keratocytes give the impression of gliding over the surface by protruding and retracting smoothly without forming obvious attachments [51]. Cells crawl along a surface in response to external stimuli which can be physical, chemical, diffusible or non-diffusible signals that are detected by receptor molecules on the cell membrane. This then sets off a signalling cascade within the cell, enabling the processes required for movement, such as the restructuring of the actin cytoskeleton [52]. A crawling cell maintains a relatively constant overall appearance, but its internal components experience a steady flux and rearrangement [27]. The cell becomes polarized, leading to the accumulation of molecules to specific areas of the cell. Phosphatidylinositol (1, 25, 26) trisphosphate (PIP_3) is one of the first molecules to become polarized to the leading edge of the cell in response to chemotactic agents and acts to recruit other molecules to the membrane [51]. This can then lead to the formation of

lamellipodium with the recruitment of Rac and Cdc42, as outlined in 3.3.1. Locomotion is usually described as a two phase flow, with the actin polymer network the aggregate phase and the percolating cytosolic saline with proteins, such as G-actin, the solvent phase [27]. Bereiter-Hahn *et al.* also lists the forces which drive cell migration as, tension, hydrostatic pressure (including local osmotic pressure), pressure generated by actin polymerisation and adhesion to the extra cellular matrix. Only cells which have an acto-myosin cortex can exert a hydrostatic pressure on their interior as mathematical and qualitative models agree that cell volume remains constant [27]. It has been reported [51] that cells show different migratory behaviour *in vitro* to *in vivo*. Cells migrating *in vivo*, characteristically, are more directed, forming long stable protrusions in the direction of travel.

The traction forces of migrating cells have been measured by a method developed by Harris *et al.* [53], using a silicone rubber substrate which wrinkled as cells exerted a traction force on it. They found an inverse relationship between the tension exerted onto a solid substrate and speed of locomotion. The direction of the tension force relative to the direction of crawling varies between cell types. Oliver *et al.* [54] notes that keratocytes produce most of their tension at a right angle to the direction of movement, whereas Bereiter-Hahn *et al.* [27] state that in fibroblasts, traction corresponds with the direction of movement. This difference is due to the layout of adhesion points and stress fibres in the cells. In fibroblasts stress fibres start from focal adhesions in a zone just behind the leading edge. At the rear end, focal adhesions detach and disassemble allowing it to follow the propagating front. Keratocytes are nearly devoid of focal adhesions and instead have minor traction forces between the distal part of the lamella and the cell body. The cells elongate perpendicular to the direction of movement, as do most of the fibres which are therefore anchored at lateral areas to the substrate [26].

Cells gain purchase on the surface using focal adhesions (FAs) [52] which also play an important role in cell signalling. These begin as protrusions at the leading edge of the cell. They are formed by the polymerisation of actin filaments and are stabilised through the formation of adhesive complexes, regions where integrin receptors, actin filaments and associated proteins group together [55]. The dot like focal complexes at the front of the cell can undergo changes in structure and properties to stress-fibre-associated contacts and through to fibronectin-bound fibrillar adhesions [31]. Immunofluorescence and immunoelectron microscopy have been used to reveal the complexity of FAs [56] showing some of the multitude of proteins contained within them.

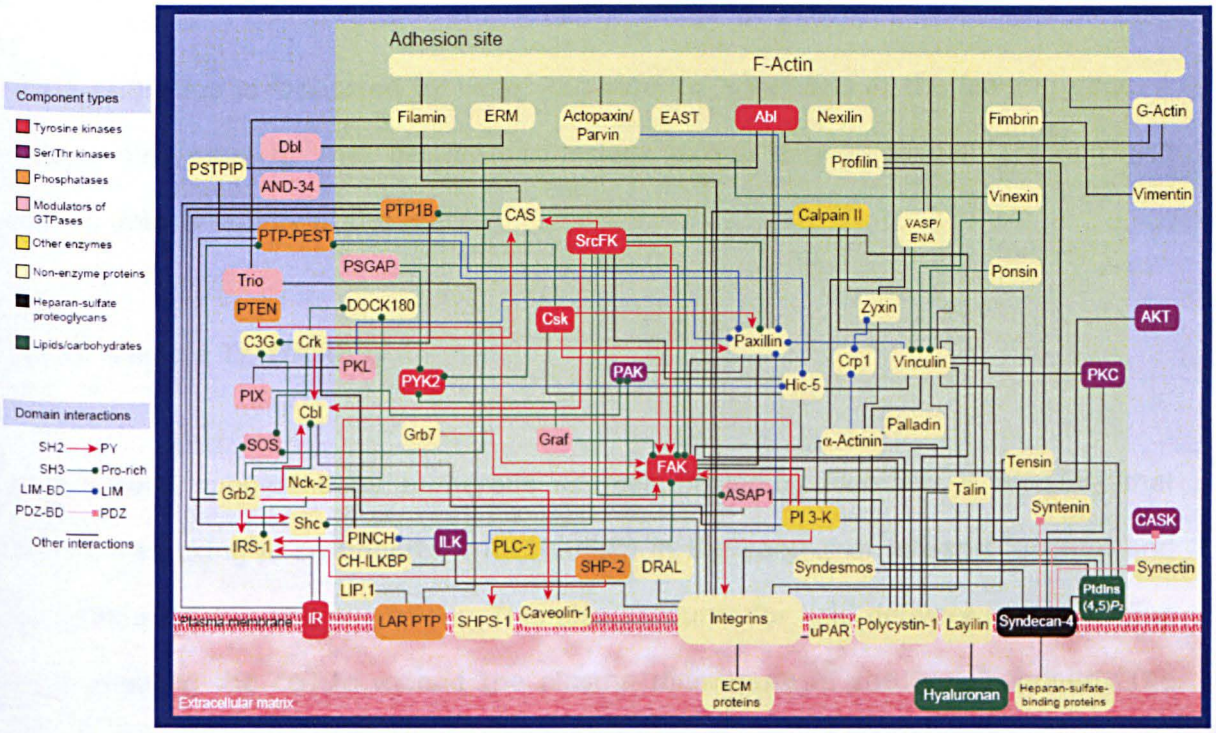

Figure 2.7. Schematic diagram showing the complexity of Focal Adhesions (From: [56]).

Integrins have been identified as the main transmembrane extracellular matrix (ECM) receptors and mediators of adhesion in FAs [57]. Membrane based integrins,

stimulated by contact with a surface protein, instigate a complex signalling cascade which subsequently leads to changes in the cell, including cellular morphology and the generation of contractile forces by motivating the actin network [26]. Integrins are heterodimers formed of α- and β- subunits. They are comprised of three domains: a large extracellular domain which is responsible for ligand binding, a cytoplasmic domain and a transmembrane domain [56]. Integrins display heterogeneity, however, specific integrins can bind different ECM molecules and a specific ECM molecule can be bound by many different integrins [56]. Vinculin is one of the most prominent proteins in the FAs which is involved in the linkage of integrin adhesion molecules to F-actin [56]. Figure 2.7. schematically shows the complexity of FAs and how they provide a link between F-actin and the substrate.

Rapid migration is facilitated by weak Rac-induced adhesions at the leading edge. A compromise must be met between adhesions strong enough to gain traction, yet able to detach rapidly at the rear.

2.1.6. Vesicle Trafficking

It has been suggested by numerous sources, including Fletcher *et al.* [58] that vesicle trafficking is an important mechanism in the control of integrin function and thus cell adhesion and migration. This also accounts for lipid delivery to the leading edge allowing the cell to extend the plasma membrane at the lamellipodium. The precise trafficking pathways are unclear [58], but it has been suggested that its role ranges from recycling of adhesion molecules to bulk membrane flow. Abercrombie *et al.* [59] used time lapse microscopy to show membrane flow in fibroblasts migrating over cover slips coated with loosely adhered carbon particles. Some carbon particles became attached to the dorsal surface of the cell and migrated away from the

leading edge in a straight line, at rate of 2 μm / min. The carbon particles came to rest and accumulated at the rear of the cell, suggesting that the surface membrane is taken up and transported to the leading edge, allowing the cell to extend itself. If all regions of the leading edge were equally active, the rate of rearward migration of the membrane would mean that the entire surface would be taken up every 25 minutes [60]. However, experiments using lines photobleached into the stained membranes of randomly migrating neutrophils did not find sufficient evidence of rearward flow [60]. It is also proposed that the role of vesicle trafficking may vary between cell types and through different phases of cell motility. For instance, cells such as fish keratocytes that migrate at 30 μm / h and have a crescent morphology [61] vary greatly from Madin-Darby canine kidney (MDCK) cells which migrate at 20 μm / min, maintain cell-cell contacts and form a triangular morphology [61]. This would suggest that both cells required different regulatory mechanisms, such as faster recycling pathways for FAs in keratocytes, different levels of expression of adhesion molecules and different requirements of leading edge actin polymerisation and acto-myosin contraction [58].

As will be described further in Section 3: *Mathematically Modelling Spreading: Theory*, these intricate processes will be largely neglected from the model due to their complexity. To produce a tractable mathematical formulation of the reactive flow model, it is necessary to ignore the microscopic details of the motion and configuration of the network and solution phases, such as actin treadmilling and the interaction between the cytoskeleton and FAs, and to focus instead on a representation in terms of average fields. Several studies have shown [145, 146, 147], by comparing models to experimental observations, that this is a fully plausible method of modelling without the need to employ extremely complicated mathematics.

2.2. Modelling and Cell Morphology

2.2.1 Cell Shape Relating to Underlying Physics and Biochemistry in Migration

From the circular shape of cells stationary on flat surfaces and the half-moon shape of motile fish keratocytes [54], the elongated shape of fibroblasts [27] and the pulsating amoeboid shape of neutrophils, different cell types adopt many different morphologies whilst migrating. D'Arcy Thomson [62] suggested that the multitude of cell shapes observed correlate directly with the underlying mechanical phenomena. It is along the lines of this theory that the modelling work that this study intends to provide data for will be based.

2.2.2. Boundary Kinetics

A major influence on the shape of migrating cells is their dynamic boundaries; the balance between extension and retraction [63]. One of the simplest examples is that of the gliding keratocyte. An accompanying graded radial extension (GRE) [60] model describes a steady state situation whereby local extension of the cell boundary is perpendicular to the cells edge. In order to maintain its shape, the rate of extension must be graded from a high rate at the centre of the leading edge, to zero at the sides. Likewise, at the rear of the cell, retraction is fastest at the centre of the trailing edge and slowest at the sides.

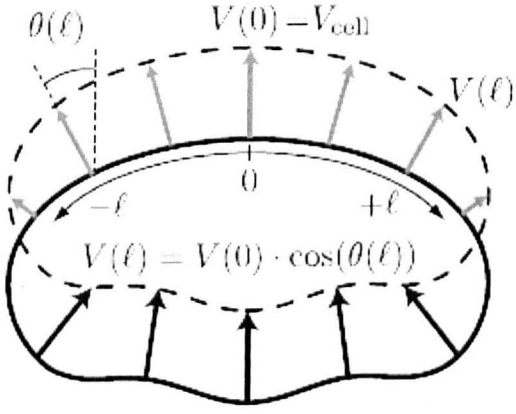

Figure 2.8. The graded radial extension model [35]. The cell boundary of a keratocyte is shown before (solid) and after (dashed) forward migration. In order to maintain a constant shape, the protrusion (light) and retraction (dark) have to be graded along the boundary. The extension rate as a function of arc length, *l*, is denoted *V(l)*. Cell shape is determined from the local angle between the vector normal to the boundary and the direction of crawling, *θ(l)*, which is given by the equation shown. (From [35]).

With more complex movements and morphologies, which may not be in steady state, a rule based geometric model may be used based on the perimeter [60]. The rates of protrusion and retraction are regulated by a model that incorporates local stimulation and global inhibition of protrusion activity. The rules are such that local protrusion is calculated from lateral protrusion signals, with a stochastic positive feedback loop accounting for increased protrusion in already-protruding regions. The retraction signal is initiated by a global inhibition rule, where the retraction rate is constant along the boundary and proportional to the total protrusive activity. The points along the cell perimeter either protrude or retract along spokes radiating from the centroid of the cell, rather than extending in a direction locally normal to the

boundary. This model is able to accurately reproduce the shape and trajectory of amoeboid Dictyostelium cells.

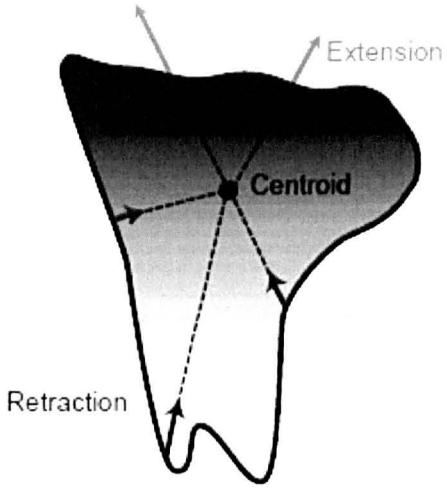

Figure 2.9. Rule based non steady state boundary conditions model. (From: [60]).

To advance beyond this, models need to consider the underlying biophysics and biochemistry to account for shape and movement [69].

2.2.3. Actin and lamellipodial morphology

The combination of the actomyosin cytoskeleton, focal adhesions and the cell membrane largely determine the cell morphology. A biophysical model [64] attempting to describe why lamellipodium are so flat, ~0.1-0.2 μm, proposes a positive feedback loop where polymerising barbed ends push and curve the leading edge of the membrane. It suggests hypothetical membrane associated actin-nucleation complexes could have curved membrane domains which preferentially target them to membrane regions with high curvature.

The protrusive regions of the cell membrane can be described as two distinct zones, the lamellipodia and the lamella [65]. Actin at the lamellipodium assembles at the leading edge and disassembles within a few microns. This is joined to a second network in the lamella, where myosin contraction is coupled with substrate adhesion. Alexandrova [65] observed a boundary of intermittently spaced FAs between the lamellipodia and the lamella. The boundary formed a concave arc shape between the FAs which act like 'jetties' and the boundary as 'arches' which the retrograde actin flow breaks against, see figure 2.10. Nascent FAs appeared ahead of the boundary which, within a few seconds, moved towards these new FAs at the same speed as local protrusion of the leading edge.

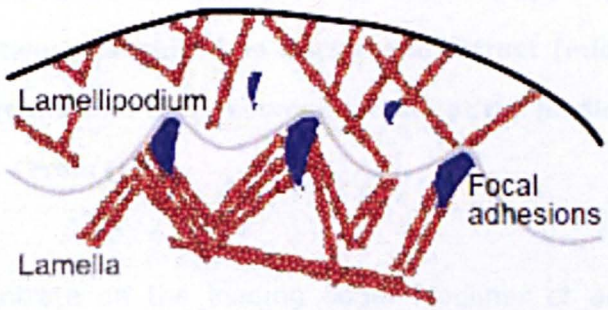

Figure 2.10, Schematic diagram of the observations by Giannone where the boundary formed a concave arc shape between the FAs which act like 'jetties and arches' which the retrograde actin flow breaks against. (From: [65]).

In contrast, Giannone *et al.* [65] proposed from his studies that the lamellipodial actin network lies above the lamellar network. He suggests that the myosin clusters periodically pull the lamellipodium rearward relative to the lamella leading to a buckling of the leading edge. This describes the cycles of protrusion and retraction

that Abercrombie noted in his studies [50] making it a more logical explanation of the mechanism.

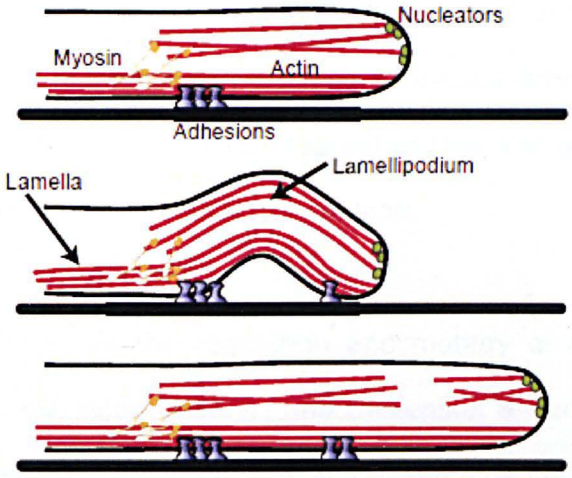

Figure 2.11. Schematic diagram of the leading edge dynamics as described by Giannone. The lamellipodium sits on top of the lamella (top). Myosin motors pull on the lamellipodial network causing it to buckle and retract (middle). Consequently, the lamellipodium breaks, and then resumes growth at the leading edge, resulting in protrusion (bottom). (From [65]).

Many studies concentrate on the leading edge. Mogilner *et al.* [66] developed a mathematical model describing the key details of actin dynamics in this region. Their model predicts that the optimal density of barbed ends is roughly proportional to membrane resistance and was able to match observed values given by Boquet [67]. It predicted that the rate of steady motion is nearly independent of thymosin β4 concentration, an actin-sequestering agent [33], which is also in agreement with the literature [68]. Their treadmilling model predicted that ADP-G-actin distribution on disassembly from the minus ends of actin filaments has a maximum close to the front of the cell, but due to diffusion is nearly homogeneous. This agrees with Carlier

et al. [48]. Their model also predicts that protrusion velocity is inversely proportional to the resistance force, which has not been fully tested.

Mogilner *et al.* [10] also produced a mathematical model that showed the thermal motions of polymerising filaments can produce a directed driving force. This was an improvement from earlier models which suggested that the actin filament was stiff and that thermal fluctuations only affected the load.

Models which concentrate on the regulation and motility of actin turnover include Carlier *et al.* [36], as mentioned earlier, and Dickenson & Purich [69]. Dickenson & Purich proposed a mechanochemical model for force generation through affinity modulated, clamped filament elongation, proposing that filaments can elongate while remaining tethered to a motile surface. They broke down the mechanism into three steps, which they labelled Lock, Load and Fire fig (2.12). The Locking step is where the terminal actin-ATP subunit binds to a clamp on the surface of an actin filament, in the loading step, actin-ATP monomers bind to a filament end and the fire step is where ATP hydrolysis on the clamped subunit weakens the filament's affinity for the clamp. As filaments elongate independently, with ends anchored within a cross linked network, they experience different states of loading; going through a cycle of elongation, compression and tension. Each stage of the three step cycle increases compression on the leading filaments, or relieves tension on the taut lagging filaments. They use step like motion of about 5.4nm observed by Kuo and McGrath [70] in Listeria monocytogenes to validate their model. The authors chose not to account for any force-induced dissociation of the filaments from the clamp or breakages of the filaments under tension. Nor did they account for filament binding interactions that may affect the stiffness or motility of the filaments, such as cofilin; or any consideration of the hydrodynamic profile of the propelled object, or other

viscous resistance to motion. They also avoided detailed modelling of filament dynamics and filament-filament interactions.

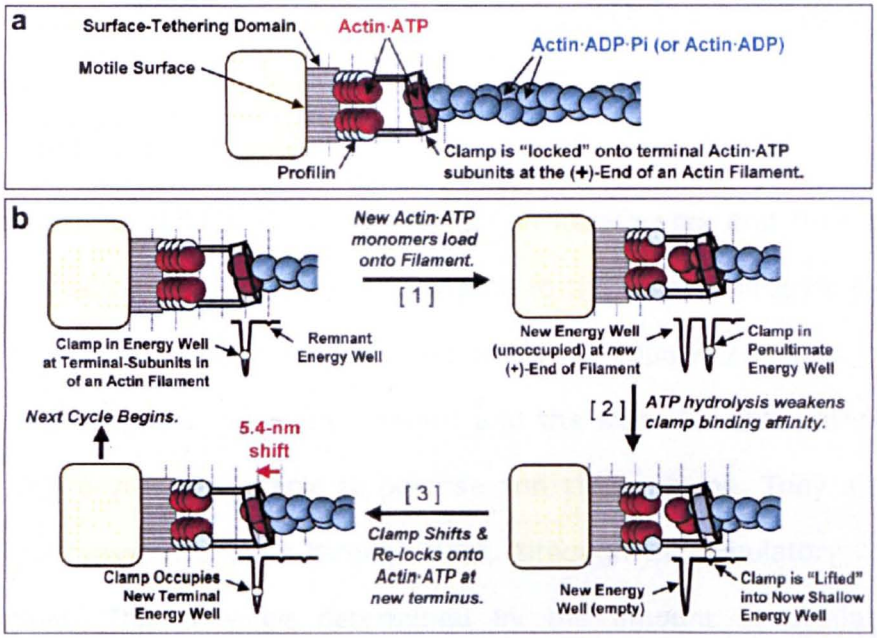

Figure 2.12. Schematic diagram illustrating the clamped filament model. (From: [41]).

2.2.4. Motility and shape in Keratocytes

Keratocytes are often chosen as a modelling subject as they maintain a constant shape, speed and direction over relatively large distances [54]. They can also be successfully modelled without incorporating signalling molecules or microtubules, suggesting that, in this cell type at least, they are not necessary for movement. Euteneuer *et al.* [71] show that the global regulatory role of membrane tension is important in cell shape and that local actin assembly at the leading edge and disassembly at the rear are both modulated and coupled by forces imposed on the actin network by the membrane. They theorise that the graded distribution of actin filament density is crucial for the graded protrusion of Keratocytes, as described earlier. The growing filaments compete for resources to branch out new filaments,

while existing filaments get capped and lag behind the leading edge. Filaments at the centre of the leading edge are able to outcompete those at the sides as they are uninhibited by adhesion complexes competing for similar molecular resources at the rear corners of the cell.

Although myosin is not crucial for movement in keratocytes and they continue to move after myosin inhibition, it does contribute to the motility process [72]. Myosin is able to contract the actin network weakened by depolymerisation, which may contribute to pulling the cell body forward and the sides inward. Without myosin, stationary keratocytes are unable to polarise and start moving. They also reported that cell area does not change through time, although the regulatory mechanisms remain unclear. This may be determined by the amount of available plasma membrane which could be regulated by exchange with intracellular sources. Adhesions and myosin may play a role in supplementing membrane area regulation and controlling cell size.

For actin treadmilling to translate into cell movement, there must be coupling with adhesion molecules. It has been reported that adhesion is graded from front (strongest) to rear (weakest), but regulation of this is unclear [73]. They suggest that rapid assembly of integrin, talin, vinculin and other focal adhesion molecules occur where nascent actin networks form, followed by aging which leads to weakening as they approach the cell rear.

2.2.5. Motility and shape in Fibroblasts

As mentioned earlier, the fibroblast presents a more challenging subject to be modelled. Fibroblasts have discrete mature adhesion sites at their outer edge [74]. These sites are connected by actin fibres which outline the cell periphery in a sequence of convex arcs and protrusive activity between them can be slow. The first model explaining the shape and radius of the arcs was based on a balance between elastic line tension in the actin fibres (F) and surface tension (T) of a cell membrane/actin cortex, described by the Laplace law $T = F/R$, giving a radius of $R = F/T$ (shown in figure 2.13). By inhibiting myosin, the model would predict that the line tension of the actin fibres would decrease, leading to increased curvature of the boundary. This was observed experimentally by Thery *et al.* [75].

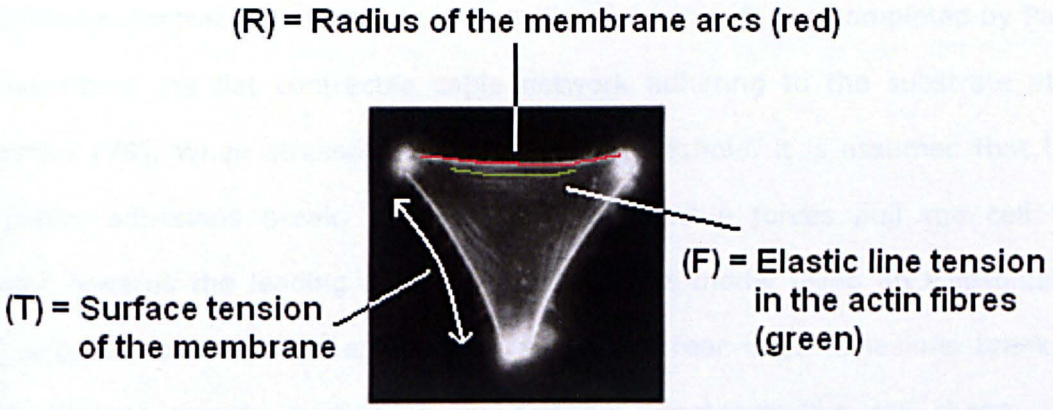

Figure 2.13. Elastic line tension was measured in the actin fibres (green) along with surface tension of the cell membrane/actin cortex, to give the radius of the convex arcs (red) between adhesion sites. (Modified from: [74])

The shape of fibroblasts depends on the location of the discrete adhesion sites, at the same time, the formation of these sites depends on cell shape [76]. This has

been observed experimentally by plating cells on polygonal adhesive islands [77]. An explanation of this, put forward by Lewis *et al.* [78] observing fibroblasts on cover slips using a modified inverted microscope for Hoffman modulation contrast microscopy, may be that adhesion maturation is triggered and maintained by force, whereby at the corners, stress fibres from both sides pull the adhesion inward, causing maturation. Along the smooth parts of the cell boundary, the stress fibre forces pulling on an adhesion site act in opposite directions and cancel each other out, so adhesions disassemble.

It is argued that the nature of the adhesion sites is what causes the different shapes of keratocytes and fibroblasts. Discrete strong adhesions play a minor role in keratocytes, whereas their role is significant in fibroblasts, disrupting protrusion of the actin network as described above [77].

An adhesion-contraction model of the lamellipodial network was completed by Paul *et al.* describing the flat contractile cable network adhering to the substrate at the periphery [79]. When stressed above a certain threshold, it is assumed that these peripheral adhesions break, whilst internal contractile forces pull the cell body forward towards the leading edge. On applying the model using an ellipsoidal cell with a broad leading edge and narrow sides, the rear edge adhesions break and sharp corners emerge leading to the crescent keratocyte-like cell shape. When starting with an ellipsoidal cell with a narrow leading edge and broad sides, the adhesions to the rearward half of the sides break, but not those at the very rear, leading to a triangular fibroblast-like shape with concave sides. Mogilner [63] proposes that this shows that the extent of lateral spread of actin protrusive activity along with global retraction, governed by myosin and/or membrane tension, and force dependent adhesion control the multiplicity of cell shapes.

2.2.6. Biochemical Pathways and Microtubules

The complex biochemical pathways with their multiple feedbacks and crosstalks play an important role in modulating the mechanical complexes and thus have a large effect on cell shape [80, 81]. The activation and distribution of signalling molecules depends on cell shape and in turn, their distribution affects cytoskeletal dynamics contributing to cell shape. A reason for this dependence is that signalling molecules are activated at the cell membrane and diffuse through and get de-activated in the cytoplasm. This leads to a cell-shape-dependent gradient in the distribution of these activated signalling molecules. It is unclear whether these spatial molecular distributions scale with size in a specific dynamic geometry [82], or have inherent spatial scales [83].

Microtubules also play a role in cell motility and polarity and may also determine the length of some motile cells [84].

Microtubules are composed of the basic protein subunit, tubulin [85]. This occurs as an α/β heterodimer and both subunits exist in numerous isotypic forms in many organisms and are encoded by different genes. Additionally, both α- and β- subunits may undergo a variety of posttranslational covalent modifications, including acetylation, detyrosylation, phosphorylation, polyglutamylation, and polyglycylation. Studies suggest that some modifications appear to perform specific functions including formation of particular organelles and interactions with specific proteins [71]. To form microtubules, the dimers of α- and β-tubulin bind to GTP and assemble onto the (+) ends of microtubules while in the GTP-bound state [86]. After the dimer is incorporated into the microtubule, the molecule of GTP bound to the β-tubulin

subunit eventually hydrolyses into GDP through inter-dimer contacts along the microtubule protofilament.

2.2.7. Shape in the 3D Environment

There is no definitive answer as yet as to whether motile structures, such as the lamellipodia and filopodia, exist or behave the same way in 3D environments as they do in 2D. It is likely that cells *in vivo* have similar structures. Yamaguchi *et al.* [87] observed pseudopods in carcinoma cells crawling on ECM fibres which seemed to be functionally equivalent to lamellipodia.

Figure 2.14 Cultured Rous sarcoma virus (RSV)-transformed baby hamster kidney (BHK)21 cells have large, prominent, ring-shaped podosomes (arrow) that, like podosomes in macrophages, also contain F-actin (red) as well as the endocytic motor protein dynamin-2 (green). Yellow indicates colocalisation. (From: [88]).

Structures which vary from those seen in the 2D environment include podosomes [88], as seen in figure 2.14 and invadopodia [89], seen in figure 2.15 and 2.16 which protrude from the ventral surface of pseudopodia of cancer cells. Podosomes have a ring like morphology with a core of actin 'dots' surrounded by a vinculin rich structure. Invadopodia are long thin projections that extend deep into the ECM. Both depend on the actin dynamics and signalling molecules as described for lamellipodia

and filopodia. Their unique features include co-localisation of focal adhesion proteins and actin, dependence on Src kinase signaling and enrichment in matrix-degrading proteases.

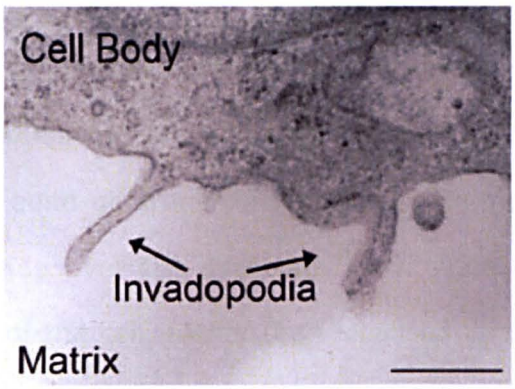

Figure 2.15 Electron-micrograph image of cancer-cell invadopodia. Ultrathin vertical-section electron micrograph of an SCC-61 oral squamous carcinoma cell, attached to fibronectin, reveals multiple invadopodia protruding into the underlying matrix. Scale bar 500 nm. (From: [88]).

A joint modelling and experimental study looking into the inhibition of cellular invasiveness by cross-linked ECM hypothesised that the size of invadopodia is determined by a peculiar stochastic dynamic instability process, where they start growing with constant rates and retreat at rates dependent on the properties of the ECM [88].

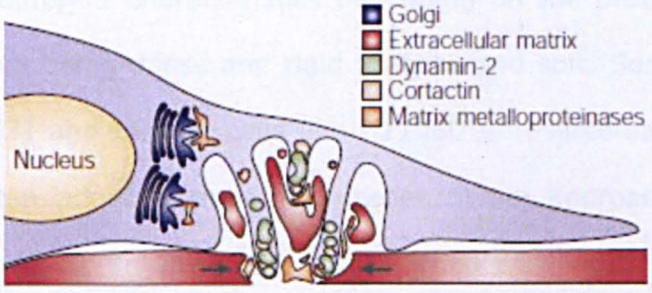

Figure 2.16. Schematic diagram depicting the organisation and key components of invadopodia as inferred by correlative light-electron microscopy and serial reconstruction. The arrows indicate the sites into which the invadopodia are about to extend. (From [88]).

There are also significant differences in overall cell morphology between 2D and 3D surfaces. The uropod and leading zones of cells in both 2 and 3D look similar, but the intermediate lamella is quite different consisting of cylindrical protrusions unlike in 2D where it spreads wide over the substrate [90]. Adhesion complexes are also found along the length of the cell, rather than localised to the periphery as seen in cells on 2D surfaces. Cells also generally migrate much faster in the 3D environment, more dependent on myosin contraction and inefficient tail retraction does not hamper leading edge protrusion [63]. Explanations put forward for these differences relate to the different contact areas that changes in topology produce and the different membrane geometries adopted. In cells spread on flat surfaces, for example, the membrane is tense, which can assist in retraction of the rear, so the process is less dependent on myosin contraction. Also, if the rear of the cell becomes stuck, membrane tension will hinder protrusion of the leading edge. In the 3D environment, membrane area is not a limiting factor, so the rear of the cell does not restrict protrusion of the front.

Cells also exhibit different characteristics depending on the properties of the ECM, which can vary from being dense and rigid to loose and soft. Some cell types, such as lymphocytes [63] and tumour cells like HT1080 fibrosarcoma and MDA-MB-231 carcinoma [91], can adopt a smoother, mesenchymal approach when migrating through dense tissue and an amoeboid motility when crawling through softer tissue. For movement over the dense rigid ECM, the cells make protrusions to the ECM

fibres and pull up the cell body using actomyosin contraction, similar to the 2D environment. However, when the rigid pores in the tissue are smaller than the cell's nucleus size, the cell uses matrix metalloproteinases to cleave the matrix fibrils, in a region localised several microns behind the leading edge. This breakdown forms the limiting step in this type of migration [92], so cells may switch to amoeboid motility when the cell can move through flexible pores. This type of migration pushes, rather than pulls, the cell body [91, 93] by generating hydrostatic pressure behind the nucleus aided by myosin contraction.

2.2.8. Modelling the Cell Crawling Cycle

A number of models have been produced which attempt to account for the cell-crawling cycle. As described above, most theoretical models of cell motility examine individual components rather than the cell as a whole. There are, however, four closely coupled components that are deemed essential for the production of an inclusive model [7]:

1. The actin network and cytoplasm;
2. The 'free' plasma membrane;
3. Adhesion of the cell to a substrate and
4. The underlying molecular biology that controls and coordinates 1-3.

Models which cover the whole cell are less common and tend to be one or two-dimensional or use simplified geometries. Bottino *et al.* [86] mathematically modelled how nematode sperm crawl using a lamellipodial protrusion. Nematode sperm use major sperm protein (MSP) rather than an actin cytoskeleton for locomotion and lack detectable molecular motors and most actin-binding proteins.

The model reproduces the major features of crawling sperm. They constructed a finite element model in which localised filament polymerisation and building generate the force for lamellipodial extension and the contraction that pulls the rear of the cell forward is powered by energy stored in the gel formed from filament bundles at the leading edge. The nematode sperm cell was chosen as the subject of the model because the MSP machinery, unlike actin, is dedicated only to locomotion and only a small number of additional proteins are required to function, unlike the multitude involved with actin. The cytoskeletal dynamics can also be visualised easily as they take place in an organelle-free lamellipod. The model corresponds with observed values for velocity, persistence, robustness, traction forces and adhesion forces.

DiMilla *et al.* [90] mathematically modelled the effects of adhesion mechanics on cell migration and speed. The one-dimensional model was developed to try and answer questions such as whether there is an optimal adhesiveness for cell movement, how changes in receptor and ligand density and/or affinity affect the rate of migration and if cell rheological properties influence movement speed. Their model incorporated cytoskeletal force generation, cell polarisation, and dynamic adhesion as requirements for constant cell movement. They also looked at modelling the mechanisms underlying the asymmetry between cell adhesion-receptors and cell polarity. They divided the cell into six compartments in a viscoelastic-solid model to describe the cell mechanics during motion figure 2.16. The four middle compartments are identical and contain Hookean springs and viscous dashpots in parallel with a contractile element. The leading lamellipodia and trailing uropod also contain springs and dashpots as well as the R_{bu} and R_{bl} elements which account for cell body adhesion bond connections. On comparison with values in the literature they found that their model showed the expected biphasic dependence of movement

speed with adhesiveness for laminin, fibronectin and E8 (cell binding) fragment of laminin and supported the cell cycle described by Trinkaus [92] and Lackie [94].

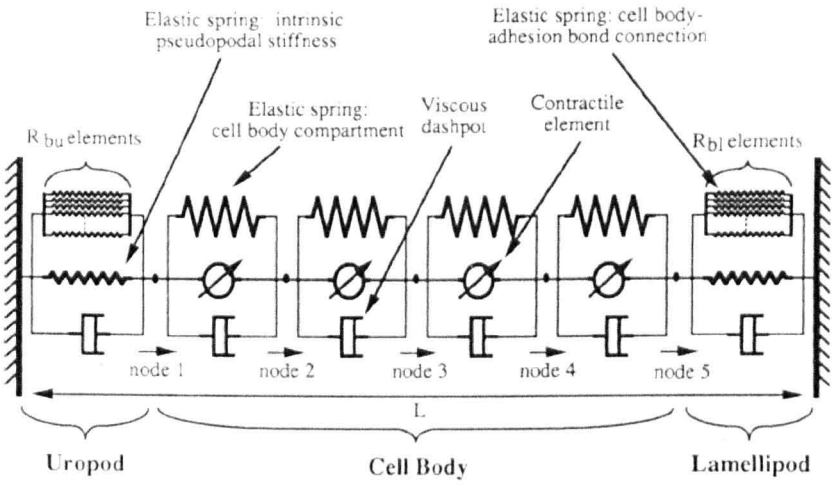

Figure 2.17. Schematic representation of the six compartment viscoelastic-solid model to describe cell mechanics during motion. (From: [95]).

A much more complicated model was produced by Oliver *et al.* [7] which is a generic self-consistent model for the full crawling cycle of a single cell on a flat surface. The model incorporates each of the four components outlined above. Special attention is given to the effect of cell motion on the contact line physics, consisting of the chemical and mechanical mechanisms for protrusive and retractive forces near the outer cell periphery. The model is able to give a multivalued relationship between the contact line angle and velocity of the cell. The author concludes that the main limitations of the model to be addressed in future work come from the use of a crude submodel for the underlying biology and that it is assumed that the dorsal plasma is adhered to the substrate everywhere, rather than at specific focal sites.

In order to produce the model, Oliver *et al.* [7] used detailed observations of live and fixed cells acquired by a variety of techniques as well as using work by McKinlay *et al.* [96]. This was required as the primary focus of cell motility literature concerns

individual parts of the crawling cycle, rather than looking at the cell as a whole [7]. High vacuum scanning electron microscopy (SEM), environmental SEM (ESEM) and confocal laser scanning microscopy (CLSM) were employed to observe the early morphological response of HObs to commercial purity titanium and 316L stainless steel. Using time-lapse imaging, they broke down the main types of locomotion corresponding to Abercrombie's cell-crawling cycle to gain estimates for the relative length and velocity of the cell body and pseudopodia.

They observed that non motile cells had a non polarised morphology which they likened to a 'fried egg' with the main cell body (with a diameter of 10-50μm) resembling the yolk and the pseudopod (with a width of 1-10μm) resembling the albumin, see figure 2.18. They noted that although the cell remains stationary, the pseudopodia pulsate normal to the cell body at different and random locations around the cell periphery. The pulses had a lifetime in the order of minutes and either formed what were described as 'hemispherical blebs' when moving out from the body, or 'ruffles' when moving back in.

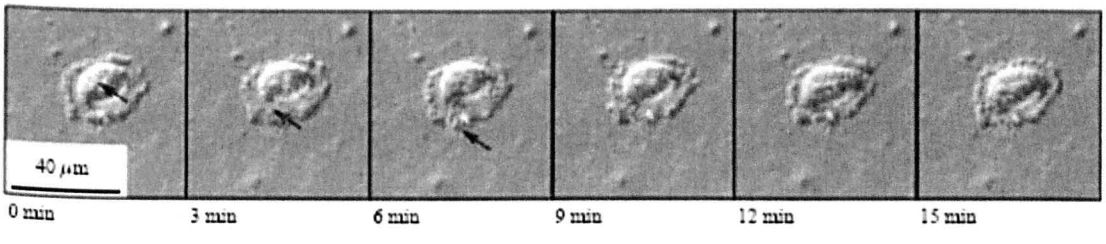

Figure 2.18. Time lapse images showing non motile HObs. The arrows show: Cell body (0min), pseudopod (3min) and 'bleb' (6min). (From: [7]).

Most of the population of well spread HObs tended to be polarised and motile, as seen in figure 2.19. They had a triangular morphology, when viewed from above, with two inactive trailing edges and the third a convex, pulsating leading edge that

generates ruffles and blebs. The cell body was again distinguishable from the pseudopodia and uropodia.

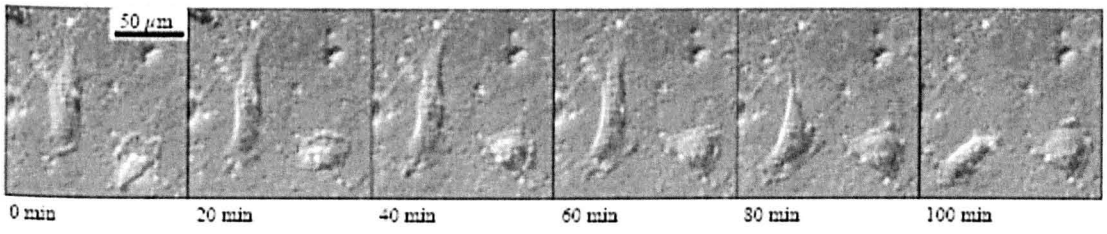

Figure 2.19. Time lapse images showing polarised, motile HOb on the left. (From: [7]).

They observed that HObs may take on a more complex outer periphery if they extended more than one pseudopodia with 10-50% attaching to the substrate, with eventually one dominating. They observed two types of sustained locomotion:

1. A constant gliding whereby the cell maintained its triangular periphery. Whilst moving in this way, the cells were observed to have a speed of approximately 10^{-1} - 1 μm min^{-1}.

2. A two step stage, the first step being the protrusion of a thin, broad, sheet like pseudopod which adheres to the surface, followed by a faster stage where the cell body moves up towards the leading edge. During the slow stage, they recorded the leading edge moving at 10^{-1} – 1 μm min^{-1} for 30 – 90 minutes, while the cell body was almost stationary. At the end of this first stage the dimensions were recorded with the outer periphery as a long thin triangle of length 50 – 100 μm and maximum width 10–50 μm. During the fast second stage the main cell body moved at 1 – 10 μm min^{-1}.

2.3. Confocal Laser Scanning Microscopy

In order to validate the model, data on spreading had to be collected experimentally. Confocal laser scanning microscopy was chosen as a technique because of its resolution and ability to scan through the z plane of the cells.

CLSM is a type of fluorescence microscopy which can be used to build high resolution images of comparatively thick samples of tissues and live or fixed cells.

2.3.1. Development

Confocal microscopy has its origins in a system developed by Marvin Minsky in 1955 to image neurones in the brain. He was unable to capture images using this early machine meaning that images of the sample would be visible for no more than 10 s [97]. The technique remained undeveloped until the early 1970s when the first biological images were published by Hader at al [98]. The word 'confocal' appears to have been first used by Brakenhoff in 1979 meaning a microscope in which the illumination is confined to a diffraction limited spot in the specimen. The detection is similarly confined by placing an aperture in front of the detector in a position optically conjugate with the focussed spot. The instrument detects a fluorescent point in an approximate accordance to an inverse fourth power rule in relation to distance from the plane of focus. This results in an optical sectioning effect, whereby the glare from out of focus regions is eliminated. Brakenhoff also demonstrated experimentally that the resolution of CLSM was improved by a factor of the square root of 2 over conventional microscopy, as measured by the full-width at half maximum intensity of the point spread function. Usage of CLSM still remained limited due to the difficulty of causing the spot to raster over the surface, often with groups

relying on moving the entire specimen and stage relative to the optics [99]. An alternate approach was developed by Petran *et al.* [100], where the whole sample was illuminated with many spots by placing a spinning Nipkow disk in an image plain.

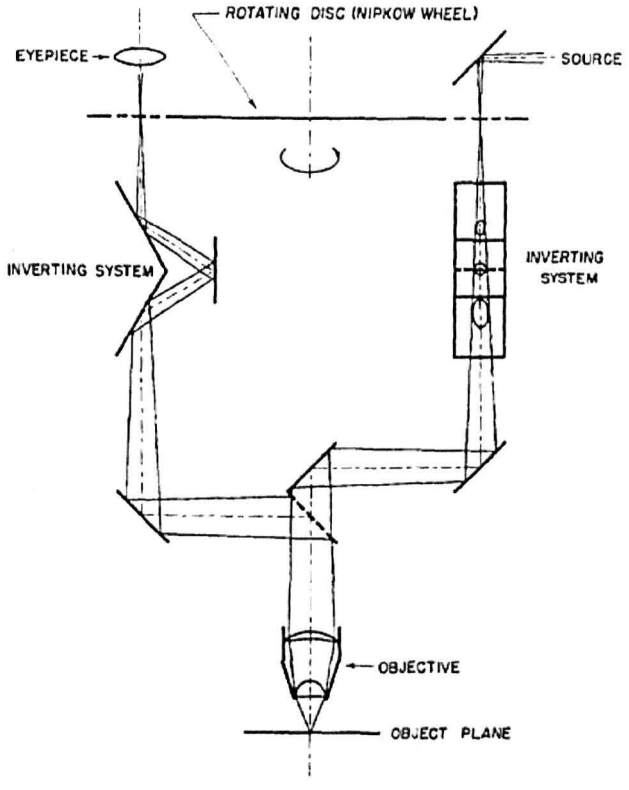

Figure 2.20. Schematic diagram of Petran's Spinning disk CLSM. (From: [100]).

Each focused spot was directed through an individual corresponding confocal aperture, diametrically opposite on the disk. It is reported [100] that this worked well in reflection mode, but only the fluorescence of the brightest specimens could be visualised as it attenuated the illumination so badly. The major advance came with adopting scanning to produce a 'flying spot' and enlarging the focal aperture. To achieve the flying spot, the beam must fill the back aperture of the objective lens and must rotate around a point in this aperture plane, producing a corresponding

translation of the focussed spot in the plane of focus. To achieve a fast scanning speed, White *et al.* [101] developed a system using a slow oscillating mirror and a fast polygonal mirror, with the two linked by a unit-power refractive telescope. White also found that a focal aperture of a few tens of micrometers in diameter, as used on all previous confocal microscopes, was not required. This enabled the aperture to be constructed as an iris diaphragm, which could be opened and closed to compromise between signal strength and confocal stringency. This feature proved quite an advance, allowing the optical path to be aligned without micromanipulation, multiple optical channels to be co-aligned under ordinary tolerances, the use of optimal circular apertures and the end to blockages due to microscopic particles of dust [102].

2.3.2. Principles

CLSM employs a laser light source to excite a fluorescing agent within an imaged sample. Both gas and solid state lasers of a specific wavelength, or several wavelengths then filtered, can be used as the illumination source. The resolution is maximised by the addition of a beam expander which increases the diameter of the beam to fill the objective and filters out noise of the Gaussian beam by passing the laser through a pinhole at the point in the expander where the light is focused into a neck.

Upon excitation, the fluorescent agent emits a longer wavelength that is directed back along the same optical path as the incident beam. The emitted light is then separated by use of a beam splitter or dichroic mirror through a set of filters which allow only a narrow bandwidth comprising the peak of the emission wavelength

curve to pass. The light then passes through the pinhole aperture towards a photo multiplier tube detector.

Corle and Kino [102] state that CLSM theoretically outperforms widefield microscopes using identical optics and light sources by approximately 10 %. Whilst theoretical resolution is unobtainable due to lens aberrations, the following equations demonstrate the practical transverse plane resolution of a confocal and widefield microscope.

$$r_{xy-confocal}(FWHM)_{point} = \frac{0.56\lambda}{NA}$$

$$r_{xy-confocal}(FWHM)_{point} = \frac{0.61\lambda}{NA}$$

As can be seen in the equations above, the resolution is a function of the wavelength of the illuminating light and the objectives numerical aperture *NA*.

Resolution of a two point source is, according to Rayleigh's criterion, achieved where the principle diffraction maximum of one point coincides with the first minimum of the other. This means that the minimum resolving distance is equal to the radius of one Airy disk.

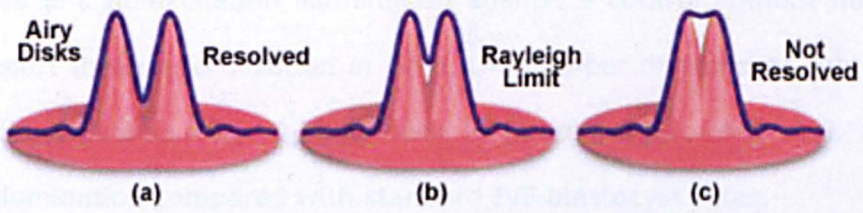

Figure 2.21. shows a schematic representation of Rayleigh's criterion, showing the overlapping of two Airy points denoting the limit of resolution.
(From: micro.magnet.fsu.edu).

2.3.3. Membrane stains

2.3.3.1 Imaging live cells and Issues with staining

Imaging live cells is challenging. Primarily, there are two problems that can arise when using fluorophores for live cell imaging; namely photobleaching and fluorophore toxicity. Photobleaching occurs due to prolonged or high intensity laser light exposure and can be minimised by using lower power NA lenses, short scan-dwelling time and adopting a 'bottom up' imaging protocol [101].

Illumination by laser light and fluorophore toxicity can damage living cells [103]. The effect can again be minimised by lowering the intensity and exposure time of the cell to the laser [101]. It is also suggested that the confocal pinhole aperture should be in an open configuration [104]. This will sacrifice some spatial resolution, particularly in the axial dimension, but the signal to noise ratio will be improved for a given level of illumination. The toxicity of fluorophores has yet to be fully studied. A report by Phillips *et al.* [105] found no evidence of cytotoxicity by studying the resting membrane potential of fluorophore loaded mouse eggs and zygotes both unilluminated and at excitation illumination against a control without fluorophores. They did report that on fertilization *in vitro*, the number of embryos that developed to the blastocyst stage was 10-30% lower in fluorophore loaded eggs exposed to excitation illumination compared with standard IVF blastocyst rates.

Specific fluorophores have been identified and developed for visualising cell membranes as well as sub cellular elements, nucleic acid and organelles [106]. A number of fluorophores are commercially available, with fluorescein isothiocyanate (FITC) and Tetramethylrhodamine-5(and 6)-isothiocyanate (TRITC) being common

examples. These isothiocyanates act as nucleophiles to react with amino, sulfhydryl, imidazoyl, tyrosyl or carbonyl groups on proteins, so can be linked to specific antibodies which attach to a specific target. Both exhibit high absorptivity, high fluorescence quantum yield and water solubility. FITC was the first molecule functionalised with an isothiocyanate reactive group (-N=C=S) which replaces a hydrogen atom. It fluoresces green with excitation and emission spectrum peak wavelengths of 495 nm and 521 nm. TRITC is also functionalised with (-N=C=S), but fluoresces red with excitation and emission wavelengths of 557 nm and 576 nm.

There are a number of commercially available probes available to visualise the membranes of live cells. Three that were investigated in this study were epicocconone, DiI and FPE.

2.3.3.2. FPE membrane probe

Fluoresceinphosphatidylethanolamine (FPE) is widely used to visualise the cell membrane [107]. It consists of two major structural components; the phosphatidylethanolamine segment enables the probe to be readily incorporated into the lipid bilayer of the cell membrane and a fluorescein headgroup. FPE can also be used as an indicator for events such as the binding of a charged molecule to the membrane surface as it has a xanthene ring system which can undergo protonation or deprotonation which leads to a change in the fluorescence emission [109].

2.3.3.3. DiI membrane probe

DiI (1,19-dihexadecyl-3,3,39,39-tetramethylindocarbocyanine [diI-C_{18}-(3)]) is a fluorescent carbocyanine dye which embeds in the lipid bilayer of cell membranes

[110]. The stain is weakly fluorescent in water but highly fluorescent and photostable when incorporated into membranes, exhibiting high extinction coefficients (EC >125,000 $cm^{-1}M^{-1}$ at their longest-wavelength absorption maximum) and short excited-state lifetimes (~1 nanosecond). Once applied to cells, the dye diffuses laterally within the plasma membrane, resulting in staining of the entire cell [111].

2.3.3.4. Epicocconone membrane probe

Epicocconone is a commercially available stain which is derived from the fungus *Epicoccum nigrum* [112], see figure 2.22. The small natural azaphilone molecule is able to diffuse into live or fixed cells and stains both cell membranes and lipophilic organelles.

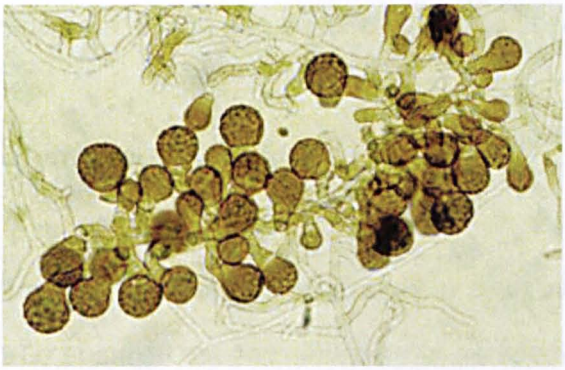

Figure 2.22. Micrograph of the fungus Epicoccum nigrum, as used in Epicocconone stain. (From: [113]).

Epococconone, a heterocyclic natural product derived from the fungus *epicoccum nigrum* [114]. It is taken up by the cell by unfacilitated diffusion with staining occurring in a time-dependent manner, starting with the outer plasma membrane, then lipophilic organelles in the cytoplasm such as the ER, Golgi and lipid rafts. Epococconone reversibly reacts with proteins to form an epicocconone-amine adduct

with an internal charge transfer complex that is highly fluorescent in the hydrophobic environment around the proteins. The fluorescence is further enhanced in lipophilic environments. The stain has been tested for cytotoxic or inhibitory effects on 56 human cell lines, with no detrimental effects observed at concentrations ≤5 µl [109].

2.3.4. Immunocytochemistry

Immunocytochemistry is a technique that uses antibodies that target specific peptides or protein antigens in the cell via specific epitopes. The technique was first developed by Coons *et al.* [115], by being the first to label an antibody with a fluorescent dye and use it to identify an antigen in tissue sections. Because an antigen-antibody reaction is specific, positive identification of cell and tissue constituents can be made with a high degree of confidence [116].

2.3.4.1. Production of antibodies

Antibodies, predominantly in the form of y-globulins, are raised by immunizing animals with antigen. To ensure that the antibody is as specific as possible, the antigen must be completely pure or synthetic. The antiserum produced by the animal host will not, however, be directed specifically to the injected antigen and the antibodies produced, but for parts of the antigen molecule. The blood is then centrifuged to remove red blood cells, leaving antiserum, the plasma containing the antibody, along with the animal's natural antibodies [116].

2.3.4.2. Monoclonal antibodies

To produce 'pure' monoclonal antibodies which have absolute specificity for a single epitope on the antigen molecule, a protocol by Milstein *et al.* was developed [117]. The technique involves fusing lymphocytes with mouse myeloma cells in culture. This fusion allows the hybrid cells to continue to grow and divide in culture. Each cell produces only one type of antibody and the cultured hybrid myeloma cells are gradually cloned into cell lines producing one antibody only. The procedure consists of screening the culture fluid from the various clones for antibody by radioimmunoassay, ELISA, or immunocytochemistry.

Cross-reactivity may occur if the monoclonal antibody is directed at an antigenic sequence shared by more than one substance. Another disadvantage of a monoclonal antibody which can arise may derive from its monospecificity. A monoclonal antibody, reactive with only one site on the antigen molecule, may result in fewer antibody molecules being bound to the antigen and subsequently detected by the labeling method, resulting in weaker staining. The epitope that the antibody recognizes on the antigen molecule may be altered by fixation or processing so no staining will be seen [116].

2.3.4.3. Secondary antibodies

Secondary antibodies must be raised in a species different from those of primary antibodies. Anti-IgG secondary antibodies are the most widely used [118]. Anti-IgG secondary antibodies can recognise various IgG subtypes and these are highly suitable for double labelling experiments. The secondary antibody may be

conjugated with a fluorescent probe which will fluoresce when bound to the primary antibody, see figure 2.23. The most commonly used probes are fluorescein isothiocyanate (FITC) and Tetramthylrhodamine-5(and 6)-isothiocyanate (TRITC), see section 2.3.3.

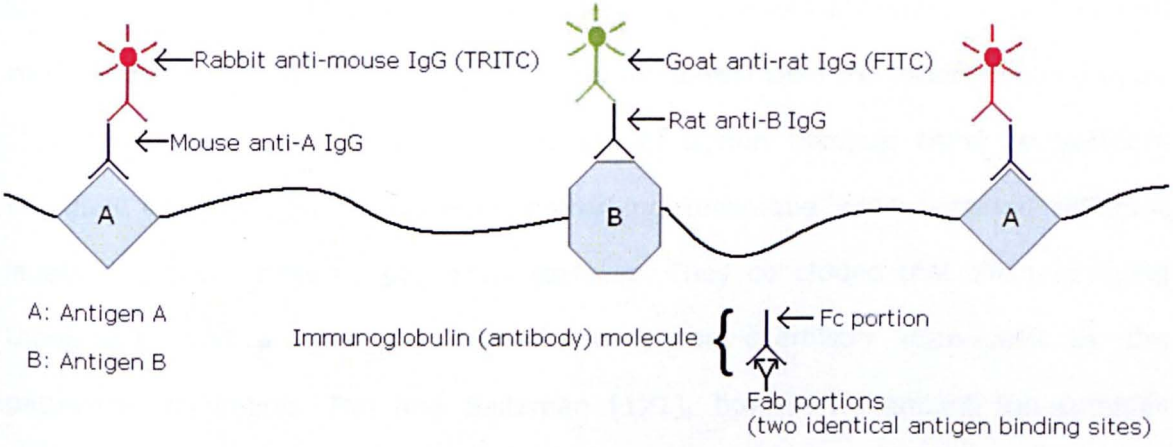

Figure 2.23. Schematic representation of fluorescent labelling.

2.4. Cell Response to biomaterial surfaces

The surface chemistry of a substrate plays an influential role in the response of cells exposed to it. Several studies have shown that cells respond to a number of surface properties, including surface roughness, topography, chemistry and energy [119]. Surface topography and chemistry are reported as the two dominant properties with conflicting studies claiming that one is more influential than the other. Britland *et al.* [120] used BHK cells (a quasi diploid line of Syrian hamster cells) on surfaces modified using a photolithographic patterning technique which created different levels of adhesiveness on patterned surfaces. They concluded that the underlying topography had a dominant influence over the chemistry introduced by the patterning technique. Tan and Saltzman [121], however, highlight the complex interplay between chemistry and topography, showing that neutrophils had a variable response to grooved/ridged glass substrates dependent on the applied coating, observing completely different behaviours to the underlying topography dependent on the coating. They also noted that cell motility was influenced by the type of coating, with cells migrating at a significantly lower rate on titanium-coated surfaces. This would suggest that cell migration and the effect of microgeometry can be overridden by a strong chemical property [119].

An important factor to consider when studying surface properties of a material, is that within seconds of being placed in a biological fluid, an adsorbed protein layer will form on a material surface, determining the cellular response to that material [119]. This protein adsorption may be dictated by the surface chemistry of the outermost molecular layer, it is postulated that human tissues interact with only the top atomic layers of a substrate, to depths from 0.1 to 1 nm [119]. Protein adsorption is a dynamic process, influenced by surface properties, which involve non-covalent

interactions such as electrostatic forces, hydrogen bonding, hydrophobic interactions and van der Waals forces. There is competition between proteins binding to a surface, with some binding more strongly and displacing others dependent on surface chemistry. These proteins may provide binding ligands for cell focal adhesion molecules such as integrins which, as outlined in section 3.4 of this report, trigger signals that direct cell function. Proteins that cells readily bind to, such as fibronectin and vitronectin, may undergo a conformational change upon adsorption which is influenced by the surface chemistry of the substrate. This will affect the way in which a cell will react to a surface, sometimes presenting a conformation to which the cell will not bind. The subsequent effect that this has on binding strength between a material surface and integrins has been widely studied [119]. Keselowsky *et al.* [122] found that CH_3, OH, COOH and NH_2 terminated self assembled monolayers (SAMs) varied adsorbed fibronectin conformation, determined by differences in binding affinities of monoclonal antibodies raised against the central binding domain. They found that OH had the strongest binding affinity, followed equally by COOH and NH_2, then CH_3. Keselowsky also showed that $\alpha_5\beta_1$ integrin - fibronectin binding followed the same trend, however, α_v integrin - fibronectin binding followed a different trend, whereby the interaction with COOH was strongest followed by OH and NH_2 with equal strengths and then CH_3.

2.4.1. Magnetron Sputtering

There are many ways to modify a surface, however to change the surface chemistry radically then a coating rather than a surface modification technique is often required. The advantages of coatings that conform to the underlying substrate is that chemical changes can be investigated without the influence of changes in

topography. In this study, PVD magnetron sputtering was employed, using the equipment shown in figure 2.24, the principles of which are outlined in this section.

Figure 2.24. PVD Deposition Chamber, Nottingham University.

Sputtering is a vaporisation process whereby an energetic bombarding species impacts the surface, physically ejecting atoms by the transfer of momentum [123]. The technique involves the use of glow discharge or an ion beam to generate a flux of ions or energetic neutrals capable of colliding with a material surface or target. When high energy incident ions or neutrals collide with the target surface, atoms or clusters of atoms are ejected by impact transfer [124], but atoms will only be ejected if the collision energy is greater than the material's lattice energy. The ejected atoms are then re-deposited onto the substrate. The thickness of the deposited material can be varied, but is typically less than 1 μm in thickness and is termed a thin film [125].

Direct current (DC) sputtering is the simplest form of sputtering and employs a conductive target material to sputter deposit thin films.

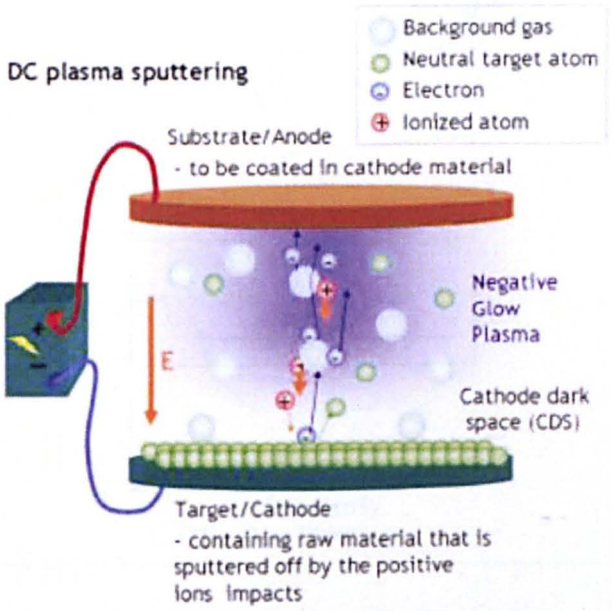

Figure 2.25. Schematic illustration of Direct current (DC) sputtering. (Modified from: etafilm.com)

As seen in figure 2.25, a cathode and an anode, are situated in the deposition chamber which is normally evacuated to better than 10^{-6} Torr. The chamber is then filled with a noble gas, commonly argon, at a pressure between 1 to 200 mTorr and a negative DC voltage is applied across the target, the cathode, in the range 10^2 to 10^3 Watts. The substrate is attached to an electrically grounded anode which completes the circuit. This causes electrons to be ejected from the cathode which then act to ionise the argon producing a positive argon plasma. These ions are then attracted to the cathode at energies dependent on the voltage across the system. As the ions travel towards the target material, they commonly recombine with electrons producing energetic neutrals [125]. On impact, target material is removed and is sputter deposited everywhere in the chamber. These sputtered atoms are generally composed of neutral single atoms, however, a small percentage of ions exist [124].

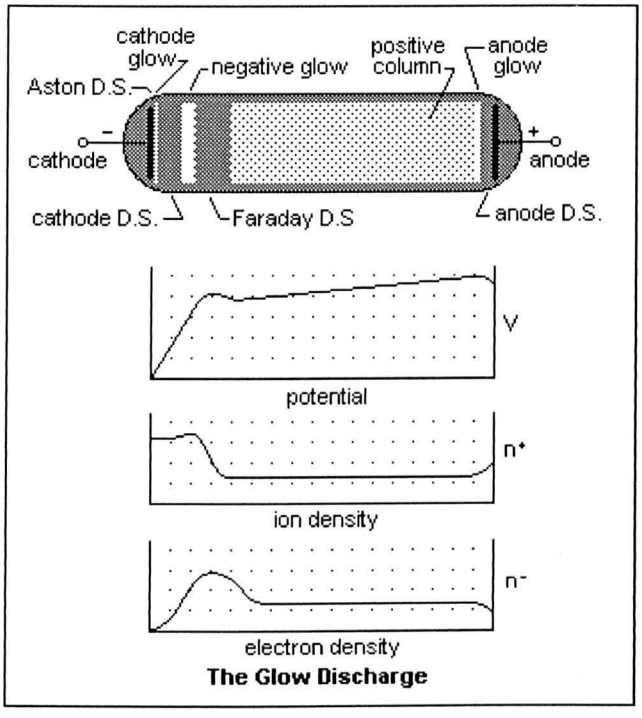

Figure 2.26. The structure of a DC Plasma glow discharge between a cathode and anode. (From: mysite.du.edu).

Figure 2.26 shows the structure of a DC glow discharge between a cathode and anode. The Aston dark space closest to the cathode contains low energy electrons and high energy positive ions which move to opposite electrodes. Preceding this dark space is the cathode glow region. The coloured glow observed is caused by neutralisation of positive ions. In the cathode dark space electrons are energised to the point where they begin to impact ionise neutrals, however, the region is dark as there is relatively little ionisation. The large drop in the voltage across the dark region is the cathode sheath [126] and the resulting electronic field causes the acceleration of ions towards the cathode. A visible emission is seen due to interactions between secondary electrons and neutrals leading to excitation and de-excitation, termed the negative glow region. Following this, there is the Faraday dark space, positive column and the anode. Often the substrate is placed in the negative glow region and so these do not normally appear.

Sputtering is only one of the scenarios which may occur when ions and energetic neutrals impact with the cathode or target. If the particle is of lower atomic mass than the target material it may be reflected. An incident particle may become implanted into the surface or a secondary electron, characteristic x-ray or photon can be ejected. Structural rearrangements such as atom vacancies, interstitials or changes in stoichiometry in compound targets may occur. These three changes are known as radiation damage. The sputtering process will result in material being ejected in all projections with a quantity arriving at the substrate surface forming the thin film. The erosion rate of ions removing target materials can be characterised by the sputtering yield, S, which is defined as the mean number of emitted atoms per incident particle. This value can vary hugely between different incident particles and target materials, but experimentally lie between 10^{-5} and 10^{3} atoms per incident particle [127].

2.4.2. Magnetrons

When a magnetic field is used alongside an electric field, secondary electrons are directed into a cycloidal path giving a high ionising efficiency [128] by confining the glow discharge to the target region. This enables higher deposition rates due to the magnetic confinement than sputtering alone. The path length and residence times of the electrons in the near-cathode region can be multiplied by increasing the 'magnetic trapping'. This also increases the probability to undergo ionisation collisions, in turn increasing the sputtering flux by up to ten times, thus increasing the deposition rate [129]. Planar magnetrons are used most often. These are typically circular or rectangular in geometry, ranging from 2.5 cm to 8 cm in diameter. They erode preferentially where the magnetic field is parallel to the target

surface, resulting in a 'racetrack' in the annulus region. This has lead to experimentation with cylindrical target geometries, which have a longer lifetime and increased sputtering rates, however, they are often much more expensive to manufacture.

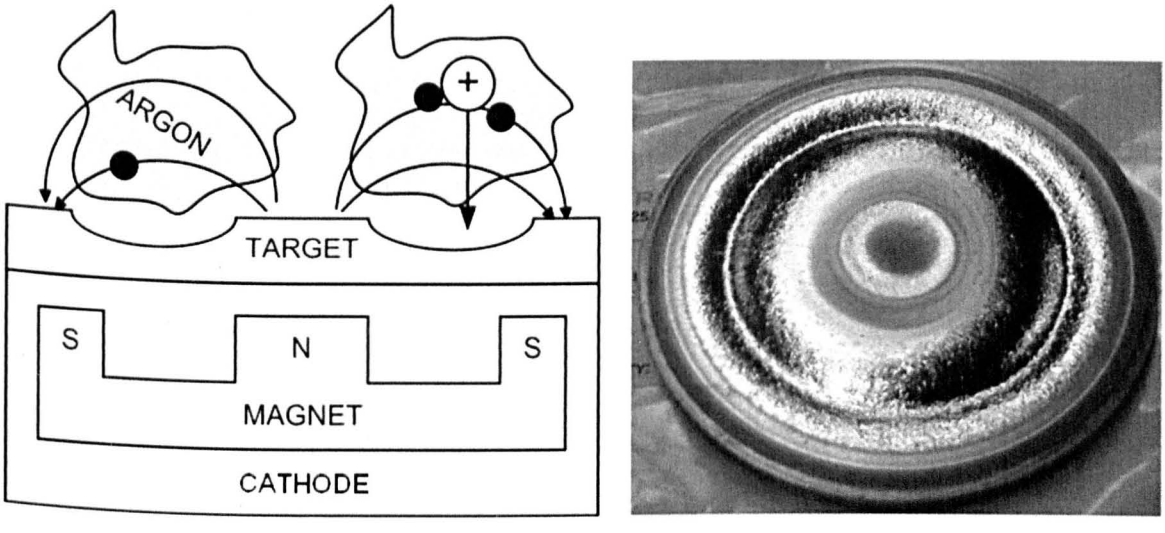

Figure 2.27. Schematic diagram of a magnetron (left) alongside a Ti target (right), showing how the plasma forms where the magnetic field is parallel to the target surface, resulting in erosion in this area creating a circular 'racetrack'. (From: unsw.edu.au)

There are two types of magnetron that can be used; balanced and unbalanced. A balanced magnetron has a uniform strength magnetic field which leads to decreased current density of the ion flux arriving at the substrate as the source to substrate distance increases. By using an unbalanced magnetron, this problem can be resolved as stray magnetic fields are used to concentrate ion flux density further away from the target surface, closer to the substrate. There are two designs of unbalanced magnetron; type I has a strong inner pole and weak outer and type II is

arranged vice-versa. In industrial applications, type II is generally used as its ion to deposited atom ratio can be as high as 2:1, whereas type I is only 0.25:1 for a given distance from the sample [123].

2.4.3. The Growth of Thin Films

It is reported that there are three mechanisms of thin film growth [126]. These are; the Stranski-Krastanov, Frank-Van der Merwe and Volmer Weber, however, all have a comparable order of events. As the plasma starts to sputter material, small mobile clusters begin to form on the substrate surface, which initially incorporates incoming atoms and molecules. As the islands grow, they begin to connect and coalesce with neighbouring island clusters, behaving as a liquid. This process continues until the substrate surface is covered by a uniform film, occurring within the first few nanometres of deposition [126].

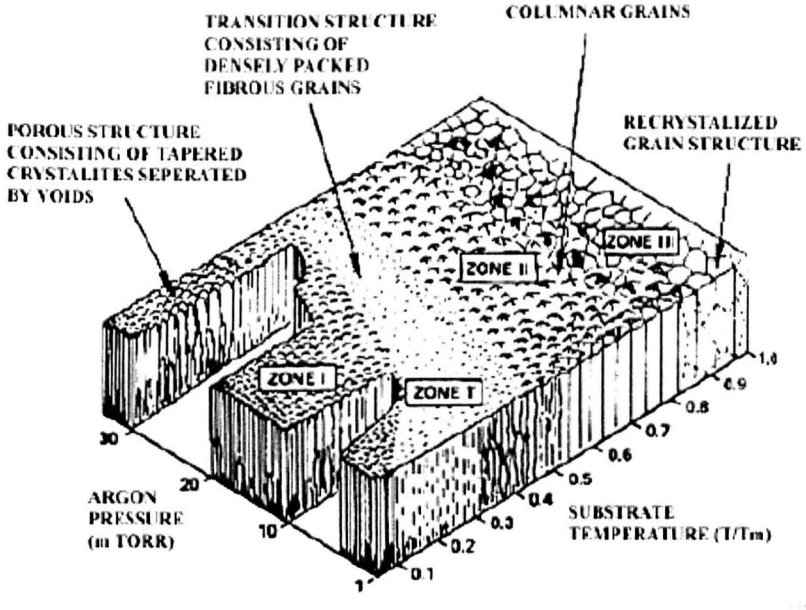

Figure 2.28. Thornton-Messier structure zone model for sputter deposited films. (From: pvd-coatings.co.uk).

Thorton and Messier proposed a zonal model for sputter deposited films, seen in figure 2.25. The first zone has a closely packed, columnar microstructure with round and tapered grains that have open boundaries. This zone is formed when substrate temperatures are less than 0.3 of the melting temperature with partial pressures in excess of 10 mTorr. This microstructure is adopted as the adatoms do not have the mobility required to overcome substrate surface features. These films have a high surface area and a poorly defined crystal structure. Zone T is formed if the growing film is bombarded with energetic ions and neutrals which leads to erosion of the surface. This results in fewer voids than zone 1 and is smoother with a higher density. The microstructure is characterised by dense, fibrous columnar grains which are an intermediary stage between the structures of zones 1 and 2. The structure of zone 2 is heavily influenced by the surface diffusion of adatoms in the T_s/T_m region of 0.5 - 0.8, which produces a denser film. Zone 3 films are formed when the T_s/T_m ratio is larger than 0.8. Bulk diffusion is the dominant factor in determining this dense microstructure, which is similar to that of other bulk materials.

2.4.4. The use of TiN in Biomaterials

TiN was chosen in this study as it is commonly used as a coating for biomaterials. TiN coatings have been used in many applications and is noted for its high erosion- and corrosion-resistance along with its biocompatibility [130]. The coating can reduce bacterial colonisation, making it a popular choice for dental applications [131], and decrease the amount of metal ions which leach from an implant into biological fluids [132].

The coating is most widely used in the dental industry. Here it is mainly used to coat Co-Cr-Mo alloy prostheses, which not only improved the aesthetic appearance of the

implant due to its gold colouration, but has high wear resistance and is considered biocompatible [133]. The corrosion resistance and biocompatibility of PVD deposited TiN was assessed by Brauner [96] by carrying out cell culture experiments on impermeable deposits with no detrimental effects. The material was also shown not to aggravate corrosion behaviour between itself and the base metal. Corrosion of implants is undesirable as this not only leads to a pH change locally, but the release of metallic ions has been shown to affect cellular metabolism [134]. A study by Kola *et al.* [135] also showed the corrosion resistance of sputtered TiN on AISI 316L stainless steel in saline solution, however the presence of pinhole defects could be corrosion initiation sites on thinly coated samples.

Turkan *et al.* [136] studied the use of TiN in coating CoCrMo orthopaedic implants to limit metal ion release. The accumulation of metal ions in the body over the lifetime of an implant has been thought responsible for clinical problems such as aseptic loosening and even the formation of carcinomas. Using simulated body fluid (SBF), they showed when measuring the fluid using atomic adsorption spectroscopy, a 3 μm film of TiN prevented the release of cobalt and chromium from the substrate, whereas in the as polished metal, cobalt was preferentially dissolved.

Ma *et al.* [137] studied the wear performance of TiN coatings on Ti-6Al-4V using a novel method of plasma nitriding and plasma-enhanced chemical vapour deposition. Abrasive wear testing showed a significant decrease in wear volume loss in the coated samples. However, they also found that poorly adhered coatings caused a negative effect on wear behaviour, leading to three-body abrasion with hard TiN particles.

There are conflicting results as to whether TiN coatings can reduce bacterial colonisation. Grössner-Schreiber *et al.* [131], concludes that there was a significant reduction in the number of adherent bacteria on inherently TiN and ZrN and thermically oxidated titanium surfaces compared to polished titanium [131]. Sarro *et al.* [226], however, showed that there was rapid bacterial colonisation using *Staphylococcus aureus* on TiN coated Ti-6Al-4V compared to the base metal. Jeyachandran *et al.* also produced results using the oral bacteria *Porphyromonas gingivalis* showing that more bacteria had adhered on the TiN film compared to a Ti film with a native oxide layer and a Zn-FHA film.

2.4.5. The use of Titanium Oxides in Biomaterials

Whilst Titanium Oxides (TiO) films are not used as widely in the biomaterials field, there have been recent studies suggesting that the surface could be used as antithrombogenic coating. Zhang *et al.* [138] carried out experiments on platelet adhesion and protein adsorption on non stoichiometric titanium oxides along side *in vivo* studies to investigate thrombus formation. They concluded that TiO had excellent anticoagulation performance in the *in vivo* studies and the release of the cell adhesion molecule, GMP 140, from platelets on TiO was lower than low temperature isotropic carbon (LTI-carbon). The morphology of the adherent platelets remained round and isolated.

Randeniya *et al.* [139] showed that osteoblast morphology had advanced to polygonal from spherical and total cell count was higher on TiO surfaces compared to DLC surfaces. It is also widely reported in the literature that increased cell adhesion can be linked to increased surface energy of metal, polymer and hydroxyapatite materials.

Summary

This review has detailed the initial sedimentation, attachment and spreading of cells and looked at the primary underlying mechanical and signalling mechanisms which drive the events of later spreading.

The ways in which numerous authors have approached modelling aspects of the cell, as mentioned above, which relate to morphology have also been looked into along with experimental data to support these theories.

Experimental means of providing data on living cells as they attach and spread to aid the development and testing of models have been described, specifically looking at CLSM and live staining techniques, as well as immunocytological techniques for assessing differences in aspects such as cytoskeletal organisation to varying surface chemistries.

PVD has been reviewed in detail as a method of applying a surface coating in order to gain data of spreading cells on surfaces with differing chemistries, along with two PVD surface coatings with different chemistries that are used in the biomaterials field.

3. Mathematically Modelling Spreading: Theory

3.1. Introduction

The experimental data collected in this research is intended to aid the design of, and test a novel mathematical model, building on previous work by Oliver *et al.* [7]. This will provide a systematic, quantitative approach to understand the mechanisms of adhesion and migration of mammalian cells over biomaterial surfaces. The cell will be modelled as a two-phase, reactive poroviscous droplet, for which a one- dimensional model has been analysed [7]. This study was intended to aid the formulation and testing of a higher dimensional version of the model. An overview of the considerations and assumptions of the model is outlined below. For a more comprehensive description, see Oliver *et al.* [7].

3.2. Cells as viscous droplets

The model is based on principals set out by Hocking and Rivers [140] in their model of droplet spreading. Their hypotheses on contact radius, contact angle and droplet volume will be used to model cells during early adhesion and spreading. Hocking and Rivers state that there must be slip between the fluid and the solid boundary near the rim of the drop to avoid a force singularity. This contrasts with earlier Navier-Stokes equations which have no-slip boundary conditions. In order to overcome this, the no-slip conditions are simply relaxed in the vicinity of the moving contact line and replaced by a Maxwell condition, whereby the amount of slip is proportional to the local velocity gradient, with the constant of proportionality being the slip coefficient [134]. The magnitude of the slip-coefficient is determined by the area where the slip is significant and is also a measure of the scale of surface roughness.

Accurately measuring the moving contact line is imperative when looking at spreading. This is a complicated entity. Young in 1805 was the first to derive an expression for the static contact angle, θ_s. He assumed that the three material boundaries as shown in

figure 3.1: liquid/gas, liquid/solid and solid/gas, each pose a constant surface tension denoted by σ_u, σ_w and σu_s, respectively.

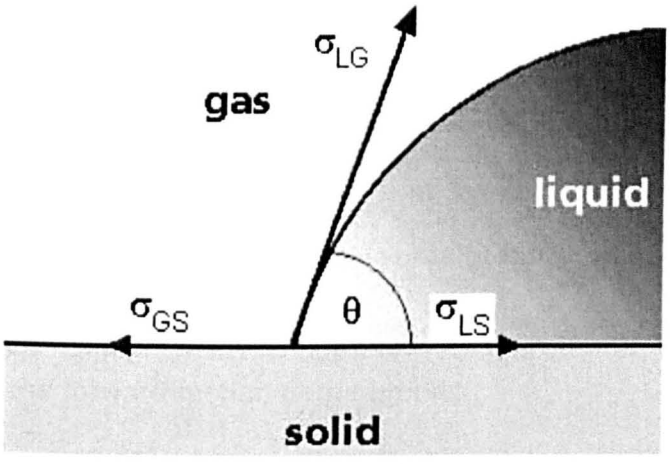

Figure 3.1. Schematic diagram of the three material boundaries. (Modified from: kruss.de)

For static equilibrium to be reached, he proposed that their horizontal components must equal zero at the contact line. This is expressed as

$$\sigma_{LG} \cos \theta_S = \sigma_{GS} - \sigma_{LS},$$

which is referred to as Young's equation. Young argues that this derivation is not totally satisfying from a mechanical point of view. In order to balance the vertical component of the surface-tension forces at the contact line, a reaction force must be imposed in the solid. Along with Young, Laplace and Gauss were considering the interface between two fluids around this time. All their investigations assumed that physical quantities, such as density, were discontinuous across the interface. Poisson (1831), Maxwell (1876) and Gibbs (1876) recognised that the interface actually represented a rapid but smooth transition of physical quantities between the bulk and fluid values. Gibbs proposed the idea of a surface of discontinuity and surface excess quantities in order to develop the equilibrium thermodynamics of interfaces [143].

For a viscous fluid, there is evidence that the contact angle is velocity dependent, but it has also been suggested that this evidence relates rather to the slope measured some distance behind the contact line. This is often referred to as the 'macroscopic contact angle'. There is a small region near the contact line where large stresses are present, so Hocking proposes that there will be large changes of slope in this area, which is defined the microscopic contact angle. This may mean that the contact angle remains unaltered as the drop spreads and the variation with velocity might only reflect on the area of high stress. It is therefore not unreasonable to assume that the contact angle remains constant throughout the forward motion of the droplet.

In Hocking's asymptotic analysis of the microscopic contact angle, it is not enough to use an outer region, which covers the major part of the drop, and an inner region, the same size as the slip coefficient, as there needs to be an intermediate region in which the slope is a varying function of distance from the contact line [140].

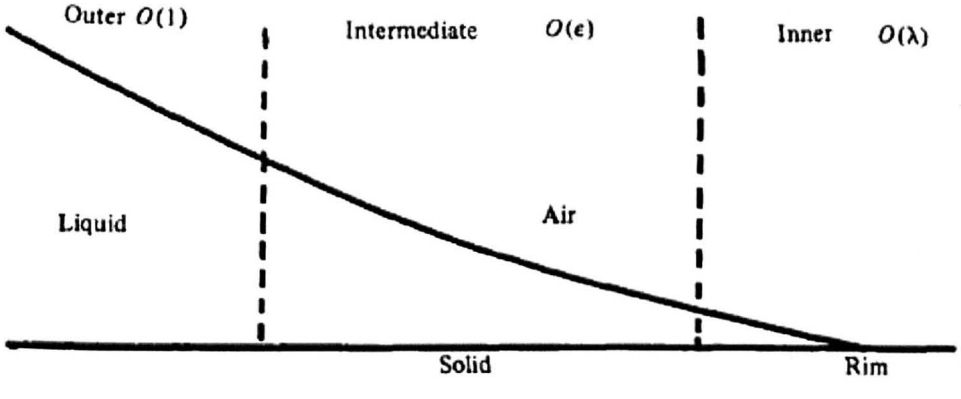

Figure 3.2. Schematic diagram of the vicinity of the rim of a spreading droplet; remote from the edge (the macroscopic contact angle) is determined only by surface tension, at the edge of the droplet the microscopic contact angle is reduced and is a function of surface tension (O) and the slip coefficient (λ), in the intermediate region, an expansion in terms of the logarithm of the slip coefficient is used, with $\varepsilon = 1 / |\ln/\lambda|$. (From: [143]).

Parameters governing the spreading of a droplet on a horizontal surface are the density ρ and viscosity μ of the liquid, the surface tension σ and the static contact angle Φ for the liquid/air/solid system, the acceleration due to gravity g, the volume V of the drop and the slip coefficient λ.

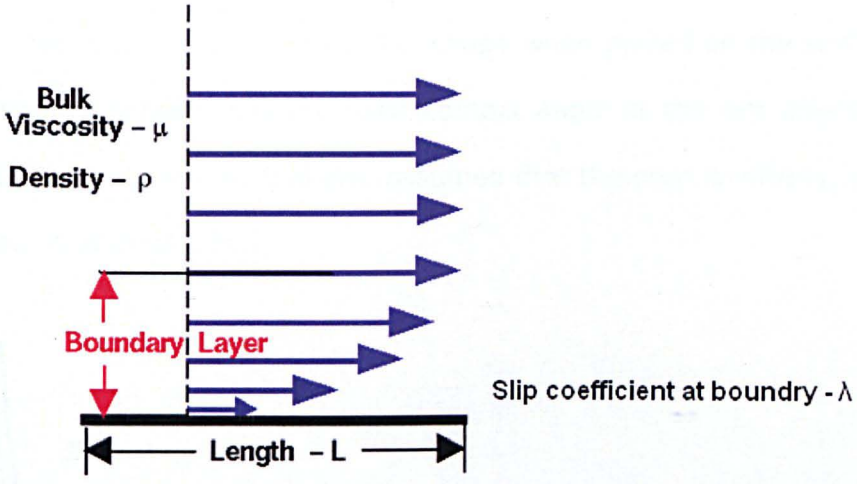

Figure 3.3. Schematic diagram of the parameters governing the spreading of a droplet on a horizontal surface. (Modified from: grc.nasa.gov)

These parameters must have values which ensure that the following assumptions are valid:

1. The Reynolds number of motion, equation below, giving the ratio of inertial forces to viscous forces, is small enough for the Stokes motion equations, which applies Newton's second law of fluid motion, along with the fluid stress and pressure, to be used.

$$R_e = \frac{\rho R U}{\mu}$$

where R is the radius and U is the typical mean fluid velocity and μ is the dynamic velocity of the fluid.

This is typically 10^{-2} in osteoblast cells, meaning that inertia is negligible and is thus suitable.

2. The Bond number, measuring the relative importance of gravity to capillary action in the spreading process, is small and the slip coefficient is small compared to the size of the drop [143].

It is assumed that the drop has some initial shape when placed on the surface and that the effect of surface tension and the fixed contact angle at the rim drives the droplet towards an equilibrium position. It is also assumed that the drop is initially, and remains, symmetric about a vertical axis.

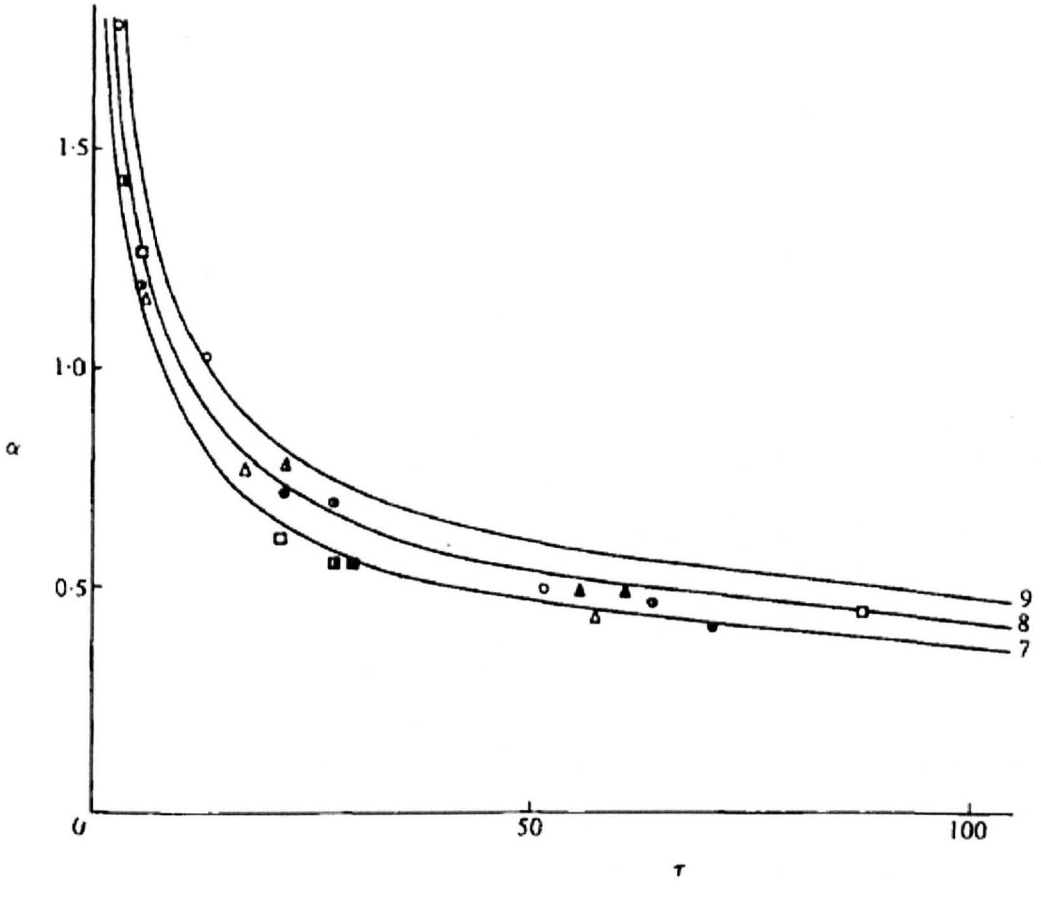

Figure 3.4. The outer contact angle as a function of the time (From: [140]).

The model predicts the evolution of the drop, as in figure 3.4., and agrees well with experimental observations.

3.3. The importance of the contact line.

There are a number of methods of measuring the contact angle. The most common is by placing a drop of liquid on a flat, horizontal surface. The droplet may be placed by an external device located above the surface, or forced through a small hole in the surface. The contact angle can then be measured directly by drawing a line tangent to the gas/liquid interface at the contact line on an enlarged photograph, or indirectly by using the solution for the shape of the meniscus, derived by Padday *et al.* [225], along with the measured height of the apex of the drop and its volume. A similar method can be used using a partially submerged vertical flat plate. The contact angle may be determined again from a photograph, or by measuring the vertical position of the contact line with respect to the undisturbed level of the liquid, along with the solution for the shape.

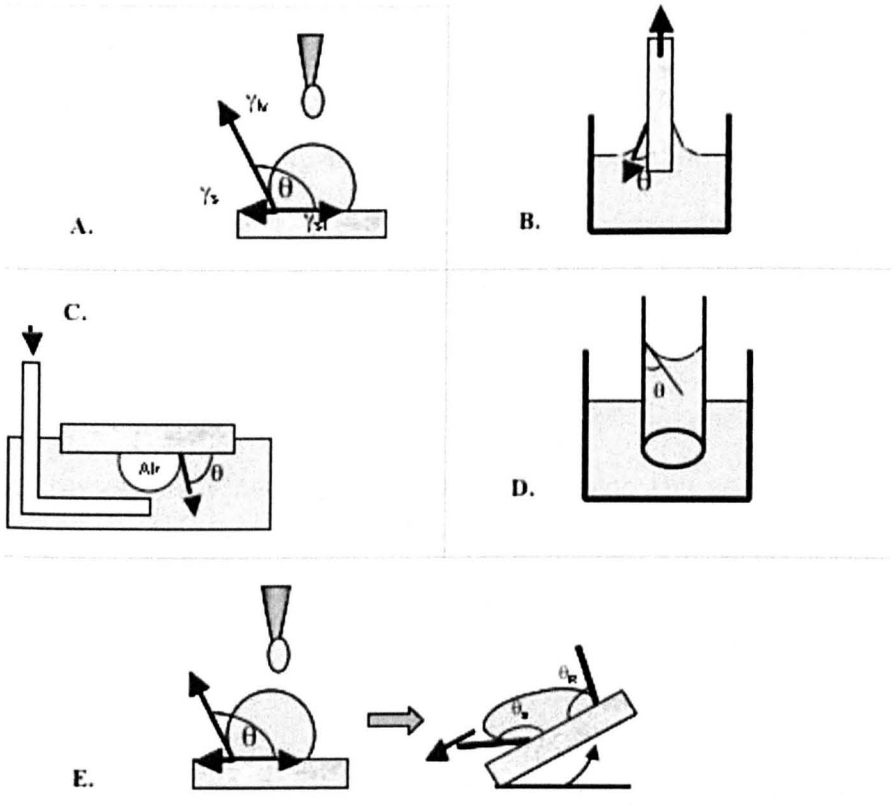

Figure 3.4. Methods of determining the contact angle; (A.) Sessile or Static drop. (B.) Wilhelmy plate method. (C.) Captive air bubble method. (D.) Capillary rise method. (E.) Tilting substrate method. (Adapted from: [6]).

The contact line may also be found by measuring the force necessary to keep the plate partially submerged in the liquid at a known depth, with a calculation of the force balance. The plate may also be tilted with respect to the vertical so that the liquid/gas interface appears horizontal all the way up the contact line. It is reported that all these methods have varying degrees of accuracy [140]. The limiting factor comes with the reproducibility of the measurements, with contact angles rarely reported with less uncertainty than ± 1.0 ° to 2.0 °.

Frisch and Thoumine [144] applied this wetting theory to predict the kinetics of fibroblast spreading onto an adhesive substrate, with simplified assumptions on cell structure and geometry. They used three parameters in their model: cytoplasm viscosity, cortical tension and cell-substrate surface tension. They treat the interior of the drop as a highly viscous fluid bounded by a cortex, which comprises the folded plasma membrane and an actin-rich underlying layer. The use of this simplified view of the fibroblast structure is in agreement with several other studies [145, 146]. Their model neglects surface elasticity and takes both cortical tension and the internal viscosity as constant, as they previously showed that they vary little during cell spreading [147]. The effect of the nucleus is also omitted from the model so as not to introduce a difficult boundary problem [148] and because it only accounts for a small fraction of the cell volume. They determined the adhesion force between the cell and the surface by using the adhesive energy per unit area w_a. This parameter is only valid if the adhesion is uniform, which the authors argue is the case with fibroblasts adhering to glutaraldehyde-coated glass. Cell volume is also assumed to remain constant during spreading, shown by experimental data [147]. The hydrodynamic approach assumes that molecular dissipation at the tip is negligible and that the major losses are due to shear flow in the liquid wedge at the contact line [149]. Their model simulations predict that the contact radius will increase quickly at early times (<1 h) before reaching a plateau by 3.5 h.

Their model shows the cells to be in a regime of almost complete spreading, where the contact area would increase to infinity. In practise, however, fibroblasts stop spreading after about 6 h, become polarized and begin to crawl in random directions. They propose that the end of spreading may be due to the fact that the plasma membrane is pulled taut, since, as described in section 2.4.5., there is a finite reservoir of plasma membrane in the form of wrinkles that can accommodate changes in cell shape. They also note that the spreading process is quickly reversible: cells round up in a few minutes when the pericellular matrix is digested by trypsin (a proteolytic enzyme), which reduces the adhesion energy to zero.

They suggest that possible refinements of their model could include: (i) a more accurate analysis at large contact angles, corresponding to early adhesion times; (ii) addition of cortical elasticity, which seems to be present in fibroblasts; and (iii) contribution of the nucleus: it appears to be more rigid than the cytoplasm in endothelial cells and may thus slow down the spreading dynamics.

The model for which this experimental work is intended will build on principles laid out by Dembo and Harlow [150], whereby the cytoplasm is dealt with using a reactive two-phase flow solution. Cytologists agree that the cortical cytoplasm of motile cells contains a complex filament network mixed with a solution of aqueous phase. The actomyosin polymer network is the main constituent of this filament phase that is responsible for active force generation, with the solvent phase comprising the dissolved filament units, G-actin monomers, and other constituents such as organelles. This phase undergoes Darcy- and Fick-type flow through the poroviscous actin network. It is termed a 'reactive flow' model as the significant chemical interchange between the two phases must be taken into account, which models polymerisation and depolymerisation of the actin network, with turnover on a timescale of 10^{-3} min.

In the model, Dembo and Harlow treat the cell membrane as the stationary walls of a rigid reaction vessel which fully encloses the cytoplasm. Both the phases are assumed to behave as homogeneous Newtonian fluids, the network housing a viscosity 1000 times greater than that of the solution phase.

To produce a tractable mathematical formulation, the authors state that it is necessary to ignore the microscopic details of the motion and the configuration of the network and solution phases and to instead concentrate on a representation in terms of average fields. In order to formulate a field theory for the cytoplasm, it is necessary to quantify the relative concentrations of network and solution phase near a particular location. This is done by using fractional volumes of the networks and solutions since there must be mass conservation of the cytoplasm.

The model aims to provide a macroscopic view of the cytoplasm and thus uses simplifications and assumptions that describe the cell membrane at this level. In summary, the four main assumptions are: (a) that membrane acts as an impermeable boundary, (b) the cytoplasm consists of only two phases, (c) the solution and network phases are "homogeneous," (d) the network and solution phases are Newtonian fluids and will be discussed in detail below.

A). Impermeable Membrane Boundary

The assumption of the membrane acting as an impermeable, stationary boundary which contains the cytoplasm is warranted despite displacement caused by cell locomotion. They argue, using the example of a cell crawling over a flat surface, that the membrane undergoes many random fluctuations in configuration which has a negligible effect on the cytoplasm behaviour, on average, over large distances. This assumption is

insufficient for fine details of membrane motion or in very large motions which occur rapidly. This assumption is made due to the difficulty in describing the transmission of forces from the cytoplasm to the membrane and from external objects. The membrane will experience inward contractile forces from the actin network, tangential viscous shear forces from the network and solution and inward and outward forces produced by pressure gradients across the membrane. Nevertheless, the author's adopt the simplest possible model of constant surface tension.

B). Two-Phase System

Although described as two-phases, the cytoplasm can, in fact, be divided into three distinct phases. This third phase consists of microtubes, intermediate filaments and other structural materials. Their approach is to view these materials as components of a porous architectural scaffolding that has a rheology of an elastic or viscoelastic solid which can be described by a continuous density distribution. The only consequence of this 'structural matrix' is to produce a frictional drag on the other two phases.

c). Homogeneity

The model assumes that the two phases are homogeneous. The distribution of G-actin varies in polarised cells. The model does not take into account diffusion of G-actin in the solution phase, convection of G-actin due to flow of this phase or the recruitment or redundancy of G-actin due to the formation or disassembly of the contractile network. They argue that under most conditions the solution phase of the cytoplasm will be well mixed so that there should be no significant changes in the distribution of G-actin.

D). Newtonian Fluid

The authors define a Newtonian fluid as 'an isotropic material in which the stress is a linear function of the rate of strain'. Whilst this is sufficient for the model, Taylor and Condeelis found evidence of non-Newtonian rheology in the network phase, which may arise due to a dependence of the stress on the past history of deformation (such as described by Maxwell [151]), or because of non-random orientation of network filaments (anisotropic fluid or liquid crystal). They state that a more complex approach which accounts for this non-Newtonian rheology may eventually be valid, but the difficulty in obtaining realistic estimates of these coefficients, along with the difficult analysis this poses, justify the simplification.

3.4. The current model

The model [7] that this study is gaining experimental data for requires the dynamic contact line to be measured for attaching cells, a parameter yet to be identified experimentally. By using a model which accounts for the four closely coupled components of the cell crawling cycle, the dynamic contact line enables predictions to be made on spreading and morphology.

As mentioned in Section 2.2.8., the cell crawling cycle can be described using four components. These being: the dynamics of (1.) The actin network and cytoplasm; (2.) The 'free' plasma membrane; (3.) Adhesion of the cell to a substrate and (4.) The underlying molecular biology that controls and coordinates (1-3.).

The cell-scale model for active cell motion consists of simple sub-models for each of the components (1.) to (4.). The first modelling simplification assumes that the cell has the configuration of a droplet partially wetting a flat surface, so that the plasma membrane adheres to the substrate at the 'contact line' as it advances and unadheres as it retracts.

The second step was to develop the simplest possible physically plausible sub-models for (1.) to (4.). As described, the actin network and cytoplasm was modelled as a composite of two 'reacting' fluids. The dorsal plasma membrane is assumed to be adhered to the substrate, adhesion being modelled by allowing the network phase to 'slip' along the substrate according to a Navier slip law. The underlying molecular biology is modelled using generic 'biochemical messengers' which simulate the average macroscopic mechanical effect of the large number of proteins associated with the actin network; the messengers are taken to be activated by the cell near either the plasma membrane or the contact line, to diffuse through the cell and to be deactivated as they control and coordinate the actin network distribution through the phenomenological constitutive laws needed for the mechanical component (1.).

The main modelling prediction is a near contact line law, which is given by:

$$\Theta^3 - \Phi^3 = \frac{3\mu(n)\ln(R/\lambda)}{\gamma}\left(3nV - J(V,n,...)\right)$$

where Θ is the dynamic contact angle (which remains to be determined by experimental means as the cell is spreading), Φ is the static contact angle, n the network density at the contact-line, J is the mass transfer rate from G- to F-actin at contact line and V equals the outward normal velocity of contact line.

When J is greater than 0, giving a smaller 'effective' contact angle, this will lead to an area of protrusion. Conversely, when J is less than 0, with a larger 'effective' contact angle, retraction will occur.

4. Materials and Methods

4.1. Introduction

This chapter details the experimental procedures and techniques used for this study. In order to provide data to test the mathematical model, images of cells attaching over extended periods were necessary. A major challenge of live cell imaging is maintaining viable cells that function as naturally as possible for the duration of the experiment. Fluorescence illumination can be harmful for cells and causes photobleaching and phototoxicity. The use of high power lasers as the excitation source adds to this challenge. Whilst bearing this in mind, the cell had to be imaged in sufficient detail to be able to produce accurate three dimensional reconstructions, requiring enough z-slices to piece the cell back together gaining information on the dynamic contact line, and with sufficient contrast to confidently determine the edge of the cell in each slice.

The images gained then had to be processed in such a way that information on the contact angle, contact radius, height and volume of the cell could be gained. This required a custom algorithm to be specifically written to achieve these aims. This included rebuilding the slices to create a three dimensional representation of membrane morphology, from which other measurements could be gathered.

Firstly, the chapter will give the details of cell culture, staining and methods to measure spreading cells in vitro as well as static fixation methods used for morphological comparison. The custom Matlab algorithm for processing the CLSM images is then detailed. Section 4.4 then gives the methods used for the deposition of Titanium Nitride and Titanium Oxide thin film coatings along with analytical techniques used to characterise these surfaces using XRD, XPS, Ellipsometry, profilometry and cell the response using immunocytochemistry.

4.2. Cell Culture

Human Caucasian osteosarcoma, TE85, cells (Health Protection Agency Culture Collections, Salisbury, UK) were cultured on tissue culture plastic in 10 ml Dulbecco/Vogt modified Eagle's medium (DMEM) supplemented with 10% foetal bovine calf serum (FBS), 1% non-essential amino acids, 2mM $_{L}$-glutamine, 20mM HEPES, 2% penicillin and streptomycin (Invitrogen, UK) and 50 $\mu g ml^{-1}$ ascorbic acid (Sigma, UK). Cell cultures were maintained in a humidified 95% air/5% CO_2 incubator at 37 °C with the medium changed every two days.

4.2.1. Cell Seeding for imaging

HOS cells between passages 42 and 50 were used in the experiments. Confluent flasks of HOS cells were incubated with 2ml trypsin/HEPES (0.02% trypsin, 10 mM HEPES in Ca, Mg-free PBS) for 5 min at 37 °C. An aliquot of 10 ml of fresh media was then added to the flask and the cells and media transferred to a 20 ml universal and centrifuged in a Jouan CR422 centrifuge for 5 minutes at 1200 rpm. The supernatant was resuspended in 1 ml Hank's Balanced Salt Solution (HBSS). Cell counting was performed using a trypan blue exclusion stain that stains non-viable cells. An aliquot of 50 µl of cell suspension was mixed with an equal amount of trypan blue. This was then applied to a haemocytometer and placed under a Nickon Eclipse TS100 microscope. The cells were seeded onto petri dishes with integral borosilicate glass coverslips (Iwaki, Japan) (subsequently referred to simply as petri dishes) which had previously been filled with DMEM for 60 mins prior to cell seeding and washed three times in PBS at 37 °C, to a density of 1×10^4 cells cm^{-2} in 3 ml of DMEM (without phenol red) containing FBS.

4.2.1.1. LavaCell epicocconone staining

3 µM LavaCell© epicocconone fluorescent stain (Gellcompany, Germany) was added to the resuspended cell supernatant in HBSS just prior to seeding, as described in section 4.2.1.

4.2.1.2. CellBrite DiI Staining

A 5 µM concentration of CellBrite© DiI stain was added to HOS cells in suspension in serum-free DMEM and incubated for 20 minutes at 37 °C. The labelled suspension was then centrifuged at 1500 rpm for 5 min, after which the supernatant was removed and the cells resuspended in 37 °C DMEM without phenol red. The centrifugation process was repeated twice more before the cells were seeded in the petri dishes to a density of 1 x 10^4 cells cm^{-2} in 3 ml of DMEM (without phenol red) containing FBS.

4.2.1.3. Fluoresceinphosphosphatidylethanolamine (FPE) Labelling

Adherent HOS cells were labelled with FPE dye (Institute of Biophysics, Imaging & Optical Science) as follows; 15 µl FPE dye (2 mg/ml) in methanol/chloroform was added into a polycarbonate tube. The organic solvent was removed under a stream of nitrogen gas followed by re-solvation with 15 µl ethanol. 5 ml sucrose buffer (10 mM Tris, 280 mM sucrose pH 7.5) was added to the tube and mixed. DMEM was removed from the cells which were then washed 3 times in 37 °C PBS. The cells were incubated in the stain solution for 45 min at 37 °C, after which the cells were again washed in PBS and fresh DMEM (without phenol red) containing FBS added.

4.2.1.4. Cell cytotoxicity test

Cells stained as mentioned above were incubated alongside cells prepared in the same manner but without the addition of stain, in a humidified 95% air/5% CO_2 incubator at 37 °C for 24 hours. The cultures were then compared visually using a Nickon Eclipse TS100 microscope and counted using a haemocytometer. No significant variation between cultures was observed for any of the stains.

4.2.3. Confocal Microscopy

The stained cells were examined live on a Leica SP2 inverted confocal laser scanning microscope (CLSM) using the 561 nm helium-neon laser (emission 570-620 nm) and a Lecia 63.0x1.40 oil objective. The microscope was positioned within a Perspex case maintained at 37°C using a blown air Oko Lab heater and thermocouple. The microscope required optimisation in order to maximise the length of time that the cells could be imaged, whilst maintaining them in a healthy state. It was found that the best images were produced with the airy pinhole set to 2.5 and the laser power set to 4 %. Digital image files with a 512 x 512 pixel resolution were recorded at micrometer steps throughout the cell's entirety at 5 min intervals from 15 to 90 min post seeding.

Preliminary experiments were performed to find the minimum number of z steps necessary to produce accurate three dimensional representations of cells. The largest possible z step size was sought to allow for longer imaging periods as it reduced the cells' exposure to the laser. The main parameter required for the model was the contact angle between the cell and the substrate, so the accuracy of this measurement was chosen to determine the validity of the technique. This was achieved by performing an experiment using a z step increment of 0.1 μm on the same population of cells at 15, 45 and 90 min. The algorithm was employed to process all of the z steps and then produce subsequent reconstructions only using every second file to represent a 0.2 μm step,

third file to represent a 3 μm step and so on, to represent scanning through at different z heights. The largest z step which gave a contact angle in agreement with that calculated using the smallest z steps of 0.1 μm was chosen. The optimum step size was thus found to be 1.9 μm.

4.2.4. SEM Preparation

After the incubation period, the cells were fixed using the following protocol:
The cells were washed three times in pre-warmed (37 °C) PBS in situ. After the third wash, the PBS was replaced with 3 wt.% glutaraldehyde in 0.1 M sodium cacodylate buffer and left at room temperature for 30 mins. This fixative was replaced with 7 wt.% sucrose solution in 0.1 M sodium cacodylate buffer. The specimens were then washed three times in 0.1 M sodium cacodylate buffer, leaving the buffer on for 5 minutes for each wash. One percent osmium tetroxide in distilled water was added as a postfix for 45 mins. The samples were then dehydrated through a series of ethanol/distilled water washes, gradually increasing in alcohol concentration (20 vol.% x 2 min, 40 vol.% x 5 min, 60 vol.% x 5 min, 80 vol.% x 5 min, 90 vol.% x 5 min and 100 vol.% x 5 min x 2). Specimens were then submerged in hexamethyldisilazane (HMDS) for 5 mins. This was then replaced with fresh HMDS and left to dry overnight. The samples were then palladium coated prior to SEM viewing to prevent sample charging.

4.2.4.1. Scanning Electron Microscopy (SEM)

SEM images of cells were obtained using a Phillips XL-30 scanning electron microscope (LaB_6) at accelerating voltages between 10-20 KeV and a working distance of 10 mm. Cells adhered to borosilicate glass cover slips were mounted on aluminium stubs with adhesive carbon tabs and palladium coated using an Edwards high vacuum evaporator unit to coat samples with an approximate thickness of 5 nm.

4.3. Image Processing

Below is the Matlab algorithm used for Image Processing, with explanations, using figure 4.3.1. as an example.

This code was written by the author and later modified by Laura Gallimore, a DPhil student at the University of Oxford [160]. Some parts of the code were taken from the Matlab file sharing website, as indicated. The processing is used to create accurate, three dimensional representations of the cell membrane. By achieving this, data on the contact radius, dynamic contact line, membrane slope and speed and cell volume can be calculated. This information on the cell can then be used to further develop and verify the two-phase reactive flow models.

Below is the initial Matlab™ Image Processing algorithm developed by the author. Briefly, the processing involved converting the images to binary form and detecting the edge using the Prewitt first derivative method. This was chosen due to its resilience to Poisson type noise [161] and its use of averaging to further reduce the effects of other noise types [162]. The object pixels were then dilated, holes in the body filled and objects not part of the cell body around the periphery deleted. The perimeter of this was then overlaid on the original image of the cell to visually check for accuracy.

The code is explained below, using figure 4.3.1 of one confocal z stack slice of recently adhered HOS cells on borosilicate glass.

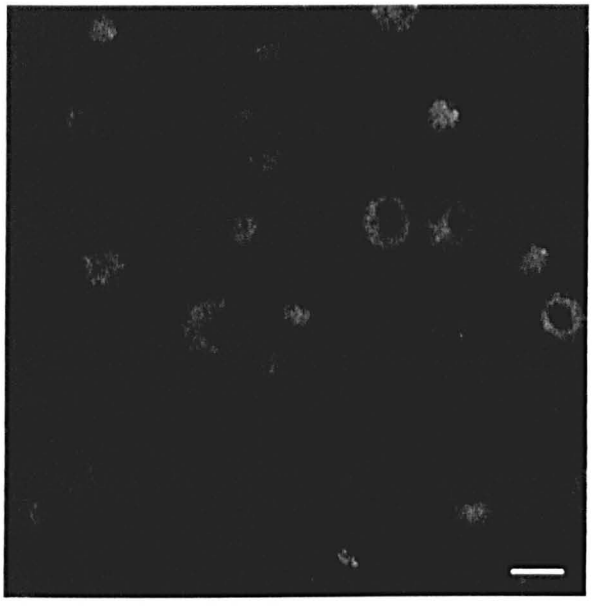

Figure 4.3.1 CLSM 512 x 512 pixel (238 x 238 µm) grayscale image of one z slice through HOS cells attching to borosilicate glass. Scale bar 20 µm.

- The following section of code loads the images into Matlab in the form of .tif files.

```
%clears all variables from the workspace
clear all;
close all;

%specify folder containing images
directory = ('c:\example');
```

- In the following section, the step size between the confocal z stacks used in the image acquisition is added with layer_sep so that the edge of the cell in each optical section can be used to create a contour plot. The image size is given in pixels and microns.

```
layer_sep = 1.017584; %in um
imsize = 512; %in px
actsize = 238.1; %in um
```

- This section allows for manual resizing of the image to give the an area of interested if the whole field is not required, for instance cropping the image so only one cell is visible.

```
Nxmin = 75;
Nxmax = 450;
Nymin = 50;
Nymax = 425;
```

- This section reads in all the .tif files from the analysis folder and stores a range of information in the file_name array. With '.name' the name of each file can be extracted

```
while z <= file_number

%loads image from the from specified folder
I = imread(fullfile(directory,file_name(z).name));
```

- The following section thresholds the image and allows a different threshold to be applied to different images, which may be necessary if the intensity of the stain varies. Thresholding an image is a simple form of segmentation, producing a binary image. Pixels are either marked as an object '1' above a threshold value, or background '0' below the threshold.

Prewitt is a first derivative method of detecting the *edge* (the perimeter of the 'object' produced by thresholding) using pixel intensities. In detecting edges, the intensity gradient is measured at a point in the image. This is shown in figure 4.3.2. with the binary gradient mask added.

```
[junk, threshold] = edge(I, 'prewitt');
intensity = 1.00;
BWs = edge(I,'prewitt', threshold);
```

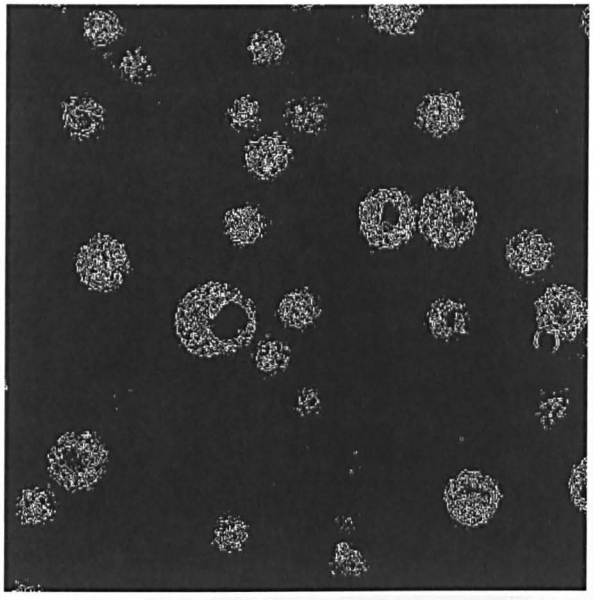

Figure 4.3.2. Image showing the application of the binary gradient mask.

```
%applies a dilation filter
se =strel('disk',4,4);
BWsdil = imdilate(BWs,se);
```

The morphological structuring element, se = strel('disk', R, N) creates a flat, disk-shaped structuring element, where R specifies the radius as can be seen in Figure 4.3.3. the radius *R* must be a nonnegative integer. *N* is the neighbourhood, this is a rectangular block of pixels to which the structuring element will be applied. For a binary image of 1s and 0s, 1 defines the neighbourhood for the morphological operation. This dilates each neighbourhood by a given shape/radius dependent on the chosen structuring element as illustrated in Figure. 4.3.3. and shown applied to the CLSM image in 4.3.4.

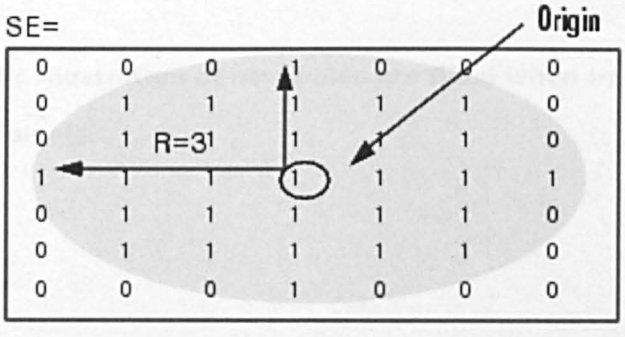

Figure 4.3.3. Schematic illustration of the disk structuring element (From: [162]).

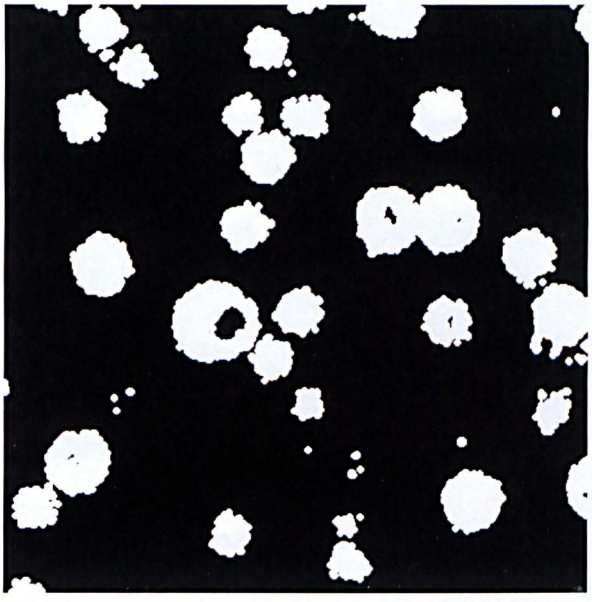

Figure 4.3.4. Applying the strel dilation filter to the binary gradient mask.

```
%filling of holes remaining within the white cell body
BWdfill = imfill(BWsdil, 'holes');
```

- Holes are Filled by changing 0s to 1s when the 0 is surrounded by a neighbourhood of 1s, for example, this can be represented schematically as and is demonstrated in figure 4.3.5. and applied to the CLSM image in 4.3.6.

```
0000100000     to     0000100000
0001010000            0001110000
0010000100            0011111100
0001010000            0001110000
0000100000            0000100000
```

Figure 4.3.5. Schematic illustration of how holes are filled when background pixels are surrounded by object pixels.

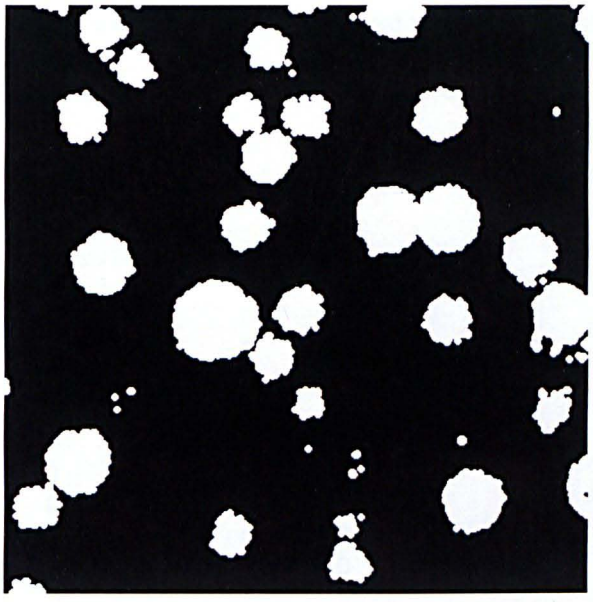

Figure 4.3.6. Image showing holes filled.

- The code below deletes any object connected to, but not part of, the border using a specified neighbourhood connectivity.

```
%suppresses light structures connected to image border
BWnobord = imclearborder(BWdfill, 4);
%removes objects of a specified size eg. 3000
BWnobord = bwareaopen(BWnobord, 3000);
```

The following binary image is subjected to different neighborhood connectivitys to illustrate the effect of `imclearborder`.

```
BW =
     0     0     0     0     0     0     0     0     0
     0     0     0     0     0     0     0     0     0
     0     0     0     0     0     0     0     0     0
     1     0     0     1     1     1     0     0     0
     0     1     0     1     1     1     0     0     0
     0     0     0     1     1     1     0     0     0
     0     0     0     0     0     0     0     0     0
     0     0     0     0     0     0     0     0     0
     0     0     0     0     0     0     0     0     0
```

Using a 4-connected neighborhood, the pixel at (5,2) is not considered connected to the border pixel (4,1) as it is separated by a column of zeros, so it is not deleted.

```
BWc1 = imclearborder(BW,4)
BWc1 =
     0     0     0     0     0     0     0     0     0
     0     0     0     0     0     0     0     0     0
     0     0     0     0     0     0     0     0     0
     0     0     0     1     1     1     0     0     0
     0     1     0     1     1     1     0     0     0
     0     0     0     1     1     1     0     0     0
     0     0     0     0     0     0     0     0     0
     0     0     0     0     0     0     0     0     0
     0     0     0     0     0     0     0     0     0
```

Using an 8-connected neighborhood, pixel (5,2) is considered connected to pixel (4,1) so both are cleared.

```
BWc2 = imclearborder(BW,8)

BWc2 =
     0     0     0     0     0     0     0     0     0
     0     0     0     0     0     0     0     0     0
     0     0     0     0     0     0     0     0     0
     0     0     0     1     1     1     0     0     0
     0     0     0     1     1     1     0     0     0
     0     0     0     1     1     1     0     0     0
     0     0     0     0     0     0     0     0     0
     0     0     0     0     0     0     0     0     0
     0     0     0     0     0     0     0     0     0
```

This operation is applied to the CLSM image in figure 4.3.7.

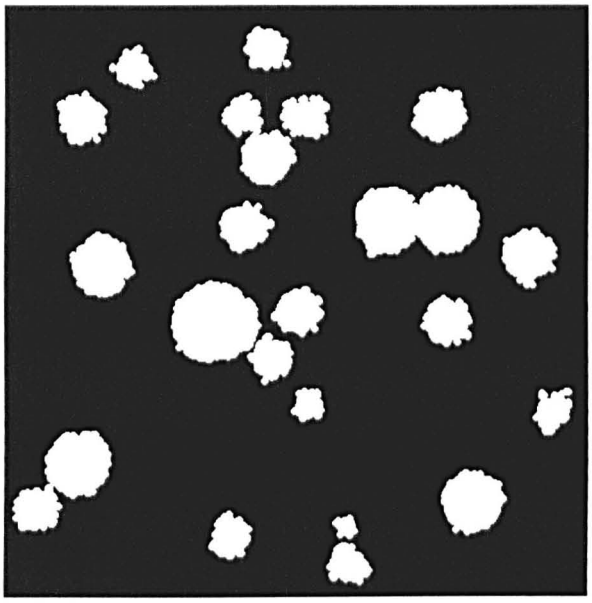

Figure 4.3.7 Image cleared of objects not attached to the border.

- The following smoothes the image by searching through neighbourhoods, using the disk structuring element and if all neighbours are 1s, then the pixel is set to 1. If any are 0s, then it is set to 0. This is applied to the CLSM image in figure 4.3.8.

```
seD = strel('disk',4,4);
BWfinal = imerode(BWnobord,seD);
BWfinal = imerode(BWfinal,seD);
```

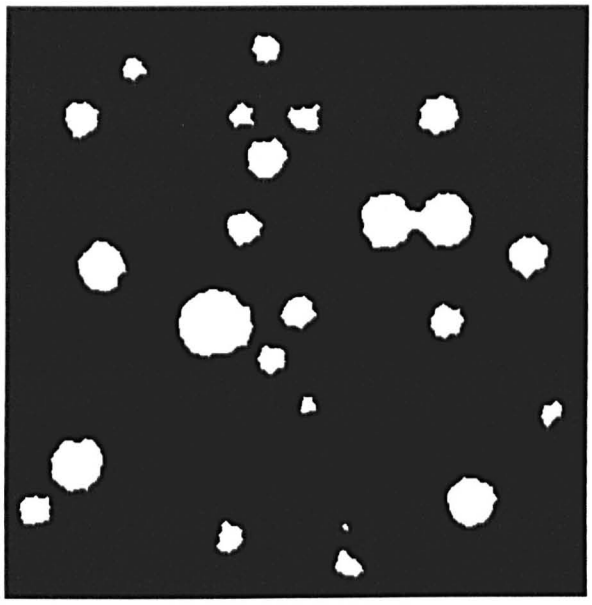

Figure 4.3.8 Cells are returned to their original size.

- This function removes small objects of a defined size.

```
%removes objects of a specified size eg. 3000
BWfinal = bwareaopen(BWfinal, 3000);
```

It can be split down into the following steps:

1. Identify connected components.

```
L = bwlabeln(BW, conn);
```

2. Calculate the component's area.

```
S = regionprops(L, 'Area');
```

3. Remove objects with an area below the specified size.

```
bw2 = ismember(L, find([S.Area] >= P));
```

This is applied to the CLSM image in figure 4.3.9., where small objects have been deletd.

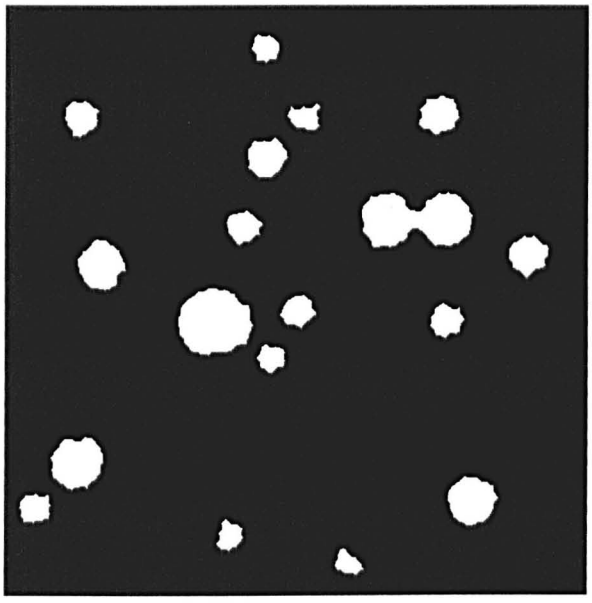

Figure 4.3.9. Small objects have been deleted using the bwareaopen function.

- The following identifies the outline of the binary cell image and combines it with the original image, seen in figure 4.3.10.

```
BWoutline = bwperim(BWfinal);
Segout = I;
Segout(BWoutline) = 255;
```

BW2 = bwperim(BW1) returns a binary image containing only the perimeter pixels of the object. A pixel is part of the perimeter if it is 1 and it is connected to at least one 0 pixel. Segout isolates this object.

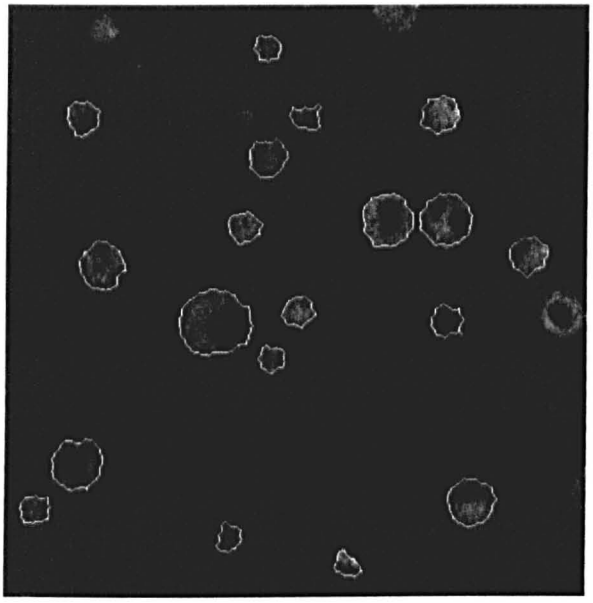

Figure 4.3.10 Cell image combined with perimeter outlines.

- The following section creates x y z data points and stores data of all images in array called X Y and Z.

```
if z == 1
    %scaling data
    X = j*(actsize/imsize);
    Y = i*(actsize/imsize);

    %storing data
    [b,c] = size(j);
    Z = ones(b,c);
    Z = Z*0;

elseif z > 1

    %scaling data
    H = layer_sep*(z-1);
    j = j*(actsize/imsize);
    i = i*(actsize/imsize);

    %storing data
    X = cat(1,X,j);
    Y = cat(1,Y,i);

    [b,c] = size (j);
    T = ones(b,c);
    T = T*H;
    Z = cat(1,Z,T);


else

    error('Unexpected situation')
```

- The next part of the code finds the geometric centre, centroid, of the cell outlines, so that they can be stacked, which can be seen in figure 4.3.11.

```
finds the center of mass of BWfinal (a binary image)
-L = bwlabel(BWfinal);
-s  = regionprops(L, 'centroid');
-centroids = cat(1, s.Centroid);
-hold on
-plot(centroids(:,1), centroids(:,2), 'b*')
-hold off


z = z + 1;
end
surfstack = surfstack + BWfinal;
```

The above creates an array with the background set to 0. The addition of an image to the previous increments the previous one, creating a stack, which is used for the surface plot.

```
%Creation of a 3D plot from the stored data
figure, plot3(X,Y,Z,'ok','MarkerSize',3);
axis('equal');
```

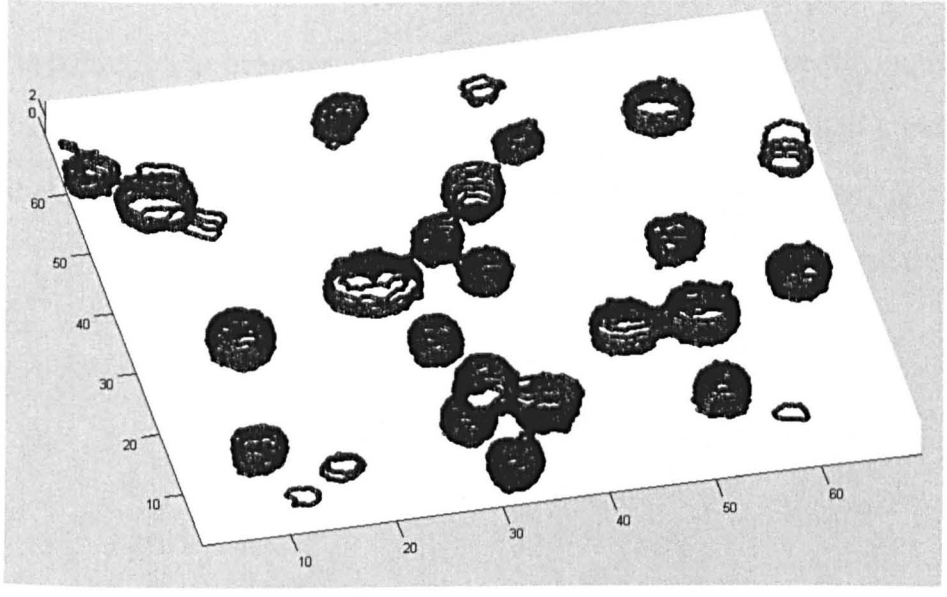

Figure 4.3.11 cell outlines from the confocal z stack overlayed with the appropriate z height between contours.

- The surface is created, by draping it over the contour plot

```
%scales the "surfstack" stack
surfstack = surfstack*layer_sep;
```

```
% Turn the scanned point data into a surface
gx= min(X):(max(X)-min(X))/40:max(X);
gy= min(Y):(max(Y)-min(Y))/40:max(Y);
g=gridfit(X,Y,Z,gx,gy);
figure
colormap(hot(256));
surf(gx,gy,g);
camlight right;
lighting phong;
shading interp
line(X,Y,Z,'marker','.','markersize',4,'linestyle','none');
title 'Use topographic contours to recreate a surface'
```

The above code was further developed by Laura Gallimore [160] to increase the accuracy of finding the cell outlines using an active contours model. This is a framework for delineating an object outline by attempting to minimize an energy associated to a given contour as a sum of the internal and external energy. From an initiation point outside the contour, the framework, referred to as 'snake', dynamically moves towards the object contour by minimising its energy iteratively [163].

The code starts by quickly processing the confocal slices and roughly identifying cells and storing this information. The code then works through each individual cell in greater detail, using the active contour method and giving estimates on the accuracy of the fit of each contour. From the resultant contour plot, a spherical cap is fitted to give data on the contact line, radius and cell volume and height.

- The first section clears any variables in the Matlab workspace and closes any open figures/files. The file containing the confocal .tif images is then called for.

```
clear all
close all

directory = ('c:\14_05_10\series 4 cells');
```

- The layer separation between the confocal z stacks is then added manually below. Imsize and actsize would not normally be varied.

```
layer_sep = 1.872354; %in um
imsize = 512; %in px
actsize = 238.095238; %in um
```

- A file is then specified for the processed images and other data to be written to.

```
fid = fopen('c:\14_05_10\series 4 cells'\results.txt','wt');
```

- Individual time point files can then be specified as below, along with the top and bottom of the cells.

```
times=0:10:170;
bottom=11*ones(length(times),1);
top=[1;1;1;1;1;1;1;1;1;1;1;1;1;1;2;2;2;2];
```

- The algorithm then codes to count through each time point

```
for tt=1:length(times)
%for tt=1

%define variables
% i = 0;
% j = 0;
% L = 0;
% X = 0;
% Y = 0;
% Z = 0;
% T = 0;
% b = 0;
% c = 0;
z = 1;
surfstack = 0;
```

- This section reads in all the .tif files from the analysis folder and stores a range of information in the file_name array. With '.name' the name of each file can be extracted.

```
file_name = dir (fullfile(directory, num2str(times(tt)), '*.tif'));


%get number of files in array
[file_number, a]=size(file_name);

%% Load Images
```

- The image analysis starts with this section of the code

```
%while z <= 13
```

- Count through each stack from bottom to top

```
for z = bottom(tt):-1:top(tt)

%loads image from the from specified folder
[I,map] =
imread(fullfile(directory,num2str(times(tt)),file_name(z).name));
%figure, imshow(I), title('original image');
```

- The image is then passed through a threshold and the object pixels are dilated using the disk structuring element.

```
tlevel = graythresh(I);
BW = im2bw(I(200:512,1:400),tlevel);
%figure, imshow(BW)
% applies a dilation filter
se =strel('disk',4,4);
BWdil = imdilate(BW,se);
%figure, imshow(BWdil), title('dilated gradient mask');
```

- The holes are then filled.

```
BWdfill = imfill(BWdil, 'holes');
%figure, imshow(BWdfill), title('binary image with filled holes');
```

- The following section deletes any object connected to, but not part of, the border using a specified neighbourhood connectivity.

```
 BWnobord = imclearborder(BWdfill, 4);
%removes objects of a specified size eg. 3000

BWnobord = bwareaopen(BWnobord, 300);
%figure, imshow(BWnobord), title('cleared border image');
```

- The disk structuring element is then reused to dilate the object pixels so that the cell returns to its original size. This initial section of the code is to give an estimate of where the cells are. The connectivity can then be calculated so that individual cells can be cropped.

```
%% Re-dilate Cells

se2 =strel('disk',4,4);
BWnobord = imdilate(BWnobord,se2);
%BWnobord = imdilate(BWnobord,se2);
```

- The filled disks are then stacked, enabling the cells to be detected in 3D by connectivity. This concatenates matrices in the 3rd (z) direction, a function of matlab.

```
if z==bottom(tt)
    BWfill3D=BWnobord;
else
    BWfill3D = cat(3, BWfill3D, BWnobord);
end


%increments z to load new image
%z = z + 1;

end
```

- Individual cells are then isolated. This labels each of the connected objects, the cells, with a different number which can be plotted as different colours. Cell_no is a Matlab function that records the number of cells found in one image, with 18 being an option for what counts as connected.

```
[L,cell_no] = bwlabeln(BWfill3D,18);
```

- A 'number of cells' by 6 matrix is then set up to store cropping values. The following code then cycles through the cells and finds all pixels that are part of that cell. The largest and smallest pixel positions in the x and y directions are

then stored. This is needed as the same box will not be cropped around each cell at different time points.

```
crop_store=zeros(cell_no,6);

for q=1:cell_no
[i,j,k]=ind2sub(size(BWfill3D),find(L==q));
    crop_store(q,1)=min(i);
    crop_store(q,2)=max(i);
    crop_store(q,3)=min(j);
    crop_store(q,4)=max(j);
    crop_store(q,5)=min(k);
    crop_store(q,6)=max(k);
end % for q counting through cells
```

- The cell outlines are then found and stacked. Measurements are also recorded and the image cropped to focus on one cell.

```
for q=1:cell_no
%for q=7
    % initialise vectors X,Y,Z to be empty for each cell
    X=[];
    Y=[];
    Z=[];
    % variable to count number of points in each layer
    num_slices=crop_store(q,6)-crop_store(q,5)+1;
    Zcount=zeros(num_slices,1);
    baselayer=1;
```

- The following re-defines the border around the cell. This step is needed to ensure that the whole cell has been captured, as the faster, earlier processing of the whole image is not as accurate.

```
    % measurements for this cell
    l1=round((crop_store(q,2)-crop_store(q,1))/3);
    l2=round((crop_store(q,4)-crop_store(q,3))/3);


    % step through layers belonging to a cell
    for p = crop_store(q,5):crop_store(q,6)

Iwhole=imread(fullfile(directory,num2str(times(tt)),file_name(p).name)
);
        Idiff = anisodiff(I,10,0.14,0.5,1);
```

- This section of the code was taken from open source Matlab central code sharing website which uses principles of anisotropic diffusion to smoothen the image. This

process maintains edges by choosing the diffusion coefficient to vary spatially in such a way as to encourage intraregion smoothing in preference to interregion smoothing [164].

```
        % crop image to focus on one cell
        Ipic = I(max(crop_store(q,1)-
11,1):min(crop_store(q,2)+l1,size(I,1)), ...
                    max(crop_store(q,3)-
12,1):min(crop_store(q,4)+l2,size(I,2)));
        Icrop = Idiff(max(crop_store(q,1)-
11,1):min(crop_store(q,2)+l1,size(I,1)), ...
                    max(crop_store(q,3)-
12,1):min(crop_store(q,4)+l2,size(I,2)));
        %figure, imshow(Ipic, 'InitialMagnification','fit')
        Ipic=im2double(Ipic);
```

- Here, the pixel values are scaled to make use of the whole range, making the cell images more visible.

```
        Icrop = (Icrop-min(min(Icrop)))/(max(max(Icrop))-
min(min(Icrop)));
        %figure, imshow(Icrop, 'InitialMagnification','fit')

        % find position of points that make up cell outline on this
layer
```

- The next section generates an initialisation for the active contours code. This is similar to the earlier section of the code which quickly identifies a cell, but is used on the smoothed image of one cell. The initialization starts outside of the cell as the contour moves inwards. The initialisation needs to start close to the cell, as if it is too large and hits the edge of the region, then it is rejected. White regions which may be from neighbouring cells around the edge of the specified region are also deleted, as the active contours method cannot run with contours that run out of the region. The code has three attempts to get a successful initialisation. On the second attempt a different threshold may be used. The third attempt generates an ellipse.

```
%tlevel = graythresh(Icrop);
BW = im2bw(Icrop,0.1);%0.22
%figure, imshow(BW)
% applies a dilation filter
```

```
se =strel('disk',4,4);
BW = imdilate(BW,se);
%figure, imshow(BW,'InitialMagnification','fit')
BW = bwareaopen(BW, l1*l2);
BW = imclearborder(BW,4);
BW = imfill(BW,'holes');
BW = bwperim(BW);
%figure, imshow(BW,'InitialMagnification','fit')
[i,j]=find(BW);

N=length(j);
if N==0
    BW = im2bw(Icrop,0.1);
    BW = bwareaopen(BW, l1*l2);
    BW=imfill(BW,'holes');
    BW = bwperim(BW);
    [i,j]=find(BW);
    NN=length(j);
    fprintf('failed to generate initialisation automatically,
2nd attempt: t%i c%i layer%i \n',times(tt),q,p);
    if NN==0
        fprintf('failed to generate initialisation
automatically used circle instead: t%i c%i layer%i \n',times(tt),q,p);
        theta=(-pi:0.2:pi)';
        x=l1*cos(theta)+2.5*l1;
        y=l2*sin(theta)+2.5*l2;
    else
        [theta,bin]=cart2pol(j-sum(j)/NN,i-sum(i)/NN);
        [bin2,P]=sort(theta);
        j=j(P);
        i=i(P);
        index=convhull(j,i);
        x=j(index);
        y=i(index);
    end
else
    [theta,bin]=cart2pol(j-sum(j)/N,i-sum(i)/N);
    [bin2,P]=sort(theta);
    j=j(P);
    i=i(P);
    index=convhull(j,i);
    x=j(index);
    y=i(index);
end
```

- The points that make up the initialisation are stored for the contour code in consecutive order. This is done by converting these points to polar coordinates, so that they can be ordered by angle in the matrix P. To ensure that none of the initializations are horseshoe shaped, which may occur if the dark nuclear region is near the edge of the cell, the Matlab function Convhull is used to calculate the convex hull of the points generated.

```
%plot(x,-y,'-b'), axis equal
```

```
%figure
[x,y,iter,flag]=snake_att5_140510(Icrop,50,x,y,0);
```

The above calls for the subroutine which includes the active contours code. This is based on work by Mansard *et al.* [163] who demonstrated the accuracy and reproducibility of the technique using MR vascular images. This method is advantageous as there is simplified parameter tuning, fast convergence, and minimal user interaction, which could cause variations in the result. The function is heavily based on code written by Jack Lee [165], with adaptations made by Laura Gallimore [160]. An active contour begins as a curve that changes from an initial basic shape by moving towards an edge, by means of external-force action and internal-force reaction. The external forces act to attract the curve toward the boundaries of objects within the image, while the internal forces work to conserve its expected shape. Without the need for a detailed *a priori* knowledge of the expected shape, the internal forces direct the continuity and the smoothness of the resulting curve. The algorithm reaches its end point when equilibrium is reached between the internal and external forces [163].

```
if flag
    fprintf('No outline captured for: t%i c%i layer%i, no data
points stored \n',times(tt),q,p);
    continue % will skip code onto next p value
end
```

The following section plots the contour over the cell image and saves it, so that it may be visually checked later.

```
%hold off
figure(1)
clf;
set(gcf,'Color','w');
imshow(Ipic,'InitialMagnification','fit')
hold on
plot(x,y,'.r')
title (sprintf('iterations: %i  intensity ratio: %3f   ave
inside: %3f  ave outside: %3f  ave ratio %3f',...
                iter,rI,ai,ao,ra));
hold off
name=sprintf('t%i_c%i_stack%i_2.png',times(tt),q,p);
```

```
        saveas(gcf,fullfile(directory,num2str(times(tt)),name));
        %close gcf
```

- This section stores the X,Y,Z values as pixel numbers as the active contours code interpolates the data as non-integers.

```
        if baselayer
            X=x;
            Y=y;
            Z=(p-1)*ones(length(x),1);
            baselayer=0;
        else
            X=[X;x];
            Y=[Y;y];
            Z=[Z;(p-1)*ones(length(x),1)];
        end
    end % for p counting through layers
```

- The following section re-scales the pixels and fits a sphere over the contours. The code will give the average distance from the sphere along with the maximum distance that a point contour is from the fitted sphere.

```
    X = X*(actsize/imsize);
    Y = Y*(actsize/imsize);
    Z = layer_sep*Z;
    name=sprintf('t%i_c%i_xyz2.mat',times(tt),q);
    save(fullfile(directory,num2str(times(tt)),name),'X','Y','Z');

    if isempty(X)
        fprintf('No data points found for: t%i c%i \n',times(tt),q);
        sph=zeros(4,1);
        r2=0;
        rinf=0;
        %continue % will skip code onto next q value, next cell
    else
        % call to function to calculate best fit sphere
        [sph,resnorm,res]=fit_sphere_ls(X,Y,Z);
        % average distance from sphere
        r2=sqrt(resnorm/length(Z));
        % max distance from sphere
        rinf=max(abs(res));
    end % if no X,Y,Z data

    % Comparative plots
%%%
```

```
%       plot3(X,Y,Z,'.k')
%       hold off
```

- The following section prints data to the file opened specified at the start of the code.

```
    fprintf(fid, '% d', tt);
    fprintf(fid, '% d', cell_no);
    fprintf(fid, '% d', q);
    fprintf(fid, '% d', crop_store(q,1));
    fprintf(fid, '% d', crop_store(q,2));
    fprintf(fid, '% d', crop_store(q,3));
    fprintf(fid, '% d', crop_store(q,4));
    fprintf(fid, '% d', crop_store(q,5));
    fprintf(fid, '% d', crop_store(q,6));
    fprintf(fid, '% 6f', sph(1));
    fprintf(fid, '% 6f', sph(2));
    fprintf(fid, '% 6f', sph(3));
    fprintf(fid, '% 6f', sph(4));
    fprintf(fid, '% 6f', min(Z));
    fprintf(fid, '% 6f', r2);
    fprintf(fid, '% 6f', rinf);
    fprintf(fid, '% d', length(Z));

    fprintf(fid, '\n');


  end % for q counting through cells

end % for tt counting through timesteps
```

The file that the data has been written to is then closed.

```
fclose(fid);
```

This gives the data on each cell as a three dimensional contour plot, to which the cell membrane can be added as a surface. From this, data on the contact line, contact radius and cell height can be gained.

4.4. Thin Films

Thin films were deposited using a system designed and constructed by Botteril [152]. The cylindrical chamber was formed from rolled stainless steel with an internal diameter of 400 mm and a height of 400 mm. The system was loaded from the top and contained upper and lower vertically opposed balanced water cooled Ion Tech B325 planar magnetrons. Substrate deposition was performed using only the lower magnetron with 75 mm diameter targets.

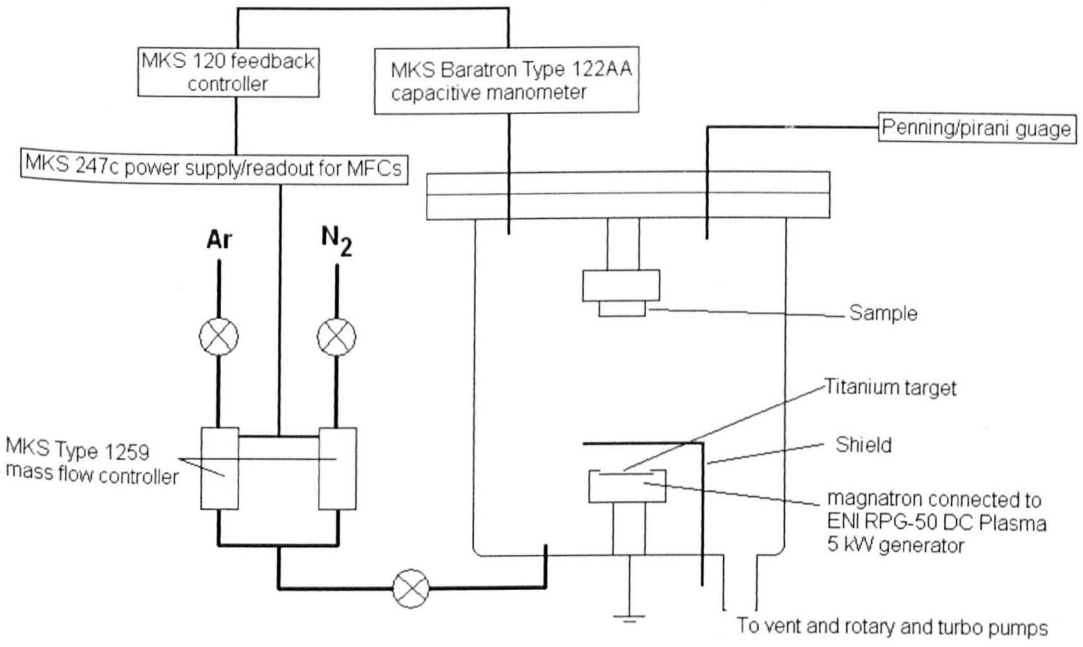

Figure 4.4.1. Schematic diagram of the PVD Deposition Chamber.

The chamber was pumped to a vacuum of 10^{-6} Torr (1.3×10^{-4} Pa) using an Edwards RV8 rotary pump and a water cooled Edwards EXT250 Turbomolecular pump.

As shown in tables 4.1 and 4.2, TiN and a non stoichiometric TiO were deposited on the petri dishes by reactively sputtering a cp titanium target mixed in Ar/N_2 86:14 and an

Ar/Air 93:07 atmosphere using an ENI RPG-50 DC Plasma 5 kW generator system. The chamber was evacuated to better then 10^{-5} Torr and the target surface was cleaned prior to deposition by pre-sputtering for 30 min at 150 W in an Ar atmosphere. Feed gas ratios were maintained using individual mass flow controllers (MKS Type 1259) accurate to 0.1 sccm flow rate. The working gas pressure was sustained using a capacitive manometer (MKS Baratron Type 122 AA) and the signal fed back to the mass flow controllers to keep the chamber pressure at 5.0 ± 0.1 mTorr. The petri dishes were sterilised in 70 % ethanol for 20 min, left under UV overnight and washed three times for five minutes in sterile PBS before cells were seeded.

Sample Thickness	Working gas	Total pressure /mTorr	Target voltage (-) /V	DC power /W	Time /min
10 nm	Ar (93%) Air (7%)	5 ± 0.1	400-480	6.8	5.88
0.2 µm	Ar (93%) Air (7%)	5 ± 0.1	400-480	6.8	118
1 µm	Ar (93%) Air (7%)	5 ± 0.1	400-480	50	192.5

Table 4.1. PVD conditions used to produce TiO surfaces of the three thicknesses studied.

Sample Thickness	Working gas	Total pressure /mTorr	Target voltage (-) /V	DC power /W	Time /min
10 nm	Ar (84%) N (16%)	5 ± 0.1	400-480	6.8	5.88
0.2 µm	Ar (84%) N (16%)	5 ± 0.1	400-480	6.8	118
1 µm	Ar (84%) N (16%)	5 ± 0.1	400-480	50	192.5

Table 4.2. PVD conditions used to produce TiN surfaces of the three thicknesses studied.

4.5. Characterisation of thin films

4.5.1.1. X-ray Diffraction Analysis (XRD)

X-rays primarily interact with electrons in atoms. When x-ray photons collide with electrons, some photons from the incident beam are deflected away from the original direction of travel. If the wavelength of these scattered X-rays remains constant, the process is called elastic scattering (Thompson Scattering) and it is these x-rays that are measured in diffraction experiments.

Diffracted waves from different atoms can interfere with each other and the resultant intensity distribution is strongly modulated by this interaction. If the atoms are arranged in a periodic fashion, as in crystals, the diffracted waves will consist of sharp interference maxima (peaks) with the same symmetry as in the distribution of atoms. Measuring the diffraction pattern therefore allows us to deduce the distribution of atoms in a material.

The diffracted X-ray beam can give data on:

1. The distance of the interatomic spacing (d-spacing).
2. The angle of diffraction.
3. The wavelength of the incident X-radiation.

These form Bragg's law:

$$n\lambda = 2d\sin\theta$$

Where

n = an integer, λ = wavelength, d = d spacing, θ = diffraction angle in degrees.

The conventional Bragg-Brentano X-ray diffraction geometry has limitations when studying ultra thin films, partly because of poor sensitivity and partly because of the presence of the interfering effect of the substrate. To ensure that the diffraction pattern

is not influenced by the substrate, a low angle of incidence of X-ray is required so as to probe the material to a specific depth. This technique is called grazing angle diffraction (GAXRD) and is based on a slight modification of conventional Bragg-Brentano geometry [153].

4.5.1.2. Experimental

X-ray diffraction (XRD) analysis was carried out on the surface of the as-deposited samples with a Bruker AXS D8 Advance X-ray diffractometer used in glancing angle X-ray diffraction mode. X-rays (λ = 1.5406 Å) were supplied by a copper source run at 40 KeV and 40 OA. The X-ray tube was fixed at 3 ° to the plane of the sample surface and fitted with 0.6 mm incidence divergence. The patterns were recorded between 20 ° and 80 ° (2θ) with a step size of 0.02 °. The samples were mounted on Perspex holders using plasticine.

4.5.2. X-ray Photoelectron Spectroscopy (XPS)

When an incident x-ray is absorbed by an atom, it leads to the ejection of an electron, termed photoionisation, either from the core or a valence electron. A small number of these ejected electrons from the top 1 to 10 nm of the surface may escape the material in a vacuum in the process of photoemission. As the energy of the x-ray is known, the electron binding energy of each of the emitted electrons can be determined using the equation below:

$$E_{binding} = E_{photon} - (E_{kinetic} + \Phi)$$

Where $E_{binding}$ is the binding energy of the electron, E_{photon} is the energy of the incident x-ray, $E_{kinetic}$ is the kinetic energy of the electron as measured and Φ is the work function of the spectrometer (typically 4.5 eV).

Each element has a characteristic binding energy, allowing recognition of all elements with the exception of helium and hydrogen and the number of electrons detected is

directly related to the amount of that element within the area irradiated. XPS is also sensitive to chemical bonding of elements and the binding energy can vary according to the chemical state of an atom [154].

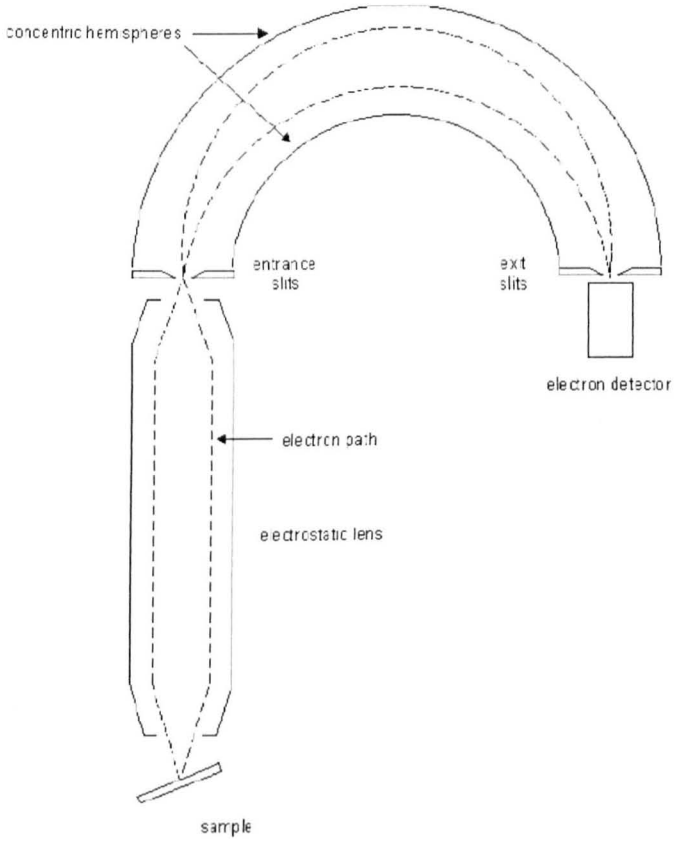

Figure 4.5.1. A concentric hemispherical analyzer (CHA) used for the detection of electrons in XPS. (From: [154]).

Al (1486.6 eV) or Mg (1253.6 eV) are commonly used as the x-ray emission source, with these sources sometimes being monochromated by single or multiple Bragg reflections from suitable crystals. This allows only the Kα lines to be used for the production of photoelectrons increasing the resolution by lowering the energy spread from between 0.7 - 0.8 eV to approximately 0.2 eV, however, this diminishes the counts. By moving the x-ray source in close proximity of the sample (10 mm), this can be overcome. The distance is restricted by the need for a Be or Al window of 10 – 30 μm at the detector to prevent secondary electrons being detected whilst also providing a barrier between outgasing x-ray source and the ultra-high vacuum (UHV) analysis chamber (>10^{-9} Torr (1.3×10^{-7} Pa)). The emitted photoelectrons are analysed with a concentric

hemispherical analyser (CHA), figure 4.2, which either operates in constant analysis energy (CAE) or constant retard ratio (CRR) mode. CAE mode has the analyser pass energy fixed, meaning if the pass energy is 40 eV, electrons of 1000 eV will be slowed down by 960 eV in order to be detected. In CRR mode, the pass energy is adjusted to maintain a constant value for the quantity of initial electron energy divided by the pass energy. So if the retard ratio is 10 and 1000 eV electrons are to be detected, the electrons will be slowed down to 100 eV and the pass energy will be set to 100 eV. The benefits of each are that the CRR mode gives constant resolving power and the CAE gives a constant energy resolution [155].

4.5.2.1. Experimental

XPS analysis of the of the samples was performed using a Kratos Instruments Axis Ultra with a monochromated Al Kα x-ray source run at 10 KeV and 15 mA with a charge compensator. This was operated in CAE mode with a pass energy of 20 eV for high resolution scans. Data analysis was carried out using CasaXPS v.2.3.10 software with geometry adjusted for Kratos sensitivity factors.

4.5.3. Ellipsometry

Ellipsometry is a technique which measures the change in polarisation state of light reflected from the surface of a sample. It is able to determine the thickness of thin films from under 1 nm in thickness to several microns. The layers must, however, be discrete and well defined and be optically homogeneous and isotropic. The measured values are expressed as ψ and Δ.

These are related to the ratio of the Fresnel reflection coefficients, R_p and R_s for p and s polarised light, respectively [156].

$$\tan(\Psi)e^{i\Delta} = \frac{R_p}{R_s}$$

As the ratio of two values are measured, it can be a highly accurate and reproducible technique. As can be seen in the equation above, this ratio is a complex number, containing 'phase' information in Δ, making the measurement sensitive. In figure 4.3, the conversion of a linearly polarised incident beam to an elliptically polarised reflected beam is shown schematically. This is achieved by passing the beam through a quarter wave plate. For angles of incidence between 0 ° and 90 °, *p* and *s* polarised light will be reflected differently.

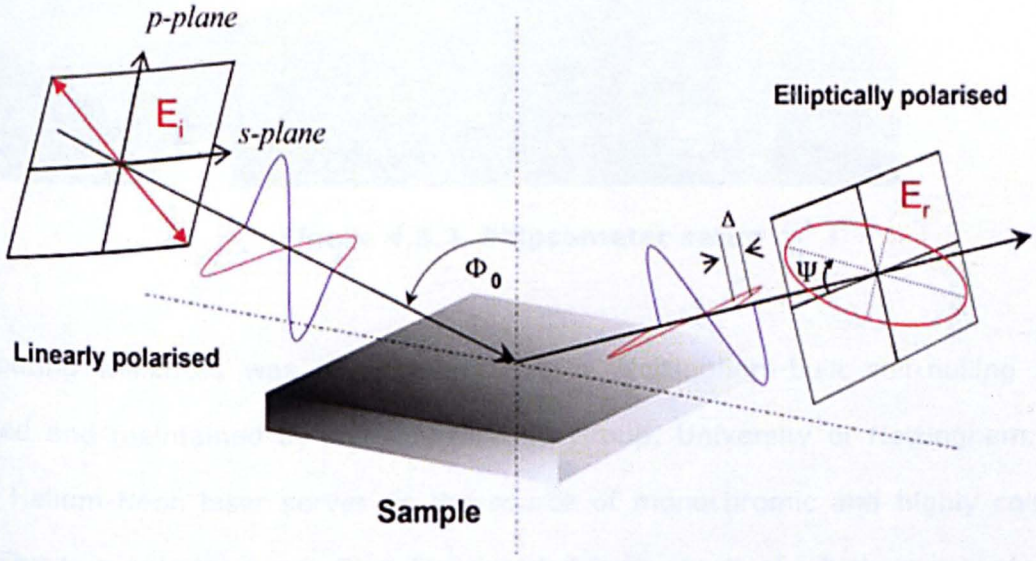

Figure 4.5.2. Schematic diagram of beam path. (Modified from [157]).

The coordinate system used to describe the ellipse of polarisation is the *p-s* system, where the *s* direction is taken to be perpendicular to the direction of propagation and contained in the plane of incidence.

To record a measurement, the fast axis of the quarter-wave plate is held in a fixed direction relative to the plane of incidence, and the two polarisers are rotated until a light intensity minimum (or null) is detected. The two angles, formed between the polarisation of the polariser/analyser and the plane of incidence, are recorded and can be used to calculate the optical properties of the sample.

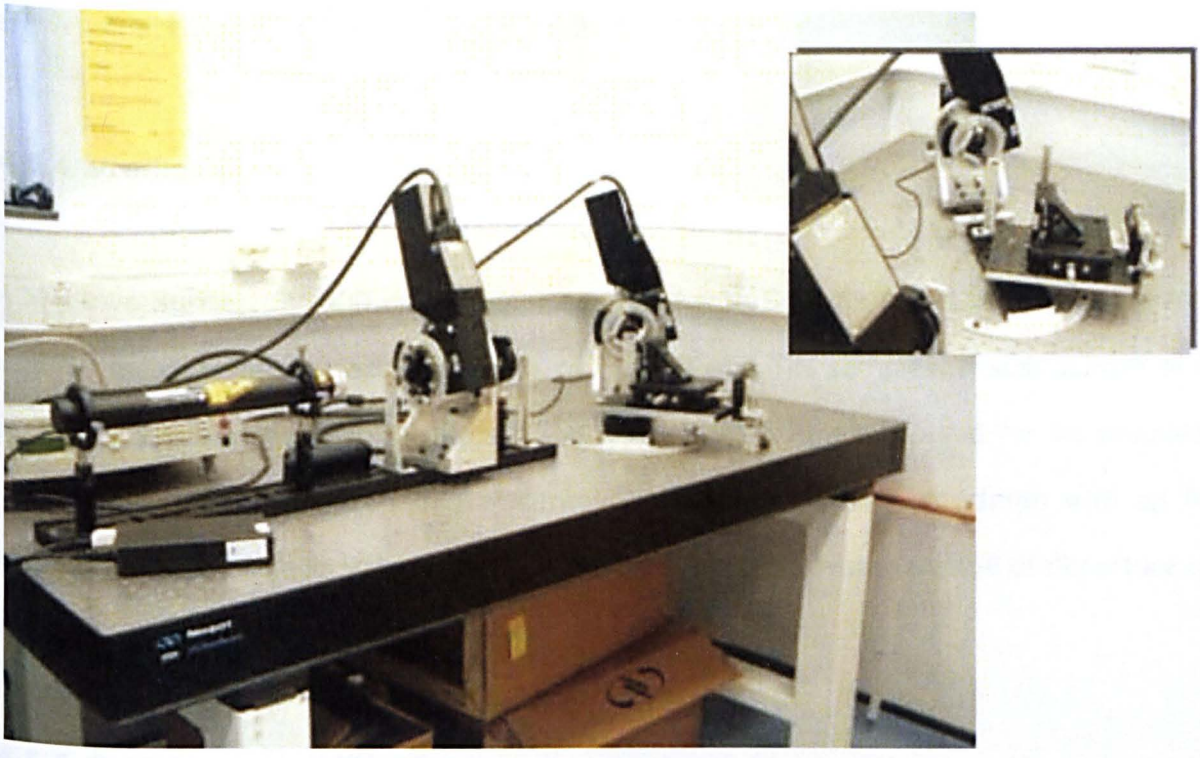

Figure 4.5.3. Ellipsometer setup

The coating thickness was determined using a Nottingham-built self-nulling system operated and maintained by the Nanoscience Group, University of Nottingham. A low power Helium-Neon laser serves as the source of monochromic and highly collimated light. The two polarisers are Glan-Thompson prisms, each of which is mounted on a rotation stage (Newport Corporation) so that the polarisation angle can be adjusted accurately. The rotation stages are controlled by software through a motion driver. The fast axis of the quarter-wave plate forms an angle of ± 45° with the incident plane. The sample is mounted on a sample stage which can be precisely adjusted. Before a measurement is taken, the direction of the surface of the sample is finely adjusted until the reflected laser shines on the centre of the photo-detector. The signals of the light intensity and the sample temperature (measured by a thermo-couple placed close to the sample) are converted to analogue electrical signals to be measured by a computer.

The raw data are then analysed by an algorithm written in Matlab to relate angles of P and A to thickness [158], shown in Appendix 1.

4.5.4. Profilometry

A Mitutoyo Surftest SV-600 profilometer equipped with Surfpak SZ v1.002 software was used to measure the surface roughness of the TiO and TiN samples..A scan length of 2 mm with a scan speed of 0.2 mm s^{-1} and a range of 4 mm was used for all samples. Calibration was carried out using a Mitotoyo Precision reference specimen with an R_a value of 2.95 μm. The R_a value is defined as the arithmetic average value of departure of the profile from the centre line.

4.5.5. Protein pre-conditioning

Borosilicate glass was coated with Fn and HSA. Human serum albumin (Sigma, UK) solutions were prepared in phosphate-buffered saline (PBS Sigma, UK) at a concentration of 4.0 mg/mL. Human plasma fibronectin (Sigma, UK) solution was prepared by dilution in PBS at a concentration 4.0 mg/mL. 2 ml of the solutions were then added to glass based Petri dishes (35 mm ø) respectively and incubated for a period of 1h at 37 °C before washing with PBS followed by cell seeding, described in section 4.5.

4.5.6. Wettability

The wettability of the borosilicate glass and glass-coated Fn, HSA and thin film TiO and TiN surfaces was measured by means of a sessile drop test. This was carried out by allowing a 20 μl drop of triple distilled water to fall 30 mm from a 1 ml syringe with a needle attached. Photographs were then taken horizontally to the drops on each surface

after approximately 1 min. These were printed in order to measure the angle between the thin film surface substrate and droplet.

4.5.7. Immunocytochemistry

Fixed cells were stained for F-actin, vinculin and β-tubulin using the following protocol. The cells were washed in pre-warmed (37 °C) PBS in situ, after which, the cells were rinsed with 1 % BSA/PBS for 5 min (BSA, Sigma, Dorset UK). This was then removed and the cells fixed for 5 min at room temperature in 4 % paraformaldehyde in PBS with 2 % sucrose. The cells were again washed three times in PBS. The cells were then permeabilised at 0 °C for 5 minutes in a solution containing 20 mM HEPES pH 7.6, 300 mM sucrose, 50 mM NaCl, 3 mM $MgCl_2$, 0.5 % Triton X-100. The cells were again washed in 1 % BSA/PBS three times. Samples were then either incubated with a 1:300 dilution of mouse anti-beta tubulin IgG (monoclonal, Chemicon UK) or a 1:400 dilution of anti-human vinculin IgG (monoclonal, Sigma) in PBS/BSA. The cells were again washed 3 times in BSA/PBS before the localisation of the primary antibodies were visualised by incubating the cells at 37 °C for 1 hour using a 1:40 dilution of rat anti-mouse (poly-clonal, Dako UK) second layer antibody conjugated with tetramethylrhodamine-isothiocyanate (TRITC).

The vinculin labelled cells were then stained with fluoro-isothiocyanate (FITC) conjugated phalloidin (10 $mgml^{-1}$, Sigma, Dorset) for 20 mins at 4 °C before washing again three times with 1 % BSA/PBS. The cells were mounted in a glycerol/PBS mountant containing 1,4-diazabicyclo [2.2.2] octane (DABCO, Sigma, Dorset UK) and viewed using a Leica SP2 inverted confocal laser scanning microscope (CLSM).

4.5.7.1. Classification of Cytoskeletal Organisation

In these experiments, the degree of cytoskeletal actin organisation and focal contact formation was classified into three types as detailed by Sinha *et al.* [159]: type I, type II, and type III. Type I organisation is representative of cells that had undergone comparatively little spreading, showing no discernible actin filaments with peripheral focal contact formation. Type II cells had well-formed cortical filaments ending in distinct focal contact sites. Type III cells had undergone spreading with a well organized array of longitudinal stress fibres aligned along the long axis of the cell body. Five fields (63X oil immersion objective) from each of two samples were examined at each time point for each surface.

4.6. Statistical Analysis

Statistical analysis was carried out using Prism® version 4.5.1 (Graphpad, California). Mean values, standard deviations (SD) and standard error of the mean (SE) were calculated using three replicates per sample. One way and two way analysis of variance (ANOVA), with significance set at 95 % followed by a Tukey post test was used to determine significant differences between the glass, Fn, albumin, TiN and TiO surfaces.

5. Results

Introduction

The results relevant to this study have been presented in 5 sections. Section 5.1 shows the results of imaging cells on borosilicate glass using CLSM and LavaCell membrane stain. Section 5.2 presents results gained from processing these images to gain three dimensional representations of the cell in order to obtain contact line data, cell height and contact radius. Section 5.3 will look at the characterisation of TiO and TiN thin films using techniques such as XRD and ellipsometry. Section 5.4 investigates characterising the surfaces using immunocytological techniques, with fixed cells stained for vinculin, β-tubulin and F-actin. This section also shows results of the morphological study of three dimensional representations of cells compared to SEM. Finally, section 5.5. details the results gained from imaging live cells on the thin film and protein pre-coated surfaces during attachment and early spreading.

5.1 Imaging on Borosilicate glass.

Three stains, LavaCell, FPE and CellBrite, were initially investigated to find a membrane probe suitable for imaging live cells over extended periods. All stains exhibited good uniform staining of the cells and initial pixel intensity values were in the same order of magnitude. As shown in figure 5.1, where pixel intensities have been normalised so that the lowest intensity suitable for image processing equals '1', LavaCell remained above the processing threshold for the longest time period. The FPE stain performed least well in the study, managing 2 to 3 time points. Cells stained with Cellbrite managing on average 8 time points before the stain's intensity became too low to prescribe an edge using image processing techniques.

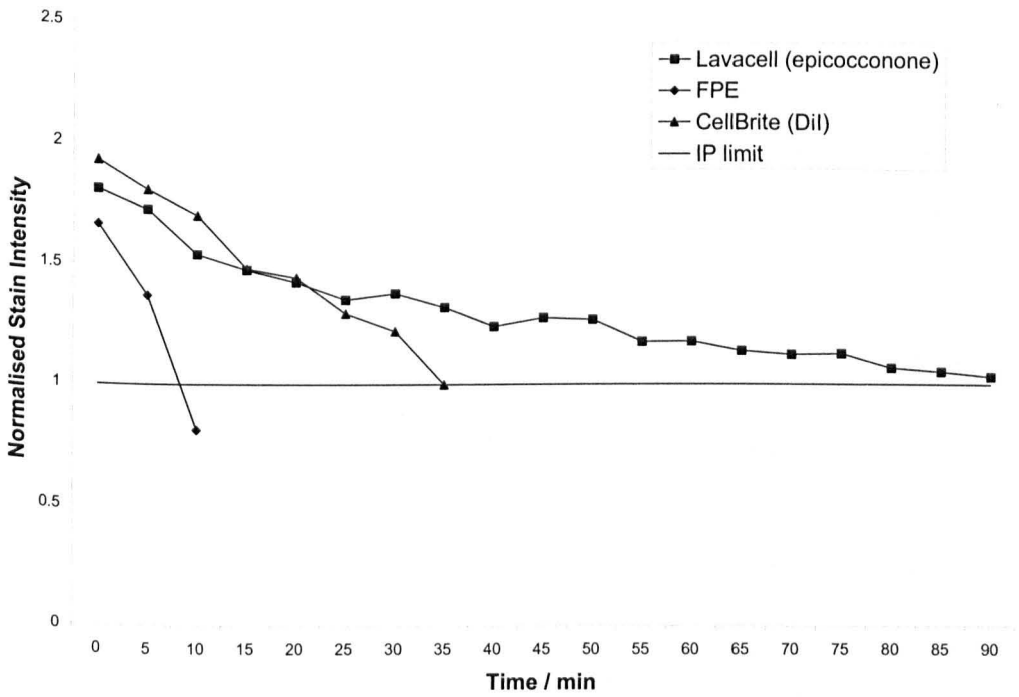

Figure 5.1. Stain intensity normalised to give the image processing limit, 1, below which edge algorithms cannot detect the outline of the cell.

Following the procedure outlined in section 4.5.2., cells seeded onto borosilicate glass based petri dishes were imaged using the LavaCell membrane probe and confocal microscopy. 512 x 512 pixel CLSM micrographs representing an area of 238.1 x 238.1 μm with a z-step size of 0.91 ± 0.069 μm were gained. On average, data were collected from 6 cells from each of 6 repeats. The cells noticeably spread over the 75 min time period, as can be seen by the cell picked out (white arrow) in figures 5.1, 5.2 and 5.3. Although the contact area of the cells increased over the time period, the cells still largely display a rounded morphology by the end of the 90 min period from seeding, with very few cells reaching a stage to start polarizing. The intensity of the stain occasionally became less consistent across the cell as the minimum concentration of stain in media was used to visualise the cells which did not provide enough to stain all internal structures as well as the membrane.

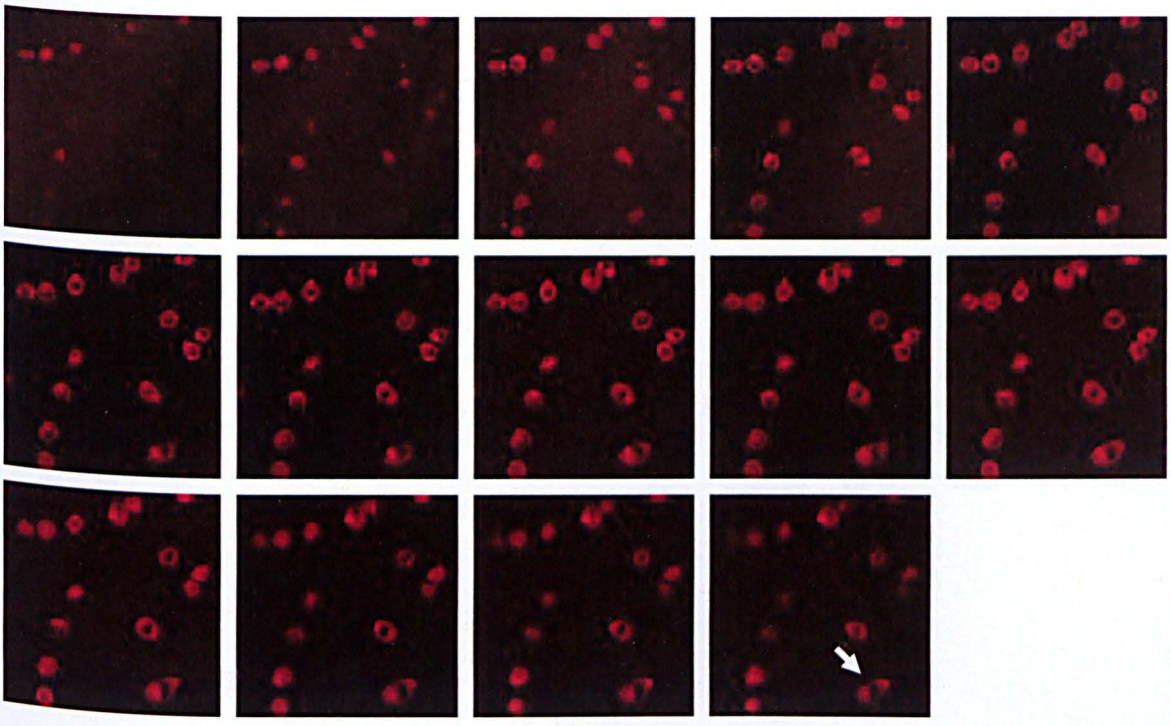

Figure 5.1.1. shows cells 20 minutes after seeding on borosilicate glass using a Leica confocal microscope with oil immersion x 63 objective. The images increase by increments of 1.91 µm through the z stack starting at top left, working left to right. The stain has bound to the cell membrane and other lipid structures, leaving a dark area corresponding to the nuclear region of the cell which is devoid of lipid. Each image 238.1 µm x 238.1 µm.

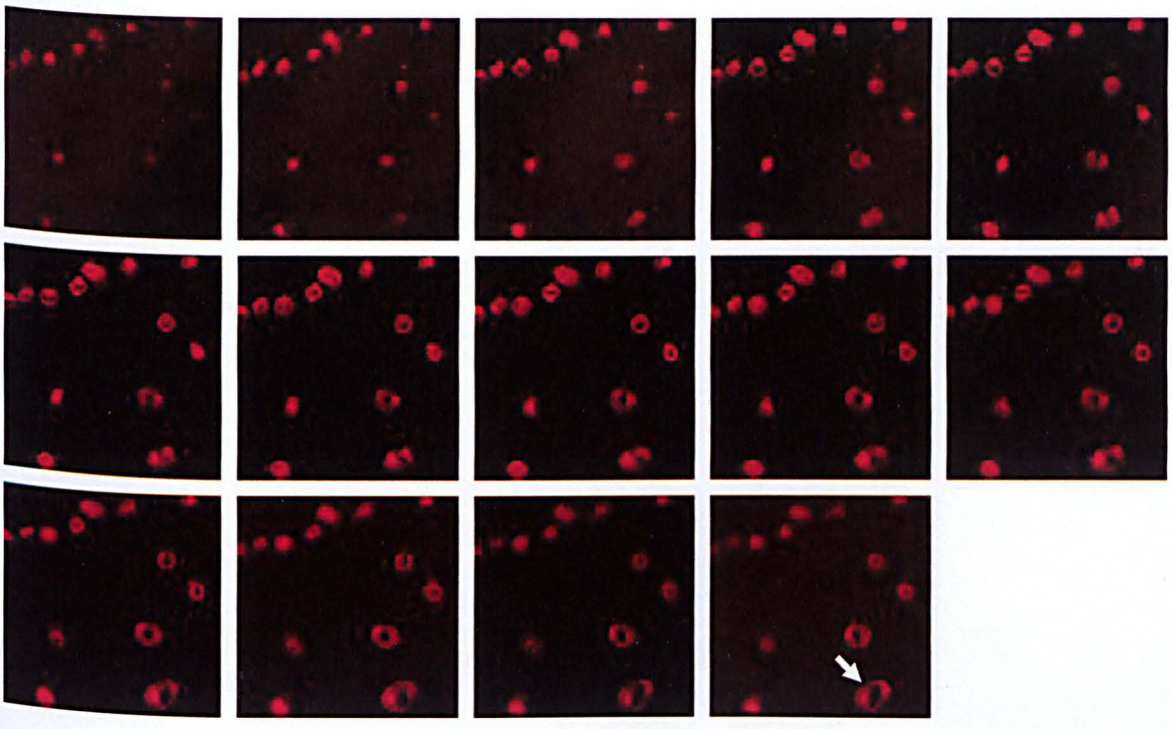

Figure 5.1.2. Shows cells 60 min after seeding on borosilicate glass using a Leica confocal microscope with oil immersion x 63 objective. The images increase by increments of 1.91 µm through the z stack starting at top left, working left to right. Each image 238.1 µm x 238.1 µm.

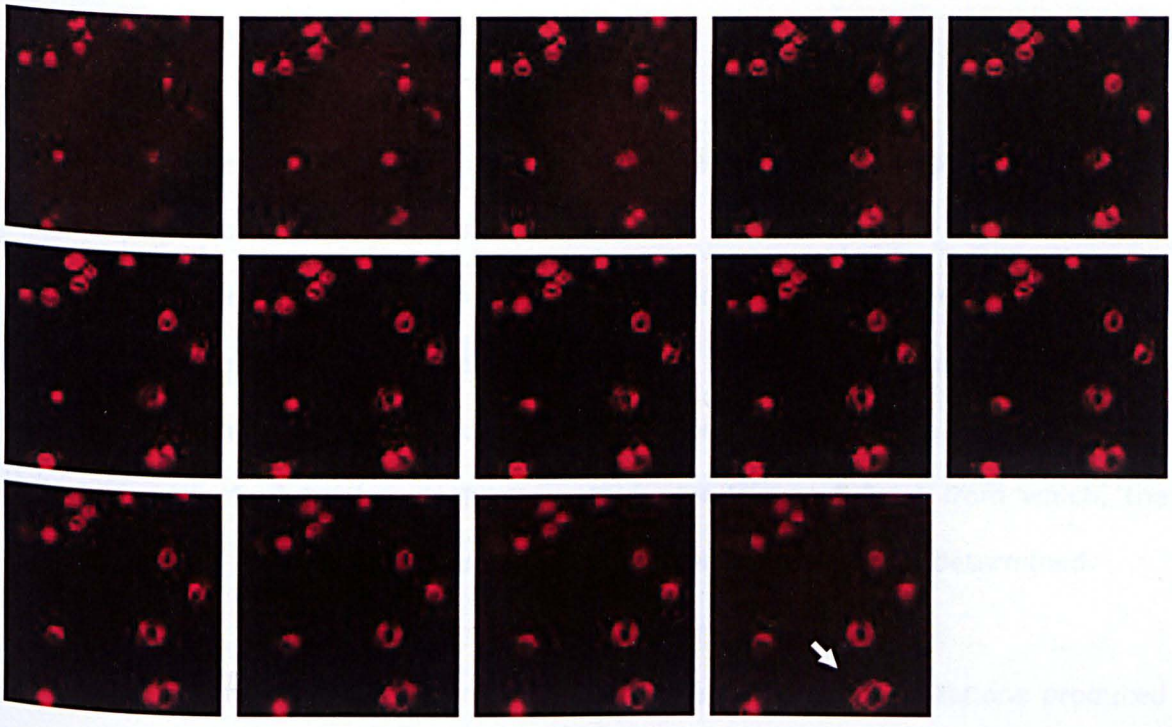

Figure 5.1.3. HOS cells 90 min after seeding on borosilicate glass using a Leica confocal microscope with oil immersion x 63 objective. The images increase by increments of 1.91 µm through the z stack starting at top left, working left to right. Each image 238.1 µm x 238.1 µm.

5.2.1. Image Processing

The images were then processed in Matlab using the algorithm described in section 4.3. This was able to find the outline of the cells in the individual z stacks (figure 5.2.1.) and store those corresponding to individual cells in a database. Initial experiments (figure 5.2.2.) were carried out to determine the maximum z step height to give an accurate contact angle as described in section 4.2.3. The algorithm then adds a surface to the resultant contour plot (figure 5.2.3.) from which, the contact line, cell height, contact radius and membrane slope can be determined.

SEM was used to visually compare the three dimensional representations produced by this method to fixed cells, as seen in figure 5.2.4. The cells were given a parallel preparation, whereby they were seeded as per the protocol in section 4.2.1., but then fixed for SEM viewing, as in section 4.2.4., at relevant time points after incubation in a humidified 95% air/5% CO_2 incubator at 37 °C. The cells had the x and y dimensions in the same order as the three dimensional representations.

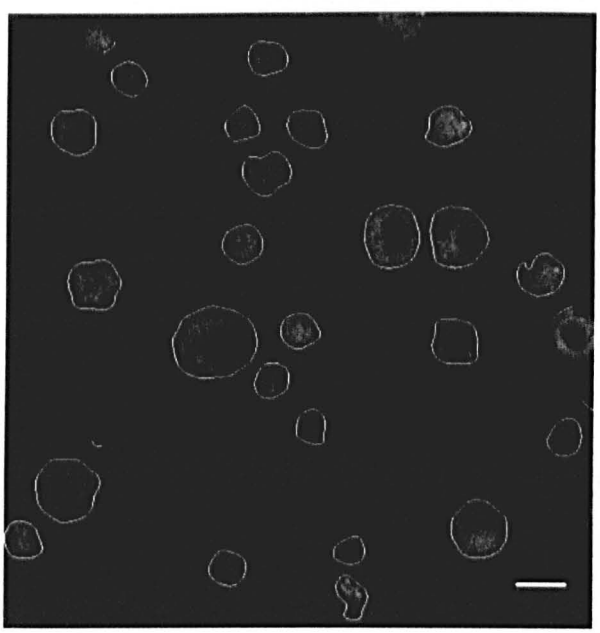

Figure 5.2.1. Cell outlines added by the Matlab algorithm. Scale bar 20 µm.

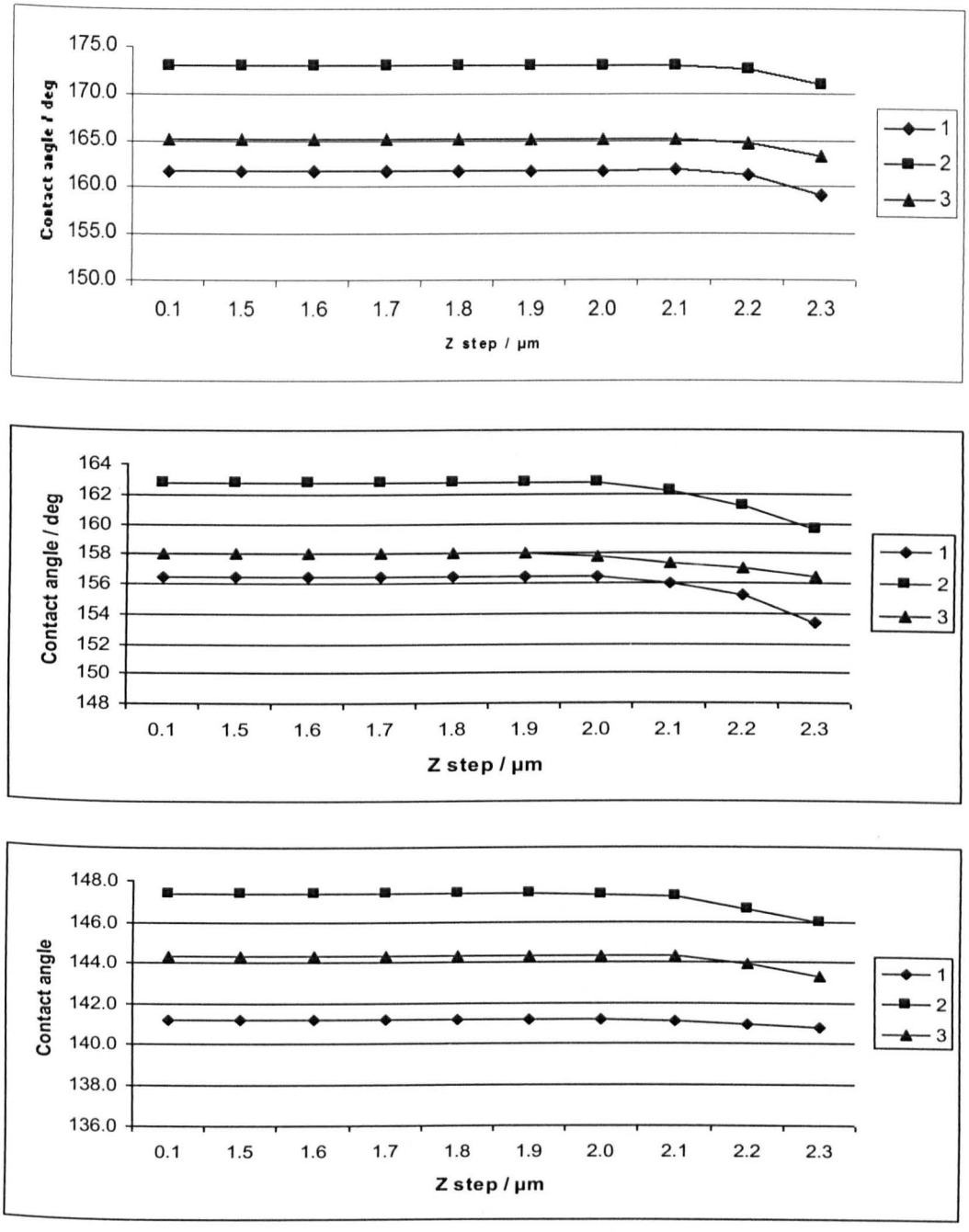

Figure 5.2.2. Graphs showing contact angle measurements using three dimensional representations comprising different z-step heights to set the maximum step size for image processing. Cells imaged at 15 min (top), 45 min (middle) and 90 min (bottom).

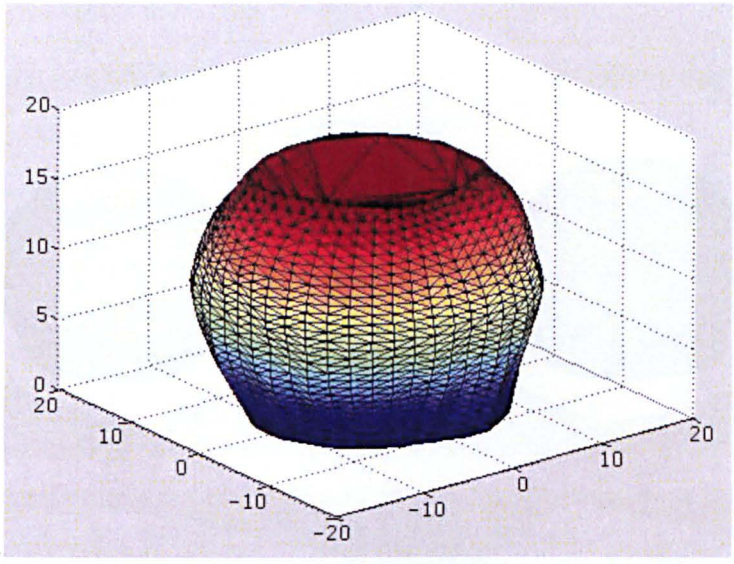

Figure 5.2.3. Three dimensional representation of a cell from the data set above. From these cell representations, the contact line, cell height, contact radius and membrane slope can be determined.

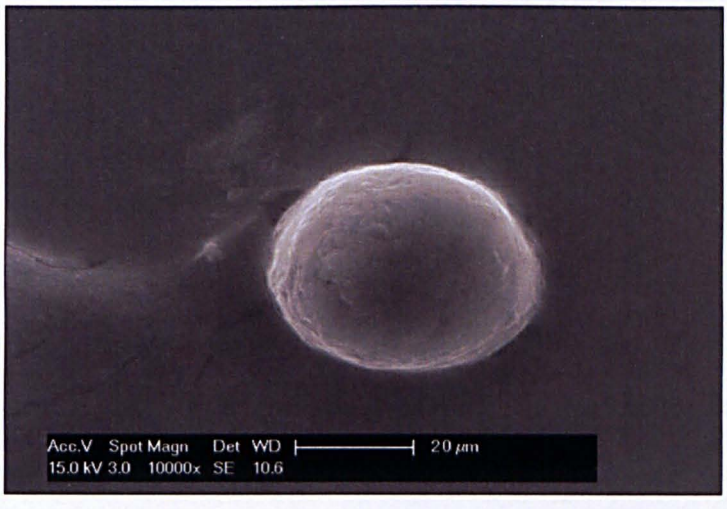

Figure 5.2.4. SEM image of a cell fixed on borosilicate glass 20 min after seeding. The cell was stained with LavaCell replicating the conditions of the cells used for live imaging sign .

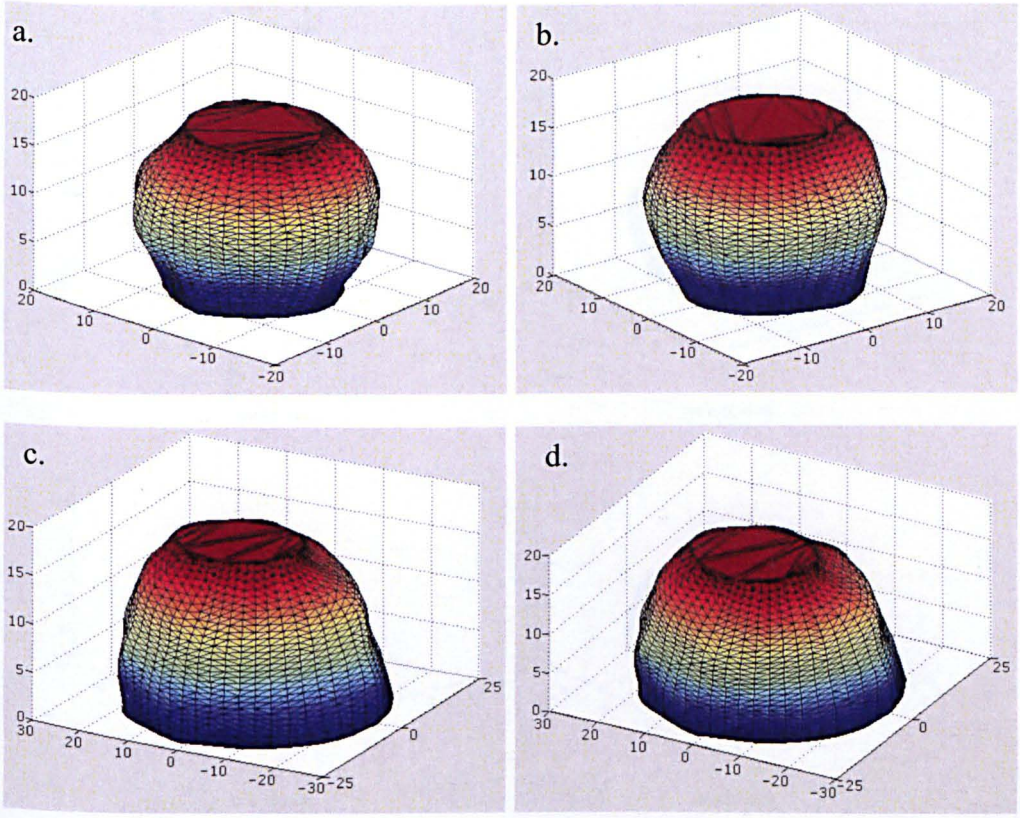

Figure 5.2.5. Three dimensional representations of membrane morphology as one HOS cell spreads over borosilicate glass taken at times a. 15 min, b. 30, c. 60, d. 90.

Figure 5.2.5. shows a representative three dimensional reconstruction of one HOS cell spreading at selected time points of 15, 30, 60 and 90 min. As can be seen, the spherical morphology is retained over the time period as the cell starts to spread and flatten from a sphere to a hemispherical shape. The CLSM and staining method has captured the cell with sufficient resolution to be able to measure the contact line around the periphery of the cell. Once set at the start of the image acquisition period, this will continue to capture this level of detail for approximately the following 16 time points.

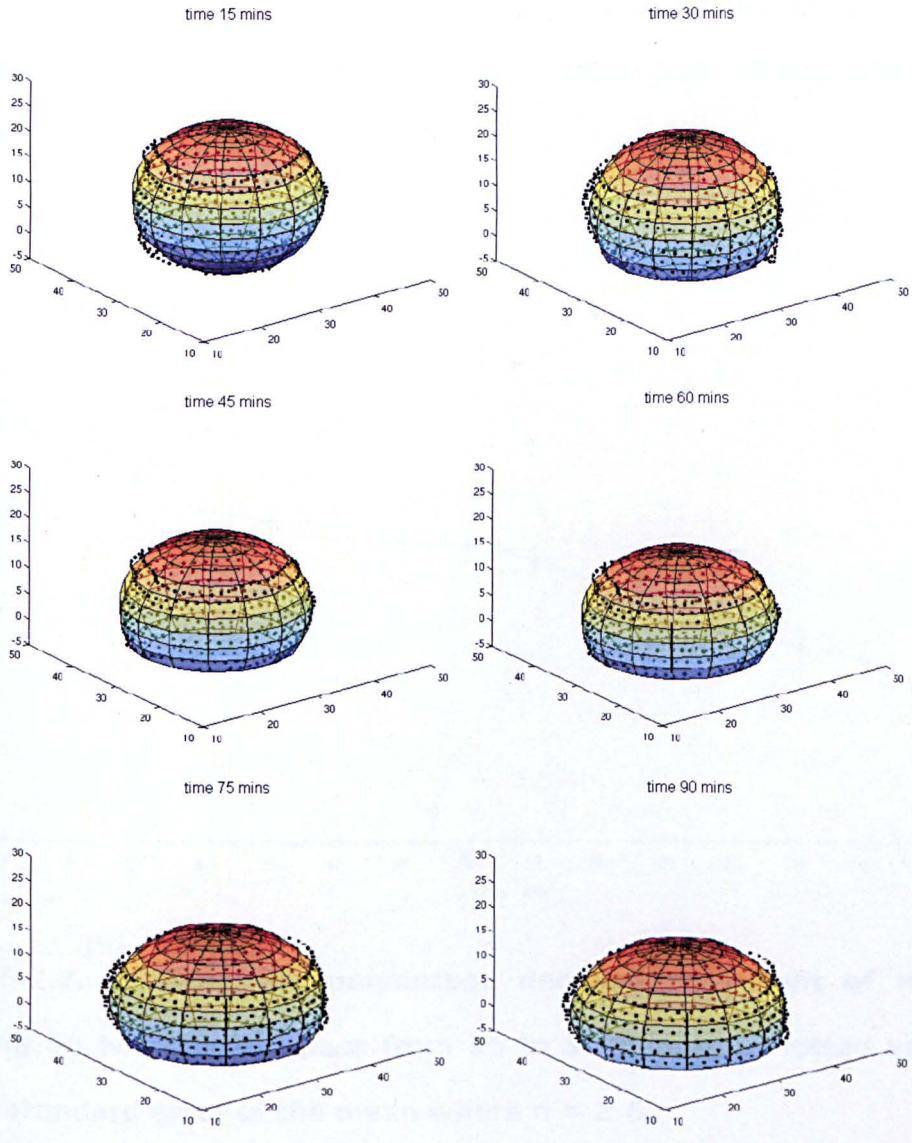

Figure 5.2.6. Contour plots with fitted spheres for one cell on Borosilicate glass as it spreads on the surface, used to calculate contact angle and determine its variation with time. Scale in μm.

As seen above in figure 5.2.6., a sphere was fitted to the contour plots so that the contact radius, cell height, and contact angle with the substrate could be determined. The figure demonstrates this applied to the contour plots of one HOS cell as it spreads from 20 to 90 minutes.

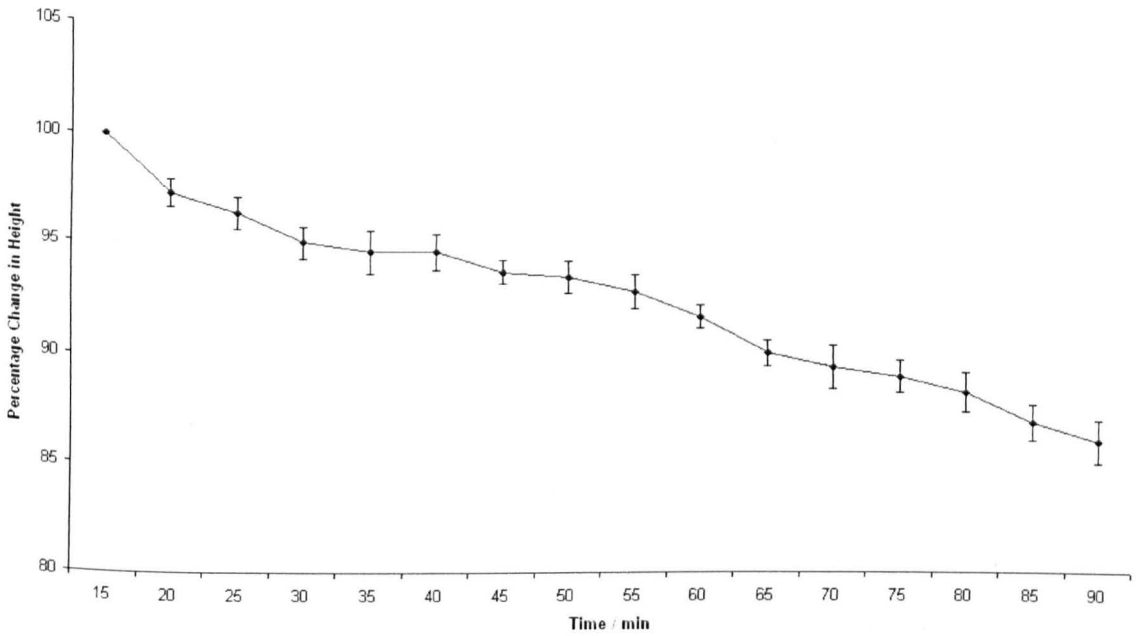

Figure 5.2.7. showing the percentage decrease in height of HOS cells spreading on borosilicate glass from 15 to 90 minutes. Plotted values are mean ± standard error of the mean where n = ≥ 6.

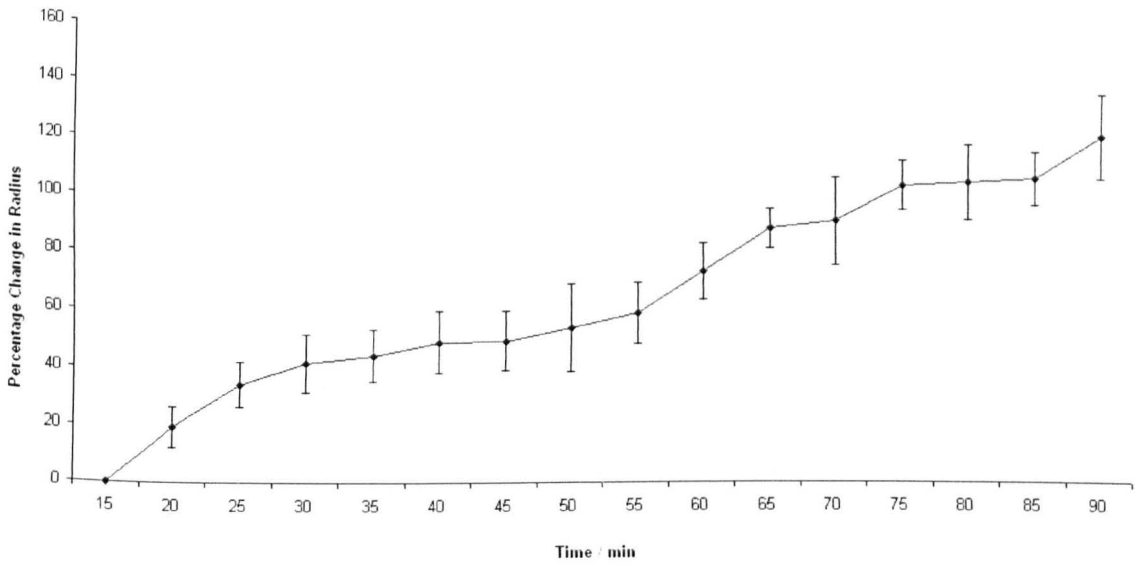

Figure 5.2.8. showing the percentage increase in contact radius of HOS cells spreading on borosilicate glass from 15 to 90 minutes. Plotted values are mean ± standard error of the mean where n = ≥ 6.

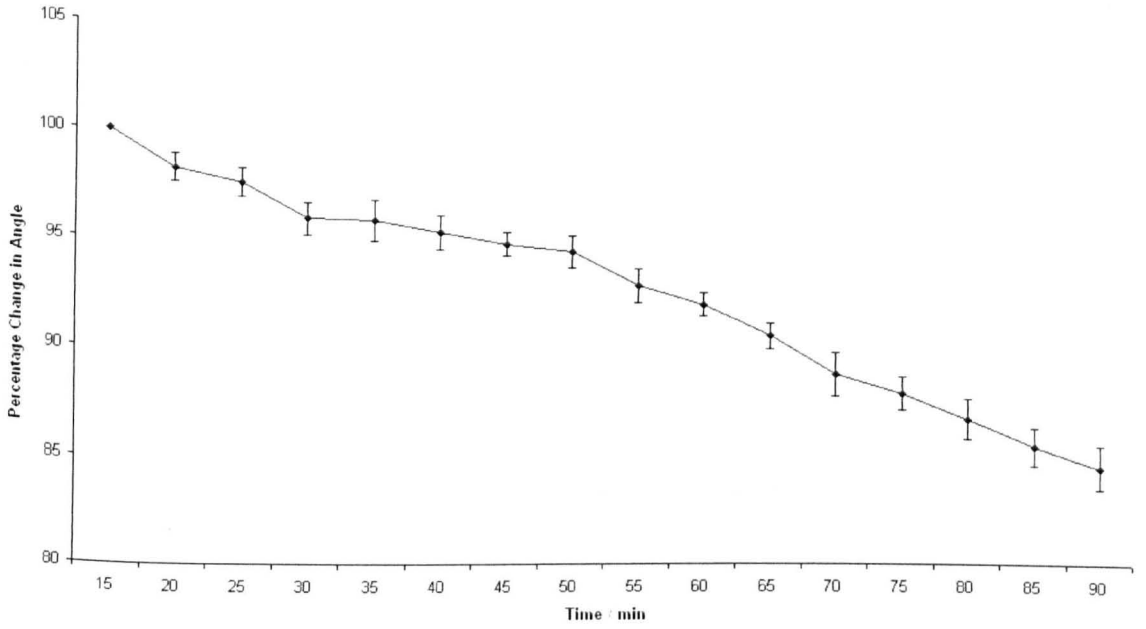

Figure 5.2.9. showing the percentage decrease in contact angle of HOS cells spreading on borosilicate glass from 15 to 90 minutes. Plotted values are mean ± standard error of the mean where n = ≥ 6.

Over the 75 minute period, the analysis shows that cell height and contact angle with the borosilicate glass surface decreased over the time period by 15 and 14 % respectively, whilst the contact radius showed a 119 % increase, as the cells begin to flatten from a sphere to a hemispherical shape on the surface. This can be seen represented graphically in figures 5.2.7., 5.2.8. and 5.2.9.

5.3. Characterisation of Biomaterial Coatings

Thin film biomaterial coatings of TiO and TiN were applied to borosilicate glass based petri dishes to determine whether the imaging method and image processing algorithm could be carried out on surfaces relevant to the biomaterial field.

As described in section 4.4. TiN and TiO were deposited using PVD. These surfaces were characterised using XRD, XPS, ellipsometry and profilometry, and the water contact angle measured.

5.3.1. Analysis of TiN Coatings

5.3.1.1. XRD Analysis of TiN

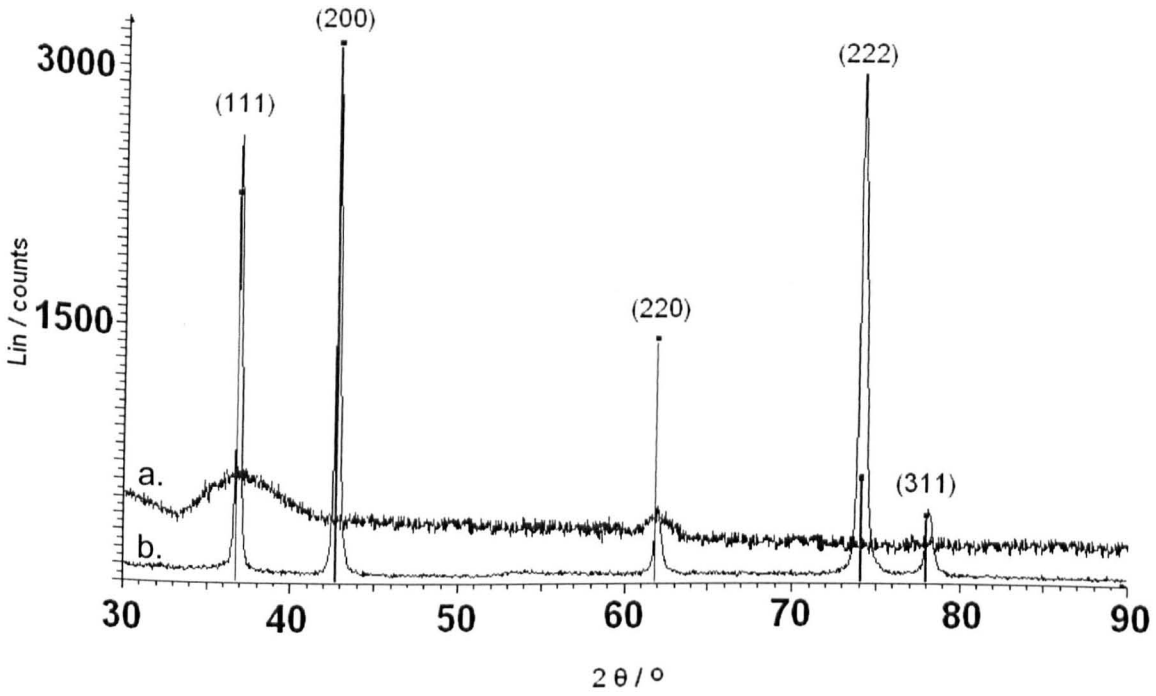

Figure 5.3.1. XRD pattern for titanium nitride thin film coatings of 0.2 μm (a.) and 1 μm (b.) samples. The peaks correspond to the database values expected for TiN. The lines with square symbols represent relative intensities of TiN from the JCPDS database.

Figure 5.3.1. shows the XRD pattern confirming the presence of FCC TiN (JCPDS-ICDD card 00-038-1420) in the deposited films. As the coating gets thinner, a more nanocrystalline structure is expected, seen by the less distinct peaks in (a.). The grain size reduced from 8 nm in the 1 μm sample to less than 4 nm in the 0.2 μm sample, using the Scherer equation [94].

5.3.1.2. XPS Analysis of TiN

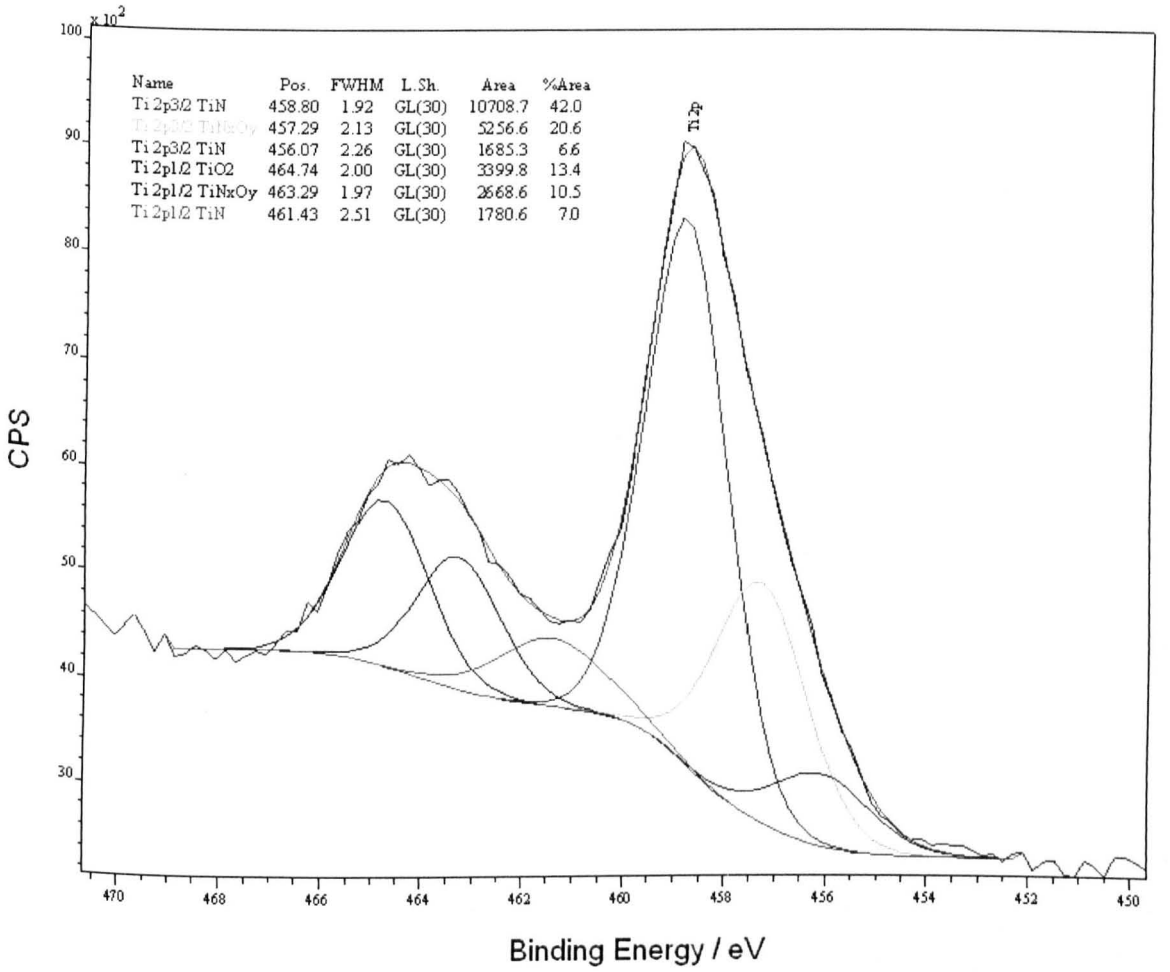

Figure 5.3.2. shows deconvoluted Ti 2p XPS spectra for the titanium nitride thin film surface.

Deconvolution of the Ti 2p spectra gained by XPS for the 10 nm film showed that TiN and TiN_xO_y were the most abundant species present on the surface at 55 and 31 % respectively, with a small amount of TiO_2, 13 %, also present.

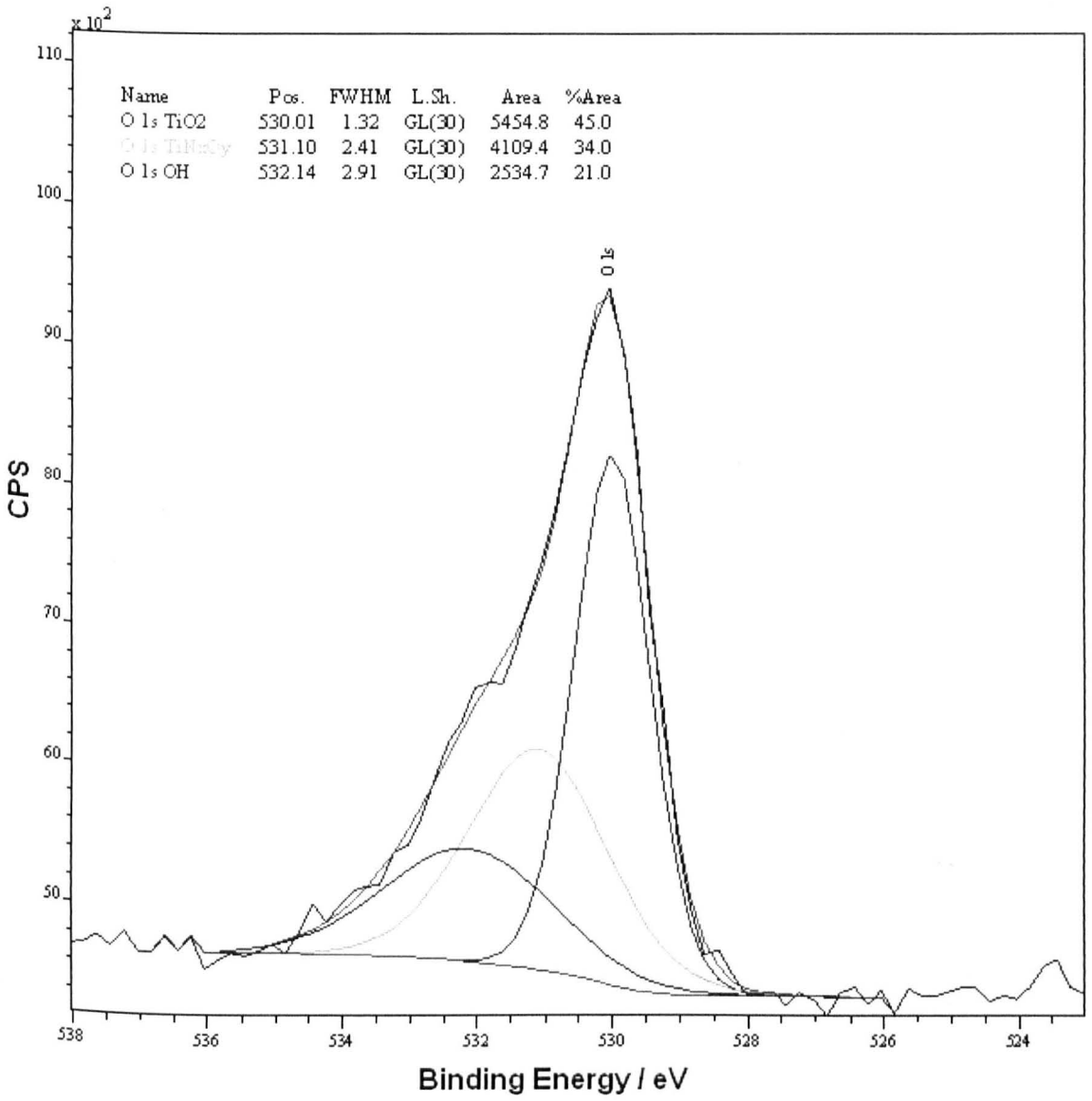

Figure 5.3.2. shows deconvoluted O 1s XPS spectra for the titanium nitride thin film surface.

The O 1s spectra showed the presence of OH groups on the surface with a relative area of 21 %. These can act as preferential binding sites for cells and proteins [119].

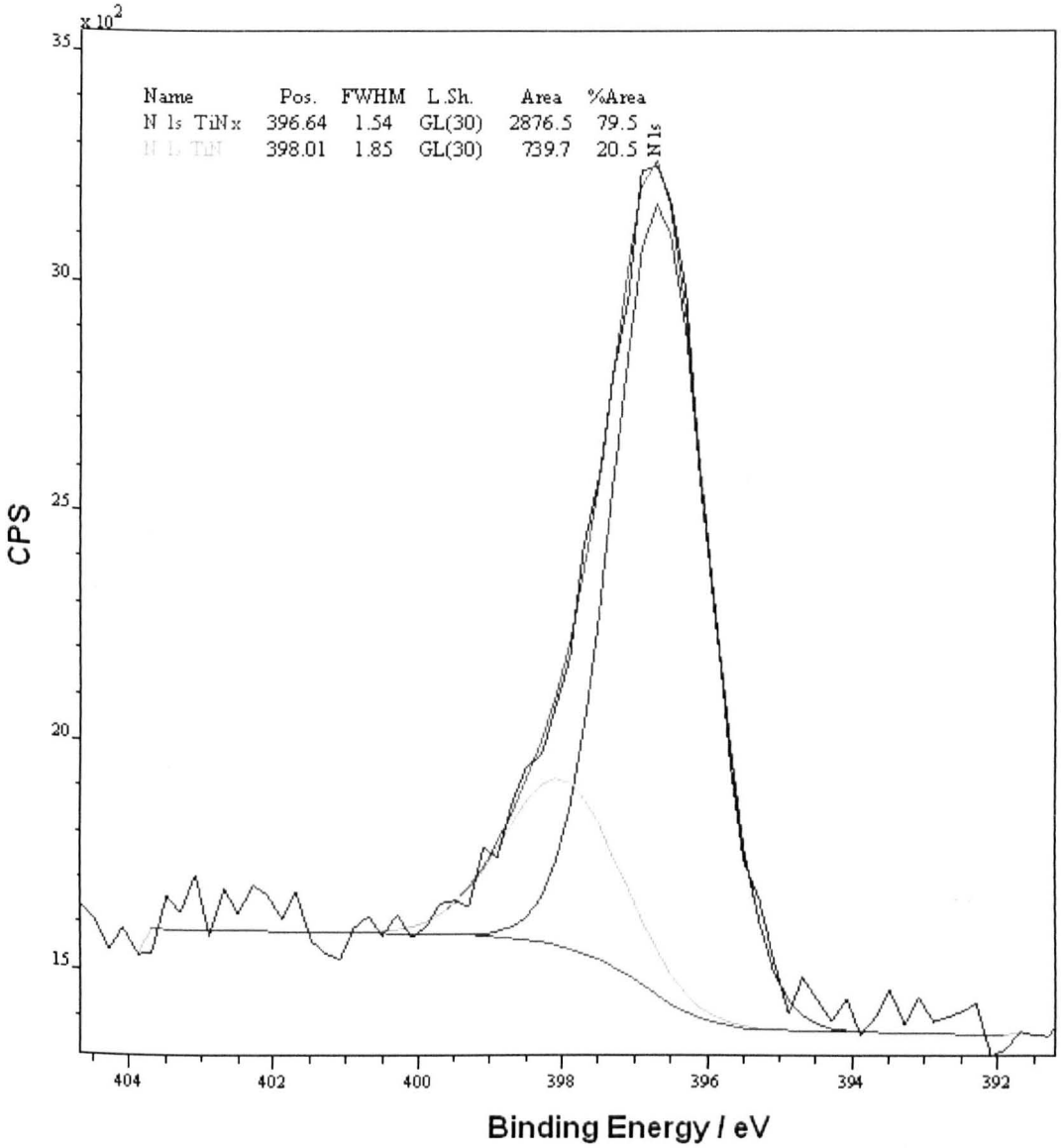

Figure 5.3.3. shows deconvoluted N 1s XPS spectra for the titanium nitride thin film surface.

The N 1S spectra in figure 5.3.3 confirmed that the binding energy was that expected of nitrogen in TiN.

5.3.2. Analysis of TiO Coatings

5.3.2.1. XRD Analysis of TiO

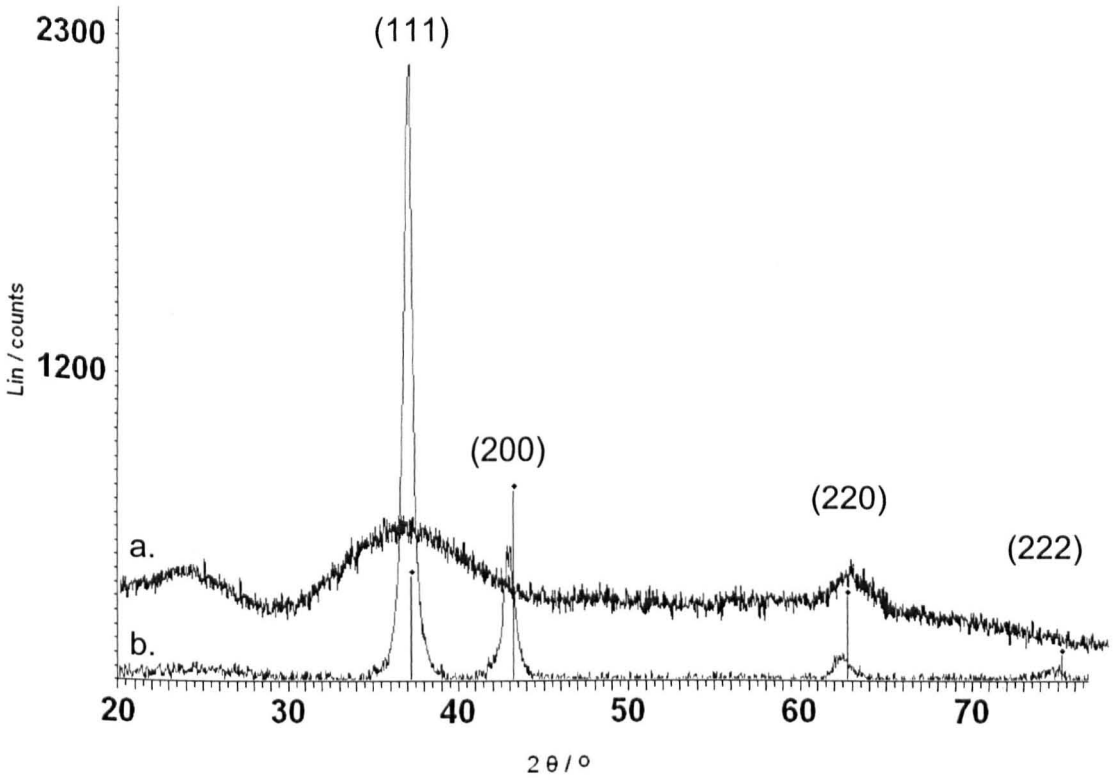

Figure 5.3.4. XRD pattern for PVD deposited titanium oxide surfaces of 0.2 µm (a.) and 1 µm (b.) samples. The pattern shows that a non-stoichiometric TiO surface was achieved.

XRD confirmed the presence of FCC TiO (JCPDS-ICDD card 01-077-2170) in the deposited films. Again, the heights of the peaks suggest that the thicker 1 µm sample had a more crystalline structure than the thinner 0.2 µm. The measured peaks are shifted to the left of the database values, suggesting stress in the coating. The grain size in this sample reduced from 7 nm to less than 4 nm as the coating thickness was decreased from 1 µm 0.2 µm, using the Scherer equation [94].

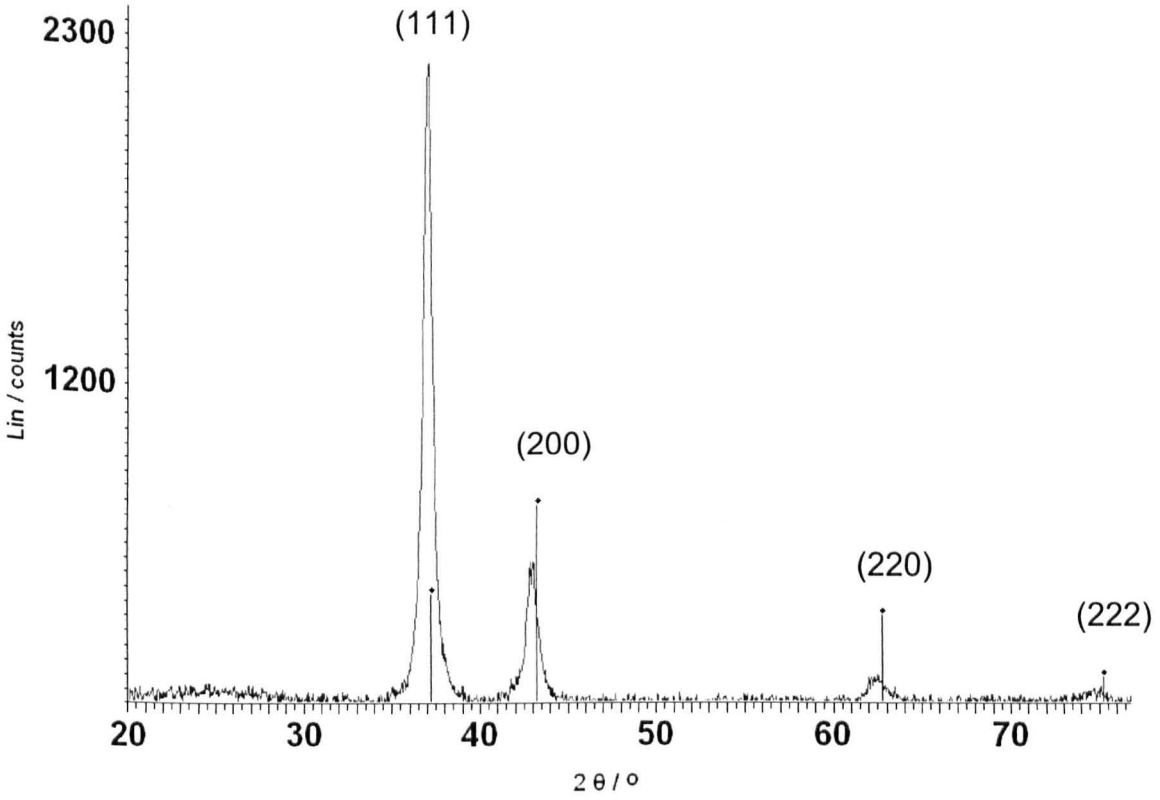

Figure 5.3.5. XRD pattern of TiO sample after being submerged in cell growth media for 1 hour.

Figure 5.3.5. shows that the structure is unaltered by submersion in growth media. The shift in the peaks seen in figures 5.3.4. and 5.3.5. from the database values (lines with dots) is due to residual stress in the coating, discussed further in section 6.5.2.1.

5.3.2.2. XPS Analysis of TiO

Analysis of the XPS Ti^{2+} spectra, figure 5.3.5, showed peaks indicative of TiO_2, with small amounts of TiO, TiN and Ti metal on the surface. As XPS analysis has a sample depth of only 4 nm, a high amount of TiO_2 due to surface oxidation was expected on this sample.

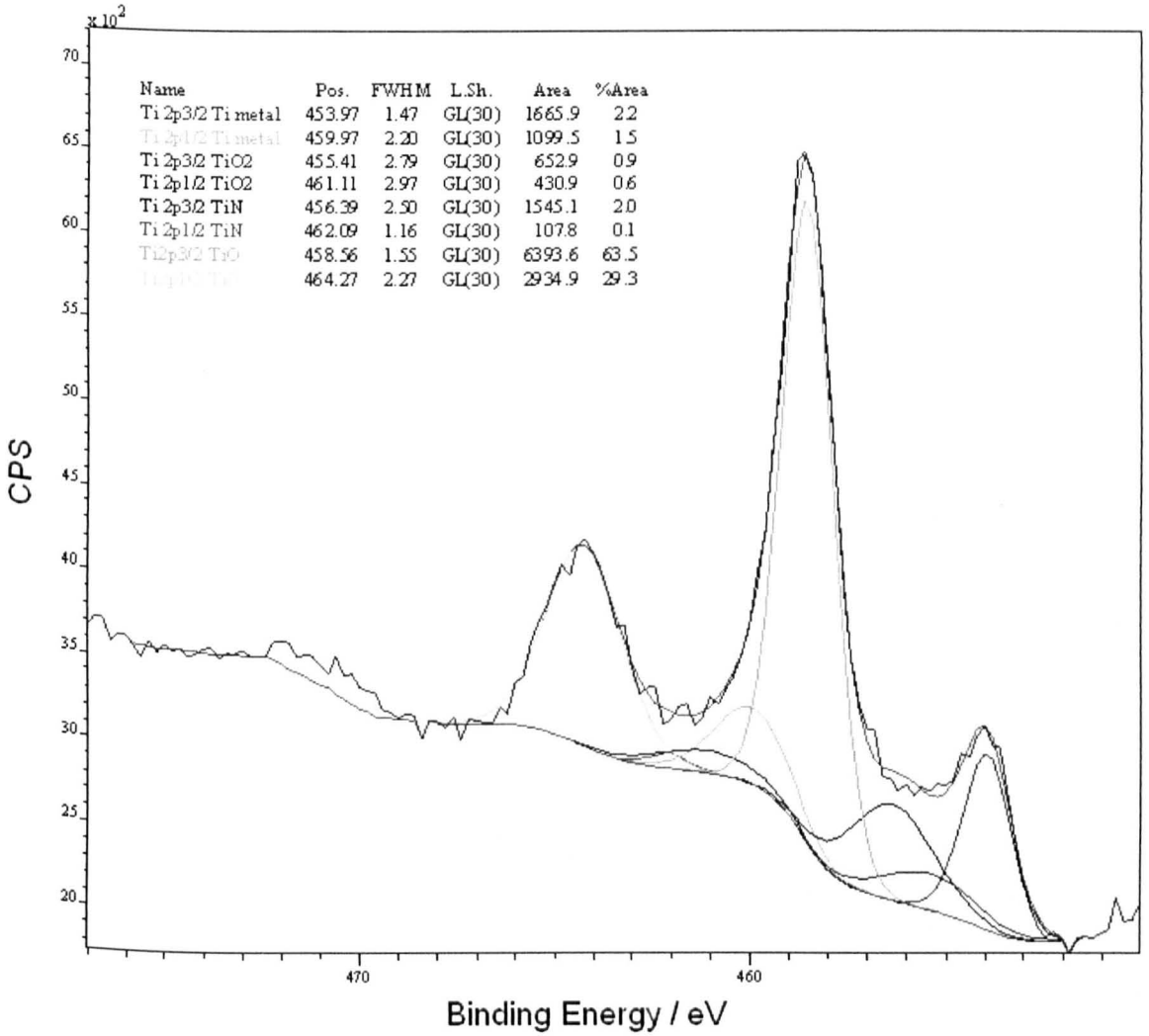

Figure 5.3.6. shows the Ti 2p XPS spectra for TiO thin film surface. The spectra shows that the predominant Ti species is Ti^{2+} corresponding to TiO. There are traces of TiO, TiN and Ti also present on the surface.

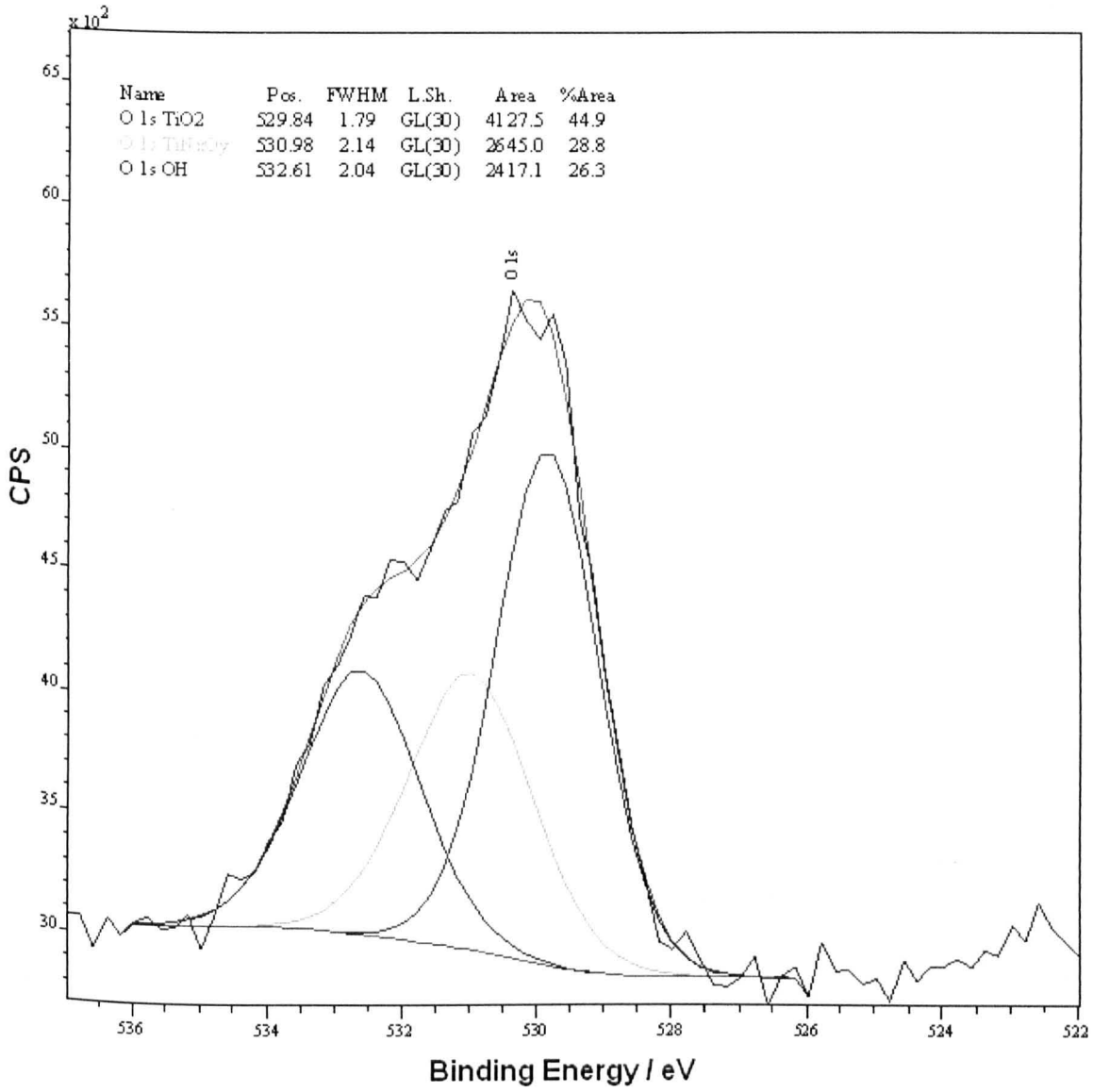

Figure 5.3.7. shows the O 1s XPS spectra for TiO thin film surface.

The O 1s spectra showed the presence of more OH groups on the surface than the TiN sample with 26.3 % as opposed to 21.0 %, which can act as preferential binding sites for cells and proteins [119].

5.3.3. Wettability

The wettability of the borosilicate glass and thin film surfaces was measured by means of a sessile drop test. This was carried out by allowing a 20 µl drop of triple distilled water to fall 30 mm from a 1 ml syringe with a needle attached. Photographs were then taken horizontally to the drops on each surface after approximately 1 min and the process repeated five times. The photographs were printed in order to measure the angle between the thin film surface substrate and droplet. The results are presented in table 5.1.

Surface	Angle / Deg	
Glass	32	± 2.0
TiO	10	± 2.2
TiN	45	± 1.6
Glass	32	± 2.0
Fn	25.1	± 2.7
HSA	75	± 2.0

Table 5.1, Showing the wettability of Borosilicate glass (Glass), TiN and TiO Fn and HSA surfaces. ± indicates standard deviation of the mean.

The water contact angles for the sputtered thin film and protein surfaces (table 5.1) show that the wettability varies between all 5 surfaces. The HSA coating produced the lowest wettability, with a water contact angle of 75°, increased from 32° for the glass substrate. This result is much higher than the expected observed contact angle for a protein adsorbed on a surface. This would be expected to reduce the contact angle below 32° due to the hydrophilic outer regions exhibited by all proteins in their tertiary structure. This surface will still be used in the experiments and referred to as HAS, but without further analysis, it cannot be conclusively said that this surface

truly is HAS. TiN was slightly less hydrophobic, with a contact angle of 45°, followed by borosilicate glass at 32° and Fn at 25°. TiO was the most hydrophilic at 10°.

5.3.4. Ellipsometry

The TiN and TiO thin film coating thickness was determined using ellipsometry as described in section 4.2.1.3., with the raw data being analysed in Matlab (algorithm in the Appendix).

Time / min	Thickness / nm	
60	102.61	± 2.1
45	76.5	± 1.6
30	50.43	± 1.8
5.88*	10.00*	± 4.86

Table 5.4. Thicknesses recorded for TiN and TiO samples after different exposure times to the target.

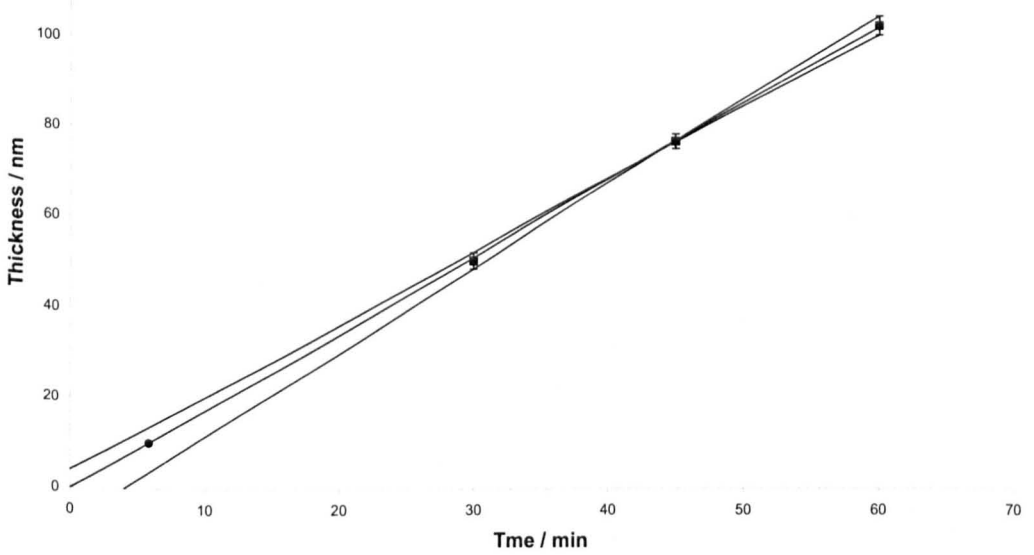

Figure 5.3.7. Graph used to determine the thickness of the thin film coatings using results gained experimentally by ellipsometry (squares) to gain 10 nm thickness (circle).

From the data summarised in table 5.4 and figure 5.3.7., the sputter rate was found to be 1.7 nm min^{-1} (at 6.8 W cm^{-2}). As a coating of 10 nm, required for optical transparency (section 6.5.3.), was below the sampling depth for ellipsometry, it was therefore calculated that to achieve a coating of 10 nm, the sample should be exposed to the Ti target for 5.88 min.

5.3.5. Profilometry

Profilometry was performed to investigate whether the PVD coating process altered the topography of the substrate. As seen in table 5.5. and figure 5.3.8, the PVD coatings did not alter the R_a values from that of the glass surface.

Surface	R_a / µm	
Glass	0.024	± 0.001
TiN	0.024	± 0.002
TiO	0.023	± 0.001

Table 5.5. Surface roughness Ra values of Glass, TiN and TiO.

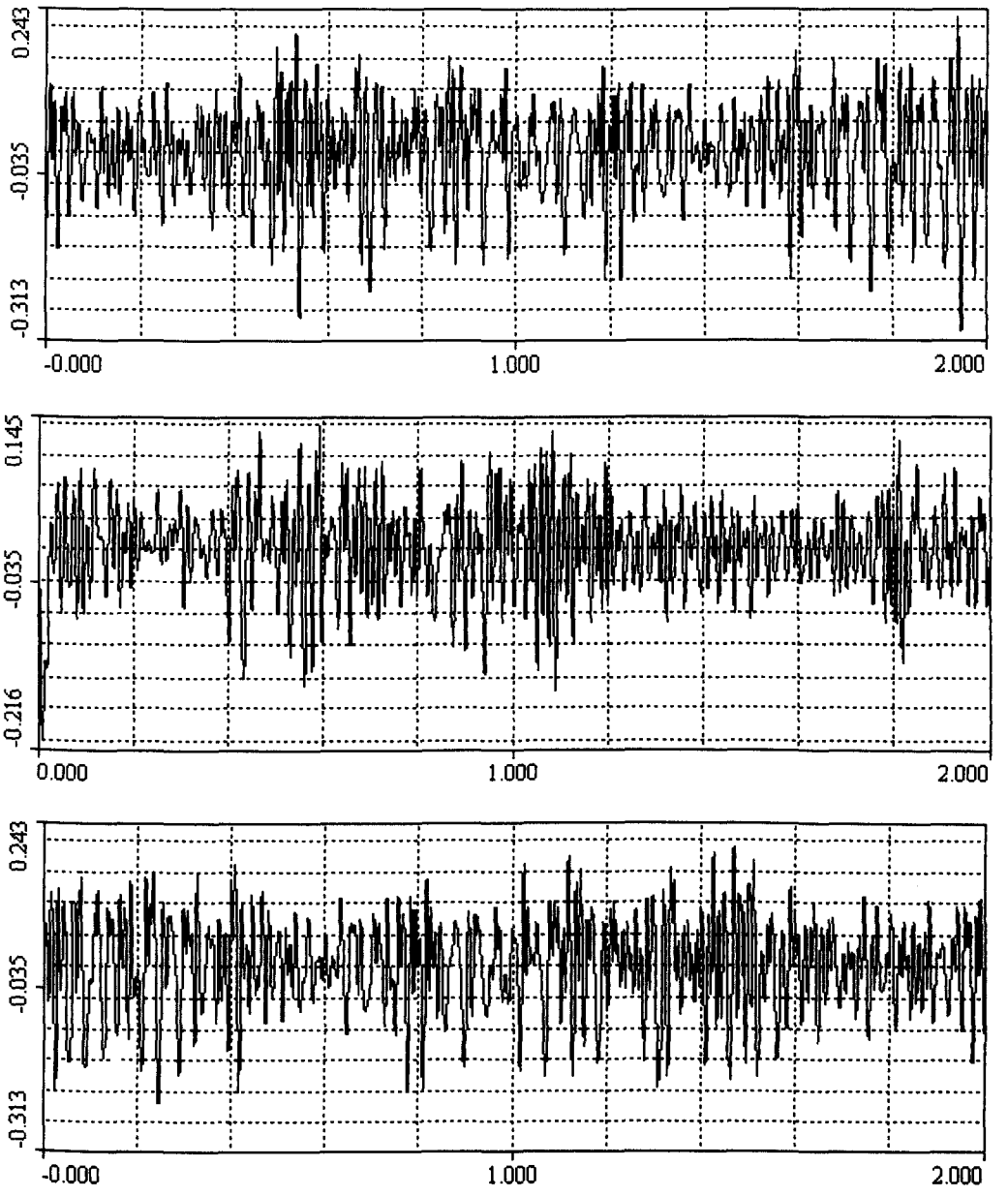

Figure 5.3.8. Surface roughness profiles of Glass (top) TiN (middle) and TiO (bottom).

5.4. Immunocytochemistry and Morphology

As part of the material characterisation, HOS cells on each surface were fixed at 25, 60, 90 and 180 min time points from seeding were stained for vinculin, β-tubulin and F-actin as a means of comparing morphology to live cells and visualising cytoskeletal organisation. Five fields (63X oil immersion objective) from each of two samples were examined at each time point for each surface. Presented are cells representative of each surface and time point.

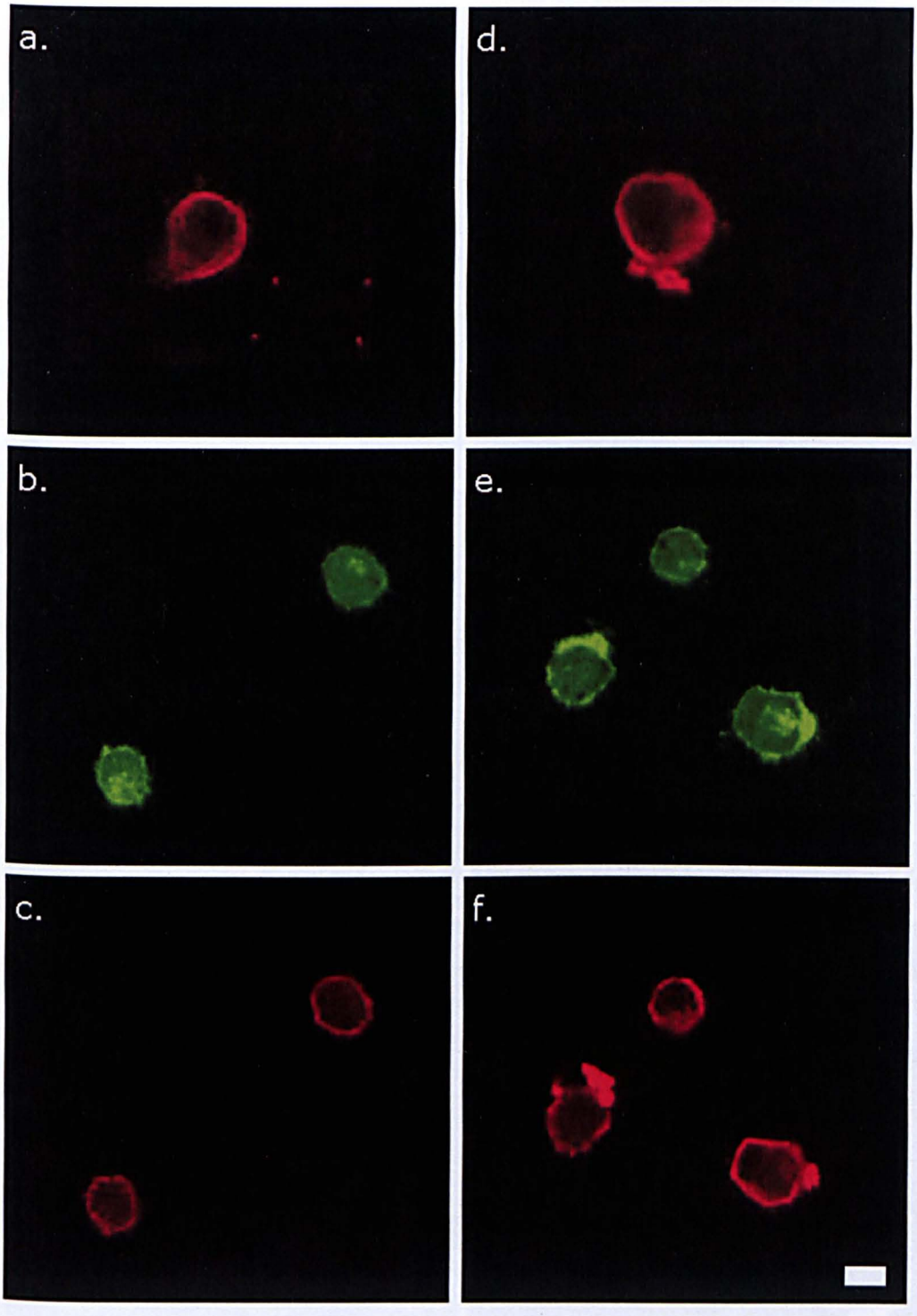

Figure 5.4.1. β-tubulin (top row), F-actin (middle row) and vinculin (bottom row) localisation on HSA (a.),(b.),(c.); Fn (d.),(e.),(f.) at 25 minutes. Scale bar 10 μm.

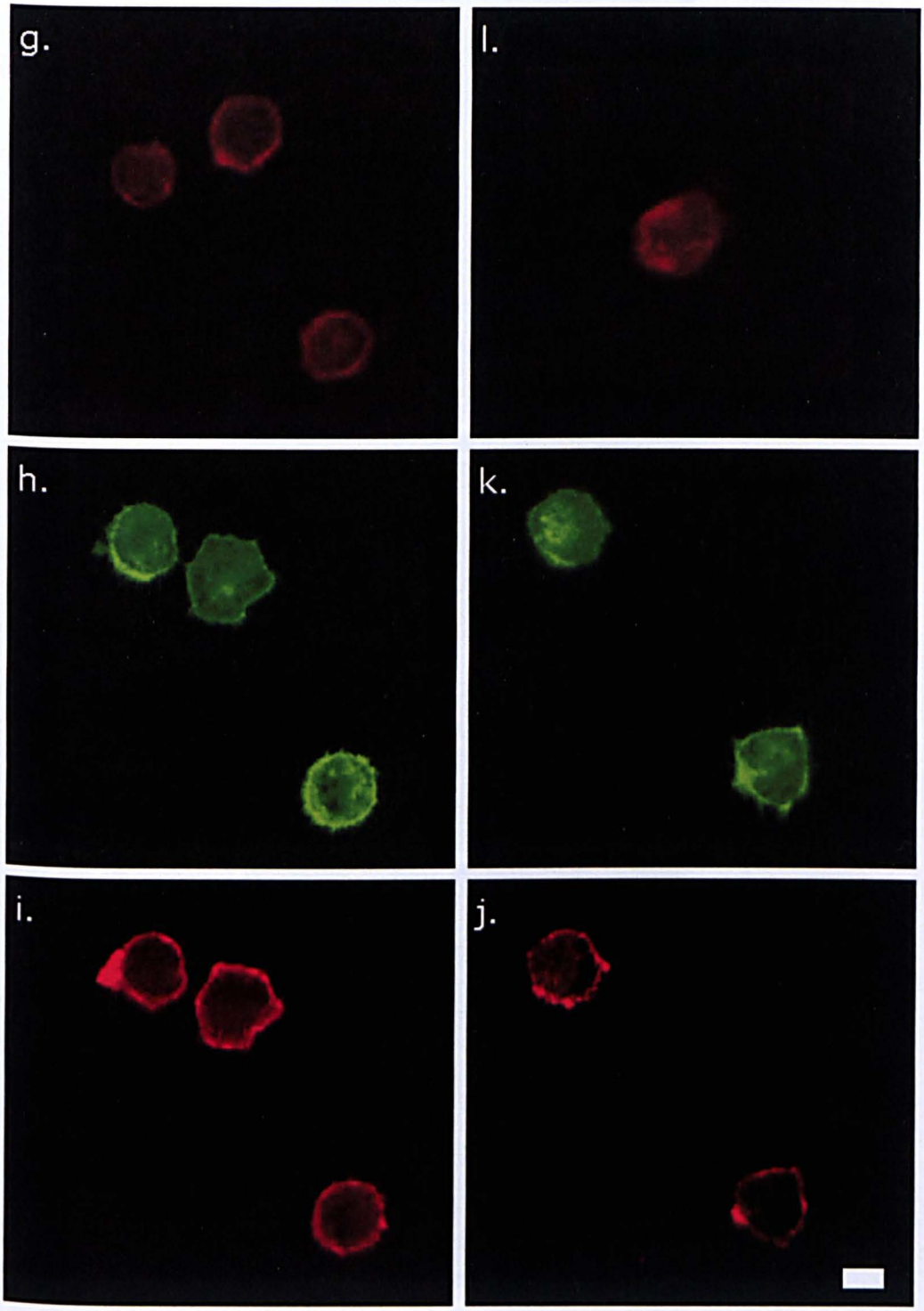

Figure 5.4.1. continued. β-tubulin (top row), F-actin (middle row) and vinculin (bottom row) localisation on TiO (g.), (h.), (i.) and TiN (j.), (k.), (l.) at 25 min. Scale bar 10 μm

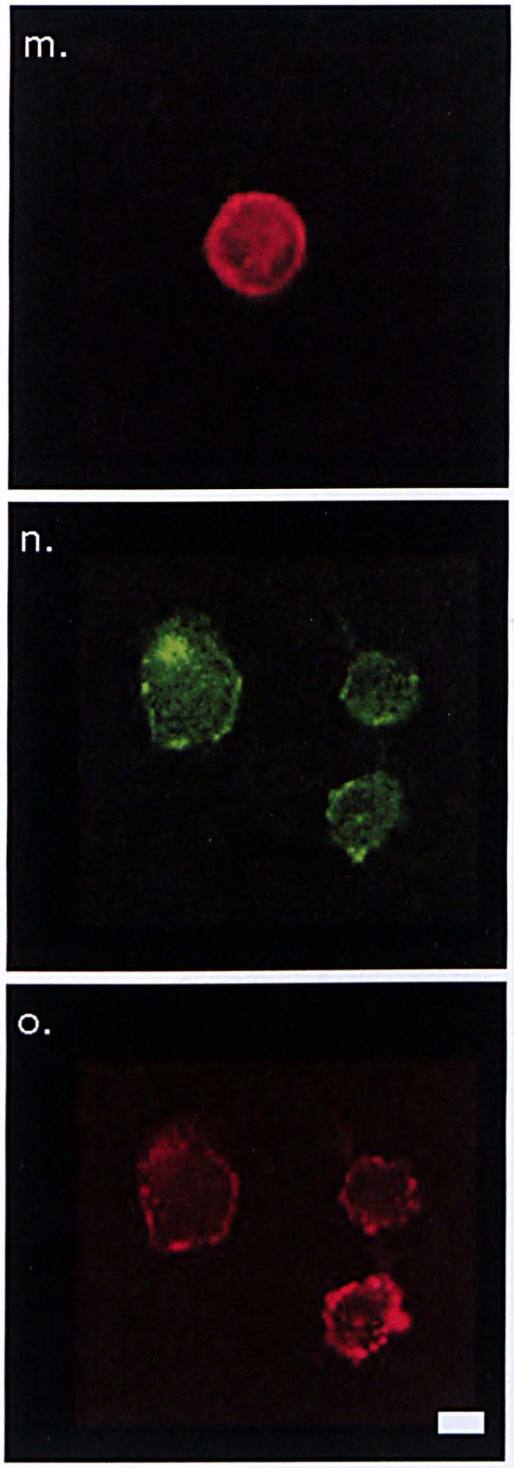

Figure 5.4.1. continued. β-tubulin (top row), F-actin (middle row) and vinculin (bottom row) localisation on Glass (m.), (n.), (o.) at 25 min. Scale bar 10 μm

Cells stained at 25 minutes show little evidence of cytoskeletal organisation with F-actin being diffuse throughout the cells. Cells stained for β-tubulin show a close arrangement of microtubules with an intense area in the centre of the cell where the fibres extend from the perinuclear region to the cortex. All cells show a higher concentration of vinculin around the periphery of the cell, with areas of most intensity suggesting that plaques are beginning to form.

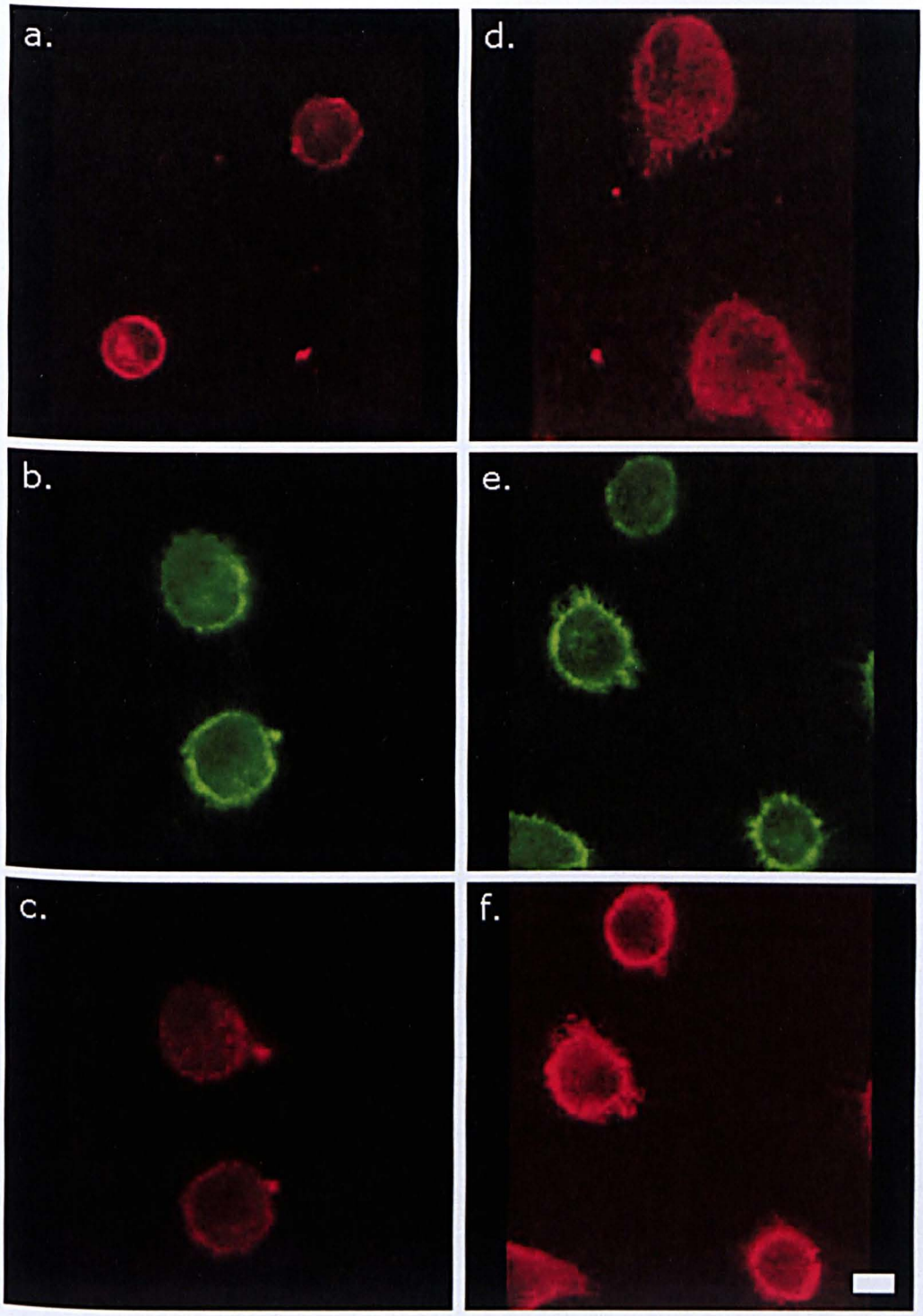

Figure 5.4.2. β-tubulin (top row), F-actin (middle row) and vinculin (bottom row) localisation on HSA (a.), (b.), (c.); Fn (d.), (e.), (f.) at 60 min. Scale bar 10 μm.

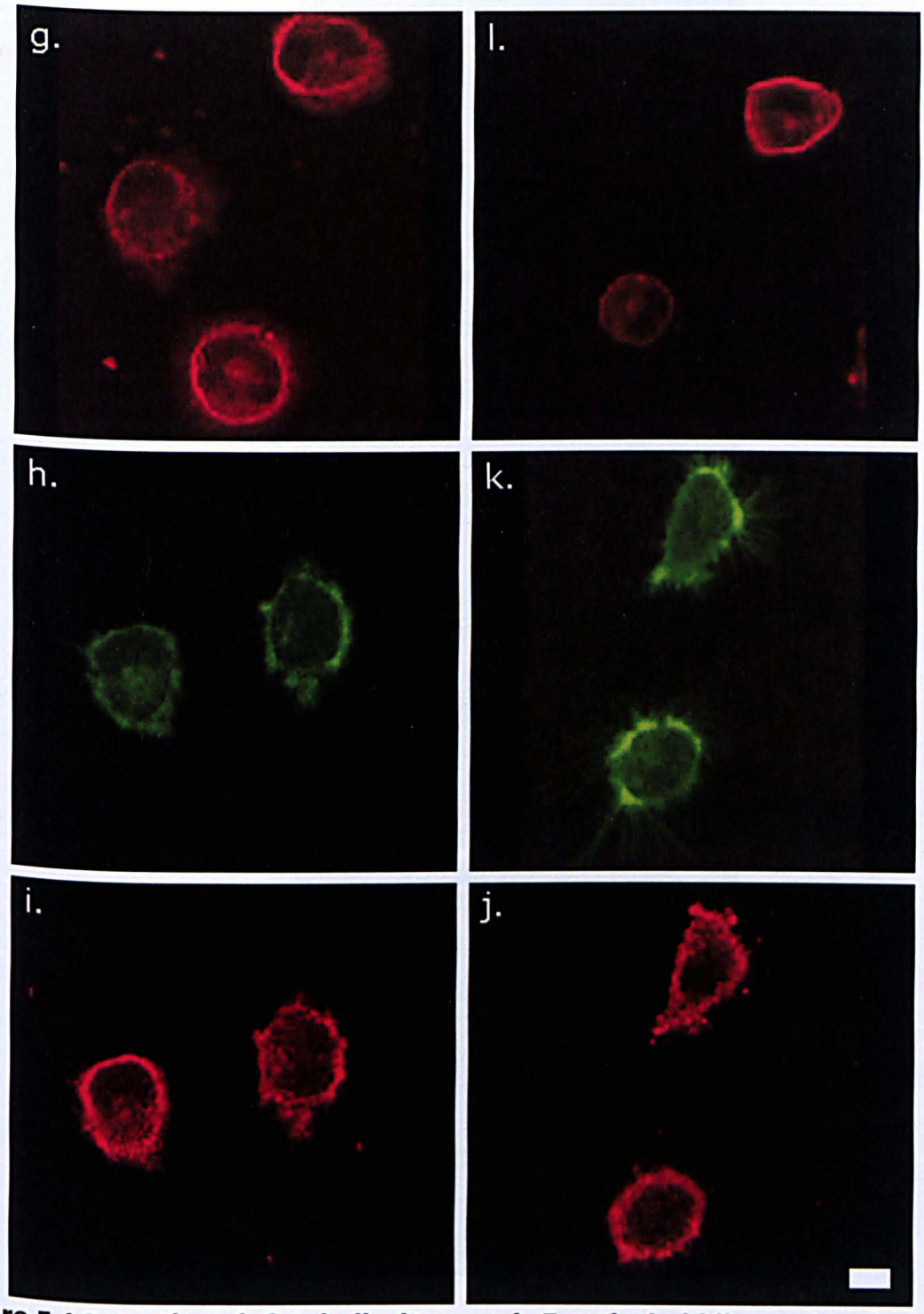

Figure 5.4.2. continued. β-tubulin (top row), F-actin (middle row) and vinculin (bottom row) localisation on TiO (g.), (h.), (i.) and TiN (j.), (k.), (l.). Scale bar 10 μm

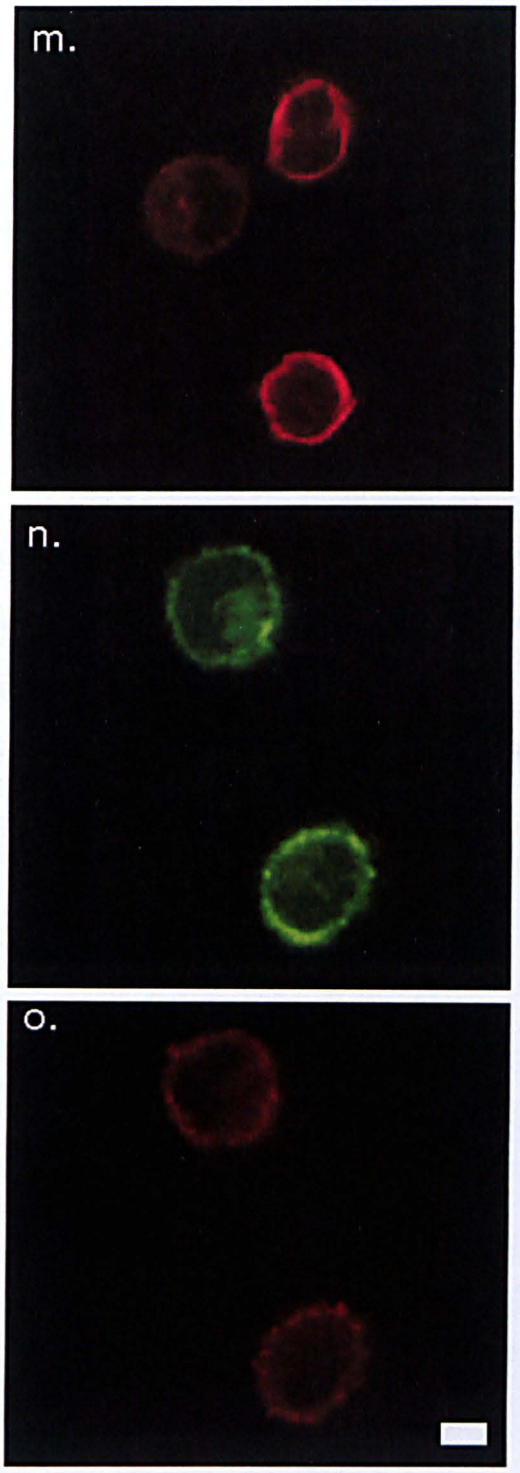

Figure 5.4.2. continued. β-tubulin (top row), F-actin (middle row) and vinculin (bottom row) localisation on Glass (m.), (n.), (o.). Scale bar 10 μm

The cells fixed at 60 mins after attachment show different degrees of cytoskeletal organisation across the surfaces. A higher intensity of actin can be seen in cells attaching to Fn which are not apparent in cells attaching to glass and HSA (figure 5.4.2. (b.), and (n.)). Some cells on Fn showed an actin type II structure described in section 4.5.7.1.

Cells attaching to TiN and TiO have a similar staining distribution at this time point, however cells attaching to TiN have noticeable fillopodia. Cells attaching to these surfaces have evidence of cortical actin filament formation with some radial filaments suggesting cells predominantly were progressing to an actin type II structure. β-tubulin is, again, predominantly more visible in the centre of the cell where the microtubules concentrate. Most of the cells in each population still primarily exhibit rounded morphologies.

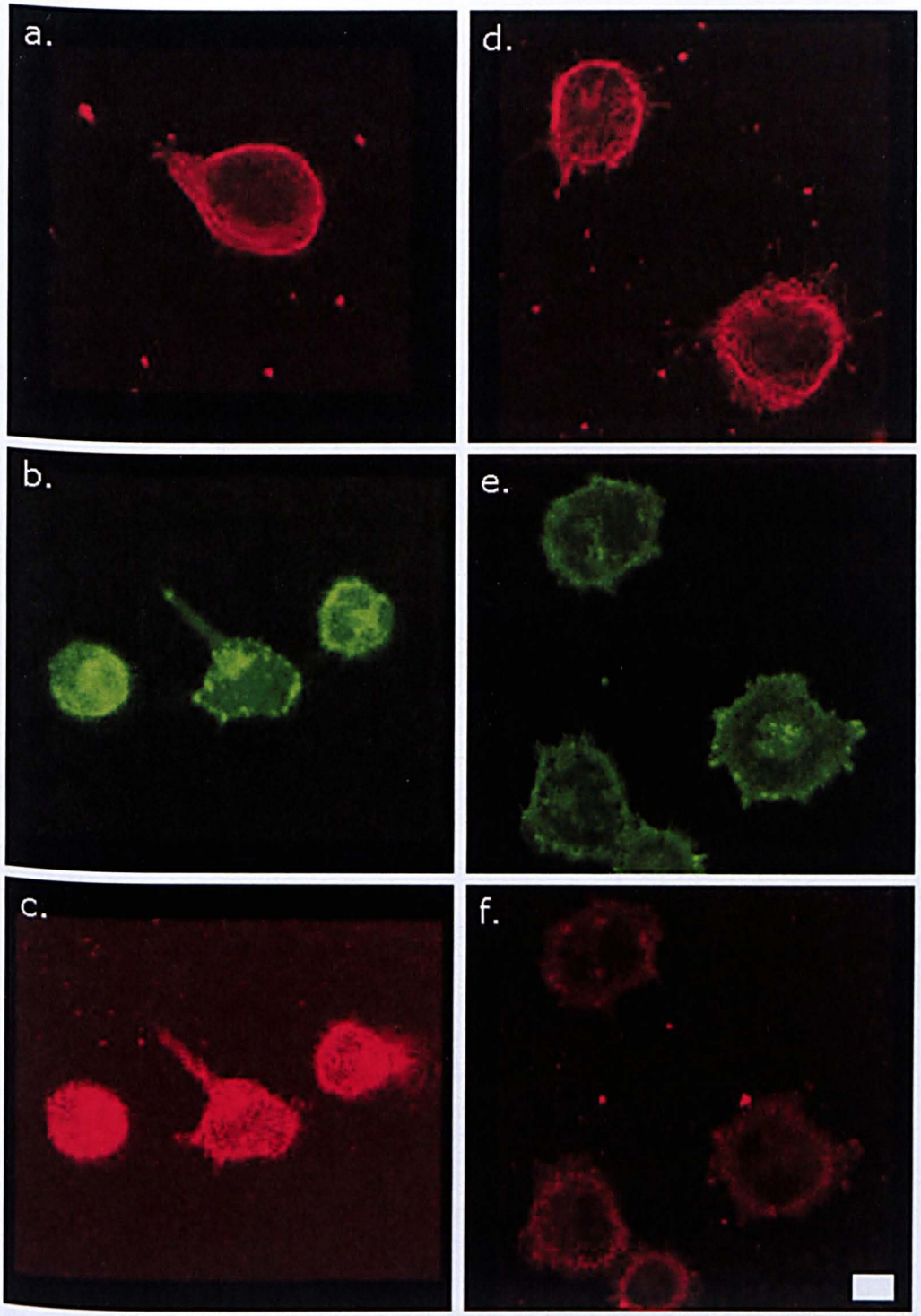

Figure 5.4.3. β-tubulin (top row), F-actin (middle row) and vinculin (bottom row) localisation on HSA (a.), (b.), (c.); Fn (d.), (e.), (f.) at 90 min. Scale bar 10 μm.

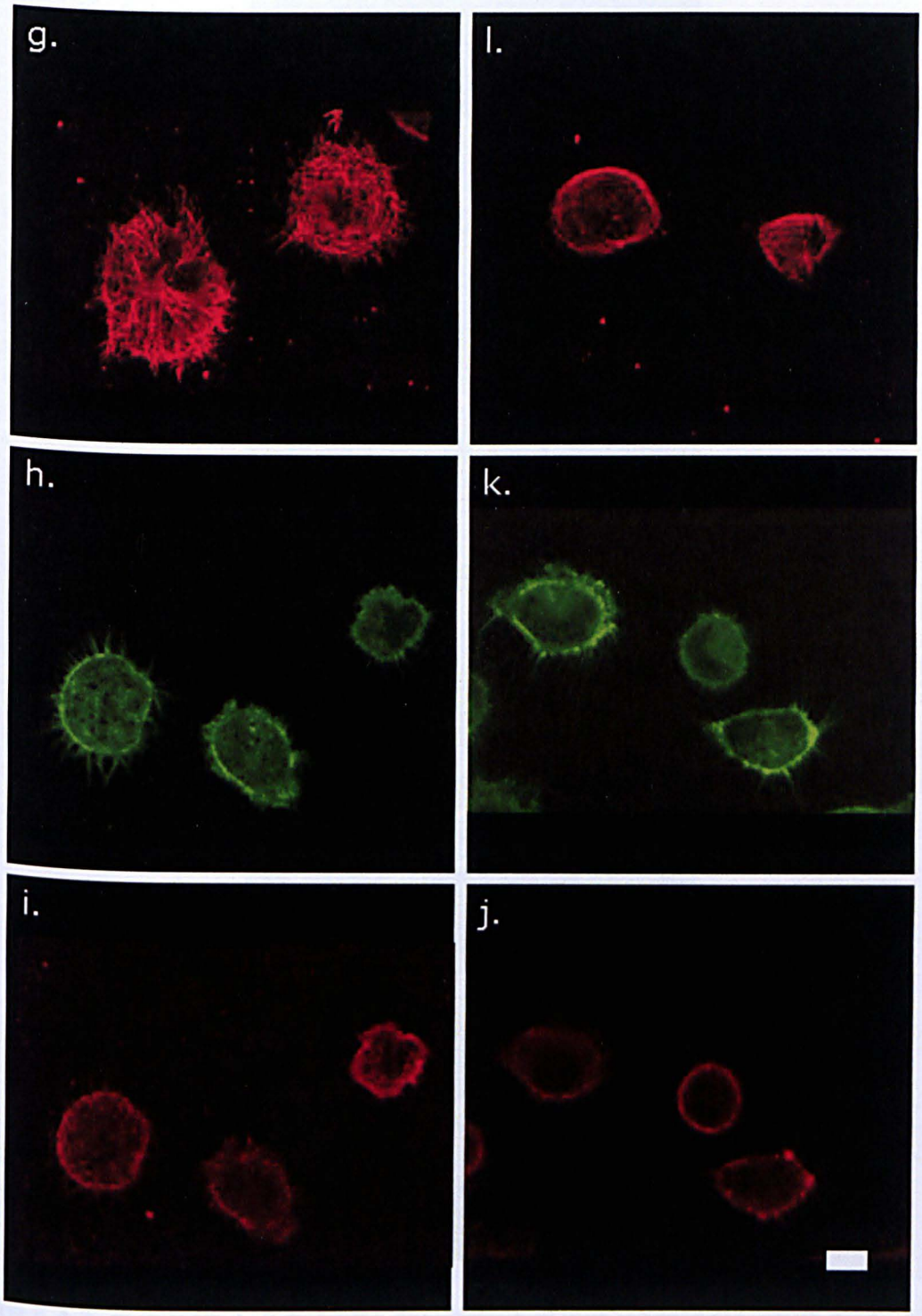

Figure 5.4.3. continued. β-tubulin (top row), F-actin (middle row) and vinculin (bottom row) localisation on TiO (g.), (h.), (i.) and TiN (j.), (k.), (l.). Scale bar 10 μm.

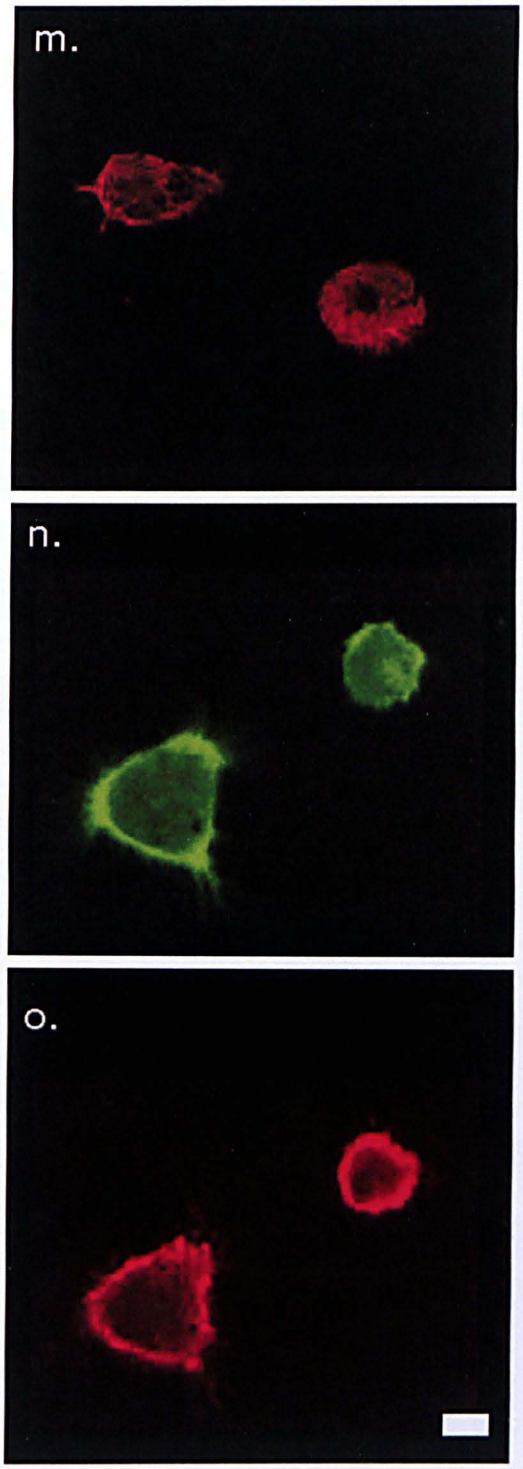

Figure 5.4.3. continued. β-tubulin (top row), F-actin (middle row) and vinculin (bottom row) localisation on Glass (m.), (n.), (o.). Scale bar 10 μm.

All cells visualised at 90 minutes showed some degree of cytoskeletal organisation and localisation of vinculin.

Cells attaching to both TiN and TiO showed fillopodia at this time point with a similar proportion, around 40 %, of cells showing a type II actin structure.

Again, cells attaching to Fn showed the more advanced cytoskeletal orgainisation showing a less diffuse staining pattern for F-actin than those on HSA.

Cells on all surfaces still exhibit a rounded contact area at this time point.

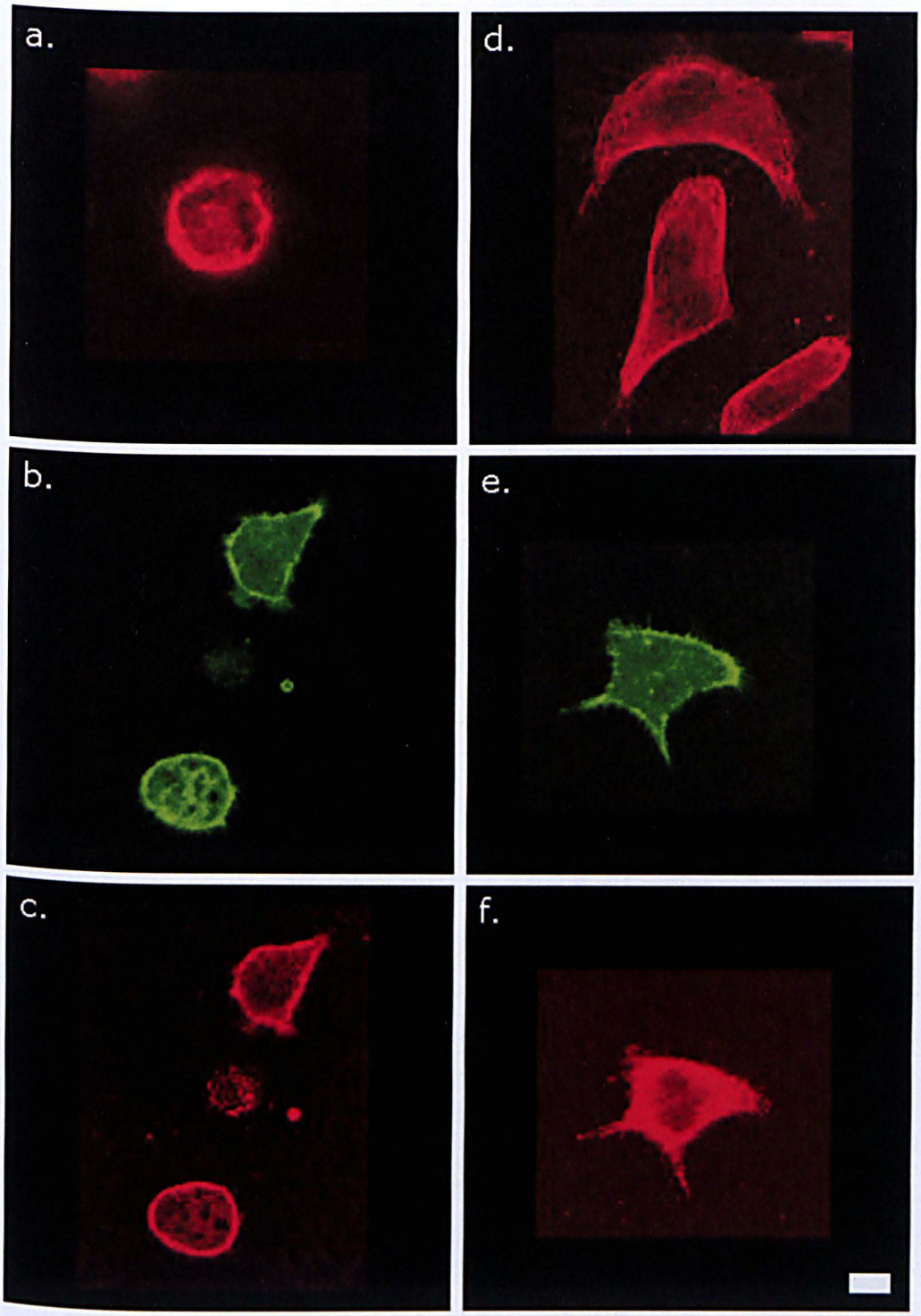

Figure 5.4.4. β-tubulin (top row), F-actin (middle row) and vinculin (bottom row) localisation on HSA (a.), (b.), (c.); Fn (d.), (e.), (f.) at 180 min. Scale bar 10 μm.

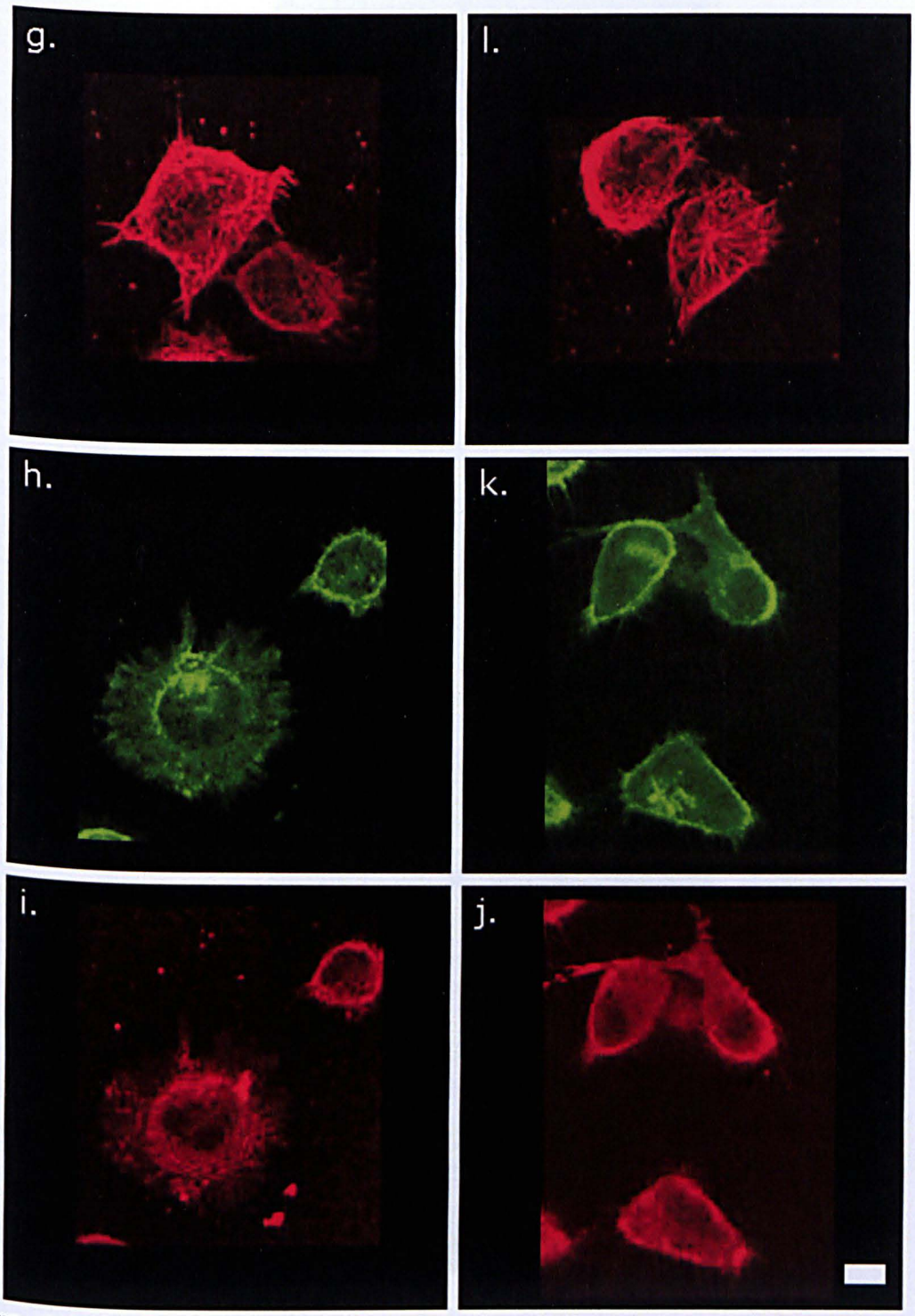

Figure 5.4.4. continued.β-tubulin (top row), F-actin (middle row) and vinculin (bottom row) localisation on TiO (g.), (h.), (i.) and TiN (j.), (k.), (l.). Scale bar 10 μm.

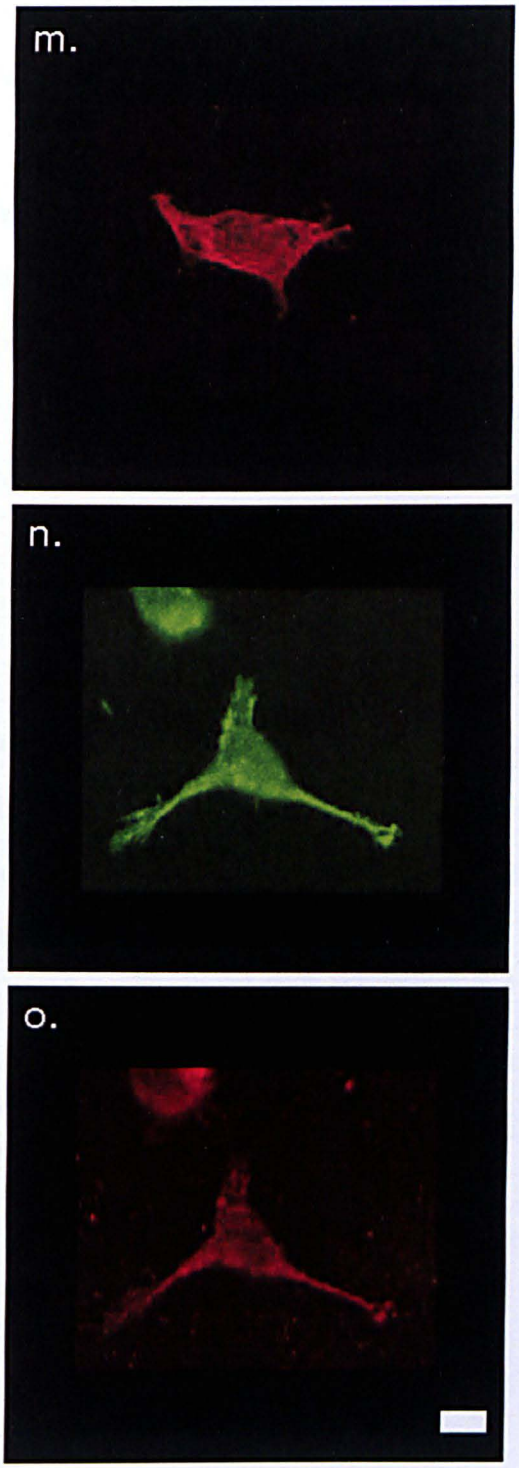

Figure 5.4.4. continued. β-tubulin (top row), F-actin (middle row) and vinculin (bottom row) localisation on Glass (m.), (n.), (o.). Scale bar 10 µm.

HOS cells fixed and stained after 3 h showed a range of different morphologies and a greater degree of cytoskeletal organisation.

HOS cells remained largely rounded on HSA but showed a greater degree of cytoskeletal organisation than cells at 60 min. In contrast, those cells attaching to Fn and glass had different morphologies. Cells on glass had long protrusions whereas those on Fn appeared to have broader lamellipodia and more cells with an actin type II structure, 94.3 % compared to 37 % and 52 % on glass and HSA respectively (see figure 5.4.5.).

Cells attaching to TiO and TiN had a range of morphologies and exhibited distinct and spaced microtubules and a greater proportion of cells showed actin type II organisation than at 60 min. Unlike the cells adherent on glass which had long protrusions by this time, some cells on TiO had broad lamellipodia and on both TiO and TiN cells were displaying polygonal morphologies.

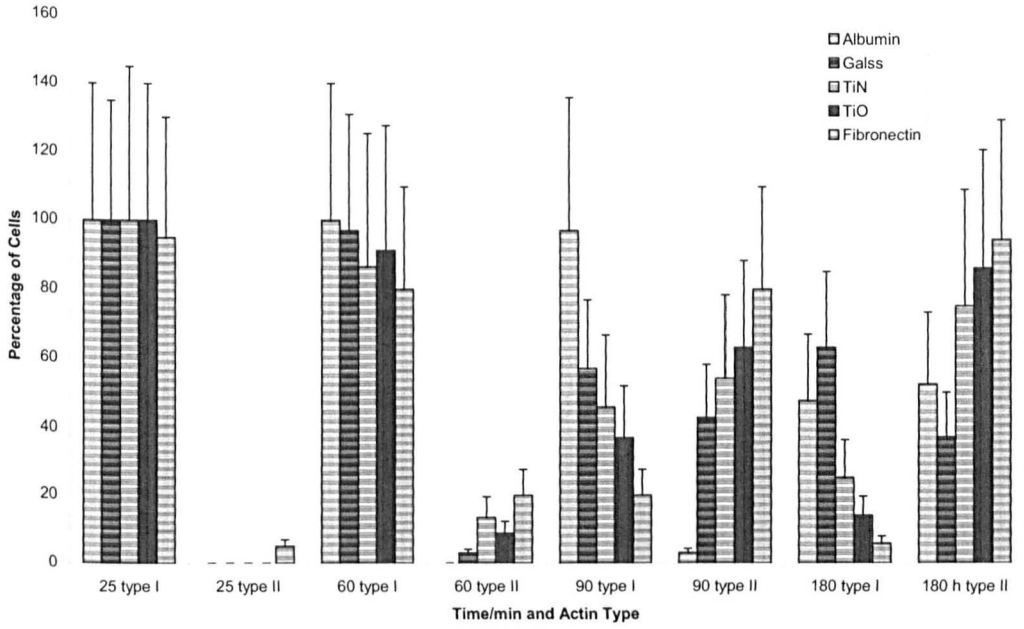

Figure 5.4.5. The percentage of HOS cells exhibiting types I and II actin organization after culture on the five surfaces for 25, 60, 90 and 180 min. Plotted values are mean ± standard error of the mean where n = ≥ 6.

HOS cells exhibit differing degrees of cytoskeletal organisation over the time points, as can be seen in figure 5.4.5. (classified by criteria described in section 4.5.7.1). Initially, the cells on all surfaces largely display type I characteristics. By the 3 h time point, there are more cells with type II organisation on all surfaces apart from glass and HSA.

Three dimensional representations were constructed from CLSM images of live HOS cells at 3 h for visual comparison against immuno- and SEM fixed cells. Cells representative of the populations on the four coated surfaces were chosen as a comparison against cells fixed for SEM and immunocytochemistry.

Five areas of each of three replicate samples were studied. It became apparent that there were common patterns of spreading, fillopodial protractions, outline of the lamellipodia and location of the lamellipodia in relation to the cell body that also corresponded to the patterns observed in the CLSM reconstructions. Images representing these patterns are shown in 5.4.6.

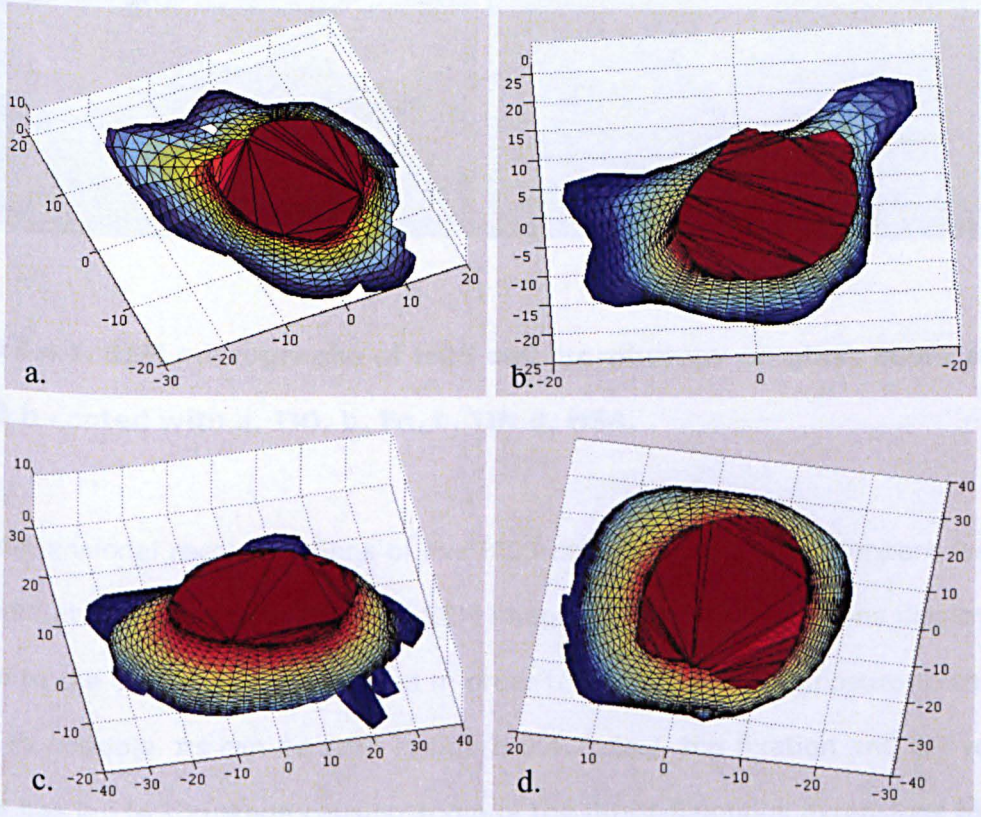

Figure 5.4.6. Representative morphologies produced from CLSM micrographs of HOS cells attaching to a. TiO, b. Fn, c. TiN, d. and HSA at 3 h after seeding. Scale μm x 10

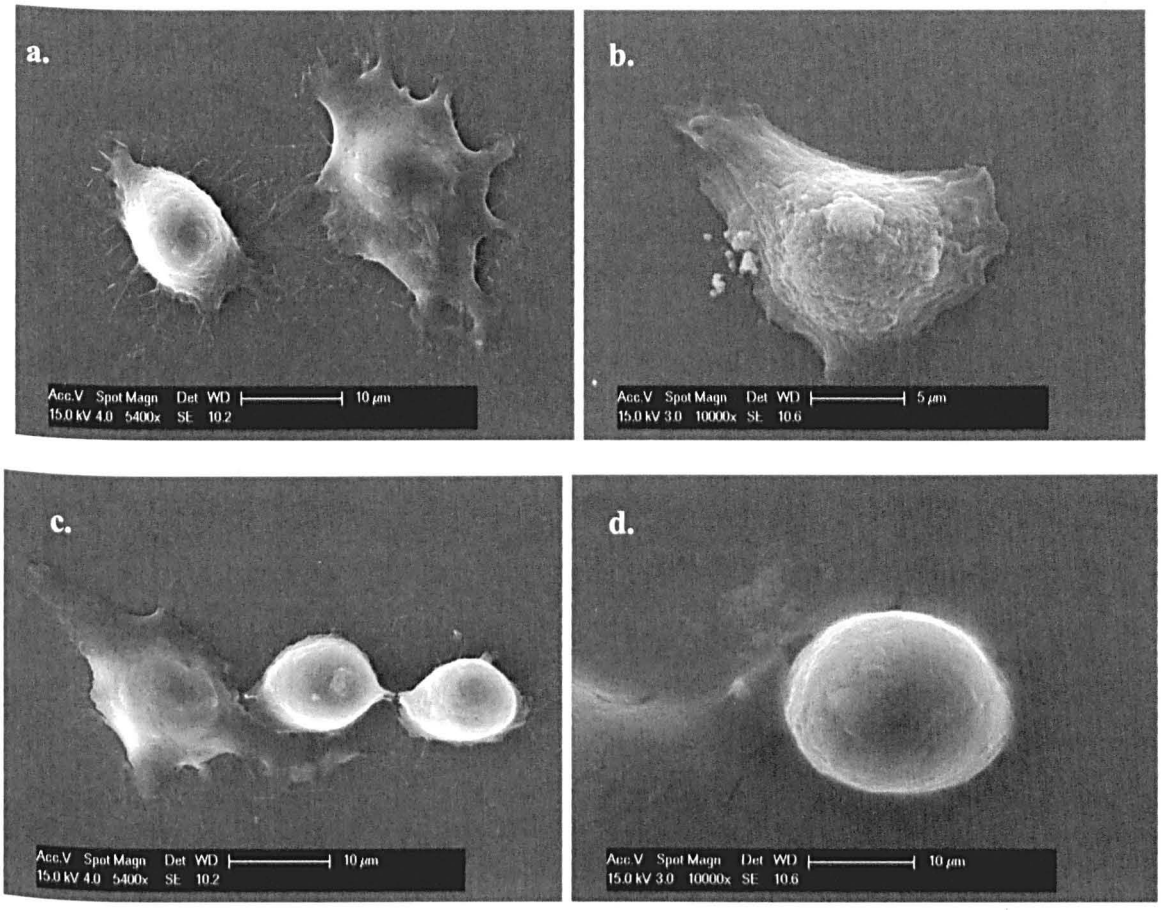

Figure 5.4.7. SEM micrographs of HOS cell morphology on glass cover slips after 3 h coated with a. TiO, b. Fn, c. TiN d. HSA.

Three dimensional reconstructions of live HOS cells imaged at 3 h compare well with cells fixed at the same time point for SEM imaging. The reconstructions display a flat top due to the size of the z-step used in order to keep the cells exposure to the laser as low as possible. As can be seen in figure 5.4.7. (a.), the fixation and dehydration process has led to shrinkage causing some of the finest filopodial extensions to tear.

5.5. Live cell studies on Thin Film and Protein Pre-Coated Glass Surfaces.

HOS cells were seeded on the four coated substrates (table 5.1) and each imaged every 5 min from 15 to 90 minutes after seeding. For each of the 16 time points, typically 14 z stack slices with a step size of 0.91 ± 0.069 μm were gained with, on average, 6 cells in each field. Experiments on each surface were repeated 6 times, giving, on average, spreading data for 36 cells. As can be seen in figures 5.5.1., 5.5.2. and 5.5.3., visually discernable differences between the images are not always apparent, so only the bottom confocal z slice showing the contact radius from each sample is shown at three representative time points, 15, 60 and 90 min, from the acquisition period.

CLSM on HOS cells imaged on 10 nm transparent thin film biomaterial coatings and glass coated with Fn and HSA showed that the cells again maintained a rounded morphology over the image acquisition period of 75 min. Analysis of the images show that cell height and contact angle with the surfaces decreased over the time period, whilst the contact radius increased. There were no significant differences between the rate at which this occurred over the different surfaces, as seen in figures 5.5.4, 5.5.5 and 5.5.6.

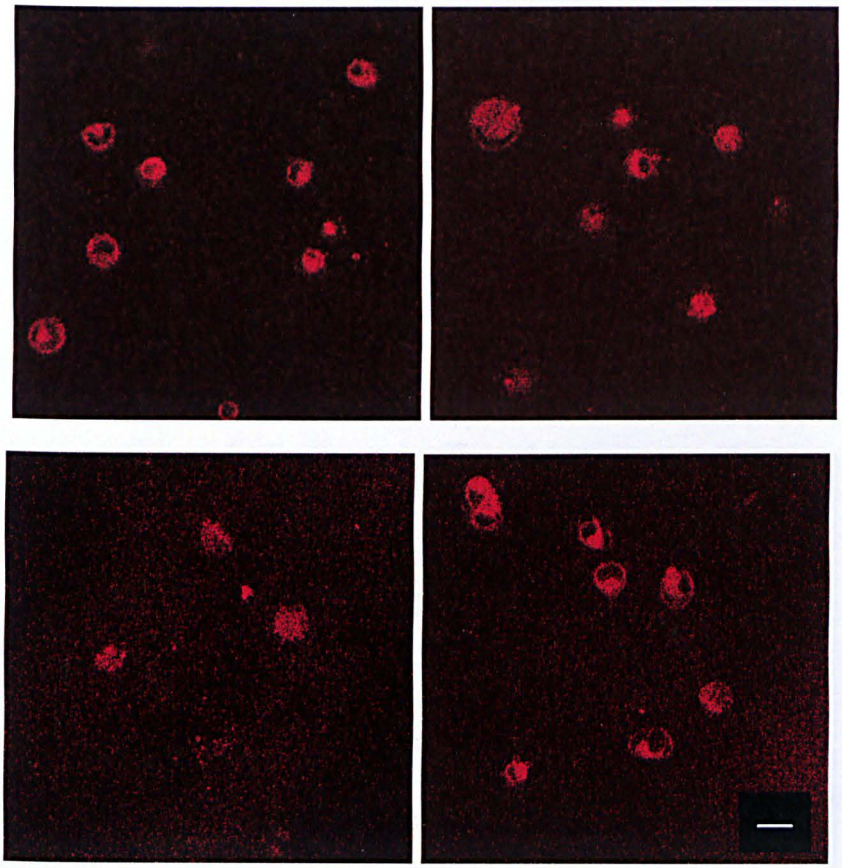

Figure 5.5.1. Bottom CLSM z stack of cells imaged on HSA, Fn, TiO and TiN coated borosilicate glass at 15 min after attachment showing contact area. Scale bar 20 µm

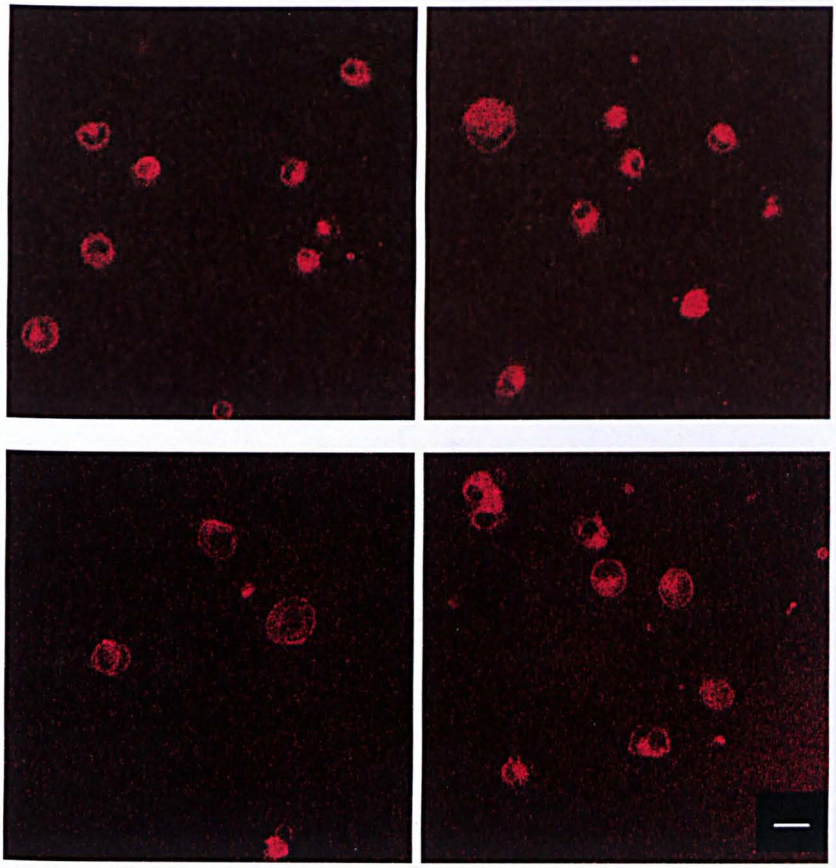

Figure 5.5.2. Bottom CLSM z stack of cells imaged on HSA, Fn, TiO and TiN coated borosilicate glass at 60 min after attachment showing contact area.

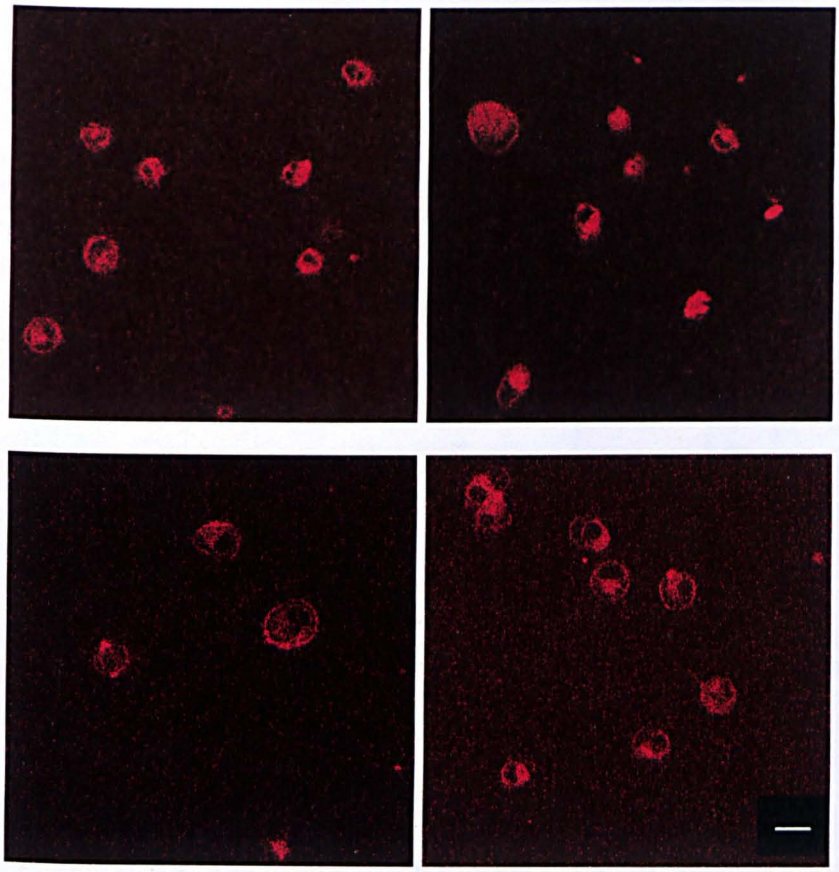

Figure 5.5.3. Bottom CLSM z stack of cells imaged on HSA, Fn, TiO and TiN coated borosilicate glass at 90 min after attachment showing contact area.

Figures 5.5.4, 5.5.5 and 5.5.6 show the analysed results for changes in HOS cell height, contact radius and angle over the 75 min image acquisition period.

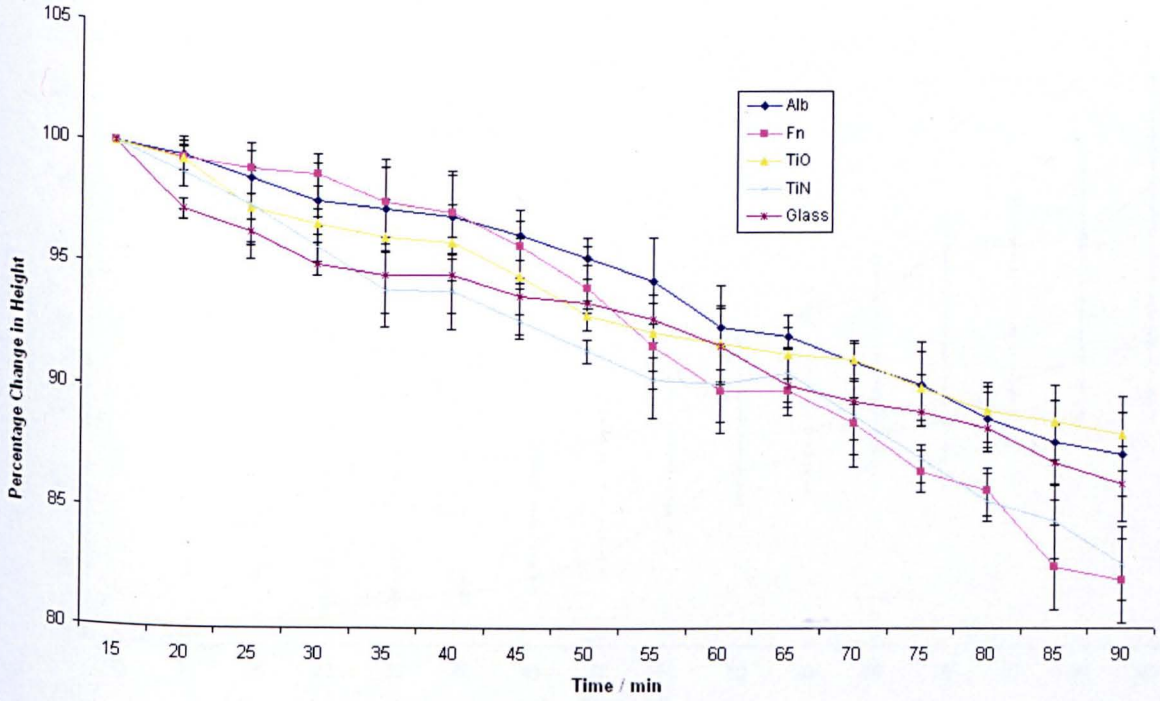

Figure 5.5.4. showing the percentage decrease in height of HOS cells spreading on HSA, Fn, TiO, and TiN coated surfaces and borosilicate glass from 15 to 90 minutes. Plotted values are mean ± standard error of the mean where n = ≥ 6.

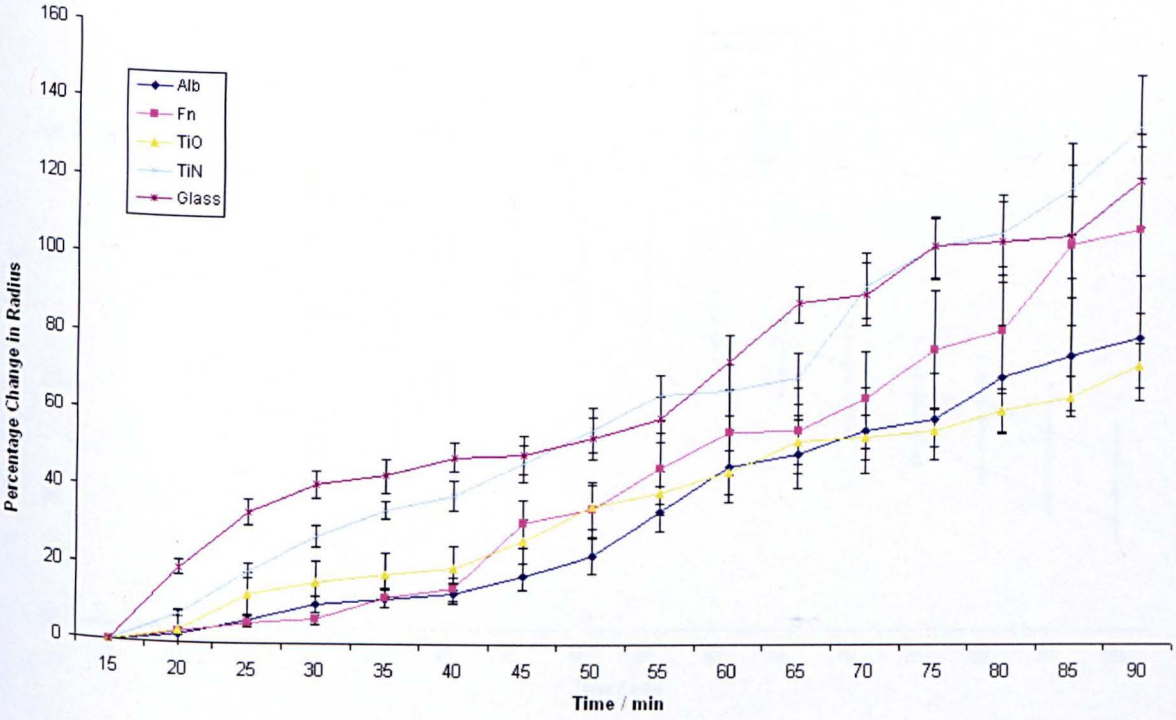

Figure 5.5.5. showing the percentage increase in contact radius of HOS cells spreading on HSA, Fn, TiO, and TiN coated surfaces and borosilicate glass from 15 to 90 minutes. Plotted values are mean ± standard error of the mean where n = ≥ 6.

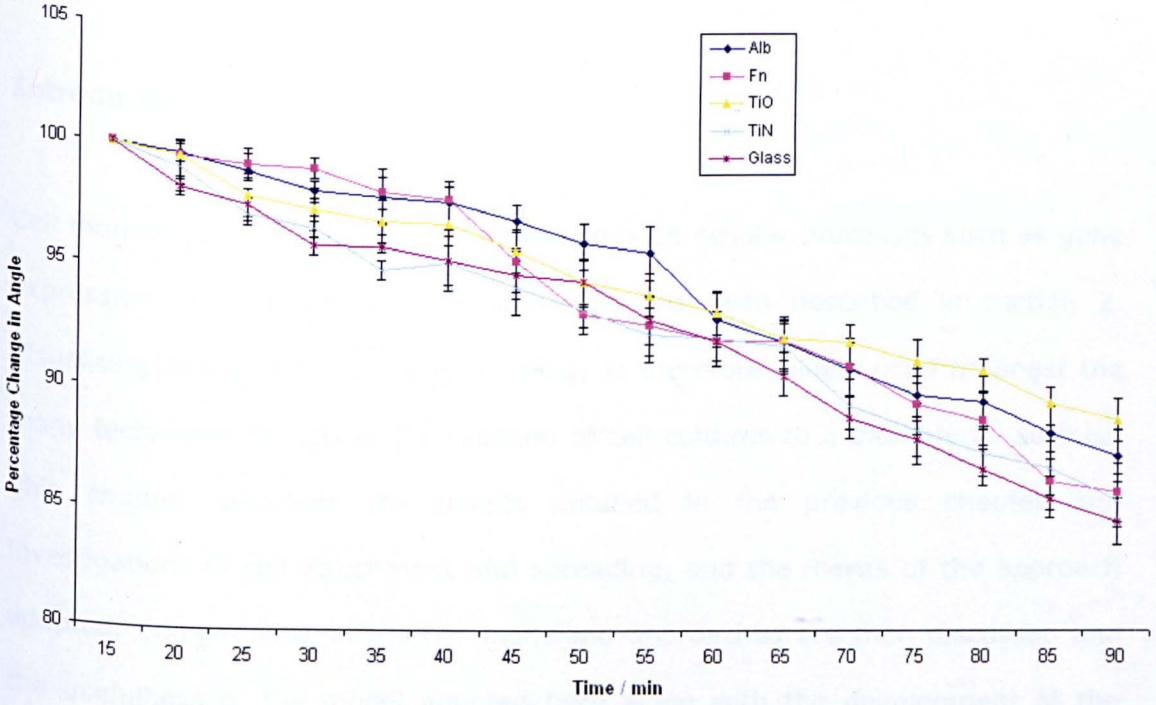

Figure 5.5.6. showing the percentage decrease in contact angle of HOS cells spreading on HSA, Fn, TiO, and TiN coated surfaces and borosilicate glass from 15 to 90 minutes. Plotted values are mean ± standard error of the mean where n = ≥ 6.

Over the 75 minute period, the analysis shows that cell height and contact angle with the surfaces has decreased over the time period, whilst the contact radius increased from. This can be seen graphically in graphs 5.5.4, 5.5.5 and 5.5.6. There was no detected significant difference of the cells' behaviour between the surfaces.

6. Discussion

Introduction

Cell morphology has fundamental implications on cellular processes such as gene expression, proliferation and migration, as has been described in section 2. Visualising and describing cell morphology is therefore widely used amongst the many techniques to assess the reaction of cell cultures to a biomaterial surface. This chapter discusses the results detailed in the previous chapter into investigations of cell attachment and spreading, and the merits of the approach adopted. Comparisons with other modelling approaches are then discussed and the usefulness of the model adopted here along with the development of the model beyond attachment and spreading into motility itself. In addition, the applicability of the model and experimental approach in other cell types and systems will be explored. The chapter starts by discussing cells imaged using LavaCell on borosilicate glass and the data gained through image processing.

6.2 LavaCell Membrane Probe

LavaCell was the membrane probe used throughout this study. Two other stains were initially tried, along with LavaCell, to determine which was most suited to the requirements of this study. As seen in figure 5.1 FPE was discounted as the intensity of the stain dropped to a point where image processing was not possible after exposure to the laser from approximately 3 time points. The stain also required the longest preparation time which also required the cells to be adherent on the substrate. Because of its short imaging time, a protocol for labelling cells so that imaging could begin nearer attachment was not sought. DiI was more successful and cells could be stained on attachment, but again, the stain's intensity diminished, on average, after only 8 time points.

HOS cells stained with LavaCell could be imaged taking confocal sections through the height of the cell (z direction) at steps of 1.91 ± 0.069 μm every 5 minutes for a period of 75 to 80 minutes with sufficient stain intensity for image processing. This heterocyclic lipophilic stain is a natural product derived from the fungus *epicoccum nigrum* [114]. It is taken up by the cell by unfacilitated diffusion with staining occurring in a time-dependent manner, starting with the outer plasma membrane, then lipophilic organelles in the cytoplasm such as the ER, Golgi and lipid rafts. This process was 85 % complete by the start of image acquisition 15 min after seeding. Most areas of the cell become stained, except within the nuclear membrane, leading to 'donut' shaped images (for example figures 5.1.1., 5.1.2., 5.1.3.) where the confocal slices bisect the nucleus in early stage spherical cells. Epococconone reversibly reacts with proteins to form an epicocconone-amine adduct with an internal charge transfer complex that is highly fluorescent in the hydrophobic intramembrane environment around transmembrane proteins. The fluorescence is further enhanced in lipophilic

environments [114]. As the unbound stain did not fluoresce, washing steps were not required so the stain could be added immediately after cell seeding when the cells were settling and beginning to attach on the surface. If washing stages were required, it would be necessary to wait after seeding the cells until they were attached sufficiently to withstand the shear forces of washing, delaying the time when the imaging could start. Many studies report 'early' time points at a period of 1 h after seeding, however, in this study it was imperative to start imaging close to seeding in order to assess the early stages of spreading.

The stain has been tested for cytotoxic or inhibitory effects on 56 human cell lines, with no detrimental effects observed at concentrations ≤5 μM [109]. The results in this study concur with these findings, with usable images gained to 90 min after seeding with a concentration of 3 μM stain. HOS cells stained with LavaCell looked visually similar when compared to an unstained control when imaged 90 min after seeding in full medium placed in a 37°C, 5% CO_2 incubator and visualised using a Nikon inverted phase contrast microscope at x 40 magnification.

Optimisation of the laser intensity and pinhole diameter was required to maintain the illumination intensity at a minimum to prevent photodynamic damage [65] whilst still capturing detailed images of the cell's periphery over the full time period. This was achieved by imaging with the airy pinhole open at 2.5, which, while reducing resolution, decreased the intensity of the laser beam to which the cells were exposed, as the laser power could be reduced from 11% to 4%.

6.3 Imaging cells on Borosilicate Glass

The HOS cells were imaged on borosilicate glass to enable the development of an image processing algorithm to detect the edge of the cells in CLSM optical sections taken through the z height of the cell. Once these edges had been recognised, contour plots representing the cell could then be re-constructed to gain information such as the contact line, cell height, and contact radius of the spreading cell. Capturing the contact line of the cell in sufficient detail was a key requirement set by the model developers. This required that the cells were captured with sufficient resolution to gain data on the interface between the cell and surface. Methods of using smaller z step increments, which only imaged the base of the cell due to the increase in laser exposure, were tried. It was found, however, that using a larger z step increment of 1.91 ± 0.069 μm provided enough data to reconstruct the contact angle whilst also allowing the whole cell to be imaged.

The 512 x 512 pixel CLSM micrographs representing an area of 238.1 x 238.1 μm were gained for cells seeded on borosilicate glass with a z step of 1.91 ± 0.069 μm (figure 5.1.1.). The cells display a rounded morphology at the start of imaging which is still largely the case by the end of the 90 min period from seeding, with very few cells reaching a stage to start polarizing. This would indicate that the cells are still in an early stage of attachment over the imaging period. These observations are in agreement with several osteoblast morphological studies [166, 167] using different imaging techniques on various substrates, including glass, where overall cell morphology is predominantly rounded at a period of 90 minutes or greater. Puleo *et al.* [167] stained neonatal rat calvarial osteoblast cells attaching to borosilicate glass for F-actin and cells fixed at 6 h after attachment still displayed a rounded morphology, becoming polygonal by 12 h.

Meyer *et al.* [166] also reported that primary bovine osteoblasts were still mostly rounded on borosilicate glass after 120 min.

The brightness of the images decrease over the time period, in accordance with figure 5.1., showing that photobleaching is occurring and limiting the image acquisition period, but not to an extent that detail of the cell's periphery was lost. The intensity of the stain occasionally became less consistent across the cell becoming evident as the cell spread (figure 5.1.1., 5.1.2., 5.1.3, white arrow) and interestingly, although not a noted observation, is evident in images of HCT-116 colonic epithelial cells by Choi *et al.* [168] using the same stain.

The cells were successfully imaged for periods of 75 minutes, gaining enough detail for image processing, without causing any detrimental effects to their behaviour. Whilst this period represents an extended time in terms of visualising live cells using fluorescent microscopy, this is still short compared to the timescale of cell spreading, which evolves over several hours. This means that we have concentrated only on the initial phase of adhesion and spreading, looking at this dynamic process over the first 90 minutes, as the initial spherical shape flattens, becomes hemispherical and begins to lose symmetry. This comprehensively sets the grounding for further work to concentrate on the later stages of spreading, being cell polarisation and the further advancement of lamellipodia.

6.4 Image Processing

The image processing algorithm was able to detect the outlines of the cells on the CLSM micrographs. The algorithm processed all the cells within the field, with data on each individual cell being stored in a directory for further analysis. The

edge detection was checked visually and by comparing pixel intensities inside and outside the cell. In total, including coated surfaces, data on over 180 cells at 14 time points were subjected to image processing during these studies.

Edge detection of objects in a digital image is a notoriously difficult challenge and can be argued to be a somewhat subjective approach as there are a wide range of detection methods, which may perform well in some applications, but poorly in others [169, 170]. What looks a clearly distinguishable edge to the human eye might be a small variation in greyscale pixel values over a number of pixels, making it very difficult to discern by an edge detection method.

For the initial edge detection method, the Prewitt first derivative operator was applied, as the effect of noise due to the wide pinhole aperture was reduced by averaging [161]. This gave the best visual result compared to other detection algorithms, such as Canny and Roberts [162] (see figure 6.1). Most edge finding operators use differentiation to detect edges [162]. Taking a profile of pixel intensities across an image, the derivative of constant sections of this profile returns zero, whereas for sections where a change occurs, the derivative returns a nonzero value. For a two dimensional image, the partial derivative is used to give a gradient. The gradient magnitude gives the amount of difference between pixels in a neighbourhood and the gradient direction gives the direction of the greatest change, the edge normal [171]. A threshold is then applied, so that only changes of a magnitude above a set value are labelled as an edge.

Prewitt is a first derivative method of detecting the edge using pixel intensities [162]. The Prewitt kernel is based on the idea of central difference; for a two dimensional image:

$$\frac{\partial I}{\partial x} \approx [I(x+1,y) - I(x-1,y)]/2$$

Where I is intensity and x and y are pixel coordinates.

This method is sensitive to noise, which is reduced by averaging, the sensitivity of which can be specified or chosen automatically by the Matlab *edge* function. This function ignores all edges where the intensity is less than the threshold specified. It returns edges at those points where the gradient of I is maximum [162].

Other options that were tried are Sobel, Roberts, The Laplacian of Gaussian and Canny [162]:

The Sobel method finds edges using the Sobel approximation to the derivative which gives greater weight to the central pixels when averaging. The Sobel operator uses the same equation as the Prewitt method, but smoothing using a larger neighbourhood.

The Roberts method finds edges using a {+1,-1} operator that calculates the forward differences equation [171] between two pixels in a neighbourhood.

$$\frac{\partial I}{\partial x} \approx I(x+1,y) - I(x,y)$$

The kernels produced in this method are too small to give an accurate representation of the edge in the presence of noise, as can be seen in figure 6.1. (c.).

The Laplacian of Gaussian method uses the second derivative to find an edge. In principle, it first blurs the image with a Gaussian smoothing operator and then applies the Laplacian operator. The Laplacian applies an approximation to the second derivative using a rectangular neighbourhood in both the x and y

directions. It achieves this by differentiating the Gaussian to give a closed-form solution for the Laplacian of Gaussian:

$$\Delta^2 G(x,y) = \left(\frac{r^2 - \sigma}{\sigma^4}\right) e^{-r^2/2\sigma^2}$$

Where Δ is the gradient operator, G is the Gaussian operator and $r^2 = x^2 + y^2$

The Canny method finds edges by looking for local maxima of the gradient of I. The gradient is calculated using the derivative of a Gaussian filter. The method uses two thresholds, to detect strong and weak edges, and includes the weak edges in the output only if they are connected to strong edges.

$$\left(-\frac{x}{\sigma^2}\right) e^{-\frac{x^2}{2\sigma^2}}$$

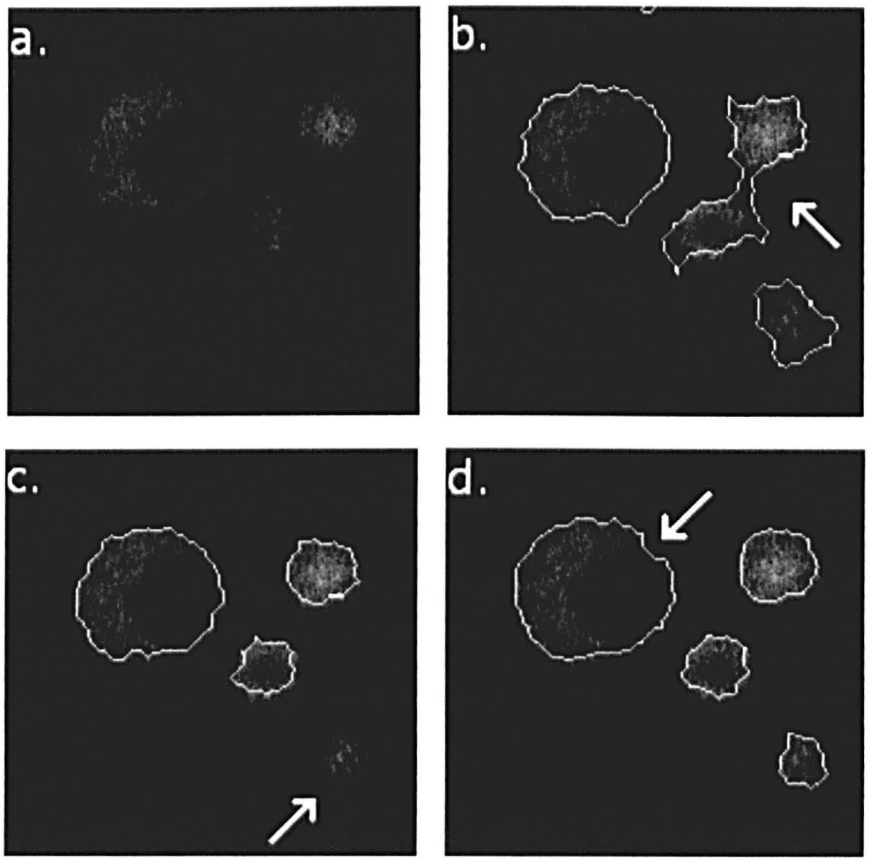

Figure 6.1. Image showing various methods of edge detection using a confocal z slice of HOS cells 30 minutes after seeding. a. original greyscale image, b. Canny, c. Roberts and d. Prewitt.

As can be seen in figure 6.1., each of the first three edge detection methods have their drawbacks. Each method was performed with the same level of thresholding to give a comparison of the technique. The Canny method (fig 6.1. b.) was too sensitive to noise and has drawn an edge far outside of the cell in many areas, especially the small cell bottom right, and has linked the two cells to the right of centre in the image. The Roberts method (fig 6.1. c.) is not sensitive enough and has given an edge within the cell and has failed to recognise the cell in the bottom right. The Prewitt method (fig 6.1. d.) was used in the initial image processing as this gave the best approximation of the edge of the cell using standard techniques. The edge has been drawn in towards the nucleus (white arrow) where the nucleus is close to the periphery of the cell. This can be overcome by smoothing the outline and using structuring elements in the later steps of the image processing algorithm.

Further analysis was then performed, using the algorithm, whereby 50 data points are stored for each contour, each with x,y,z locations. A spherical cap was then fitted to the resultant contour plot for each time point, with the cap's volume remaining constant throughout. This uses the least squares fit, labelling the co-ordinates of the *i*th point at time *j* by (x^j_i, y^j_i, z^j_i), the sphere centre at time *j* by (X^j, Y^j, Z^j) and the radius of the sphere at time *j* by R^j, the distance of each point from its spherical cap is

$$\sqrt{\left(x_i^j - X^j\right)^2 + \left(y_i^j - Y^j\right)^2 + \left(z_i^j - Z^j\right)^2} - R,$$

were R^j is given in terms of Z^j and the cap volume V. The equation for R^j is

$$2R^j + 3R^j Z^j - Z^{j^3} - \frac{3V}{\pi} = 0.$$

Euclidean based norms are calculated for each time point. These are divided by the radius of the corresponding sphere, giving an idea of the relative error between the spherical cap and the data points.

The analysis shows that cell height and contact angle with the borosilicate glass surface decreased over the time period from 22.1 to 19.5 μm and 162.7 to 137.50 ° respectively, whilst the contact radius increased from 4.1 to 9.0 ± 2.1 μm. This is in agreement with [26], where cells on a number of surfaces were shown to spread as a viscous droplet. The volume of the cell varied in the order of 1 to 2 μm over the time period. This should remain constant [24, 26, 27, 55]. This variation could result from the difficulty to prescribe a definite top to the cell as some stain is excited in the area directly below the focal plane leading to some fluorescence from this area to be captured and slight variation of what is defined as the edge of the cell. The algorithm's assumption that each 1.91 μm optical section is filled with cytoplasm may also have had an influence on the result. Any spreading of lamellipodia can lead to a higher value as these are less than 1.91 μm thick so a misleading volume is calculated for such cells.

The results will be compared to theoretical models of spreading along with cells imaged on different surfaces to compare the effect of surface chemistry later in the chapter, in section 6.8.

The image processing works with a high degree of confidence, measuring contact angles to 0.3 degrees, by recognising the edge of the cells in optical sections and allowing three dimensional representations of the cell to be created. The Prewitt method identifies the outline of the membrane, giving contours at a z spacing found to give enough data to recreate a surface and calculate accurate contact angles.

6.5 Characterisation of Biomaterial Coatings

TiN transparent thin films produced by DC magnetron sputtering were characterised using XRD, XPS and ellipsometry. TiN was chosen due to its wide use and relevance to the biomaterials field. TiN coatings have been used in many applications and is noted for its high erosion- and corrosion-resistance along with its biocompatibility [130]. The coating can reduce bacterial colonisation, making it a popular choice for dental applications [131], and decrease the amount of metal ions which leach from an implant into biological fluids [132].

TiO was chosen as a thin film to give a contrasting surface chemistry to the TiN surface [173]. This difference in surface chemistry should elicit a different response from the cells [133, 174]. Whilst TiO films are not used as widely in the biomaterials field, there have been recent studies suggesting that the surface could be used as antithrombogenic coating [167]

6.5.1. Analysis of TiN

6.5.1.1. XRD analysis of TiN

As the 10 nm films used in this study are below the sampling depth of XRD, thicker films were analysed. Films of 1 μm and 0.2 μm were produced for analysis to assess whether the properties of the film changed with the thickness of the deposited layer in order to make assumptions about the 10 nm film. XRD confirmed the presence of FCC TiN (JCPDS-ICDD card 00-038-1420) in the deposited films. The (hkl) reflections suggest a NaCl (B1) structure whereby the nitrogen atoms occupy the octahedral interstitial sites (see figure 6.3.). The distinct peaks of the 1 μm sample suggests that the coating is not amorphous, but has a preferential orientation. The 0.2 μm sample appears to have a more

random orientation which is consistent with [175], that states that as TiN coatings thicken, the grain size increases and they are more likely to have a preferential morphology as they move from being nanocrystalline. The grain size increased from less than 4 nm in the 0.2 µm sample to 8 nm in the 1 µm sample. This would suggest that the 10 nm films used in the cell culture experiments would be randomly oriented and nanocrystalline in structure.

6.5.1.2. XPS analysis of TiN

Analysis of the XPS spectra for the 10 nm film showed that TiN and TiN_x were the most abundant species present on the surface at 42.0 and 20.6 % respectively, with a small amount of TiO_2, 13.4 %, also present. A model produced by Nyaiesh *et al.* [176] proposes that on exposure to air, TiN oxidises to 2-3 monolayers of TiO_2 which would explain the presence of the surface oxide.

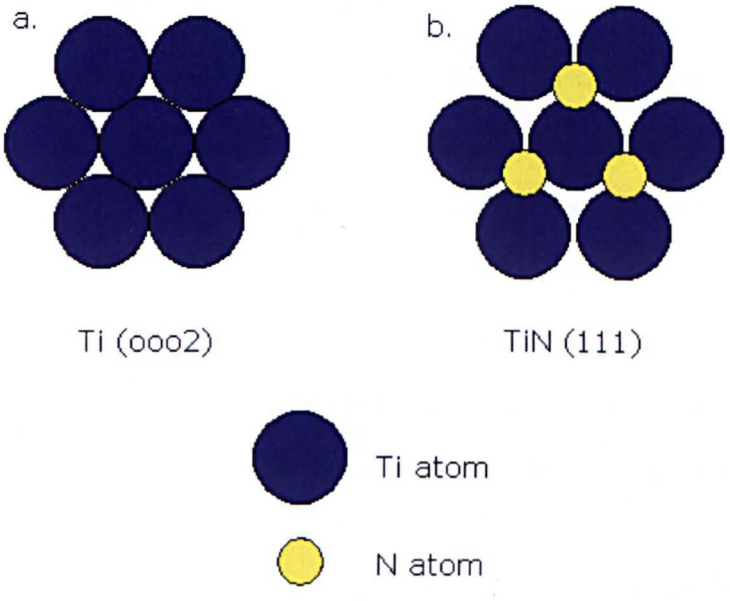

Figure 6.3. Schematic diagram showing the arrangement of titanium atoms in (a.) the (0002) plane of titanium, and (b.) the (111) plane of titanium nitride. (Modified from: [177]).

Peak deconvolution for the TiN coating XPS spectra showed the presence of more peaks than would be obtained from a stoichiometric TiN. In the Ti 2p region (figure 5.18), six individual peaks were fitted to produce a fit. These six peaks correspond to doublets from titanium in three distinct binding states, so can be discussed as three peaks. The highest peak corresponds to titanium bound in stoichiometric TiN, which is in agreement with values reported in the literature [126, 179]. Peaks 2 and 3 are assigned to a non stoichiometric TiN_xO_y phase and TiO_2, also both in agreement with reported values [133, 128]. As these two phases are not shown by the XRD results, this indicates that they are restricted to the near surface regions and so are likely to be due to contamination and expected oxidation.

6.5.2. Analysis of Titanium Oxide

6.5.2.1 XRD Analysis of TiO

XRD confirmed the presence of FCC TiO (JCPDS-ICDD card 01-077-2170) in the deposited films. Again, the heights of the peaks suggest that the samples become more nanocrystalline, with grain size reducing from 7 nm to less than 4 nm as the coating thickness was decreased from 1 μm 0.2 μm. This would suggest that the 10 nm film used for cell culture also has a nanocrystalline structure. TiO exhibits a similar NaCl crystal structure to TiN, see figure 6.4., with a very close interplanar distance [180], and both having an Fm-3m space group.

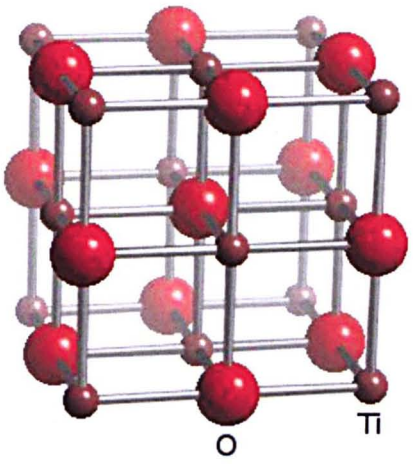

Figure 6.4. Schematic representation of the TiO crystal structure. (From: [www.webelements.com]).

A non stoichiometric TiO can range over the compositions from $TiO_{0.7}$ to $TiO_{1.25}$ at temperatures below 990 °C. The crystal structure of these has varying proportions of Ti and Oxygen vacancies, deduced from a comparison of pycnometric and X-ray densities by Mary *et al.* [181]. For the composition $TiO_{0.7}$, the titanium lattice is almost perfect, but approximately one third of the oxygen sites are vacant. For the $TiO_{1.25}$ structure, the oxygen lattice is almost perfect, but a quarter of the titanium sites are vacant, with the vacancies being randomly distributed for both structures. The peaks shift noticeably to lower angles than the database values (figure 5.3.3. and 5.3.4.). This is attributed to the increase in residual stresses created by nitrogen in the crystal lattice, which is shown to be present by XPS and is consistent with findings by Mahalingam *et al.* [226].

6.5.2.2. XPS Analysis of TiO

The deconvoluted XPS spectra showed peaks indicative of TiO_2, with small amounts of TiO, TiN and Ti metal on the surface. Peaks located at 458.56 and 464.27 eV correspond to reported values in the literature for Ti $_{2p3/2}$ and Ti $_{2p1/2}$ of

TiO_2, which are assigned to Ti^{4+} in amorphous TiO_2, providing that titanium is fully oxidized [182, 183]. It should be noted that since titanium and titanium suboxides are oxidized easily in air to form TiO_2, the samples surface XPS spectrum might not convey the complete story of the subsurface, shown by the XRD results, as XPS only analyses the top 4 nm of the surface. The presence of a small amount of TiN with peaks located at 456.39 and 462.09 eV can be explained as air was used rather than CP oxygen for the sputtering process.

To determine whether submersion in cell growth media during imaging experiments further oxidised the TiO surface, samples were placed in media for 100 min. XRD and XPS analysis carried out after submersion showed that the material remained unaltered.

6.5.3. Ellipsometry of TiN and TiO

The thickness of TiN samples exposed to the target for different time periods to establish sputter rate was determined using ellipsometry. As the cells were imaged using an inverted confocal microscope, the TiN films had to be optically transparent. A coating thickness of 10 nm was therefore chosen as this is commonly used as a protective and conductive film on solar cells and is reported in the literature as being optically transparent [184, 185]. It is also reported that human tissues interact with only the top atomic layers of a substrate, to depths from 0.1 to 1 nm [119], so this thickness is sufficient to mask the underlying substrate.

The measured thickness of three samples showed a linear relationship between coating thickness and sputtering time when all other variables remained constant. It was therefore possible to extrapolate back to find an exposure time that would

give a coating of 10 nm in thickness. Using the lines of worst fit from the error bars of the measured results, as shown in figure 5.3.7., it was calculated that the coatings have a thickness of 10 ± 4.86 nm.

6.5.4. Wettability

The water contact angles for the sputtered thin film and protein surfaces (table 5.1.) show that the wettability varies between all 5 surfaces. The HSA coating produced the lowest wettability, with a water contact angle of 75° which seemed low, but is in agreement with a value reported in the literature [186]. TiN was slightly less hydrophobic, with a contact angle of 45°, in agreement with [134], followed by borosilicate glass at 32° [187] and fibronectin at 25°, in agreement with [189].

The TiO surface was the most hydrophilic of surfaces studied, with a contact angle of 10°, in agreement with literature values [181]. Thus the TiO surface possesses the highest surface energy of the five surfaces and HSA the lowest.

6.6. Immunocytochemistry

Cells were stained to show cytoskeletal and FA organisation in order to determine whether the different surfaces investigated within this study had an effect on spreading cells and if these changes had an influence on the overall morphology of the cell. These results could then be compared to the spreading dynamics of the attaching cells from 15 to 90 min by measuring the contact radii and morphologically compared to three dimensional reconstructions of live cells and SEM images of fixed cells at corresponding time points.

Cells on each surface fixed at 25, 60, 90 and 180 min time points from seeding were stained for vinculin, β-tubulin and F-actin. Five fields (CLSM 63X oil objective) from each of two samples were examined at each time point for each surface. The fixed cells exhibited morphologies on each surface comparable to cells imaged live at the corresponding time points. The contact radius of these cells also increased with a similar rate to the cells imaged live over the period of 15 to 90 min after attachment, see figure 6.5.

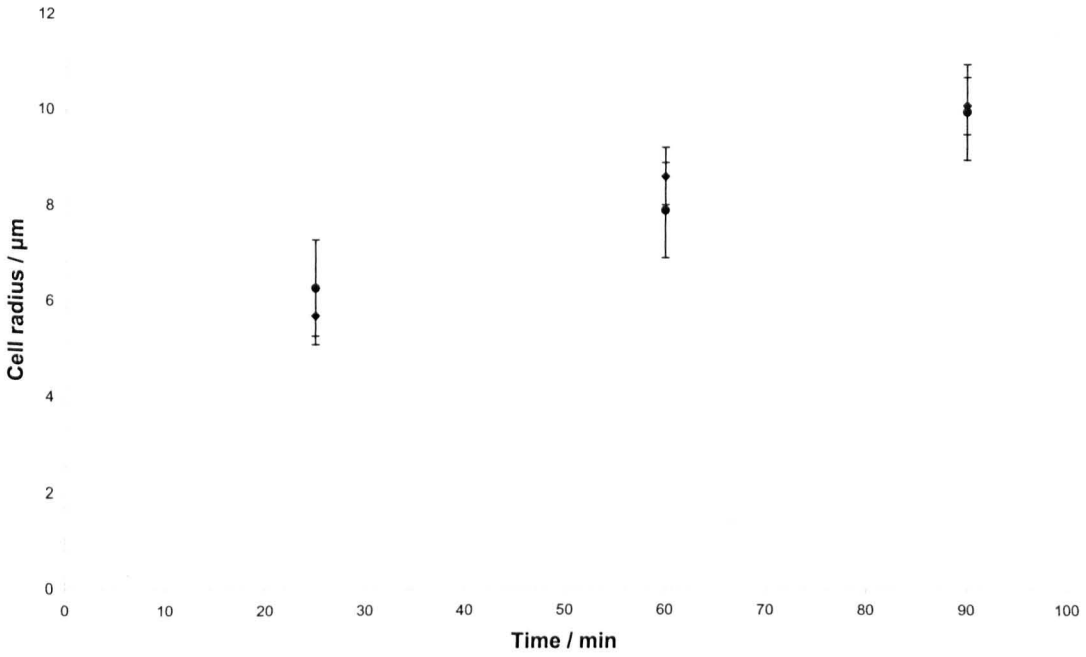

Figure 6.5. Average cell contact radius for live cells on all surfaces (circle) and cells fixed and stained for F-actin on all surfaces (squares). Plotted values are mean ± standard error of the mean where n = ≥ 5.

The cells fixed at 25 min after attachment had largely spherical contact areas. These cells show very little evidence of cytoskeleton organisation, with the same level of fluorescence throughout the cell showing that actin was diffusely distributed. This indicates that the cell is still spreading in the passive stage over the surface, with no input from its motile machinery [25, 26] as the mechanisms are not in place for it to start applying forces to protrude the membrane. The cells also demonstrated a diffuse distribution of vinculin around their periphery which would be an indicator of areas where the formation of adhesion plaques will initiate so that the cell can start to become bonded to the substrate [192].

The cells fixed at 60 min after attachment show different degrees of cytoskeletal organisation across the surfaces. Cells attaching to TiO and TiN have a greater degree of cytoskeletal organisation to those attaching on glass. Cells attaching to

these surfaces have evidence of cortical actin filament formation with some radial filaments suggesting cells predominantly were progressing to an actin type II structure [159], categorised as described in section 4.5.7.1. Microtubules are also more clearly visible on cells on both coated surfaces whereas the cells attaching to glass remain largely unchanged from those fixed at 25 minutes. The cells attaching to TiN also have filopodial extensions at this stage. This would suggest that the proteins adsorbed onto the glass surface are not as conducive to cell attachment as those on the TiN and TiO surface. This could be due to the conformation adopted by the proteins on the surface or the composition of the ad-layer which differs due to competitive binding influenced by surface chemistry.

The protein pre-coated surfaces also differ from each other. Those attaching to Fn had a greater degree of cytoskeletal organisation with more vinculin located around the periphery shown by a higher intensity there. The cells attaching on HSA are similar to those on the glass remaining largely unaltered from 25 minutes.

Most of the cells in each population still primarily exhibit rounded morphologies with some cells displaying filopodial extensions (for example see figure 5.4.2. (k)). This shows that there has not yet been sufficient time for the cell to noticeably alter its morphology and agrees with work by Xiong *et al.* and McClary *et al.* [200, 214]. Although there was no significant difference between the contact radius of the cells attaching to each surface, the cells are clearly more advanced in the stages of attachment on some surfaces rather than others.

All cells visualised at 90 minutes showed some degree of cytoskeletal organisation and localisation of vinculin. This shows that although spreading rates are still comparable at this stage, the cells are beginning to react differently

to the surfaces. This indicates that although the thin film coatings have only a thickness of 10 nm, this is a sufficient thickness to elicit the different responses seen with the bulk materials [119].

Cells attaching to TiO and TiN showed the most clear microtubule formation (see figure 5.4.3. (g.)), where fibres can be seen to run from perinuclear regions to the cell periphery. One of the main effects of microtubules on morphology has been shown to be their antagonism with actomyosin in contractility [63] which can be the result of several issues: the mechanical properties of microtubules, which are stiff struts in compression that resist actomyosin contraction [215]; the role of microtubules as paths whereby kinesins deliver regulators of actomyosin dynamics to the cell edges [216]; and the interaction of microtubules to deplete molecular activators of actomyosin contractility [217]. It is also theorised that microtubules interrelate with cell shape in other ways as well. Microtubule plus ends could be drawn to the cell's leading edge by dynein motors which are localised there, so orienting the microtubule-organising centre and Golgi apparatus toward the leading edge [218]. Microtubules also mediate delivery of Golgi-derived vesicles to the leading edge, providing membrane and associated proteins needed for forward protrusion [219].

The increased organisation of F-actin on TiN and TiO could be due to the presence of OH groups on the surface, shown by XPS in sections 5.3.2. and 5.6.3. respectively, which have been attributed in other studies to influence initial attachment [122, 220]. As mentioned in section 2.4, studies by Keselowsky *et al.* [221] demonstrated that the binding of $\alpha_5\beta_1$ integrin bound with the highest binding affinity to OH terminated self assembled monolayers and that vinculin

localised to large (>3 μm) oriented complexes on NH_2 and COOH chemistries while only forming high numbers of smaller clusters on the OH groups and only poorly defined structures on CH_3 surfaces.

The cells on TiO and TiN surfaces had needle like filopodial extensions which may be due to the cells extending out to attach to OH groups which may be spaced over the surface in TiO and TiN rather than the uniform coating of Fn. The cells still predominantly exhibit a rounded morphology, with a few cells starting to spread asymmetrically and polarise.

Numerous studies suggest that a higher adhesion rate will occur on fibronectin- as opposed to HSA-coated substrates. This is mainly due to a specific binding between fibronectin receptors on osteoblasts and their extracellular ligands [166]. Fn adsorption in competition with HSA is significant to cell recognition of the substrate and ability to produce ECM components. Therefore, the substrate needs to provide sufficient amounts of serum-derived adsorbed adhesion factors to facilitate initial cell adhesion; this subsequently leads the cell to deposit its own ECM. To facilitate cellular ECM deposition, adsorbed serum proteins are believed to have to be adhered loosely to allow for displacement by cell-derived Fn which also need to maintain a favourable presentation of binding sites to cells [22, 205]. Loss of Fn's secondary structure has been correlated with the elimination of integrin-mediated cell responses such as actin stress fibre formation in fibroblasts [205, 222]. There is evidence that coadsorbing Fn with HSA at some Fn-to-HSA ratios 'rescues' these cell responses, on surfaces where Fn will adopt an appropriate conformation for binding, suggesting that some degree of molecular packing prevents loss of integrin-binding activity [134, 214, 222, 223].

HOS cells at 3 h after seeding show a range of different morphologies on the surfaces and a greater degree of cytoskeletal organisation. This would appear to be in agreement with work by Scotchford and colleagues imaged cells attaching to self assembled monolayers with different terminal groups showing that after 1.5 h cells exhibited notably different degrees of cytoskeletal organisation, along with some polarised cells, but it was not until 3 h time points that primary human osteoblasts had markedly different overall morphologies on the different surfaces. Sausa *et al.* [206] who imaged mouse osteoblastic MC3T3-E1 cells on HSA and fibronectin coated substrates 4 h after seeding observed a clear difference between the rounded morphology of cells attaching to HSA as opposed to a range of morphologies from rounded to polygonal on Fn.

Yang *et al.* [202] noted that attachment was by filopodial extension, with long spindle like structures extending from the cell body being visible on SEM micrographs at 3 h after attachment. To varying degrees, cells stained for F-actin on all surfaces had filopodial extensions at 90 min, some (figure 5.4.4. (k.)) extending in the order of around 20 μm. These fine features, most less than 0.5 μm wide, were not observed on cells imaged live using LavaCell. These features were not able to be visualised as laser intensity levels had to be kept to a minimum to prevent photobleaching of the stain and photodynamic damage to the cells [224] during the 75 min period. Although this compromise means that these features of spreading cells are not able to be incorporated into three dimensional representations of the cell's morphology, the shape of the cell body and wide lamellipodia can be visualised over this period. This means that for the first modelling stage, which is shown to be reliant on contact line and contact radius dynamics (section 3.1.), the omission of these features does not substantially alter the results gained.

6.7.1. Three dimensional reconstructions of cell morphology on surfaces with different chemistries.

The technique of using computer reconstructed three dimensional representations of cells is underused. There are very few published studies whereby such techniques have been employed. Those using reconstructions, however, note the usefulness of the technique in gaining data on cell morphology.

Three dimensional representations of live HOS cells adherent at 3 hours look visually similar to cells at this time point fixed for both SEM and stained for viewing using CLSM. The cells still had a distinct cell body, but lamellipodia had started to advance out over the surface. Uggeri *et al.* [190] also produced three dimensional reconstructions of live osteoblast cells on different surfaces. They found that cells exhibited both rounded cell body and polygonal morphologies at 6 h after attachment. Their method of three dimensional reconstruction was used purely as a qualitative visual technique and thus was unable to quantify cell parameters as in this study. Images were only taken of the cells at two time points, 6 and 24 hours, rather than imaging cells every 5 min for 75 min. This study shows that the image analysis can be used to quantify the morphology of attaching cells, giving a range of measurements, over an extended time period, rather than at set intervals.

Uggeri and colleagues were also able to study the effect of topography of titanium disks, whereas this study has been limited to the use of 10 nm transparent coatings. They overcame this by inverting the samples once seeded cells had attached to the surface and placing them on glass bar spacers within a flow chamber [191]. This technique would not be suitable for this study as weakly

adherent cells could easily be sheared from the surface when transferring and inverting the samples.

Wieland *et al.* [227] also produced a method of reconstructing cells from optical sections. Again, these images were taken at individual time points rather than over extended time periods. They report that they are able to gain data on cell volume and thickness from their reconstructions, but do not mention any other parameters. They draw attention to the usefulness of being able to manipulate the cell in order to be able to observe the whole morphology of the cell.

6.7.2. Reconstructed morphological analysis compared to SEM

SEM, used alongside other techniques is one of the standard approaches in studying cell morphology [4, 192]. The three dimensional representations were compared at time points to show initial attachment and spreading. Visually, the three dimensional reconstructions of the confocal slices look similar to HOS cells on glass and the coated surfaces at corresponding time points. The reconstructions have captured the lamellipodial extensions seen in the SEM micrographs, but have been unable to reproduce the detail of microspikes. The reconstructions have the advantage that the cells are live during the image acquisition and, as previously mentioned, data can be easily gained from them.

The confocal imaging also negates the numerous problems that can be associated with the preparation stages in fixing the cells for SEM viewing. The dehydration stage must be carried out slowly and carefully to avoid shrinkage of the cell, often rupturing fine processes such as filopodial and even the lamellipodia. If the osmolarity of the buffer, and other components, within the fixative is not equalized to the cell growth medium, then the change in osmotic pressure will

lead to osmotically induced artefacts. Changes in pH and temperature of the cultures prior to and during fixation also result in changes in the appearance of many cellular structures such as microspikes and ruffles. Weakly attached cells may be washed from the surface during preparation and cell layers may also delaminate from the surface material [196]. The three dimensional reconstructions are also easier to manipulate to gain data on the cell, such as contact angles and contact radius as well as negating the need for the long and careful preparation steps required for SEM imaging.

In spite of these drawbacks, SEM imaging is still a useful insight into the morphology of adherent cells and is widely used as a comparative tool. It was therefore chosen as one means of comparing the three dimensional representations of cells produced by the image processing algorithm.

6.8. Image processing of cells attaching on different surface chemistries.

Cells were seeded onto PVD TiN and TiO surfaces so that the effect of surface chemistry could be investigated without changing topography and HSA and Fn pre-coated glass to assess the effect of protein pre-coating on the attachment and spreading of HOS cells.

The image processing analysis on cells seeded on the thin film and protein pre-coated surfaces showed that the rate of spreading was consistent with the cells seeded on borosilicate glass. The image analysis shows that the cells were of a similar height during the early time points and reached a height comparable with those on the glass at the later time points. The contact radius and angle also behaved in an analogous manner to the borosilicate glass with no significant differences between any of the populations on the surfaces.

The results indicate that the cells spread on the different substrates at the same rate. There are contradictory reports in the literature as to whether cell spreading is initially dependent or independent of the surface chemistry of the substrate, and whether spreading is regulated by either the diffusion of integrin toward focal adhesions [194, 195, 196], by actin polymerization [197, 198, 199] or is limited by its mesoscopic structure [24, 25, 26, 200, 201]. The points will be discussed further in this section in relation to results gained from immunocytological and live attachment studies.

It would appear from the image processing analysis that the cells on all substrates are in the early stage of spreading, as the cells have maintained a roughly circular contact shape on the surface and have spread at similar rates which is in agreement with figure 6.7. The rounded contact shape of most of the cells after 90 min are consistent with studies of morphology on a number of different surfaces. Yang *et al.* [202] found that morphology was still rounded at this time point using osteoblast precursor cells on Fn and HSA treated titanium surfaces. Ko and colleagues [203] found osteoblasts fixed and imaged using SEM were still rounded after 6 h on titanium substrates, as did Puleo [167] who imaged osteoblasts on borosilicate glass, titanium and hydroxyapatite after 6 h.

The analysis of the cells show that they are following a spreading regime consistent with Frisch and Thoumine's [144] experimental and modelling work for cells on adhesive surfaces. Although they used chick embryo fibroblasts spreading on glutaraldehyde-coated glass microplates, the authors state that their spreading model should be applicable to other cell types and surfaces. Comparison of the data gained in this study to that of Frisch and Thoumine's shows that the rate of change and scale of the contact radius is the same for the period from 20 to 90 min (figure 6.6). As the image acquisition didn't begin

before 15 minutes after seeding, the analysis appears to indicate that the initial exponential cell spreading phase seen by Frisch has already occurred by this point. As seen here, they also note the validity of treating the spreading cell geometry as a spherical cap and by using phase contrast microscopy were able to show that cells maintained a hemispherical morphology on the surface up to 3 h, beginning to polarise by 6 h.

Although they have no experimental data to show cells spreading on different surfaces, Frisch and Thoumine predict that initial spreading will be dependent on surface chemistry and propose different rate curves dependent on surface adhesiveness. Whilst both the TiO [173] and TiN [130, 133] coatings along with Fn pre-conditioning [204, 205] could be described as adhesive in this study, and so would be expected to be comparable with Frisch and Thoumine's theory, the HSA pre-coated surface is not [192, 206]. The results gained show that there was no significant difference between the rate of spreading on the HSA protein pre-coating and any other surface examined. This result may indicate that the mesoscopic structure is, in fact, more dominant in determining the rate of cell spreading than surface chemistry, as suggested by Cuvelier *et al.* [26]. The HSA surface could also have been made more 'adhesive' by the DMEM supplemented with FBS that the cells were seeded in. It has been shown that coadsorbing Fn with HSA at some Fn-to-HSA ratios 'rescues' the cell response [206] which may have occurred in this study with the Fn being one of the proteins present in the serum.

Immunocytochemistry showed that there were differences in the HOS cell reactions to the PVD and protein pre-coated surfaces, which is described in section 6.6. However, the different degrees of cytoskeletal organisation have not translated to an overall change in spreading dynamics by 90 min.

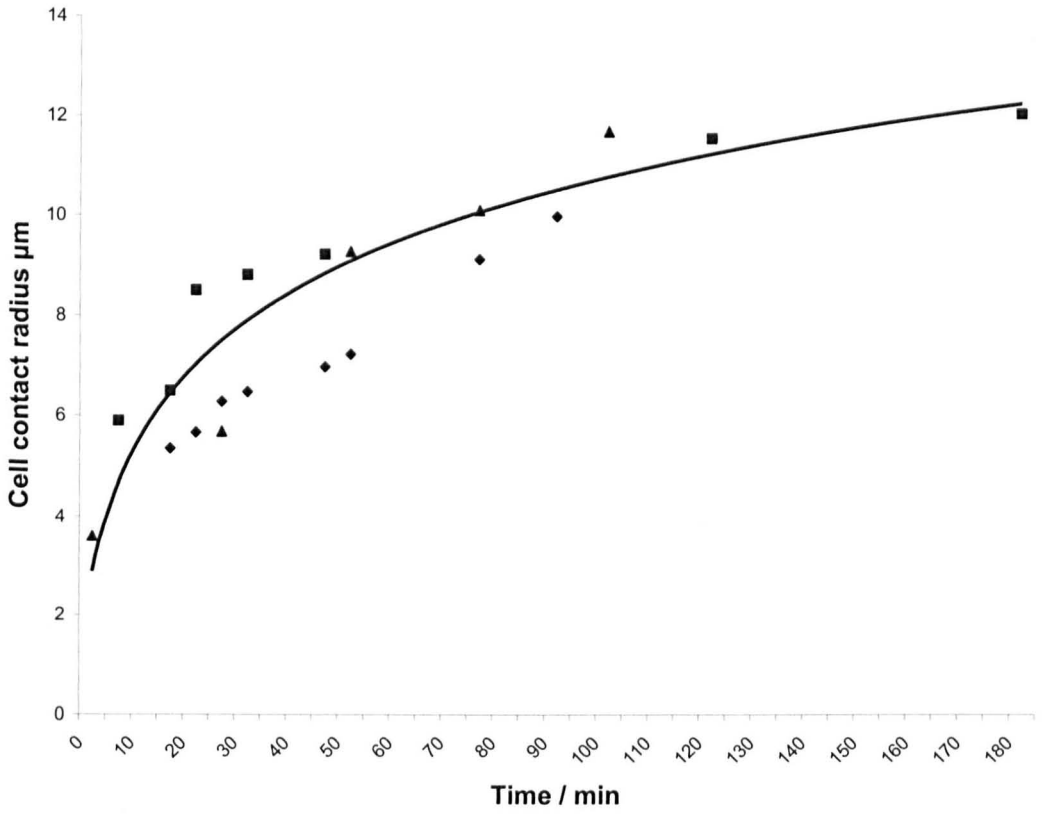

Figure. 6.6. Data from the current study (diamonds) compared with Frisch and Thoumine's theoretical spreading curve [138] and experimental data of fibroblasts plated on glass cover slips treated with saline and glutaraldehyde (squares) and against experimental data of cells spreading taken from Cavalcanti-Adam *et al.* [207] (triangles).

The change in contact angle is also consistent with the theory put forward by Hocking and Rivers [140] on the spreading of a viscous drop. Whilst this also prescribes an initial exponential phase that the experimental data does not show, suggesting again that the image acquisition began after this time, the data follows the steady state trend after this period.

As mentioned in section 6.3, the cells appear to be in the initial phase of attachment, between contact and spreading, shown schematically in figure 6.9. The results gained show that an overview of overall cell morphology can be used to describe the early spreading of cells on a substrate. This suggests that macroscopic analysis of the membrane shape on attachment is a good indicator

of the rate of spreading and that the spherical cap modelling can be carried out to a period of 90 minutes. These data show that the modelling theory of Dembo *et al.* [150], whereby a macroscopic view of the cytoplasm and the cell's mechanical structure is used, is adequate in describing the spreading kinetics of cells at early time points.

The absence of any significant difference in cell spreading can be explained by comparing the results with experimental data and theory by Cuvelier *et al.* [26]. They suggest, based on results in figure 6.7., that the rate of initial spreading is independent of cell type, substrate and adhesion receptors, but that different surfaces may exhibit varying lag times where the cytoskeleton reorganises itself before the cell begins to spread in the 'active phase' seen in figure 2.2. No lag times were discernable in this study up to 90 min suggesting that they may occur in the period after the image acquisition ended as the cell begins to polarise.

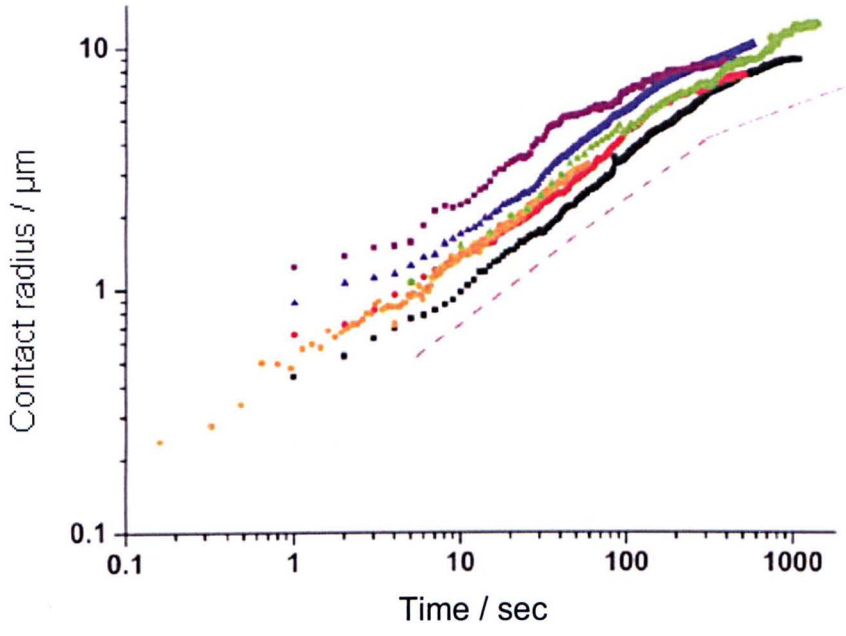

Figure 6.7. Cuvelier *et al.* demonstrated that cells spread at the same rate independent of type and substrate. The different curves are representative of a variety of experimental conditions corresponding to: (black square) HeLa cell/fibronectin (1 µg/ml) substrate; (green triangle) E-cadherin S180 cell/E-cadherin substrate; (red circle) Cdc42DN S180 cell/fibronectin substrate; (purple square) nocodazol-treated HeLa cell/fibronectin substrate; (blue triangle) HeLa cell/polylysine substrate; and (orange circle) biotinylated red blood cell/streptavidin substrate. (From: [26]).

Cuvelier states that initial spreading is independent of the diffusion of adhesion receptors toward the growing focal adhesions or by actin polymerisation, shown in figure 6.7. They explain this theory, along the lines of Frisch [144] and Dembo [150], by likening the cell to a viscous adhesive cortical shell which encloses a less viscous interior. So although spreading is driven by biomolecular interactions, the cell is dynamically limited by its mesoscopic structure and material properties at early time points (see figure 6.8.). The lack of cytoskeletal organisation at this stage of spreading seen experimentally, described in section 6.6, would suggest that at this stage, the spreading behaviour of cells are solely dependent on the factors mentioned above.

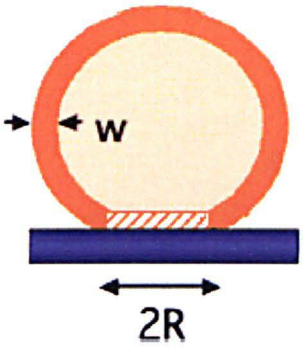

Figure 6.8. Schematic Representation of the Cell as a viscous shell enclosing a liquid for intact cells. (From: [26]). *W* gives the width of the viscous shell and *R* is the contact radius.

Work by Liu *et al*. [18] also suggest that spreading kinetics are independent of the substrate. They argue that significant cell adhesion events, such as contact, attachment, spreading and proliferation are similar on all surfaces independent of surface chemistry/energy. They propose that the only difference is the time periods in which each occur after a constant initial rate of spreading as the cells work to significantly remodel the cell-substratum interface. They found that low attachment efficiency and long induction periods before cells engaged in an exponential growth phase were observable on hydrophobic surfaces. They conclude that similar bioadhesive outcomes can ultimately be achieved on all surface types with varying hydrophilicity, but the time required to arrive at this outcome increases with decreasing cell-substratum-compatibility.

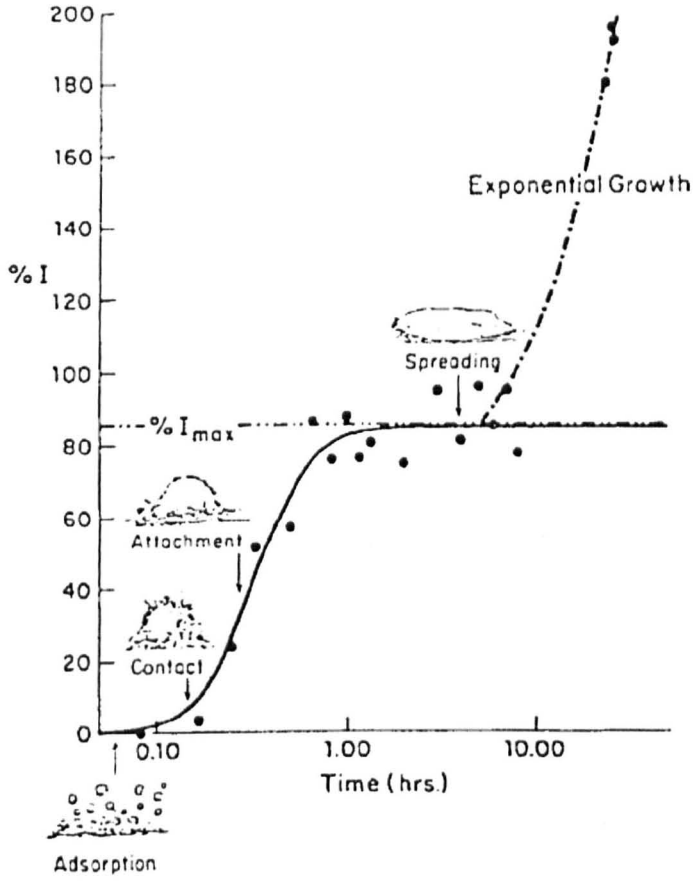

Fig. 6.9. Schematic illustration of cell adhesion and proliferation kinetics showing quantitative parameters that can be gained from the measurement of the number of adherent cells (expressed as percentage of viable cell inoculum; %I) with time. Taken from [19].

The processes of cell adhesion can be separated into four distinct steps: protein adsorption, cell–substratum contact, cell–substratum attachment, and cell adhesion/spreading, for which there are no set time periods as they can vary greatly between surfaces and cell types [18].

Protein adsorption onto a surface to form a conditioning layer is a complex process, involving molecular scale interactions with a surface that occur instantaneously comparative to the overall time required for cell adhesion [20, 21]. This protein layer will vary for each of the surfaces used in these

experiments, as their individual properties will be conducive for binding of some proteins and not others and also influence the conformation that the bound proteins adopt [119]. Whilst this was not studied here, it is important to bear in mind that the cell interactions observed are not solely due to the surface properties of the materials alone as shown by the protein coated glass.

Protein adsorption from plasma *in vivo* and serum *in vitro* occurs rapidly on a material surface forming the layer that the cells encounter as they settle on the surface. Cell contact and attachment involve the sedimentation of the cell to approximately 50 nm of a surface, at which point physical and biochemical forces begin to close the gap between the cell and surface. Initial cell contact with the substratum occurs by spreading as a viscous droplet, which is independent of the surface or cell type [24].

This stage is followed by the extension of filopodia that penetrates an electrostatic barrier between cell and the substrate surface. The filopodia act to orient the cells on the surface and begin the process of ECM secretion whereby the cell may significantly remodel the cell-substratum interface, becoming a significant factor in the cell response to a surface after 2 h [208]. It has been reported that for cells that secrete and assemble an extracellular matrix, surface properties such as chemical composition, wettability and topography may affect the ability of the cell to deposit its ECM by stabilising the protein deposits or by affecting the orientation of cell-binding domains in the deposits [22, 23]. It is reported that the time required to complete these contact and attachment steps in a stagnant culture-dish is usually in the order of around 30 min for typical soft-tissue cells [209], but this is dependent on numerous factors such as cell type, the substrate surface, and suspending fluid-phase composition [210]. As discussed in section 6.6, visualisation of filopodia was beyond the scope of this

investigation due to compromises with the CLSM setup to avoid photobleaching or photodynamic damage to the cells. Immunocytochemistry, results presented in section 5.4 and discussed in section 6.6, showed that some cells had filopodial extensions by the 30 min period, but that these did not influence the overall morphology of the cell.

Other studies produced results which indicate that significant differences in spreading on different surfaces occur after the initial constant rate, with a lag time which arises as the cell reorganises itself on the surface, with the diffusion of adhesion receptors to where the cell is in close proximity to the surface. For the membrane to adhere, integrins must be recruited from adjacent regions to join an adhesion patch, FA, with a density adequate for adhesion. Since the density in an FA is much greater than the mean density of mobile binders present on the surfaces of cells, they must, therefore, arrive at the FAs via diffusion from the parts of the cell wall which are not in close proximity to the substrate. This process of recruitment also expands the size of the patch, so the FA grows in size. The adhesion process can therefore be viewed as a first-order wetting process [211, 212] that involves nucleation and growth of areas with large binder density. The expansion of a circular adhesion zone is driven by a chemical potential gradient, which acts as the mechanism of binder recruitment and is dependent on the underlying substrate [194, 195, 196].

Reinhart-King [213] suggests that cell isotropy is dependent on surface ligand densities, spreading isotropically on surfaces with high ligand densities. The HOS cells exhibited a rounded morphology throughout the image acquisition period in this study as full growth media supplemented with serum was used. At low ligand densities, they propose that cells tend to spread anisotropically by extending pseudopodia randomly distributed along the cell membrane.

Dubin-Thaler [201] produced results which confirm that serum concentration affects spreading initiation and that increased surface matrix density resulted in faster initiation of the active spreading phase using mouse embryonic fibroblasts.

The viscous droplet model can now be developed further into a model which predicts lamellipodial extension by looking at the contact line around the base of the cell. The mathematical model is based on the two-phase poroviscous flow equations described in section 3, whereby the two-phase mixture consists of a viscous 'network' phase and an inviscid 'solution' phase. The key model parameters characterizing the cell / surface interaction are the slip coefficient and the static microscopic contact angle, both of which are taken to be constant which have been demonstrated by the constant spreading results gained in this study.

By looking at cell thickness, the network volume fraction and the location of the contact-line in the period of spreading immediately after the period studied here, it is hoped that predictions on protrusion and locomotion can be made.

Mathematical formulations detailed in [7] show the functional dependence of the contact-line velocity on the local network density provides a mechanism for the generation of asymmetry, and thus a potential mechanism for cell polarisation. Numerical simulations have been run in which the initial network density is a small random perturbation to the equilibrium density at the contact line. The results suggest that a symmetric mode is initially the most unstable one, leading to the formation of a high-density region at the centre of the cell. As the cell spreads this 'contraction' weakens until the most unstable mode becomes an asymmetric one. This results in a rapid redistribution of network into an

asymmetric configuration, leading to locomotion in the direction of increasing network density via the contact-line law.

This work has enabled the contact angles of live cells as they adhere and spread to be measured for the first time. From the novel method to produce three dimensional representations, further data on cell height and contact radius can also be measured, giving real time data on a number of parameters which can be incorporated into mathematical models which predict the spreading of cells. The study has shown that during initial attachment and spreading, to a period of 90 minutes after seeding, cells on adhesive surfaces exhibit the same spreading behaviour irrespective of surface chemistry. This has previously been shown to be the case over the first 10 to 15 minutes after attachment, but no other studies have yet had the means to measure this beyond that period.

6.9. Summary

This study has enabled a novel method of measuring the dynamic contact line, along with other morphological aspects, of attaching cells to be measured.

A means of imaging live HOS cells every 5 minutes for 75 minute periods using CLSM was developed. This allowed sufficient detail of the cell to be gained for subsequent image processing work, whilst maintaining the cells in a healthy state and without causing any detrimental effects to them via photodynamic damage.

In order to process these data to meet our objectives, a custom built algorithm was written using Matlab. This enabled the CLSM optical z sections to be rebuilt to create accurate three dimensional representations of cells. From these representations, the dynamic contact line of the cell, contact area and radius along with cell height could be measured.

SEM was used as a tool to visually compare the morphology of the three dimensional representations of cells from live studies, to those fixed at corresponding time points. These showed a good visual correlation between the two imaging methods and gave comparable cell dimensions.

In order to test the effects of surface chemistry on early attachment and spreading, thin film coatings along with Fn and HSA protein pre-conditioned glass surfaces were studied. XRD, XPS, profilometry and ellipsometry showed that 10 nm films of TiN and TiO were produced without altering the topography of the glass substrate. XRD analysis of thicker films confirmed that, in agreement with the literature, as thickness decreased, these coatings became nanocrystalline.

Immunocytochemistry showed that HOS cells reacted differently to the thin film and protein pre-coated surfaces. Over the time points studied, observable differences in the cytoskeletal organisation were noted on the different surface chemistries.

Image analysis of live cells showed that HOS cells spread at the same rate on the surfaces studied, indicating that the initial stages of spreading are independent of surface chemistry. The contact radii and cell height were comparable to those of fixed and immuno-stained cells on the surfaces at corresponding time points, showing that despite differences in cytoskeletal organisation, these changes had not yet exhibited noticeable effects on the morphology of the cell.

7. Conclusions

This study has demonstrated a means of quantifying several aspects of cell morphology as cells adhere and spread on different surfaces.

An imaging technique has been produced whereby cells are captured in adequate detail for key parameters to be measured over extended time periods. Gaining data on the dynamic contact line as cells spread has enabled the development and validation of a mathematical model to make predictions on spreading cells.

A suitable combination of staining and imaging techniques were developed to image cells in sufficient resolution at the cell membrane – substrate interface which has enabled the contact line of spreading cells to be measured, whilst maintaining the cells in a viable state, without causing any detrimental effects via photodynamic damage.

The data generated was suitable to be processed by Matlab which enabled the development an algorithm that could detect the edge of cells in optical sections and produce accurate three dimensional representations of cell morphology.

The algorithm is sensitive to changes in cell adhesion and spreading behaviour due to (i) substrate variation and (ii) protein conditioning layer variation, replicating the complex morphologies displayed by spread cells.

This methodology has provided the means for the model to be enhanced to describe the polarisation of cells at later time points and the motility of cells across a substrate. The algorithm and model can also be adapted to incorporate sub-cellular elements if experimental data for this were gained.

8. Future Work

In order to build on the work presented here there have been several areas identified with scope for further investigation.

Continuing live cell studies after the period of 90 min as they transit from passive to active spreading and start exhibiting different morphologies would build on the data gained for early attachment and spreading behaviour. This would give data on when the effects of surface chemistry elicit measurable effects on cell morphology and spreading kinetics. Measuring the contact line of cells beginning to polarise will enable the mathematical model to be developed and tested for later stage spreading and crawling. Ideally, this would be carried out using imaging techniques which would enable continuous imaging of cells from initial attachment for periods longer than 90 minutes. This may be achieved using 2-photon microscopy which subjects the cells to significantly lower levels of laser radiation than CLSM.

Gaining data for crawling cells will also aid the development of modelling for this aspect of cells. Cell migration is essential to many biological phenomena, from morphogenesis in embryonic development to wound healing, the immune response, biofilm encrustation and metastasis [12]. This is also of high relevance to the biomaterials field as cells must crawl and migrate to colonise a scaffold in tissue engineering or the surface of orthopaedic implants and fixation devices after surgery [11].

Imaging and modelling the effect of topography on cells as they adhered, spread and started to migrate over substrates would also be a useful area for development. As detailed in section 2.4., the topography of a surface can have a

dominant influence on the cell response to a surface. With numerous biomaterial devices employing topography to elicit desired responses, from spray coatings on cementless femoral stem prostheses to ridged surfaces used as nerve guides in tissue engineering, furthering our understanding in this area will clearly benefit future designs. Modelling in this area may also shed light on whether surface chemistry or topography is the dominant factor in the cell response to a surface.

The mathematical model can also be augmented to include sub-cellular elements. By using techniques such as fluorescent speckle microscopy (FSM), actin turnover may be visualised and incorporated. The inclusion of these would build a more complex model which is able to provide a good indication of the cell – material interactions occurring.

Appendix

Below is the matlab code to relate angles of P and A determined using ellipsometry to calculate thickness [158].

```
clear all
close all

n = 1:0.01:2; %refractive indexd range
h = 00:10:1000; % thickness range

t = [30 40 49.7 60 70]*(pi/180); %Angle of incidence = (180-angle)/2
aexp = [48.0840 47.5180 46.752 45.9122 45.207];
pexp = [53.5301 59.6860 68.336 80.771 96.751];


[N H T] = meshgrid(n,h*10,t);

[b c Aexp] = meshgrid(n,h,aexp);
clear b c
[b c Pexp] = meshgrid(n,h,pexp);
clear b c

n3=1.517;           %borosilicate glass
n2=N;               %TiN coating
n1=1.00;            %air
L=6328';

fprintf('*** Please wait for the calculation to finish ***')

%calculate the fresnel reflection coefficients for the s and p
%components of the light
sqrt_n2=sqrt(n2.^2-n1.^2.*sin(T).^2)./n2;
sqrt_n3=sqrt(n3.^2-n1.^2.*sin(T).^2)./n3;
r1p=(n2.*cos(T)-n1.*sqrt_n2)./(n2.*cos(T)+n1.*sqrt_n2);
r1s=(n1.*cos(T)-n2.*sqrt_n2)./(n1.*cos(T)+n2.*sqrt_n2);
r2p=(n3.*sqrt_n2-n2.*sqrt_n3)./(n3.*sqrt_n2+n2.*sqrt_n3);
r2s=(n2.*sqrt_n2-n3.*sqrt_n3)./(n2.*sqrt_n2+n3.*sqrt_n3);

% Obtain calculated value for Rho

ct=exp(-4.*pi.*H.*i.*sqrt(n2.^2-n1.^2.*sin(T).^2)./L);  %a common
term in the expression for rho_calc
Rho_calc=((r1p+r2p.*ct)./(1+r1p.*r2p.*ct)).*((1+r1s.*r2s.*ct)./(r1s+r
2s.*ct));

Rho_exp = tan(Aexp).*exp(i*(((3*pi)/2)-(2.*Pexp)));

clear Rpox Rsox ros ct1

dRho = (Rho_calc-Rho_exp);
dRho2 = dRho.*conj(dRho);
```

```
reg = sum(dRho2,3);

k = min(reg(:));

[I J] = find(reg==k);
n_best = n(J)
h_best = h(I)
```

References

1 Folkman J. & A Moscona. Role of cell shape in growth control. Nature Vol. 273. June 1978 P345-349

2 Rahul G. Thakar, Qian Cheng, Shyam Patel, Julia Chu, Mansoor Nasir, Dorian Liepmann, Kyriakos Komvopoulos, and Song Li Cell-Shape Regulation of Smooth Muscle Cell Proliferation Biophysical Journal Volume 96 April 2009 3423–3432

3 Ben-Ze'ev A. The role of changes in cell shape and contacts in the regulation of cytoskeleton expression during differentiation. J Cell Sci Suppl 1987;8:293–312.

4 Watt F M, P W Jordan, and C H O'Neill Cell shape controls terminal differentiation of human epidermal keratinocytes. Proc Natl Acad Sci U S A. 1988 August; 85(15): 5576–5580.

5 Ben-Ze'ev A. Animal cell shape changes and gene expression. BioEssays 1991;13:207–212.

6 Ratner. BIOMATERIALS SCIENCE, 2nd Edition. Elsevier Academic Press 2004.

7 Oliver JM, King JR, McKinlay KJ, Brown PD, Grant DM, Scotchford CA, Wood JV. Thin-film theories for two-phase reactive flow models of active cell motion. Mathematical Medicine and Biology (2005) 22, 53–98

8 King, J.R. and Oliver, J.M., 2005, "Thin-film modelling of poroviscous free surface flows," Euro. J. Appl. Math. 15 519-553.

9 Herant, M., Marganski, W.A. and Dembo, M., 2003, "The mechanics of neutrophils: synthetic modelling of three experiments," Biophys. J. 84 3389-3413.

10 Mogilner A. and G Oster Cell motility driven by actin polymerization. Biophys J. 1996 December; 71(6): 3030–3045

11 Brown, S. & Lemons, J. (EDS) (1996) Medical Applications of Titanium and its Alloys: the Material and Biological Issues. West Conshohocken, NJ: American Society for Testing and Materials.

12 Bray, D. (2001) Cell Movements: From Molecules to Motility. New York: Garland.

13 Chicurel, M.: Cell biology: cell migration research is on the move. Science 295, 606–609 (2002)

14 Williams, D.F. (1987) Definitions in Biomaterials. Proceedings of a Consensus Conference of the European Society For Biomaterials, Chester, England, March 3-5, 1986, Vol. 4, Elsevier, New York.

15 Oliver, J.M., King, J.R., Engel, C., Scotchford, C.A. and Grant D.M., 2006. An experimental and theoretical investigation of a symmetry breaking mechanism for cell polarization. In: Proc. ASME Summer Bioengineering Conference, Florida, USA.

16 The NJR Centre, Hemel Hempstead. National Joint Registry for England and Wales 5th Annual Report. M&M Communications Ltd ISSN1753-9374 (2007)

17 Sim B. Interactions of serum proteins with osteoblasts; role in biomaterial adhesion. In M3. (2002)

18 Liu X, J.Y. Lim, H.J. Donahue, R. Dhurjati, A.M. Mastro, E.A. Vogler. Influence of substratum surface chemistry/energy and topography on the human fetal osteoblastic cell line hFOB 1.19: Phenotypic and genotypic responses observed in vitro. Biomaterials 28 (2007) 4535.

19 Vogler A. and Bussian R. W. Short-term cell-attachment rates: A surface-sensitive test of cell-substrate compatibility. Journal of Biomedical Materials Research Volume 21, Issue 10, pages 1197–1211, October 1987

20 Andrade JD. Principles of protein adsorption. In: Andrade JD, editor. Surf Interf Aspects Biomed Polym: Protein Adsorption. New York: Plenum Press; 1985. p. 1–80.

21 Ramsden JJ. Puzzles and paradoxes in protein adsorption. Chem Soc Rev 1995;24:73–8.

22 Tidwell CD, Ertel SI, Ratner BD, Tarasevich BJ, Atre S, Allara DL. Endothelial cell growth and protein adsorption on terminally functionalized, self-assembled monolayers of alkanethiolates on gold. Langmuir 1997;13:3404–3413.

23 Vitte J, Benoliel AM, Pierres A, Bongrand P. Is there a predictable relationship between surface physical-chemical properties and cell behaviour at the interface? Eur Cell Mater 2004;7:52–63.

24 McGrath J.L.. Cell Spreading: The Power to Simplify. Current Biology, Volume 17, Issue 10, 15 May 2007, Pages R357-R358

25 Sackmann E. and R. Bruinsma. Cell adhesion as wetting transition CHEMPHYSCHEM 2002, 3, 262 - 269

26 Cuvelier D, Théry, YChu, Dufour, Thiéry, Bornens, Nassoy, L. Mahadevan. The Universal Dynamics of Cell Spreading Current Biology, Volume 17, Issue 8, 17 April 2007, Pages 694-699

27 Bereiter-Hahn J. Mechanics of crawling cells. Medical Engineering & Physics, Volume 27, Issue 9, November 2005, Pages 743-753

28 Small J.V., Stradal, Vignal, Rottner. The lamellipodium: where motility begins. Trends in Cell Biology, Volume 12, Issue 3, 1 March 2002, Pages 112-120

29 Ridley A.J., Rho family proteins: coordinating cell responses. Trends in Cell Biology, Volume 11, Issue 12, 1 December 2001, Pages 471-477

30 Nobes C.D., Hall. Rho, Rac, and Cdc42 GTPases Regulate the Assembly of Multimolecular Focal Complexes Associated with Actin Stress Fibers, Lamellipodia, and Filopodia. Cell, Volume 81, Issue 1, 7 April 1995, Pages 53-62

31 Kranewitter W.J., Danninger, and Gimona. GEF at Work: Vav in Protruding Filopodia. Cell Motility and the Cytoskeleton 49:154–160 (2001)

32 Launay S. Understanding actin turnover – no longer a mere speckle on the horizon. Trends in Cell Biology, Volume 12, Issue 5, 1 May 2002, Page 212

33 Condeelis J. Life at the leading edge the formation of cell protrusions. Annu. Rev. Cell Biol. 1993. 9:411-44

34 Kabsch W, Mannherz HG, Suck D, Pai EF, Holmes KC. Atomic structure of the actinDNase 1 complex Nature. 1990 Sep 6;347(6288):21-2.

35 Kenneth C. Holmes, David Popp, Werner Gebhard & Wolfgang Kabsch. Atomic model of the actin filament. Nature 347, 44 - 49 (06 September 1990)

36 Marie-France Carlier, Dominique Pantaloni. Control of Actin Dynamics in Cell Motility Journal of Molecular Biology, Volume 269, Issue 4, 20 June 1997, Pages 459-467

37 Walsh, T. P., Weber, A., Higgins, J., Bonder, E. M. & Mooseker, M. S. (1984). Effect of villin on the kinetics of actin polymerization. Biochemistry, 23, 2613± 2621.

38 Svitkina TM, Borisy GG. Arp2/3 Complex and Actin Depolymerizing Factor/Cofilin in Dendritic Organization and Treadmilling of Actin Filament Array in Lamellipodia. J Cell Biol. 1999 May 31;145(5):1009-26.

39 Mullins, R.D., J.A. Heuser, and T.D. Pollard. Crystal structures of actin-related protein 2/3 complex with bound ATP or ADP1998.Proc. Natl. Acad.Sci. USA.95:6181–6186)

40 Döbereiner HG, Dubin-Thaler B, Giannone G, Xenias HS, Sheetz MP. Dynamic Phase Transitions in Cell Spreading. Phys Rev Lett. 2004 Sep 3;93(10):108105.

41 Rottner, K. et al. (1999) VASP dynamics during lamellipodial protrusion. Nat. Cell Biol. 1, 321–322

42 Kaksonen M, Peng HB, Rauvala H. Association of cortactin with dynamic actin in lamellipodia and on endosomal. J Cell Sci. 2000 Dec;113 Pt 24:4421-6.

43 Stossel TP, Condeelis J, Cooley L, Hartwig JH, Noegel A, Schleicher M, Shapiro SS. Filamins as integrators of cell mechanics and signaling Nat Rev Mol Cell Biol. 2001 Feb;2(2):138-45.

44 Rivero F., B Koppel, B Peracino, S Bozzaro, F Siegert, CJ Weijer, M Schleicher, R Albrecht and AA Noegel. The role of the cortical cytoskeleton: F-actin crosslinking proteins protect against osmotic stress, ensure cell size, cell shape and motility, and contribute to phagocytosis and development. Journal of Cell Science, Vol 109, Issue 11 2679-2691, Copyright © 1996 by Company of Biologists

45 Ananthakrishnan R, Ehrlicher A. The Forces Behind Cell Movement. Int J Biol Sci. 2007 Jun 1;3(5):303-17.

46 Small JV. Lamellipodia architecture: actin filament turnover and the lateral flow of actin filaments during motility. Semin Cell Biol. 1994 Jun;5(3):157-63.

47 Holmes K.C., Popp, Gebhard & Kabsch. Atomic model of the actin filament. Nature 347, 44 - 49 (06 September 1990).

48 Carlier MF, Laurent V, Santolini J, Melki R, Didry D, Xia GX, Hong Y, Chua NH, Pantaloni D. Actin Depolymerizing Factor (ADF/Cofilin) Enhances the Rate of Filament Turnover: Implication in Actin-based Motility J Cell Biol. 1997 Mar 24;136(6):1307-22.

49 Maciver S.K. How ADF/cofilin depolymerizes actin filaments. Current Opinion in Cell Biology 1998, 10:140-144

50 Abercrombie, M. (1980) The crawling movement of metazoan cells. Proc. R. Soc. Lond., 207, 129–147.

51 Horwitz R. and D Webb. Cell Migration. Current Biology Vol 13 No 19 R756

52 Alberts B., Bray, D., Johnson, A., Lewis, J., Raff, M., Roberts, K. & Walter, P. (1998) Essential Cell Biology: An Introduction to the Molecular Biology of the Cell. New York: Garland.

53 Harris AK, P Wild, and D Stopak. Silicone rubber substrata a new wrinkle in the study of cell locomotion. Science, Vol 208, Issue 4440, 177-179

54 Lee J, Leonard M, Oliver T, Ishihara A, Jacobson K. Traction Forces Generated by Locomoting Keratocytes. J Cell Biol. 1994 Dec;127(6 Pt 2):1957-64.

55 Horwitz, A.R. and Parsons, J.T. (1999). Cell migration—movin' on. Science 286, 1102–1103.

56 Zamir E, Geiger B. Molecular complexity and dynamics of cell-matrix adhesions. J Cell Sci. 2001 Oct;114(Pt 20):3577-9.

57 Hynes RO. Integrins: versatility, modulation, and signaling in cell adhesion. Cell. 1992 Apr 3;69(1):11-25.

58 Fletcher SJ, Rappoport JZ. Moving forward: polarised trafficking in cell migration. Trends Cell Biol. 2010 Feb;20(2):71-8. Epub 2010 Jan 12.

59 Abercrombie M., Heaysman and Pegrum. The locomotion of fibroblasts in culture : : III. Movements of particles on the dorsal surface of the leading lamella Experimental Cell Research, Volume 62, Issues 2-3, October 1970, Pages 389-398.

60 Lee, J., Ishihara, A., Theriot, J.A., and Jacobson, K. (1993). Principles of locomotion for simple-shaped cells. Nature 362, 167–171.

61 Kucik, D.F. et al. (1990) Cell migration does not produce membrane flow. J. Cell Biol. 111, 1617–1622

62 Thompson, D.A.W. (1942). On Growth and Form, 2nd Edition (Cambridge: Cambridge Univ. Press).

63 Mogilner A, and K Keren. The Shape of Motile Cells. Current Biology 19, R762–R771, September 15, 2009

64 Atilgan, E., Wirtz, D., and Sun, S.X. Morphology of the lamellipodium and organization of actin filaments at the leading edge of crawling cells. Biophys J. 89, 3589–3602 (2005).

65 Dailey, M. E., Maintaining live cells and tissue slices in the imaging setup., in Imaging Neurons: A Laboratory Manual, Yuste, R., Lanni, F., and Konnerth, A. (eds.), Cold Spring Harbor Press, Cold Spring Harbor, New York, pages 10.1-10.7 (2000).

66 Mogilner A. and Edelstein-Keshet Regulation of Actin Dynamics in Rapidly Moving Cells A Quantitative Analysis. Biophys J. 2002 September; 83(3): 1237–1258.

67 Abraham VC, Krishnamurthi V, Taylor DL, Lanni F. The actin-based nanomachine at the leading edge of migrating cells. Biophys J. 1999 Sep;77(3):1721-32.

68 Boquet I, Boujemaa R, Carlier MF, Préat T. Ciboulot regulates actin assembly during Drosophila brain metamorphosis. Cell. 2000 Sep 15;102(6):797-808.

69 Dickenson, R. & Purich, D. (2002) Clamped-filament elongation model for actin-based motors. Biophys. J.,82, 606–617.

70 Kuo SC, McGrath JL. Steps and fluctuations of Listeria monocytogenes during actin-based motility. Nature. 2000 Oct 26;407(6807):1026-9.

71 Euteneuer U and M Schliwa. Persistant, directional motility of cells and cytoplasmic fragments in the absence of microtubules. Nature Vol 30. P58-61 1984

72 Keren K, Z Pincus, G Allen, E L. Barnhart, GMarriott5 A Mogilner & J Theriot. Mechanism of shape determination in motile cells. Nature 453, 475-480 (2008)

73 Lee J and K Jacobson. The composition and dynamics of cell-substratum adhesions in locomoting fish keratocytes. Journal of Cell Science 110, 2833-2844 (1997)

74 Chen C. J Alonso, E Ostuni, G Whitesides and D Ingber. Cell shape provides global control of focal adhesion assembly. Biochemical and Biophysical Research Communications 307 (2003) 355–361

75 Thery M. A Pepin, E Dressaire Y Chen and M Bornens. Cell Distribution of Stress Fibres in Response to the Geometry of the Adhesive Environment. Cell Motility and the Cytoskeleton 63:341–355 (2006)

76 Lehnert, D., Wehrle-Haller, B., David, C., Weiland, U., Ballestrem, C., Imhof, B.A., and Bastmeyer, M. (2004). Cell behaviour on micropatterned substrata:

limits of extracellular matrix geometry for spreading and adhesion. J. Cell Sci. 117, 41–52.

77 Brock, A., Chang, E., Ho, C.C., LeDuc, P., Jiang, X., Whitesides, G.M., and Ingber, D.E. (2003). Geometric determinants of directional cell motility revealed using microcontact printing. Langmuir 19, 1611–1617.

78 Lewis, L., Verna, J.M., Levinstone, D., Sher, S., Marek, L., and Bell, E. (1982). The relationship of fibroblast translocations to cell morphology and stress fibre density. J. Cell Sci. 53, 21–36.

79 Raja Paul, Patrick Heil, Joachim P. Spatz, and U Schwarz. Propagation of Mechanical Stress through the Actin Cytoskeleton toward Focal Adhesions: Model and Experiment. Biophysical Journal Volume 94 February 2008 1470–1482

80 Neves, S.R., Tsokas, P., Sarkar, A., Grace, E.A., Rangamani, P., Taubenfeld, S.M., Alberini, C.M., Schaff, J.C., Blitzer, R.D., Moraru, I.I., et al. (2008). Cell shape and negative links in regulatory motifs together control spatial information flow in signaling networks. Cell 133, 666–680.

81 Meyers, J., Craig, J., and Odde, D.J. (2006). Potential for control of signaling pathways via cell size and shape. Curr. Biol. 16, 1685–1693.

82 Maree, A.F., Jilkine, A., Dawes, A., Grieneisen, V.A., and Edelstein-Keshet, L. (2006). Polarization and movement of keratocytes: a multiscale modelling approach. Bull. Math. Biol. 68, 1169–1211.

83 Meinhardt, H., and Gierer, A. (2000). Pattern formation by local self-activation and lateral inhibition. Bioessays 22, 753–760.

84 Kharitonova, M.A., and Vasiliev, J.M. (2008). Controlling cell length. Semin. Cell Dev. Biol. 19, 480–484.

85 Hepler P. and B. Palevitz. Microtubules and Microfilaments. Ann. Rev. Plant Physiol 1974. 25:309-62

86 Heald R, Nogales E. Microtubule dynamics. J Cell Sci (January 2002)115 (Pt 1): 3–4.

87 Hideki Yamaguchi1, Jeffrey Wyckoff1,2 and John Condeelis. Cell migration in tumors. Current Opinion in Cell Biology 2005, 17:559–564

88 Alissa M. Weaver. Invadopodia: specialized cell structures for cancer invasion. Clin Exp Metastasis (2006) 23:97–105

89 Roberto Buccione, James D. Orth and Mark A.McNiven. Foot and mouth: Podosomes, Invadopodia and circular dorsal ruffles. Focus on Cytoskeletal Dynamics. Vol 5. Aug 2004 647-657

90 Doyle, A.D., Wang, F.W., Matsumoto, K., and Yamada, K.M. (2009). One-dimensional topography underlies three-dimensional fibrillar cell migration. J. Cell Biol. 184, 481–490.

91 Wolf, K., Mazo, I., Leung, H., Engelke, K., von Andrian, U.H., Deryugina, E.I., Strongin, A.Y., Brocker, E.B., and Friedl, P. (2003). Compensation mechanism in tumor cell migration: mesenchymal-amoeboid transition after blocking of pericellular proteolysis. J. Cell Biol. 160, 267–277

92 Friedl, P., and Wolf, K. (2009). Proteolytic interstitial cell migration: a fivestep process. Cancer Metastasis Rev. 28, 129–135.

93 Sharona Even-Ram and Kenneth M Yamada. Cell migration in 3D matrix. Current Opinion in Cell Biology 2005, 17:524–532

94 Cullity, B.D., Stock, S.R.(Eds.), Elements of XRD, London, 1978.

95 Dimilla, P., Barbee, K. & Lauffenburger, D. (1991) Mathematical model for the effects of adhesion and mechanics on cell migration speed. Biophys. J., 60, 15–37.

96 Brauner H. Corrosion resistance and biocompatibility of physical vapour deposition coatings for dental applications. Surface and Coatings Technology Volume 62, Issues 1-3, 10 December 1993, Pages 618-625

97 Jonesa C.W. D. Smolinskia, A. Keoghb, T.B. Kirka, M.H. Zheng. Confocal laser scanning microscopy in orthopaedic research. Progress in Histochemistry and Cytochemistry 40 (2005) 1–71

98 Hader D- P, editor. Image analysis in biology. Boca Raton, FL: CRC Press; 1992.

99 Wijnaendts van Resandt, R.W., Marsman, H.J.B., Kaplan, R., Davoust, J., Stelzer, E.H.K., Stricker, R., 1985. Optical fluorescence microscopy in three dimensions: microtomoscopy. J. Microscopy 138, 29–34.

100 Petran M, Hadravsky D. M. Egger AND R Galambos. Tandem-Scanning Reflected-Light Microscope. Journal of the optical society of America. Volume 58, number 5 May 1968

101 Errington RJ, White NS. Measuring dynamic cell volume in situ by confocal microscopy. In: Paddock S, editor. Confocal microscopy methods and protocols. Totowa, NJ: Humana Press Inc.; 1999. p. 315–40.

102 Corle T.R. and Kino G.S., Confocal Scanning Optical Microscopy and Related Imaging Systems, Academic Press, San Diego (1996).

103 Buckwalter JA. Articular cartilage injuries. Clin Orthop Rel Res 2002:21–37.

104 Dailey, M. E. (1999) in Imaging: A Laboratory Manual (Yuste, R., and Lanni, F., and Konnerth, A., Eds.), in press, Cold Spring Harbor Laboratory Press, NY.

105 Phillips K.P., Zhou and Baltz. Fluorophore toxicity in mouse eggs and zygotes. Zygote 6 (May), pp 113–123. 1998

106 Rigaut JP, Carvajal-Gonzalea S, Vassy J. Confocal image cytometry—quantitative analysis of threedimensional images obtained by confocal scanning microscopy. In: Hader DP, editor. Image analysis in biology. Boca Raton: CRC Press; 1992. p. 109–33.

107 O'Toole P.J., Morrison, Cherry. Investigations of spectrinlipid interactions using Fluoresceinphosphatidylethanolamine as a membrane probe. Biochimica et Biophysica Acta 1466 (2000) 39^46

108 Wall, J., C. A. Golding, M. Van Veen, and P. O'Shea. 1995. The use of fluoresceinphosphatidylethanolamine (FPE) as a real-time probe for peptide-membrane interactions. Mol. Membr. Biol. 12:183–192.

109 Choi H.-Y., D.A. Veal, and P. Karuso. Epicocconone, A New Cell-Permeable Long Stokes' Shift Fluorescent Stain for Live Cell Imaging and Multiplexing. Journal of Fluorescence, Vol. 16, No. 4, July 2006

110 Sund SE., Swanson, and Axelrod Cell Membrane Orientation Visualized by Polarized Total Internal Reflection Fluorescence. Biophysical Journal Volume 77 October 1999 2266–2283

111 Lassailly F, Griessinger E, Bonnet D,. Microenvironmental contaminations induced by fluorescent lipophilic dyes used for noninvasive in vitro and in vivo cell tracking. Blood (2010) 115:5347-5354

112 Epicocconone™ Fluorescent Cell Stain. Active Motif Catalog No.15004 (version A). http://www.activemotif.com/documents/135.pdf.

113 The University of Adelaide, Australia. Mycology Online http://www.mycology.adelaide.edu.au/Fungal_Descriptions/Hyphomycetes_(dematiaceous)/Epicoccum/.

114 Veal, D.A., Choi, H-Y., Sjöström , S., Cooney, B., David, S., Karuso, P. Monitoring Proteolytic Digestion using the Fluorophore Epicocconone. ASMS (American society for mass spectrometry) 55th Conference. June 3rd - 7th, 2007 Indianapolis, Indiana.

115 Coons, Albert; Creech HJ, Jones, RN (1941). "Immunological properties of an antibody containing a fluorescent group". Proc Soc Exp Biol Med 47: 200–202

116 Polack J, Van Noorden S: An Introduction to Immunocytochemistry: Current Techniques and Problems, Revised ed. Allen Press,. Oxford, Great Britain (1988)

117 Milstein C, Galfre G, Secher DS, Springer T. Monoclonal antibodies and cell surface antigens. Ciba Found Symp. 1979 Jun 27-29;(66):251-76.

118 Welson W. Wang, Dipankar Das, Xin L. Tang, Wladyslaw Budzynski, Mavanur R. Suresh. Antigen targeting to dendritic cells with bispecific antibodies. Journal of Immunological Methods, Volume 306, Issues 1-2, 30 November 2005, Pages 80-92.

119 Scotchford C.A., Edited by L Di Silvio, Cellular response to biomaterials. Chapter 18 462-473. Woodhead Publishing Limited (2008).

120 Britland S, Clark P, Connolly P, Moores G. Micropatterned substratum adhesiveness: A model for morphogenetic cues controlling cell behaviour. Exp Cell Res 1992, 198: 124–129.

121 Tan J, Saltzman WM. Topographical control of human neutrophil motility on micropatterned materials with various surface chemistry. Biomaterials 2002, 23: 3215–3225.

122 Keselowsky BG, Collard DM, Garcia AJ. Surface chemistry modulates fi bronectin conformation and directs integrin binding and specifi city to control cell adhesion. J Biomed Mater Res 2003, 66A: 247–259.

123 Rohde, S.L., Sputter Deposition, in ASM Handbook. 1994: Materials Park, Ohio. p. 573-581.

124 Stuart, R.V., Vaccum Technology, Thin Films, and Sputtering. 1983, London: Academic Press. 151.

125 Chapman, B., Glow Discharge Processes. 1980: John Wiley & Sons, Inc 406.

126 Ohring, M., Materials Science of Thin Films. 2nd ed. 2002, San Diego: Academic Press. 794.

127 Behrisch, R., ed. Sputtering by Particle Bombardment I. Physical Sputtering of Single-Element Solids. Vol. 47. 1981, Springer-Verlag: Berlin. 284.

128 Ellmer, K., Magnetron sputtering of transparent conductive zinc oxide: relation between the sputtering parameters and the electronic properties. Journal of Physics D: Applied Physics, 2000. 33: p. R17-R32.

129 Ellmer, K., Magnetron sputtering of transparent conductive zinc oxide: relation between the sputtering parameters and the electronic properties. Journal of Physics D: Applied Physics, 2000. 33: p. R17-R32.

130 Schneider, J.M., et al., Recent developments in plasma assisted physical vapour deposition. Journal of Physics D: Applied Physics, 2000. 33: p. R173–R186.

131 Narayan J., W.D. Fan, R.J. Narayan, P. Tiwari and H.H. Stadelmaier, Diamond, diamond-like and titanium nitride biocompatible coatings for human-body parts, Mater. Sci. Eng. B 25 (1994), pp. 5–10.

132 Grössner-Schreiber B., M Griepentrog, I Haustein, W D Müller, K P Lange, H Briedigkeit, U B Göbel Plaque formation on surface modified dental implants. An in vitro study Clinical oral implants research. 01/01/2002; 12(6):543-51.

133 Fisher J. , X.Q. Hu, T.D. Stewart, S. Williams, J.L. Tipper, E. Ingham, M.H. Stone, C. Davies, P. Hatto, J. Bolton, M. Riley, C. Hardaker, G.H. Isaac and G. Berry, Wear of surface engineered metal-on-metal hip prostheses, J. Mater. Sci.-Mater. Med. 15 (2004) (3), pp. 225–235

134 Cyster L. A. , K. G. Parker, T. L. Parker, D. M. Grant The effect of surface chemistry and nanotopography of titanium nitride (TiN) films on primary hippocampal neurones. Biomaterials, Volume 25, Issue 1, January 2004, Pages 97-107

135 Jones M. I., I. R. McColl, D. M. Grant, K. G. Parker, T. L. Parker. Protein adsorption and platelet attachment and activation, on TiN, TiC, and DLC coatings on titanium for cardiovascular applications. J Biomed Mater Res. 2000 Nov;52(2):413-21.

136 Kola P. V., S. Daniels, D. C. Cameron and M. S. J. Hashmi. Magnetron sputtering of tin protective coatings for medical applications. Journal of Materials Processing Technology Volume 56, Issues 1-4, January 1996, Pages 422-430

137 Türkana Uğur, Öztürkb Orhan and Eroğluc Ahmet. Metal ion release from TiN coated CoCrMo orthopedic implant material. Surface and Coatings Technology Volume 200, Issues 16-17, 27 April 2006, Pages 5020-5027

138 Ma S., Xua K., Jie W. Wear behavior of the surface of Ti–6Al–4V alloy modified by treating with a pulsed d.c. plasma-duplex process. Surface & Coatings Technology 185 (2004) 205– 209

139 Zhang Feng, Zheng, Chen, Liu, Chen, Jiang. In vivo investigation of blood compatibility of titanium oxide films. Journal of Biomedical Materials Research Volume 42, Issue 1, pages 128–133, October 1998

140 Randeniya L.K., Bendavid, Martin, Amin, Rohanizadeh, Tang, Cairney. Thin-film nanocomposites of diamond-like carbon and titanium oxide; Osteoblast adhesion and surface properties. Diamond & Related Materials 19 (2010) 329–335

141 Hocking L.M. and A. D. Rivers. The spreading of a drop by capillary action. J . Fluid Msch. (1982), vol. 1 2 1 , pp. 425-442

142 Davis SH. 1983. Contact-line problems in fluid mechanics. J. Appl. Mech. 50:977–82

143 Anderson D.M. and G. B. McFadden and A.A. Wheeler. Diffuse-interface methods in fluid mechanics. Annu. Rev. Fluid Mech. 1998. 30:139–65

144 Frisch, O. Thoumine, Predicting the kinetics of cell spreading, Journal of Biomechanics 35, pp. 1137-1141 (2002)

145 Albrecht-Buehler, G., 1987. Role of cortical tension in fibroblast shape and movement. Cell Motility and the Cytoskeleton 7, 54–67.

146 Heidemann, S.R., Kaech, S., Buxbaum, R.E., Matus, A., 1999. Direct observations of the mechanical behaviors of the cytoskeleton in living fibroblasts. Journal of Cell Biology 145, 109–122.

147 Thoumine, O., Cardoso, O., Meister, J.-J., 1999. Changes in the mechanical properties of fibroblasts during spreading: a micromanipulation study. European Biophysics Journal 28, 222–234.

148 Kan, H.-C., Shyy, W., Udaykumar, H.S., Vigneron, P., Tran-Son-Tay, R., 1999. Effects of nucleus on leukocyte recovery. Annals of Biomedical Engineering 27, 648–655.

149 Brochard-Wyart, F., de Gennes, P.G., 1992. Dynamics of partial wetting. Advances in Colloid and Interface Science 39, 1–11.

150 Dembo M. and Harlow F. Cell motion, contractile networks, and the physics of interpenetrating reactive flow. BIOPHYS. J. Biophysical Society Volume 50 July 1986 109-12

151 Zhao S., Wei G. W. High-order FDTD methods via derivative matching for Maxwell's equations with material interfaces. Journal of Computational Physics, Volume 200, Issue 1, 10 October 2004, Pages 60-103

152 Botterill, N.W., Deposition and Characterisation of thin film nickel-titanium shape memory alloys for microactuation, in M3. 2002, University of Nottingham: Nottingham. p. 207.

153 Tarey R. D. , Rastogi and Chopra. Characterisation of thin films by glancing incidence x-ray diffraction. The Rigaku Journal Vol. 4/ No. 1/ 2 / 1987

154 Smith, G.C., Surface Analysis by Electron Spectrocopy: Measurement and Interpretation. 1994, London and New York: Plenum Press. 156.

155 Briggs, D. and J.T. Grant, eds. Surface Analysis by Auger and X-ray Photoelectron Spectroscopy. 2003, IM Publications & SurfaceSpectra: Chichester.

156 Yang H. The effects of free surfaces and molecular confinement on relaxation processes in thin polymer films. 2008 University of Nottingham, Nottingham p.70-76

157 Motschmann H. & Teppner. Ellipsometry in Interface Science, in Novel methods to Study Interfacial Layers, edited by R. Miller, D. Moebius, Elsevier (2001)

158 Kevin Langley, Nanoscience Group, University of Nottingham, Nottingham, NG7 2RD.

159 Sinha R. K., F. Morris, S. A. Shah, and R. S. Tuan, "Surface composition of orthopaedic implant metals regulates cell attachment, spreading and cytoskeletal organization of primary human osteoblasts in vitro," Clin. Orthop. Rel. Res., 305, 258–272 (1994).

160 Gallimore L. Oxford Centre for Collaberative and Applied Mathematics. Mathematical Institute. 24–29 St Giles' Oxford. OX1 3LB

161 Maini, R. Sohal, S.J. Performance Evaluation of Prewitt Edge Detector for Noisy Images. GVIP Journal, Vol 6 Issue 3. December 2006

162 McAndrew, A. Introduction to Digital Image Processing with Matlab. Thomson Course Technology, Boston Massachusetts. 2004.

163 Catherine Desbleds Mansard, Emmanuelle P. Canet Soulas, Alfred Anwander, Linda Chaabane, Bruno Neyran, Jean-Michel Serfaty, Isabelle E. Magnin, Philippe C. Douek, and Maciej Orkisz1. Quantification of Multicontrast Vascular MR Images With NLSnake, an Active Contour Model: In Vitro Validation and In Vivo Evaluation. Magnetic Resonance in Medicine 51:370–379 (2004)

164 Perona P. and Malik. Scale-Space and Edge Detection Using Anisotropic Diffusion. Transactions on pattern analysis and machine intelligence, VOL. 12. NO. 7. JULY 1990

165 Lee J. Oxford Centre for Industrial and Applied Mathematics. Wolfson Building, Parks Road, Oxford OX1 3QD

166 Meyer U. T. Meyer. B. Jones. Attachment kinetics, proliferation rates and vinculin assembly of bovine osteoblasts cultured on different pre-coated artificial substrates. JOURNAL OF MATERIALS SCIENCE: MATERIALS IN MEDICINE 9 (1998) 301 – 307

167 Puleo D. A. and R. Bizios. Formation of focal contacts by osteoblasts cultured on orthopedic biomaterials. Journal of Biomedical Materials Research, Vol. 26, 291-301 (1992)

168 Choi H.Y., D.A. Veal, and P. Karuso. A New Cell-Permeable Long Stokes' Shift Fluorescent Stain for Live Cell Imaging and Multiplexing. Journal of Fluorescence, Vol. 16, No. 4, July 2006

169 Fries R. and J. Modestino, An empirical study of selected approaches to the detection of edges in noisy digitized images, TR 77-1 Electrical and Systems engineering department, Rensselaer Polytechnic Institute, 1977.

170 Modestino J. and R. Fries, Edge detection in noisy images using recursive digital filtering, Computer Graphics and Image Processing 6, 1977, 409-433.

171 Morse B.. Lecture 13: Edge Detection. Brigham Young University, Utah USA 2000. Available online: http://homepages.inf.ed.ac.uk/rbf/CVonline/LOCAL_COPIES/MORSE/edges.pdf

172 Yezzi A, S Kichenassamy, A Kumar, P Olver, and A Tannenbaum. A Geometric Snake Model for Segmentation of Medical Imagery. IEEE TRANSACTIONS ON MEDICAL IMAGING, VOL. 16, NO. 2, APRIL 1997.

173 Feng B. , J. Weng, B. C. Yang, S. X. Qu, X. D. Zhang Characterization of surface oxide films on titanium and adhesion of osteoblast cells. Biomaterials, Volume 24, Issue 25, November 2003, Pages 4663-4670

174 Van Kooten T.G., J.M. Schakenraad, H.C. Van der Mei and H.J. Busscher, Influence of substratum wettability on the strength of adhesion of human fibroblasts. Biomaterials 13 (1992), pp. 897–904.

175 Shieh, Lei Wang, Tsai, and Hsiung Hon, Effects of Coffee-Bean-Like Morphology and Graded Interlayer on Texture Evolution of Plasma-Enhanced Chemical-Vapor-Deposited Ti-C-N Films. J. Am. Ceram. Soc., 85 636–40 (2002)

176 Nyaiesh R., E. L. Garwin, F. K. King, and R. E. Kirby. Properties of thin antimultipactor TiN and Cr2O3 coatings for klystron windows. J. Vac. Sci. Technol. A Volume 4, Issue 5, pp. 2356-2363 (1986)

177 Jones M. Haemocompatibility and characterisation of candidate coatings for a heart valve prosthesis. University of Nottingham, Nottingham 1999. page 214

178 Scott M. 32,000 years of sutures. NATNEWS. May 1983;20(5):15-7.

179 Behrisch, R., ed. Sputtering by Particle Bombardment I. Physical Sputtering of Single-Element Solids. Vol. 47. 1981, Springer-Verlag: Berlin. 284.

180 Mary C., T. Le Mogne, B. Beaugiraud, B. Vacher, J.-M. Martin, S. Fouvry. Tribochemistry of a Ti Alloy Under Fretting in Air: Evidence of Titanium Nitride Formation. Tribol Lett (2009) 34:211–222

181 Watanabe D. & Castles JR. The Ordered Structure of TiO. Acta Cryst. (1967). 23, 307

182 Van Kooten T.G, J.M. Schakenraad, H.C. van der Mei, H.J. Busscher. Influence of substratum wettability on the strength of adhesion of human fibroblasts. Biomaterials 13 (1992) 897.

183 Feng B, J. Weng, B.C. Yang, S.X. Qu, X.D. Zhang. Characterization of surface oxide films on titanium and adhesion of osteoblast. Biomaterials 24 (2003) 4663.

184 Vasile M.J., Emerson, Baiocchi. Reactive pulsed laser deposition of TiN. J. Vac. Sci. Technol. A 8 1991. 99.

185 Savvides N. , Window, Electrical transport, optical properties, and structure of TiN films synthesized by low energy ion assisted deposition. J. Appl. Phys. 64 1988. 225.

186 Han J-H and Yoo. Reusable, polyethylene glycol-structured microfluidic channel for particle immunoassays. Journal of Biological Engineering 2009, 3:6.

187 Sumner AL, Menke, Dubowski, Newberg, Penner, Hemminger, Wingen, Brauersc and Finlayson-Pitts. The nature of water on surfaces of laboratory systems and implications for heterogeneous chemistry in the troposphere. Phys. Chem. Chem. Phys., 2004, 6, 604–613

188 Dussan E.B. On the spreading of liquids on solid surfaces: static and dynamic contact lines. Ann. Rev. Fluid Mech. 1979. 11: 371-400

189 Altankov G. and Groth. Reorganization of substratum-bound fibronectin on hydrophilic and hydrophobic materials is related to biocompatibility. JOURNAL OF MATERIALS SCIENCE: MATERIALS IN MEDICINE Volume 5, Numbers 9-10, 732-737, DOI: 10.1007/BF00120366.

190 Uggeri J, S Guizzardi, R Scandroglio, R Gatti.Adhesion of human osteoblasts to titanium: A morpho-functional analysis with confocal microscopy. Micron 41 (2010) 210–219

191 Gatti R, G. Orlandini, J. Uggeri, S. Belletti, C. Galli, M. Raspanti, R. Scandroglio, S. Guizzardi. Analysis of living cells grown on different titanium surfaces by time-lapse confocal microscopy. Micron 39 (2008) 137–143

192 Scotchford C.A., M. Ball, M. Winkelmann, J. Voros, C. Csucs, D.M. Brunette, G. Danuser, M. Textor. Chemically patterned, metal-oxide-based surfaces produced by photolithographic techniques for studying protein- and cell-interactions. II: Protein adsorption and early cell interactions. Biomaterials 24 (2003) 1147–1158

193 Brunk U, Collins VP, Arro E. The fixation, dehydration, drying and coating of cultured cells of SEM. J Microsc. 1981 Aug;123(Pt 2):121-31.

194 Ferguson D.M.L., L.M., Chan, P.Y., Springer, T.A., and Golan, D.E. (1996). Vizualization of CD2 interaction with LFA-3 and determination of the two-dimensional dissociation constant for adhesion receptors in a contact area. J. Cell Biol. 132, 465–477.

195 Yauch, R.L., Felsenfeld, D.P., Kraeft, S.K., Chen, L.B., Sheetz, M.P., and Hemler, M.E. (1997). Mutational evidence for control of cell adhesion through integrin diffusion/clustering, independent of ligand binding. J. Exp. Med. 186, 1347–1355.

196 Shenoy, V.B., and Freund, L.B. (2005). Growth and shape stability of a biological membrane adhesion complex in the diffusion mediated regime. Proc. Natl. Acad. Sci. USA 102, 3213–3218.

197 Chamaraux, F., Fache, S., Bruckert, F., and Fourcade, B. (2005). Kinetics of cell spreading. Phys. Rev. Lett. 94, 158102.

198 Bereiter-Hahn, J., Lu¨ ck, M., Miebach, T., Stelzer, H.K., and Vo¨ th, M. (1990). Spreading of trypsinized cells: Cytoskeletal dynamics and energy requirements. J. Cell Sci. 96, 171–188.

199 Cai, Y., Biais, N., Gianone, G., Tanase, M., Ladoux, B., Hofman, J., Wiggins, C.H., and Sheetz, M.P. (2006). Nonmuscle myosin IIA-dependent force inhibits cell spreading and drives F-actin flow. Biophys. J. 91, 3907–3920.

200 Xiong Y, P Rangamani, M Fardin, A Lipshtat, B Dubin-Thaler, O Rossier, M Sheetz, and R Iyengar. Mechanisms Controlling Cell Size and Shape during Isotropic Cell Spreading. Biophysical Journal Volume 98 May 2010 2136–2146

201 Dubin-Thaler B, G Giannone, H Dobereiner, and M P. Sheetz. Nanometer Analysis of Cell Spreading on Matrix-Coated Surfaces Reveals Two Distinct Cell States and STEPs. Biophysical Journal Volume 86 March 2004 1794–1806.

202 Yang Y, Cavin R, Ong JL. Protein adsorption on titanium surfaces and their effect on osteoblast attachment. J Biomed Mater Res A. 2003 Oct 1;67(1):344-9.

203 Ko HC, Han JS, Bächle M, Jang JH, Shin SW, Kim DJ. Initial osteoblast-like cell response to pure titanium and zirconia/alumina ceramics. Dent Mater. 2007 Nov;23(11):1349-55. Epub 2007 Jan 2.

204 Koenig AL, Gambillara V, Grainger DW. Correlating fibronectin adsorption with endothelial cell adhesion and signaling on polymer substrates. J Biomed Mater Res A 2003;64:20–37.

205 Culp LA, Sukenik CN. Cell type-specific modulation of fibronectin adhesion functions on chemically-derivatized selfassembled monolayers. J Biomater Sci Polym Ed 1998;9:1161–1176.

206 Sousa S. R., M. Lamghari, P. Sampaio, P. Moradas-Ferreira, M. A. Barbosa. Osteoblast adhesion and morphology on TiO2 depends on the competitive preadsorption of albumin and fibronectin. J Biomed Mater Res A. 2008 Feb;84(2):281-90.

207 Cavalcanti-Adam E, Volberg, Micoulet, Kessler, Geiger, and Spatz. Cell Spreading and Focal Adhesion Dynamics Are Regulated by Spacing of Integrin Ligands. Biophysical Journal Volume 92 April 2007 2964–2974.

208 Siebersa M. C., ter Bruggeb, Walboomersa and Jansen. Integrins as linker proteins between osteoblasts and bone replacing materials. A critical review. Biomaterials Volume 26, Issue 2, January 2005, Pages 137-146

209 Vogler EA, Bussian RW. Short-term cell-attachment rates: a surface sensitive test of cell-substrate compatibility. J Biomed Mater Res 1987;21:1197–211.

210 Vogler EA. How water wets biomaterials. In: Morra M, editor. Water in biomaterials surface science. New York: Wiley; 2001. p. 269–90.

211 Bruinsma, R., Behrisch, A. & Sackmann, E. Vesicles as osmotic motors. (1999) Phys. Rev. E 61, 4253–4267.

212 Komura, S. & Andelman, D. Adhesion-induced lateral phase separation in membranes. (2000) Eur. Phys. J. E 3, 259–271.

213 Reinhart-King, M Dembo and D Hammer. The Dynamics and Mechanics of Endothelial Cell Spreading. Biophysical Journal Volume 89 July 2005 676–689.

214 McClary KB, Ugarova T, Grainger DW. Modulating fibroblast adhesion, spreading, and proliferation using self-assembled monolayer films of alkylthiolates on gold. J Biomed Mater Res 2000;50:428–439

215 Brangwynne, C.P., MacKintosh, F.C., Kumar, S., Geisse, N.A., Talbot, J., Mahadevan, L., Parker, K.K., Ingber, D.E., and Weitz, D.A. (2006). Microtubules can bear enhanced compressive loads in living cells because of lateral reinforcement. J. Cell Biol. 173, 733–741.

216 Rodriguez, O.C., Schaefer, A.W., Mandato, C.A., Forscher, P., Bement, W.M., and Waterman-Storer, C.M. (2003). Conserved microtubule-actin interactions in cell movement and morphogenesis. Nat. Cell Biol. 5, 599–609.

217 Chang, Y.C., Nalbant, P., Birkenfeld, J., Chang, Z.F., and Bokoch, G.M. (2008). GEF-H1 couples nocodazole-induced microtubule disassembly to cell contractility via RhoA. Mol. Biol. Cell 19, 2147–2153.

218 Dujardin, D.L., Barnhart, L.E., Stehman, S.A., Gomes, E.R., Gundersen, G.G., and Vallee, R.B. (2003). A role for cytoplasmic dynein and LIS1 in directed cell movement. J. Cell Biol. 163, 1205–1211.

219 Prigozhina, N.L., and Waterman-Storer, C.M. (2006). Decreased polarity and increased random motility in PtK1 epithelial cells correlate with inhibition of endosomal recycling. J. Cell Sci. 119, 3571–3582.

220 Woodruff AM, Jones, Farrar, Grant, Scotchford. Human osteoblast cell spreading and vinculin expression upon biomaterial surfaces. J Mol Hist (2007) 38:491–499.

221 Mckinley, K., Allison, F., Scotchford, S., Grant, D., Oliver, J., King, J., Wood, J. & Brown, P. (2004) Comparison of environmental scanning electron microscopy with high vacuum scanning electron microscopy as applied to the assessment of cell morphology. J. Biomed. Mat. Res., 69A, 359–366.

222 Baugh L, Vogel V. Structural changes of fibronectin adsorbed to model surfaces probed by fluorescence resonance energy transfer. J Biomed Mater Res A 2004;69:525–534.

223 Grainger DW, Pavon-Djavid G, Migonney V, Josefowicz M. Assessment of fibronectin conformation adsorbed to polytetrafluoroethylene surfaces from serum protein mixtures and correlation to support of cell attachment in culture. J Biomater Sci Polym Ed 2003;14:973–988.

224 Dailey M. and M Waite. Confocal Imaging of Microglial Cell Dynamics in Hippocampal Slice Cultures. Methods Volume 18, Issue 2, June 1999, Pages 222-230.

225 Padday JA. 1996. Level Set Methods Cambridge: Cambridge Univ. Press

226 Mahalingam S. & Edirisinghe M. J. Novel preparation of nitrogen-doped titanium dioxide films. J. Phys. D: Appl. Phys. 41 (2008) 215406.

227 Wieland M., Chehroudi, Textor, Brunette. Use of Ti-coated replicas to investigate the effects on fibroblast shape of surfaces with varying roughness and constant chemical composition. J Biomed Mater Res. 2002 Jun 5;60(3):434-44.